

2003 LUCAS ANNUAL REPORT

SEPTEMBER 24, 2003

It is hard to describe the excitement we feel in this first year of the second decade of the Richard M. Lucas Center. We have been privileged to work in a time of great change and progress in medical imaging. We are very proud to see many advances made at the Center being used throughout the world to provide better understanding of biological processes and to improve patient care. Universities world-wide are rushing to develop capabilities for “bench to bedside” or “translational” research. We already have over a decade of accomplishment in this process and are accelerating our efforts.

As I look back over our first ten years, our major accomplishment was creating a team of exceptional individuals working in clinical medicine, physics, and engineering. This group has consistently contributed to the science of medical imaging with application to nearly all areas of medicine, including cancer, cardiovascular disease, neuroscience and diseases of aging. Specific accomplishments can be found in this year’s Lucas Report. The strength of our team is internationally recognized and has served us well in attracting top flight physicians, scientists, and students from all over the world. We have become a “Mecca” for individuals pursuing careers in medical imaging.

If this first decade was productive, interesting, and fun, our second decade promises to be even better. Developments in medical imaging have, until recently, been based primarily on advances in physics and engineering. It is now apparent that ideas coming from the fields of molecular biology and chemistry have the potential to radically improve our ability to image fundamental biological processes, such as gene expression, in living tissues. Stanford and the Lucas Center intend to become an international resource for this exciting research.

I am delighted to report that we have taken giant steps in 2003 which assure our prominence in this newly developing field of cellular and molecular imaging. Exceptional scientific talent requires exceptional facilities. The construction of the Richard M. Lucas Center in the early 1990’s permitted the recruitments of Drs. Gary Glover and Norbert Pelc to lead our physics and engineering efforts. To house our molecular imaging programs we began construction of a new building attached to the existing Lucas Center on July 11, 2003. On August 1, 2003 Sanjiv Sam Gambhir, an internationally recognized leader in molecular imaging, joined our faculty. Sam has not wasted a moment in attracting talent to Stanford and we now have nearly 40 individuals working in this field. With mixed emotions, we now project that by the time our construction has finished in the late fall of 2004 we will again be out of space because of the fast ramp-up in this new program and continued progress and growth in our other major areas of research. I am confident that we will develop a solution to this wonderful problem in the months ahead.

I have just recently returned from an extended sabbatical abroad which permitted me the luxury of added time to learn and think about fields that were new to me as well as to generate new ideas which may help our efforts at the Lucas Center. In my travels I was constantly asked how it was possible to develop a center which attained international stature within a decade. The location of our work at Stanford University was essential but not sufficient for our success. The Lucas Foundation through its financial support and constant encouragement has been the “secret” ingredient which has allowed us to prosper. I know that I speak for our entire faculty in conveying our deep thanks for your continued support.



Acknowledgements

With the 2003 Lucas Report we celebrate and reflect on another year of remarkable achievements and gratefully acknowledge the continued support of all our sponsors and collaborators.

Special thanks to:

The Richard M. Lucas Cancer Foundation

and

*The National Institutes of Health
NIH/NCRR P41 RR09784*

And many thanks to Kevin Murphy for the many hours of hard work and dedication in preparing this Annual Report for publication.

LUCAS CENTER 2003 ANNUAL REPORT

TABLE OF CONTENTS

Letter from Gary Glazer, M.D.	i
Acknowledgements	iii
Table of Contents	v
Lucas Overview and Updates	1
Lucas Center, Radiological Sciences Laboratory & the Center for Advanced MR Technology	3
Magnetic Resonance Research	5
<i>Neuroimaging -Technology Development</i>	5
<i>Diffusion & Perfusion Weighted Imaging</i>	5
<i>Cognitive Science</i>	7
<i>Cardiovascular Imaging</i>	8
<i>MR Spectroscopy</i>	8
<i>Interventional MRI</i>	9
Advanced Imaging Research	10
<i>3D Imaging Lab</i>	10
<i>Advanced X-ray Imaging</i>	10
<i>Outcomes and Cost Effectiveness</i>	11
Departmental Growth: Molecular Imaging Program at Stanford (MIPS)	12
Growing to Meet the Future: Lucas Expansion II	14
Lucas Center Faculty, Staff, Students & Collaborators	16
Awards & Honors	22
Grants Update: Strategic Research Development	23
Education & Training	26
NCI Training Program	26
Postgraduate Education	28
Center Updates	29
MR Systems, Education & Systems Support	29
Experimental Model Management	34
Neuroimaging	35
Cardiovascular Imaging	73
MR Spectroscopy	89
Interventional MRI	101
Molecular Imaging	109
3D Imaging	115
Advanced X-ray Imaging	129
Outcomes & Cost Effectiveness	139
Publications & Presentations	147

Lucas

Overview

& Updates

LUCAS CENTER OVERVIEW

Lucas Center, Radiological Sciences Laboratory & the Center for Advanced MR Technology

Gary H. Glover

Director, Radiological Sciences Laboratory

The Lucas Center is home to the Radiological Sciences Laboratory, a section of the Radiology Department, and in conjunction with the Electrical Engineering Department is host to the *Center for Advanced MR Technology*, an NIH-funded National Research Resource. Its state of the art imaging facilities support hundreds of on-campus and extramural researchers. The Radiology Department Chairman's offices are also located in the Center.

THE RADIOLOGICAL SCIENCES LABORATORY

The RSL comprises 10 faculty, approximately 50 graduate and postdoctoral students, 27 scientific staff and 7 administrative assistants, as well as our Administrative Director, Donna Cronister.

The faculty continue to serve in advisory roles to government and foundation agencies such as the NIH and Whitaker Foundation and in policy-making positions for international scientific societies such as the ISMRM and RSNA. A number of our students have garnered prestigious awards for their exceptional research achievements. Some of the Lab's honors of the past year are reviewed below.

Roland Bammer was invited to serve as Visiting Guest Professor in the Department of Radiology at the University of Vienna.

Susan Hobbs, post doctoral fellow for **Mark Bednarski**, was a Young Investigator Finalist for the prestigious Moore Award at 2003 ISMRM.

Matt Kirshen, a graduate student working with **John Desmond**, received a grant to conduct ethics research from Stanford's Committee on Ethical Dimensions of Neuroscience Research. He and John also obtained an OTL award to investigate brain correlates of recovery from concussion injury.

Michael Markl, scientific staff member, won the prestigious ISMRM Young Investigator Rabi Award. If that were not enough, he also garnered a RSNA Research Fellow Award last fall.

Scott Reeder, radiology resident and training fellow, also won a RSNA Research Fellow Award.

Zhifei Wen, graduate student working with **Rebecca Fahrig** and **Norbert Pelc**, won honorable mention for his poster, "X-ray tube in parallel magnetic fields" at the SPIE meeting.

Mike Moseley served the 5000-member ISMRM with great personal energy this past year as president-elect, and was installed as president at this year's meeting. Because of the SARS outbreak in Toronto and attendant travel restrictions, the meeting was postponed from May until July, which entailed a huge effort on the part of the ISMRM staff and Executive Committee, which Mike chairs. The meeting itself was a great success, in large part because of his work and that of other dedicated members. In addition, Mike serves on the steering committee for the annual meeting of the Society for Molecular Imaging.

Norbert Pelc was invited to serve on the Advisory Council of the newly formed National Institute of Biomedical Imaging and Bioengineering (NIBIB). He was also appointed Associate Chair for Research in the Department of Radiology

Gary Glover was invited to serve as a special consultant to the Director, on an Exceptional Service Appointment for the NIBIB.

RSL FACULTY RECRUITMENT

The RSL is in the process of recruiting two junior faculty to develop novel imaging approaches for pediatric radiology, in concert with Richard Barth, Associate Chair of Pediatric Radiology. This program should provide an exciting opportunity to make major advances in the fields of pediatric cancer, developmental biology, molecular imaging, cardiovascular diagnosis, therapy and basic science. In addition, two other positions will be opened shortly for faculty appointments in high field MRI, to take advantage of the soon-to-be installed 7T magnet (see below), and in the science of body MRI. In the context of the concurrent major expansion in molecular imaging with Sam Gambhir as director, major programmatic growth is thus under way in the department and the RSL.

THE NATIONAL CENTER FOR ADVANCED MR TECHNOLOGY AT STANFORD (CAMRT)

The Center is now in its eighth year of operation as a National Research Resource of the NIH's National Center for Research Resources. Outstanding progress has been made in all six of the core technology development areas that include reconstruction methods (Dwight Nishimura, EE Department, core director), imaging of brain activation (Gary Glover, core director and PI), diffusion and perfusion weighted imaging methods (Mike Moseley, core director), imaging of cardiovascular structure and function (Norbert Pelc, core director and CAMRT co-PI), spectroscopic imaging development (Dan Spielman, core director) and interventional MRI technique development (Kim Butts, core director). Some of this research is chronicled in the scientific reports that follow. The Center's National Advisory Board recently accepted James Pipe (Barrows Institute) as a new member to replace Andrew Maudsley. James will join Jeff Duerk, Dennis Parker, Adolf Pfefferbaum and Kamil Ugurbil.

LUCAS CENTER FACILITIES

The Center is undergoing an exciting, major expansion that will nearly double laboratory and office space. The expansion includes a new whole body 7T magnet, cyclotron, wet labs, hot labs, a 1000 sq. foot learning center and offices for faculty and students as well as visiting scholars. The 7T program is a research partnership with General Electric, which represents a particularly exciting opportunity. The radiolabeling facilities are part of the new Molecular Imaging Program, directed by newly recruited faculty Sam Gambhir. In addition, plans are underway to remodel the animal magnet suite for installation of a second 3T magnet.



Scene from second floor office in August, 2003. Wooden shoring is being installed between steel I beams so that digging to the next deeper level can commence. The hole will be approximately 40 feet deep, to accommodate the two sub-basements and some 300 tons of steel for shielding the magnet.

MAGNETIC RESONANCE RESEARCH

Neuroimaging

Imaging of Brain Activation - Technology Development

Gary Glover

Progress in the fMRI group (pages 37-40) has included work on spiral-in/out, high resolution imaging and development of real-time postprocessing and display. The Center has also been active in the FIRST BIRN schizophrenia testbed funded by the NCRR.

The spiral-in/out sequence has been adopted by most users of the Lucas Center performing fMRI for cognitive studies. A study was performed to compare the relative merits of this sequence at 1.5T and 3T against the spiral-in sequence (page 37). It was found that the new sequence is efficacious in reducing frontal lobe and medial temporal lobe signal dropout and in increasing activation, especially at 3T. The study was a collaboration between the Center and grad students and postdocs in the Psychology department. A manuscript authored by Ali Preston and has been submitted for publication. Other ongoing work addresses optimized methods for combining the two image timeseries, with Moriah Thomason.

A second spiral-in/out sequence is also under development, by Christine Law (page 38). This method uses a spiral design for 2 interleaves, acquiring the first interleaf as a spiral-in acquisition and the second interleaf as spiral-out. Thus, the sequence uses a single RF excitation to acquire all the data, with advantages in terms of susceptibility loss. Preliminary results are described in an abstract.

A real-time fMRI system has been set up at the 3T scanner by David Ress (page 39). The system uses a Linux-based computer to perform the postprocessing analysis of correlation coefficients and display the results as overlays that update as data are acquired. The spiral images are reconstructed on the scanner's host and transferred via ethernet. Several users are using the system for localization of activation before performing full studies.

Yanle Hu is studying the noise propagation in 3D spiral fMRI acquisitions. Theoretically, the 3D method should have improved BOLD CNR, but incoherent noise between the kz phase encodings is reducing the gains.

Finally, Stanford has been active in the FIRST BIRN schizophrenia project as a P41 contributor. Lara Foland has developed and promulgated the stimulus scripts, scan protocols and other components of the calibration process. Indeed, Stanford heads the Calibration Working Group for the eleven-site consortium. We recently scanned the first 3 of 5 human phantoms.



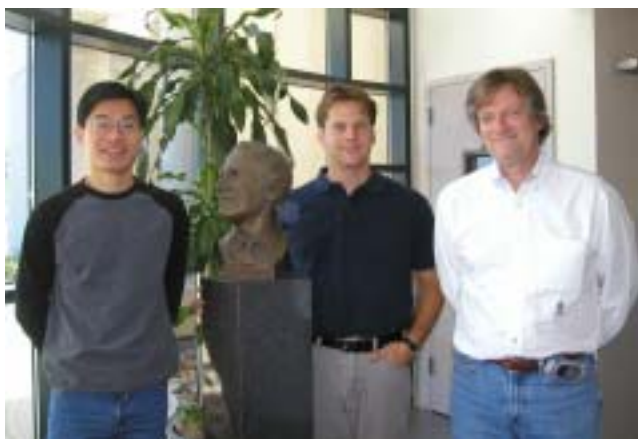
Back row: Christine Law, Rebecca Rakow, Chardonny Vance, Lucile Ress, David Ress, Laura Pisani, Moriah Thomason.

Diffusion and Perfusion Weighted Imaging

Michael Moseley

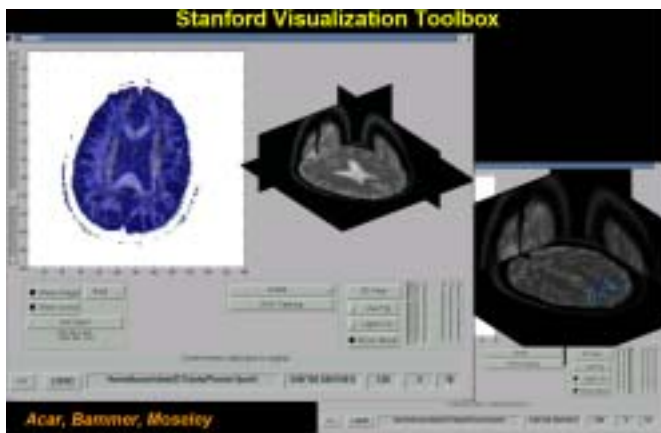
INTRODUCTION

Magnetic resonance imaging (MRI) continues to advance the state-of-the-art in neuroimaging. Our understanding of new contrast mechanisms that occur in the brain has provided completely new radiographic pictures of neuroanatomy and function over the last ten years. This last year has further advanced functional MRI which can map and measure brain tissue water diffusion rates and direction, perfusion of blood, and the brain's response to many functional activation tasks (such as vascular responses to mild reversible stresses). The rapid rate of new discoveries in neuroimaging has been brought about by a steady advance in high-speed MR imaging and by high-field magnets, such as the new 3 Tesla MRI system now at the Lucas Center. Needless to say, these new tools of high-field and high-speed MRI have redefined the horizons of neuroimaging. Our MR Neuroimaging program (pages 42-45) focuses on disease processes in "brain attacks" (cerebral stroke), tissue perfusion, as well as the new field of brain and nerve connectivity.

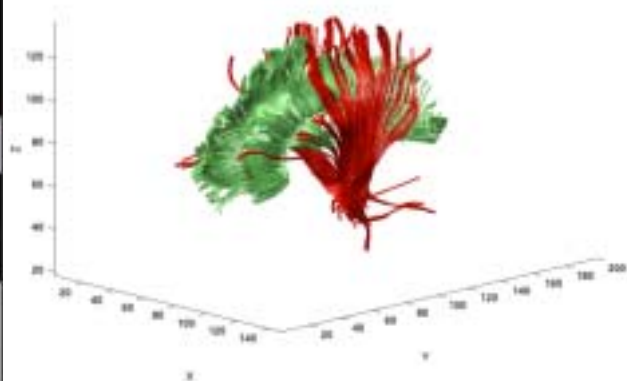


*Left to Right: Chunlei Liu, Roland Bammer, Michael Moseley.
The bust is of Richard M. Lucas.*

National University of Turkey) is currently involved in white matter tensor “fiber-tracking” neuroimaging projects as well as building a collaborative program with several graduate student involved in building a “digital toolbox” for fiber tracking applications neuroimaging here at Stanford.



Stanford Toolbox for White Matter Connectivity Mapping. This tool, developed by B. Acar and R. Bammer is the key to charting brain connections and structural alterations in maturation or demyelination due to disease, for example. The toolbox is a flexible set of algorithms and visual techniques to show the overall brain structure and test connectivity. Applications abound in pediatric and developmental clinical and research areas and are being tested in a number of clinical questions by our collaborators.



PERSONNEL

While I have been busy as the incoming President of International Society of Magnetic Resonance in Medicine (ISMRM), Roland Bammer, Ph.D. (Research Associate) has become a key individual on the research as well as the clinical side of the neuroimaging projects. This year, Roland has been awarded “Docent” status at the University of Graz, Austria and teaches there for 3 weeks per year. Roland has also recently submitted two peer-reviewed grants to the NIH and has been named as “key personnel” on seven others. Rohit Sood has been key in overseeing and developing the data acquisition and processing of the white matter diffusion tensor maps and has also become an expert pulse sequence programmer for the 1.5Tesla and 3Tesla Signa scanners. Chunlei Liu together with Burak Acar (now faculty at the

AN EXCITING YEAR

Over the last year, we have added an entirely new research program in collaboration with a number of Stanford groups in Psychiatry, Radiology, Neurology and Pediatrics. We have made major advances in mapping the brain’s orientational structure and have made several surprising findings in how alterations in brain anatomy or white matter “connectivity” are important. The concept of imaging the white matter and nerve tracts in the brain can revolutionize our understanding of how the brain works, how the functional status is affected by the “wiring” in the brain and how drugs may enhance nerve growth and regeneration. We expect rapid growth of this MRI technology and quick application to the entire field of CNS disease and indeed to a concept of mapping mental and physical performance levels. One of the more interesting tools is the development of a toolbox to track white matter fibers to and from various functional centers of the brain. These “maps” of what is connected to what may be the key in understanding disease states and cognitive performance in future years.

MORE TO COME

The coming year will advance our MR imaging tools and sharpen our focus on the critical clinical issues of detecting brain attacks with new experimental and clinical MR methods to predict eventual brain injury from attacks that may be reversible, to further map how the brain and spine are “wired”, to understand the complex physiological stresses and changes that the brain experiences during stroke, and to extend these tools to better evaluate neuroprotective drugs that can reverse a brain attack.

Neural Correlates of Behavior Using fMRI & TMS

John Desmond

Our group consists of Dr. Annabel Chen, postdoctoral fellow; Matt Kirschen, graduate student in the M.D./Ph.D. program; Jenea Boshart, M.A., laboratory coordinator; Nikhil Jagtiani, graduate student in Computer Science; and Dr. John Desmond, Assistant Professor. Our work focuses on the neural correlates of behavior using functional magnetic resonance imaging (fMRI) and transcranial magnetic stimulation (TMS) methods. Specific areas of interest and recent accomplishments include:

The contributions of the cerebellum, and cerebro-cerebellar circuits, to cognition (pages 46-47).

The cerebellum has traditionally been viewed as a structure involved in motor coordination. However, neuroimaging and patient studies have revealed unexpected cerebellar involvement in cognitive performance beyond motor behavior. We are specifically interested in cerebellar contributions to verbal working memory performance, and have been working on this topic under a grant from the NIH. "Verbal working memory" is the type of memory that one would use to hold a phone number in mind long enough to go to the telephone and dial it. In the past year we have investigated how brain activation in the cerebellum increases as a function of increasing memory load, and we've found that there is a predominately linear relationship. We have also used functional imaging at higher temporal resolution to look at the 3 phases of our task: encoding (when one is presented with letters to remember), maintenance (when the letters are silently rehearsed to keep them in mind), and utilization (when one has to use the information that is being held in mind). We have found that different parts of the cerebellum and neocortex respond to the 3 different phases of the task. We believe that this information may be important for understanding differences between alcoholic and non-alcoholic brains. We recently found that alcoholics exhibit greater brain activation in frontal and cerebellar regions when keeping information in mind, despite the fact that behavioral performance was not significantly different from non-alcoholics. Our interpretation is that alcoholic brains need to work harder in order to perform at identical levels of performance to non-alcoholics. These studies were presented at major scientific conferences: The Society for Neuroscience conference, and The Research Society on Alcoholism. An article on the alcoholic/non-alcoholic brain activation differences is now in press in the journal *Neuroimage*.

Integration of transcranial magnetic stimulation (TMS) with functional MRI. TMS and fMRI are complementary methods, because fMRI can reveal which regions of the brain activate during a cognitive task, whereas TMS can assess which of those activations are necessary for performance. Our preliminary results indicate that TMS applied to the cerebellum affects working memory performance by slowing down response time. We believe this occurs by interfering with the internal brain circuitry that holds the information in mind.

Clinical applications of functional MRI (page 48) including characterization of altered brain activation due to disease, surgical planning, and diagnosis. An important aspect of fMRI for clinical purposes is that it is powerful enough to assess brain activations at the level of the individual patient as well as at the group level. We have recently installed an automated fMRI system at Blake Wilbur hospital that is devoted to clinical fMRI studies. This system can be used to map sensorimotor, language, and memory function in patients who are about to undergo neurosurgery. The system automates a number of steps required for fMRI data analysis and ends with automatic uploading of brain sections and rendered cortical surface (with functional activity superimposed) to a web site accessible to physicians and surgeons. These features make the time-consuming and somewhat technical steps of fMRI acquisition and analysis transparent to the MRI techs, who can concentrate more on the patients. The functional imaging maps will help neurosurgeons avoid resecting tissue that is necessary for normal sensory, motor, and cognitive function.

Methodological aspects of functional MRI, such as estimating statistical power for group analyses. Such information can be used for designing neuroimaging studies with the appropriate sample size for detecting significant differences between conditions, or significant differences between populations of subjects. We have recently published this work in the *Journal of Neuroscience Methods*. We have also published a paper in *Brain and Cognition* that is aimed at clinical users of fMRI, and that describes a number of methodological factors that must be considered in the clinical application of fMRI.

In addition to these projects, we have begun a new line of research designed to study the effects of concussion on brain function. We have recruited the cooperation of the players, trainers, coaches, and physicians of the Stanford Athletic Department to conduct this study. This population was chosen because we can obtain baseline neuropsychological data



Left to right: John Desmond, Annabel Chen, Matt Kirschen, Jenea Boshart, Marlys Lesesne

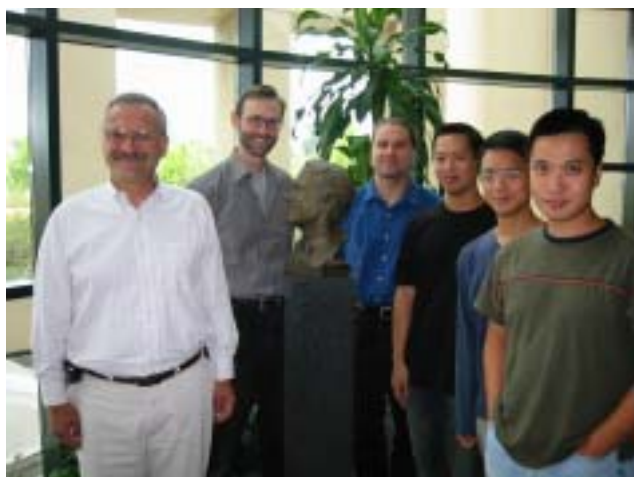
from the entire pool of athletes and observe changes in neuropsychological performance, as well as changes in brain function, in those athletes who sustain a head injury. We have recently been awarded funding from Stanford's Office of Technology Licensing to obtain pilot scan data for this project.

We published a total of 12 papers in peer-reviewed journals in the past year, and made a total of 8 presentations for symposiums, invited lectures, and scientific conferences. One paper, a collaborative project with colleagues in the Department of Psychology, was picked up by television, radio, and the Associated Press because it described differences between men and women in brain activation to emotional stimuli. Dr. Desmond and collaborators on this study were interviewed on television stations (KRON, KPIX, KGO) and radio programs such as KQED Forum.

Cardiovascular Imaging

Imaging Cardiovascular Structure and Function

Norbert Pelc



Norbert Pelc, Marc Alley, Michael Markl, Calvin Lew, Zhifei Wen, Huanzhou Yu

Excellent progress continues to be made in the area of cardiovascular MRI. A significant body of work was accomplished in phase contrast MRI. Our implementation 3D-cine (4D) phase contrast sequence is being applied for a number of research projects ranging from very basic fluid mechanics studies to research applied at flow in normal states as well as a number of diseases, such as Marfan syndrome and valvular heart disease. We have also addressed a number of technical issues in quantitative phase contrast velocity measurements. We developed an improved method for dealing with gradient field inhomogeneity and are making good progress toward a calibration and correction method for eddy current induced errors.

Another theme in our work this year was the use of "Dixon" methods for selective tissue imaging based on chemical shifts. This work has centered at developing improved methods, especially when using SSFP and FSE readouts, and also in

application of these methods to cardiovascular imaging. We are also developing an extension of this method to imaging methyl methacrylate. This project merges this technique with applications of our interventional MRI system.

Finally, we continue to make progress in our work toward imaging myocardial perfusion. This year, we analyzed artifacts resulting from the normally used sequences. It is imperative that the strengths and limitations of available methods be well understood in order for them to be properly interpreted.

MR Spectroscopy

Imaging Metabolism and Function

Daniel Spielman

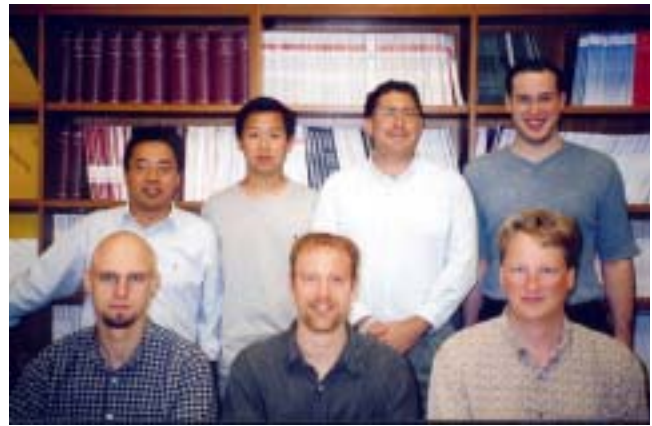
During the past year, we have made continued progress along several lines of magnetic resonance imaging (MRI) and spectroscopy (MRS) research, focused around the central theme of imaging metabolism and function.

Our project to develop a comprehensive noninvasive renal exam using dynamic contrast-enhanced MRI has continued. In particular, based on the results from a pilot project, we have further refined the techniques in an effort to develop a more robust and accurate quantitative clinical tool. Details of parts of this work are presented on page 89. Methods to improve the temporal resolution are explored on page 79.

Magnetic resonance spectroscopy provides a unique noninvasive window into metabolism, and our work in this area is aimed at both the development of novel techniques as well as the exploration of new applications. Highlights of recent technical developments include multidimensional acquisition methods for measuring a larger number of metabolites (pages 90-91), improved spectral fitting and quantification algorithms (page 92), pulse sequences with immunity to motion arti-

facts (page 93-94), and a dual-tuned ^{31}P - ^1H RF coil for studying rat brain metabolism and cellular energetics (page 95). The clinical applications of MRS continue to grow. This past year, we have further pursued the use of magnetic resonance spectroscopic imaging (MRSI) for providing patient-specific biological information needed to optimize radiation therapy treatment plans (page 96). Other exciting MRS studies of multiple sclerosis patients have demonstrated gray matter damage not seen on conventional images (page 97).

With respect to personnel, there have been no major changes this year, but several milestones. Dong-Hyun Kim completed his Ph.D. thesis and is now a postdoctoral researcher at the Lucas Center, and Yakir Levin was admitted into the Stanford MD-PhD program and has just completed his first year of medical school.



*Donghyun Kim, Calvin Lew, Dan Spielman, Yakir Levin
Dirk Mayer, David Clayton, Elfar Adalsteinsson*

Interventional MRI

Developing Tools to Monitor Minimally Invasive Therapies

Kim Butts

This year, the interventional MRI program expanded both in terms of personnel and funding. Sonal Josan began working on imaging frozen tissue, a project that was awarded an NIH R01 grant to Bruce Daniel. Laura Pisani joined the group as a postdoctoral fellow and has been working on MR temperature imaging for Graham Sommer's prostate ablation project. Karl Vigen and Viola Rieke have continued working on improving MR thermometry techniques and were both instrumental in the successful funding of an NIH R01. Karl has developed a method for temperature imaging in the liver when there is variable respiration (pages 103-104). Viola has developed a method for temperature imaging that does not require a reference scan (pages 105-106). These are both significant achievements. Jean Chen has been investigating imaging methods for MR-guided breast procedures including investigating how the proton density of adipose tissue changes with temperature (page 107). Karl, Viola and Jean presented numerous abstracts at



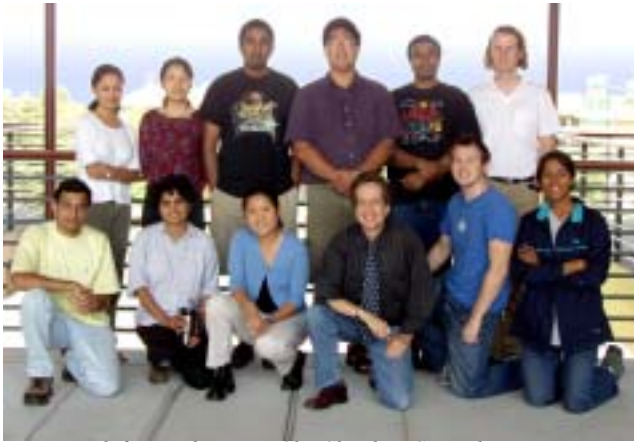
*Sonal Josan, Jean Chen, Laura Pisani
Karl Vigen, Kim Butts, Viola Rieke*

the recent meeting of the ISMRM in Toronto. Kim continued serving on the Scientific Program Committee of the ISMRM and will for one additional year. Thus, it's been a busy and productive year for everyone.

ADVANCED IMAGING RESEARCH

3D Imaging Lab

Sandy Napel



Top row left to right: Rong Shi, Shaohua Sun, Bhargav Raman, David Paik, Raghav Raman, Markus Kukuk
Bottom row left to right: Tejas Rakshe, Joyoni Dey, Fiona Loke, Sandy Napel, Anthony Sherbondy, Padma Sundaram

Sandy Napel's group addresses the field of image analysis (pages 117-127), which has become increasingly important because the number of images per patient scan has increased dramatically and now numbers in the thousands. The group focuses on volumetric visualization, structure segmentation, quantitative analysis, and computer-aided detection of lesions. Although his group works with many colleagues in the Radiology Department, notably Chris Beaulieu, Dominik Fleischman, and Geoff Rubin are active participants in the group's endeavors. This year they began work on several new projects, including *Computer-aided Detection of Lung Nodules*, funded by R2 Technology Inc., and the *Interventional Room of the Future*, funded by Siemens Medical Solutions, Inc., and they continued work on existing projects, *Computer-aided Detection of Colonic Polyps*, and *Efficient Interpretation of Vascular Images*, both funded by the National Institutes of Health. Four new patents are pending, four new papers are in press, and six abstracts will be

presented at RSNA 2003. Sandy's group has recently moved into the James H. Clark Center for Biomedical Engineering and Sciences, which promises to leverage their expertise with that of others in the Center involved in biocomputation, as well as to facilitate new collaborative projects involving analysis of medical image data.

Advanced X-ray Imaging

Rebecca Fahrig, Norbert Pelc



Standing: Arunduti Ganguly, Sung Won Yoon, Zhifei Wen, Norbert Strobel, Rebecca Fahrig, Norbert Pelc, Lei Zhu
Kneeling: Angel Pineda, Sam Mazin, Huanzhou Yu

The Advanced X-ray Imaging Techniques Group, led by Drs. Pelc and Fahrig, is involved in several new and ongoing investigations into the design, implementation and applications of digital detectors to diagnostic imaging and interventional guidance.

The X-ray/MR project (pages 131-134) investigates the integration of a digital flat panel fluoroscopy system into the bore of an interventional MR system. We have used the first implementation of the system for guidance of several different procedures in patients including brain biopsy and TIPS. A system upgrade that will significantly expand system capabilities and system stability is almost complete. Investigations to improve image quality, streamline integration and define new applications are underway. A poster presentation on aspects of this work (first author Wen) was awarded Honorable Mention at the SPIE meeting in San Diego in February 2003. This project has benefited from a close collaboration with GE Medical Systems.

Several projects using unique technology from the Scanning Beam Digital X-ray System (NexRay Inc.) are also continuing (pages 133-134). We are investigating use of the system for lung nodule detection, looking at alternate geometries and reconstruction techniques to improve the image quality of the digital tomosynthesis images. We are also considering use of the components in a CT scanner, an approach that would allow acquisition of an artifact free large volume with a single rotation of the CT gantry.

Finally, we are pleased to announce the initiation of a new collaborative effort with Siemens AX in the area of C-arm-based CT imaging (page 135). A new state-of-the-art facility for phantom and animal experiments is under construction, and should be completed by the end of 2003. Investigations to extend 3D C-arm imaging from high-contrast vessel and bone imaging to detection of low-contrast lesions and intracranial bleeds are already underway.

Outcomes and Cost Effectiveness

Sylvia Plevritis

Our research group is primarily focused on the design, execution and evaluation of breast cancer screening programs. We want to understand how many lives are saved due to breast cancer screening programs, if treatment is more effective in patients who are screened as opposed to patient who are not screened, and if newer screening technologies would make a bigger health impact. To estimate the survival benefit from screening, we have been developing computer models that simulate the individual life histories of women with and without breast cancer screening. A fundamental component of our work is a mathematical model of the natural history of breast cancer being developed by team members Sylvia Plevritis, Slava Sigal, Peter Salzman, YenLin Chia and Peter Glynn. Over the past year, we have estimated the mean growth rate of breast cancer from the HIP breast cancer screening trial (page 141). We have estimated progression rate of breast cancer from local to regional and then distant stages from data in the SEER tumor registry (page 142). To validate our natural history model, we used it to simulate the incidence and mortality outcome from the HIP screening trial. Our results indicate a smaller benefit from screening than reported by the HIP study (page 143). Because it has been suggested that the HIP overestimated the benefit of mammography, we have analyzed the HIP survival data. We determined that there is randomization evidence of a bias in favor of screening (page 144). This activity has been funded by the two NIH grants (R01 CA82904-03, Cost Effectiveness Analysis of Breast Cancer Screening; U01 CA88248-04, Breast Cancer Trend Analysis Using Stochastic Simulation).



Left to right: Sylvia Plevritis, Slava Sigal, Jarrett Rosenberg, YenLin Chia, Peter Salzman

A major application of our natural history model of breast cancer associated with an NCI-sponsored collaborative project called CISNET “Computer Intervention and Surveillance Modeling Network” (www.cisnet.gov) that aims to explain what impact screening mammography and adjuvant therapy has had on US breast cancer incidence and mortality rates from 1973 to 2000. In June 2003, we hosted a CISNET Breast Working Group meeting in San Francisco that was attended by 50+ colleagues from the NCI, Dana Farber, MD Anderson, Erasmus in Rotterdam, Rochester Huntsman, Lombardo Cancer Center at Georgetown, and University of Wisconsin. The Consortium decided that the work of the individual groups can not be published until the CISNET Consortium makes a joint statement. Dr. Plevritis was elected to be on the executive writing committee for the CISNET Consortium and has been serving as elected Chair for the CISNET Breast Cancer and Methodology Working Groups. The Consortium has asked our group to demonstrate the principles of simulation-based estimation with an example relevant to modeling the natural history of breast cancer. We developed a stochastic model of tumor growth for this purpose (page 145). Our CISNET work has been funded by NIH grant (3 U01 CA88248-04, Breast Cancer Trend Analysis Using Stochastic Simulation).

Together with the Breast Cancer Genetics Clinic at the Stanford Medical Center, our group contributed to the design and evaluation of a comprehensive breast cancer screening study of breast MRI and ductal lavage among women at high genetic risk for developing breast cancer (page 146). We are investigating detection rates of malignant and premalignant disease. This study is designed to identify early genetic alterations in premalignant and benign disease that impacts risk assessment for individual patients. The Oncology Fellow Dr. Anne-Renee Hartman critical to this project will begin her faculty career as Assistant Professor at Harvard’s Dana Farber Cancer Center starting October 2003. Oncology Fellow Dr. Allison Kurian will be joining the team. This work is funded by two multidisciplinary grants funded this year to Drs. Sylvia Plevritis and James Ford, as co-PIs. One grant was funded by the California Breast Cancer and the other by the V Foundation.

Over the past year, a Stanford undergraduate senior, Alli Widman, joined our group. She analyzed the cost-effectiveness of alternative treatment strategies. Her work was awarded the prestigious Firestone Medal for the best Honors’ thesis from a graduating senior in Human Biology. She is now working for Health Sector of Goldman Sacks in New York City.

DEPARTMENTAL GROWTH

Molecular Imaging Program at Stanford (MIPS)

Sam Gambhir

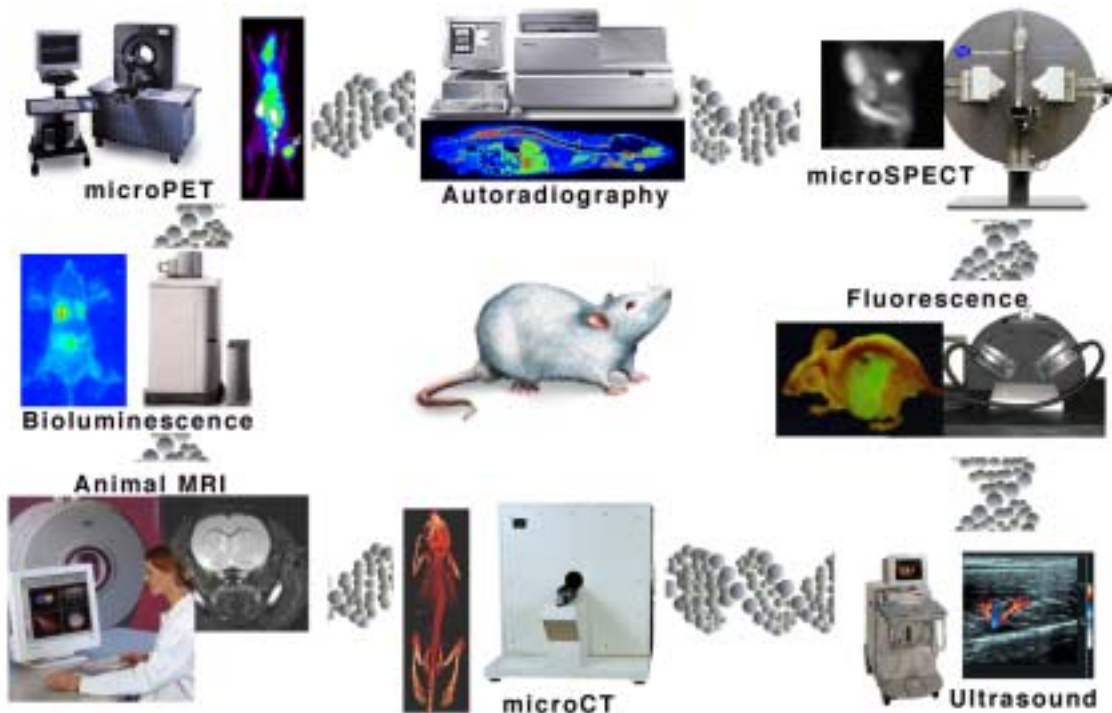
The Molecular Imaging Program at Stanford (MIPS) was established in 2003 by Philip Pizzo, M.D., Dean of the Stanford School of Medicine, and Gary Glazer, Professor and Chair of the Department of Radiology, as a multi-departmental program. Under the direction by Sanjiv Sam Gambhir, M.D., Ph.D., Professor of Radiology and co-directed by Dr. Chris Contag, Ph.D., Assistant Professor of Pediatrics, MIPS will bring together scientists and physicians who share a common interest in developing and using state-of-the-art imaging technology and developing molecular imaging tests for studying intact biological systems. Areas of active investigation are cancer research, microbiology/immunology, developmental biology and pharmacology. MIPS is also integrally linked to Bio-X, an interdisciplinary program that brings together scientists from the School of Engineering and School of Humanities and Sciences.

The program's goals are to fundamentally change the way biological research is performed with cells in their intact environment, living subjects, and to develop new ways to diagnose diseases and monitor therapies at the cellular level in vivo.

In order to diagnose disease and advance therapy at the molecular level, methods of monitoring fundamental cellular events in living subjects have to be developed. We intend to provide scientists and physicians with quantitative tools for studying biological and medical problems at the earliest stages of the disease process. We will fuse fundamental developments in the understanding of molecular and cell biology with recent progress in biomedical imaging, focusing in particular on cancer biology and gene therapy.

Our approach will be multimodal, exploring various imaging technologies, including positron emission tomography (PET), single photon emission computed tomography (SPECT), digital autoradiography, magnetic resonance imaging (MRI), magnetic resonance spectroscopy (MRS), optical bioluminescence, optical fluorescence, and ultrasound

Our laboratory is developing and validating tests for probing these activities in living animals and humans using small animal imaging technologies. Technologies such as micro positron emission tomography (microPET), bioluminescence optical imaging with a charge coupled-device (CCD) camera, fluorescence optical imaging, and micro computerized axial tomography (microCAT) are all being evaluated.



MIPS 5 KEY RESEARCH AREAS

- Creation and validation of radiolabeled and fluorescent molecular probes for use in molecular imaging
- Development of molecular imaging instrumentation that can be used safely in living subjects
- Development of molecular imaging approaches that will enable us to evaluate events in living subjects at the cellular level
- Development of software tools for visualizing and analyzing molecular imaging data
- Merger of therapeutic and imaging strategies for improved patient management

LOCATION

CLARK CENTER

The Molecular Imaging Program at Stanford will operate in several locations. Beginning in the fall, Drs. Gambhir and Contag will establish their offices in the newly completed James H. Clark Center for Bioengineering. This will provide proximity to and synergy with a critical mass of about 40 faculty from various disciplines who will also have offices located in the new building. MIPS will run several state-of-the-art imaging facilities within the Clark small animal imaging core including digital whole body autoradiography (DWBA), microPET, microSPECT/CT, optical bioluminescence/fluorescence and ultrasound.

LUCAS CENTER

When the Lucas expansion is completed in October 2004, 8000 square feet will be allocated to MIPS. The Lucas expansion will house many of the chemistry labs for the program and a cyclotron suite for production of PET radiopharmaceuticals.

CYCLOTRON SUITE

The cyclotron suite will be on the first subfloor of the Lucas expansion and will contain a GE PETtrace Tracer Production System. The GE PETtrace is a compact, automated cyclotron designed for the fast, easy, and efficient production of PET radiotracers.

STANFORD UNIVERSITY MEDICAL CENTER

The Program will also have access to clinical imaging equipment in the Department of Radiology including computed tomography (CT), magnetic resonance imaging (MRI), positron emission tomography combined with CT (PET/CT), and single photon emission computed tomography (SPECT). The Division of Nuclear Medicine is also actively linked to the program.

EDWARDS BUILDING

The start up offices for MIPS have been housed in the Edwards Building and managed by Phoebe Abt, our administrative associate, since June. We will maintain transition space there for instrumentation and chemistry labs through 2007.

FUNDING

Funding for the Program's research activities comes from a mixture of Federal (National Institutes of Health and Department of Energy), Foundation and University sources, as well as through a number of collaborations with industry.

EDUCATION

The Program will attract graduate students from a wide range of programs including Molecular Pharmacology, Cell/Molecular Biology, Electrical Engineering, and Bio-Engineering. Continuing the legacy of the Department of Radiology, we intend to attract scientists from around the world and train the future leaders of molecular imaging.



*James H. Clark Center
for Bioengineering*

GROWING TO MEET THE FUTURE

Lucas Expansion II

On July 11, 2003, the main doors to the Lucas MRS Imaging Center were sealed off. Demolition of the entrance and excavation of what had been the building's parking lot was begun. The Lucas Center, home of the Radiological Sciences Laboratory (RSL) and a major component of the federally funded Center for Advanced Magnetic Resonance Technology at Stanford, is undergoing an expansion that will more than double the size of the existing medical imaging research facility. The new space, scheduled to open October 2004, will accommodate an ultra-high field 7T MR magnet, a cyclotron, wet labs, a radiochemistry laboratory, a clean room, and associated office space. This major expansion effort is the latest growth spurt in a series of changes that have taken place since Gary M. Glazer, M.D., was appointed Chairman of Radiology in 1989.

The Lucas Center opened in 1992. RSL, under the direction of Gary Glover, Ph.D., took up residence with a handful of faculty and a very small number of postdoctoral fellows and researchers. The first Lucas Center expansion took place in 1997, when the basement was enlarged by 4,300 gross square feet to accommodate a 3 Tesla research magnet and more office space. It was during this expansion phase that the 3D visualization laboratory moved to the first floor of the Lucas Center from the Grant Building.

Increased physical capacity has consistently been followed by a growth in research effort, funding, and personnel. From about 30 people at its inception, the Lucas Center now numbers nearly 90 faculty, researchers, staff and students. The Lucas Center is full, and growth continues.

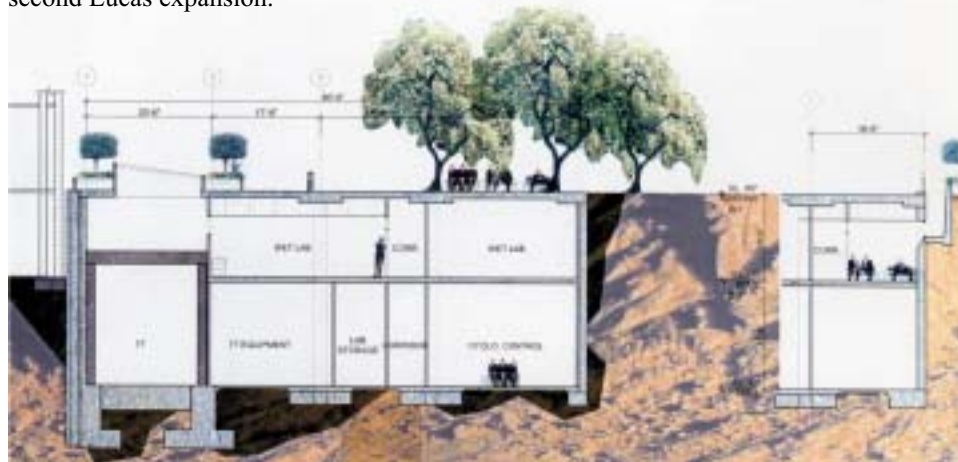
In addition to the Lucas Center's world-renowned research effort, the recruitment of Sanjiv Sam Gambhir, M.D., Ph.D., as the Chief of Nuclear Imaging and Director of the Molecular Imaging Laboratory marks the start of an important new initiative and the need for more space and facilities for the Department.

Some requirements were met when the Medical School granted space to the Department in the recently completed Clark Bioengineering Center for use as Dr. Gambhir's molecular imaging laboratory and the research portion of Dr. Napel's 3D advanced visualization laboratory.

Efforts to find housing for the proposed 7T magnet, cyclotron and additional molecular imaging laboratories nonetheless proved difficult. With no options to re-configure existing space on or around campus in a meaningful way and given current restrictions on above ground construction, the decision was made to expand underground. Thus, plans were drafted for the second Lucas expansion.



Excavation begins. Before starting workers had to remove the distinctive Lucas Center entrance.



The new construction will increase the existing Lucas Center by over 20,000 gross square feet, expanding the current basement and creating an additional sub-basement. A below-ground courtyard will bring light, landscaping, and outdoor access to the two lower levels of the building.

Elevation of proposed expansion.

A landscaped plaza with an enhanced vehicle access area and expanded bike parking will be built above the structure. The Lucas Center Plaza will fulfill an important esthetic function by creating an elegant terminus for the Medical School Mall, a major east-west bike and pedestrian corridor that runs from the Clark Center on West Campus Drive. A secondary pedestrian access route that runs north and south from the Lucas Center to the Medical School Office Building (MSOB) has also been incorporated into the design.

The Lucas Center has been a major attraction for researchers from around the world and has increased the Department's ability to form vital partnerships both in academia and industry. Our funding and research capabilities go hand in hand with our capacity to provide state of the art research facilities and attract top-flight faculty and students. The expanded Lucas Center will be a crown jewel of the Stanford School of Medicine and will increase the Department's stature as a leader in medical imaging.



Artist's concept of plaza over the Lucas expansion



Lucas Center Faculty, Staff & Students

Lucas Center Personnel and Research Collaborators

Lucas Center Faculty, Staff & Students

Faculty

Gary M. Glazer, M.D.
Gary H. Glover, Ph.D.
Mark Bednarski, M.D., Ph.D.
Kim Butts, Ph.D.
John E. Desmond, Ph.D.
Rebecca Fahrig, Ph.D.

Robert J. Herfkens, M.D.
Michael E. Moseley, Ph.D.
Sandy Napel, Ph.D.
Norbert J. Pelc, Sc.D.
Sylvia K. Plevritis, Ph.D.
Daniel M. Spielman, Ph.D.

Scientific Staff

Elfar Adalsteinsson, Ph.D.
Marcus Alley, Ph.D.
Roland Bammer, Ph.D.
Wendy Baumgardner, RVT, LATg
Jenea Boshart, M.A.
Thomas Brosnan, Ph.D.
Mary Draney, Ph.D.
Lara Foland, B.A.
Samira Guccione, Ph.D.
Diane Howard, RVT, LATg
Hsi-An (Sean) Lee, R.T.
Laura Logan, B.S., R.T.
Michael Markl, Ph.D.

Linda Novello, R.T.
Raghav Raman, M.D.
Scott Reeder, M.D.
Ruminder Samra, R,T,
Anne Sawyer-Glover, B.S., R.T. (R)(MR)
Pamela Schraedley, Ph.D.
Gongyi Shi, Ph.D.
Bronislava Sigal, Ph.D.
Marc Sofilos, R.T.
Karl Vigen, Ph.D.
Yingyun Wang, B.S.
Yishan Yang, Ph.D.
Marowan Zakhour, M.D.

Administrative and Support Staff

Maggie Bos
Nancy Bucy
Michelle Christerson
Donna Cronister
Susan Kopiwoda
Marlys Lesene
Kevin Murphy
Barghav Raman

Kala Raman
John Reuling
Flor Reyes
Lanzie Rivera
Susie Spielman
David Stough
Julia Tussing
Lakeesha Winston

Postdoctoral Fellows

Annabel Chen, Ph.D.
David Clayton, Ph.D.
Joyoni Dey, Ph.D.
Arundhuti Ganguly, Ph.D.
Jason Hsu, Ph.D.
Walter Hundt, Ph.D.
Dong Hyun Kim, Ph.D.

Jon Levin, Ph.D.
Daniel Margolis, M.D.
Dirk Mayer, Ph.D.
David Paik, Ph.D.
Angel Pineda, Ph.D.
Laura Pisani, Ph.D.
Lara Stables, Ph.D.

Graduate Students

Jean Chen, M.S.
Jamie Dermon, M.D.
Taly Gilat, M.S.
Meng Gu, M.D.
Michael Hope, M.D.
Yanle Hu, M.S.
Matthew Kirschen, M.D.
Sonal Josan, M.S.
Christine Law, M.S.
Calvin Lew, M.S.
Yakir Levin, M.S.
Chunlei Liu, M.S.
Michael Padilla, M.S.
Rebecca Rakow, M.S.

Tejas Rakshe, M.D.
Viola Rieke, M.S.
Peter Salzman, M.S.
Anthony Sherbondy, M.S.
Cindy Shi, M.S.
Shaohua Sun, M.S.
Padma Sundaram, M.S.
Moriah Thomason, M.S.
Chardonnay Vance, M.S.
Zhifei Wen, M.S.
Sung-Won Yoon, M.S.
Huanzhou Yu, M.S.
Lei Zhu, M.S.

Visiting Researchers and Scholars

Zhi-Pei Liang, Ph.D.

Undergraduates

Fiona Locke

Lucas Center Collaborators

Collaborating Stanford Departments

Over one hundred faculty, postdoctoral fellows, students and research staff from across the university are affiliated with research programs at the Lucas Center representing the following departments:

Applied Physics	Neurology
Cancer Biology	Neurosurgery
Cardiovascular Medicine	OB/GYN
Computer Sciences	Orthopedics/Orthopedic Surgery
Electrical Engineering	Pediatrics/Neonatology
ENT	Psychiatry
Functional Restoration	Psychology
Infectious Diseases	Stroke Center
Mechanical Engineering	Surgery
Medical Informatics	Urology
Nephrology	Vascular Surgery
Neurobiology	

Outside Collaborators

Active collaborations are in place with researchers from outside Stanford representing the following institutions:

Aneurex	Novartis
Bresagen	Nycomed
Chiron	R2 Technology, Inc.
Cordis	Siemens Medical Systems
Elbit	Smith Kettlewell Eye Institute
Ethicon	SRI International
FeRx, Inc.	Sterling
Galil Medical	University of California, Berkeley
Genentech, Inc.	University of California, Davis
Genetics	University of California, Irvine
GE Medical Systems	University of California, San Francisco
Lunar Corporation	University of California, San Diego
NexRay	

New Faculty, Staff, Research Fellows and Visitors at the Lucas Center and Throughout the Department

We welcome new faculty, staff, fellows and visitors from institutions locally, around the country and abroad.

Faculty

Sanjiv Sam Gambhir, M.D., Ph.D.
Professor of Radiology
Chief of Nuclear Medicine
Director of Molecular Imaging

Staff

Mary Draney, Ph.D.
Lara Foland, B.A.
Susan Kopiwoda, M.S., M.P.H.
Michael Markl, Ph.D.
Karl Vigen, Ph.D.

Postdoctoral Fellows

Snehal Adodra, M.D.
Body Imaging
Filip Banovac, M.D.
Cardiovascular Interventional
Ruby Chang, M.D.
Body Imaging
Joyoni Dey, Ph.D.
RSL
Arundhuti Ganguly, Ph.D.
RSL
Howard Harvin, M.D.
Body Imaging
Ronald Homer, M.D.
Neuroradiology Fellow
Raymond Hsu, M.D.
Body Imaging
Zubeir Jaffer, M.D.
Pediatrics
Mahesh Jayaraman
Neuroradiology Fellow
Iain Kirkpatrick, M.D.
Body Imaging
Michael Kotton, M.D.
Cardiovascular Interventional
Ray Lertvaranurak, M.D.
Neuroradiology Fellow

Jon Levin, Ph.D.
RSL
Karl Magsamen, M.D.
Cardiovascular Interventional
Daniel Margolis, M.D.
NCI Fellow
Sunita Pal, M.D.
Mammography
Saurabh Patel, M.D.
Body Imaging
Angel Pineda, Ph.D.
RSL
Laura Pisani, Ph.D.
RSL
Duncan Rougier-Chapman, M.D.
Body Imaging
Steven Sohn, M.D.
Neuroradiology
Brian Suh, M.D.
Musculoskeletal
T. Lauren Tran, M.D.
Neuroradiology
Eric Williamson, M.D.
Cardiovascular Imaging
W. Bryan Winn, M.D.
Neuroradiology

Graduate Students

Meng Gu, M.S.
Nikhil Jagtiani, M.S.
Sonal Josan, M.S.
Ping Li, M.S.
Michael Padilla, M.S.

Anthony Sherbondi, M.S.
Cindy Shi, M.S.
Moriah Thomason, M.S.
Sung-Won Yoon, M.S.
Lei Zhu, M.S.

Congratulations

It is a mark of particular pride that some of our students remain with us after their training to continue the outstanding work that they have begun here. We would like to congratulate the following people for their promotions in our program.

Research Staff from Postdoctoral Fellows

Michael Markl, Ph.D.

Karl Vigen, Ph.D.

Postdoctoral Fellows from Graduate Students

David Paik, Ph.D.

Donghyun Kim, Ph.D.

Academic Staff from Postdoctoral Fellows

Dirk Mayer, Ph.D.

Farewells

In the past year we have bid farewell to the following people. We send our best wishes with them for happiness and success in their new positions.

Administrative Staff

Julia Tussing

Managing Director, Finance & Administration

School of Medicine - Dean's Office

Postdoctoral fellows

Burak Acar, Ph.D.

Faculty

National University of Turkey

Andreas Herneth, M.D.

Radiologist

Univ.-Klinik für Radiagnostik

Vienna, Austria

Susan K. Hobbs, M.D., Ph.D.

Completing Residency

University of Minnesota

Charles Liu, M.D.

LaJolla Radiology

Rohit Sood, Ph.D.

Faculty

New Mexico

Graduate Students

Ping Li, M.S.

Feng Zhuge, M.S.

A W A R D S & H O N O R S

Spinoza Visiting Professor, *Academic Medical Center, Amsterdam*, September 2002

Michael Moseley

Steering committee member, *Society for Molecular Imaging*, 2002-2003

Michael Moseley

Research Trainee Prize, Cardiovascular Imaging Section, *Radiological Society of North America 88th Meeting*, December 2002, Chicago, IL

Michael Mark, Scott B Reeder, Marcus T Alley, Robert J Herfkens, Norbert J Pelc. Balanced SSFP and myocardial tagging for improved tag-tissue contrast and SNR.

Research Trainee Prize, Physics Section, *Radiological Society of North America 88th Meeting*, December 2002, Chicago, IL

Scott B Reeder, Zhifei Wen, Garry E Gold, Marcus T Alley, Michael Markl, Norbert J Pelc. Multi-point Dixon fat-water separation and steady-state free precession

Exhibit Award Winners: Certificate of Merit, *Radiological Society of North America 88th Meeting*, December 2002, Chicago, IL

PS Pinto PS, CB Sirlin, OA Andrade-Barreto, MA Brown, RE Mindelzun, RF Mattrey. The cisterna chyli on routine abdominal MR imaging: A normal anatomic structure of the retrocrural space.

Honorable Mention for Poster Presentation, *The International Society for Optical Engineering (SPIE)*, annual meeting, San Diego, CA, February 2003.

Zhifei Wen. X-ray tube in parallel magnetic fields

Cum Laude Award, *Society of Computed Body Tomography and MRI. 26th Annual Scientific Session*, March 23, 2003, Palm Springs, CA.

Lawrence C Chow, Eric W Olcott, F Graham Sommer. Clinical utility of double-bolus multidetector CT urography with sliding thin-slab MIP.

Lauterbur Award, *Society of Computed Body Tomography and MRI. 26th Annual Scientific Session*, March 23, 2003, Palm Springs, CA

Garry E Gold, E Han, J Stainsby, Graham A Wright, Robert J Herfkens, Jean H Brittain, Crisopher F Beaulieu. Optimization of musculoskeletal MR imaging at 3 Tesla.

President's Award Radiology Resident Research, *American Roentgen Ray Society*, May 2003, Atlanta, GA

Scott B Reeder, Marcus T Alley, Norbert J Pelc. Water and Fat SSFP Imaging with Four-Point Dixon Techniques.

Gold Medal, *Society of Pediatric Radiology*, May 7, 2003. William Northway

Rabi Young Investigator Award, *International Society of Magnetic Resonance in Medicine Annual Meeting*, July 2003, Toronto, ON

Michael Mark, Marcus T Alley, C J Elkins, Norbert J Pelc. Flow Effects in Balanced Steady State Free Precession Imaging

Finalist, Moore Award for Young Investigators, *International Society of Magnetic Resonance in Medicine Annual Meeting*, July 2003, Toronto, ON

Susan K. Hobbs

Visiting Professor, *University of Vienna - Vienna General Hospital*, July 2003

Roland Bammer

President, *International Society of Magnetic Resonance in Medicine* 2003-2004

Michael Moseley

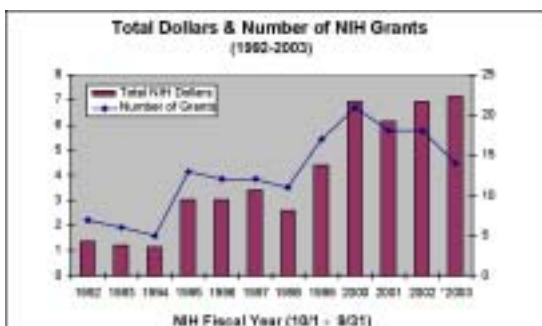
President-Elect, *Women in Neuroscience* 2003-2005

Judy Illes

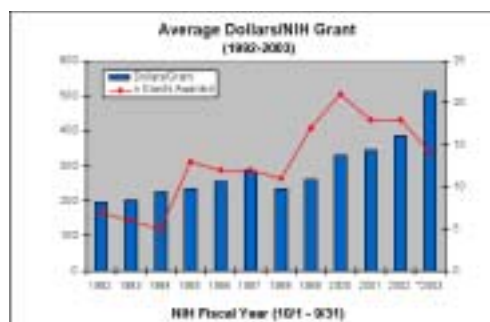
Strategic Research Development

Susan Kopiwoda

We have had an exciting year developing our research funding base as we continue to search for ways to find support for our exciting and new projects. Many of our faculty have been busy writing this year and have been successful in their efforts to procure new funding through a variety of sources, in particular highly competitive NIH awards. The following charts show the trend of NIH funding to this Department over the last several years. The 2003 numbers represent a conservative estimate since the NIH fiscal year has not ended yet and the final numbers are not available. The data supporting these charts can be found on the NIH website at www.nih.gov.



*The chart shows the number of NIH grants and the total dollars that have been awarded to Stanford Radiology Department (1992-2003). *The 2003 numbers will most likely increase as the NIH Fiscal Year closes.*



The chart suggests that, at least for fiscal year 2003, fewer but larger grants were proposed and awarded. These data reflect the number of proposals awarded, not the number of proposals submitted.

Research plans anticipating the arrival of the ultra high field 7T magnet and the cyclotron continue to mature as the new underground space for these instruments takes shape. The additional facilities that will soon be available to us will have a direct impact on our research program and lead us to anticipate a number of new projects reflecting the developing programs in 7T imaging, Molecular Imaging and PET imaging. With new resources in these areas, established investigators to lead the way and new faculty bringing fresh insights, we expect the coming year to be very busy and very exciting.

As a new member of the Department I am pleased to be working in Radiology. In the past few months I have learned a lot about the Department and am beginning to understand what might be useful to those who are looking for funding sources and what this office might offer to make the grant application process easier from early concept to final application.

CONGRATULATIONS TO JUDY ILLES

We would like to congratulate Dr. Judy Illes, Ph.D., on the success she is enjoying in her new position as Senior Research Scholar in the Department of Biomedical Ethics. Her recent efforts to define and identify ethical issues related to whole body screening procedures has been widely received and recognized. Dr. Illes has been working with Dr. Scott Atlas, professor of radiology, and both were recently interviewed and televised nationwide and covered in local and national news articles.

We wish Judy continued success and thank her for her efforts and energy in developing the Strategic Research Program in the Department of Radiology.

The following list of Active and Proposed grants gives an idea of the varied research interests being pursued in the Department.

ACTIVE SPONSORED RESEARCH PROJECTS (9/1/02-8/31/03)

FEDERAL AWARDS

Adalsteinsson, Elfar	NIH	MR Spectroscopic Imaging in Alzheimer's Disease	R01
Atlas, Scott W.	NIH	Quantitative MR of Normal Appearing White Matter in MS	R21
Bammer, Roland*	NIH	Improving SENSE MRI for Spiral & Echo-Planar Imaging	R01
Beaulieu, Christopher	NIH	Three-Dimensional CT Colonography	R01
Bednarski, Mark*	NIH	Correlative Imaging of Tumor Angiogenesis	R21/33
Blankenberg, Francis*	NIH	Imaging Apoptosis <i>in vivo</i> with Tc 99m Annexin	R01
Butts, Kim	NIH	iMRI Methods for Cancer Diagnosis and Treatment	R01
Butts, Kim	NIH	High Speed Gradient Driver Upgrade for iMRI Scanner	S10
Contag, Christopher	NIH	In Vivo Multimodality Imaging of Neoplastic Disease	P20
Daniel, Bruce	NIH	Magnetic Resonance Imaging of Breast Cancer	R01
Daniel, Bruce	NIH	MR-Guided Radiofrequency Ablation of Breast Cancer	R21/33
Daniel, Bruce	NIH	Techniques for MRI-Guided Cryosurgery of Prostate Cancer	R01
Desmond, John	NIH	fMRI and TMS Analysis of Cerebellar Cognitive Function	R01
Gabrieli, John	NIH	Cognitive Analysis of Working Memory Development	R01
Glazer, Gary M.	NIH	Advanced Techniques for Cancer Imaging	T32
Glazer, Gary M.	VA	Department of Veteran Affairs Mammography Screening Contract	VA
Glazer, Gary M.	VA	Solicitation Agreement	VA
Glover, Gary	NIH	Center for Advanced Magnetic Resonance Technology at Stanford	P41
Glover, Gary	SRI /NIH	CVD Risk Factors and Brain Morphology in Twins	R01
Glover, Gary*	UC Irvine/NIH	Functional Imaging Research in Schizophrenia Testbed	M01
Gold, Garry*	NIH	Rapid MRI for Evaluation of Osteoarthritis	R01
Illes, Judy*	NIH	Advanced Neuroimaging: Ethical, Legal, and Social Issues	R01
Moseley, Michael	NIH	DWI Assessment of Clinical Acute Stroke	R01
Moseley, Michael*	NIH	Improved PWI Methodology in Acute Clinical Stroke	R01
Napel, Sandy	NIH	Efficient Implementation of 3D Vascular Image Data	R01
Pelc, Norbert	NASA	Non-invasive Investigation of Bone Adaptation in Humans to Cumulative Daily Mechanical Loading	NASA
Pelc, Norbert	NIH	Hybrid X-Ray/MR Systems for Image-Guided Procedures	R01
Plevritis, Sylvia	NIH	Cost Effectiveness Analysis of Breast Cancer Screening	R01
Plevritis, Sylvia	NIH	Breast Cancer Trend Analysis Using Stochastic Simulation	U01
Rubin, Geoffrey	NIH	Volumetric Analysis of the Aorta and Its Branches	R01
Sommer, Graham	NIH	MRI of Renal Anatomy and Function in Chronic Ischemia	R01
Sommer, Graham	NIH	Precise MRI-Directed Sonic Ablation of Prostate Cancer	R33
Sommer, Graham	NIH	Prostate Cancer and BPH Ablation using HIFU Waveguide	R21
Spielman, Daniel	NIH	Magnetic Resonance Spectroscopic Neoplasm Imaging	R01
Spielman, Daniel	SRI/NIH	In Vivo Diffusion and Spectroscopic Brain Imaging in Alcoholism	R01

*These grants are most likely to be funded

NON-FEDERAL AWARDS

Atlas, Scott	Greenwall Foundation	Ethical Challenges in Neuroimaging
Chan, Frandics	RSNA	Characterization of Intraventricular Flow and Flow-Induced Wall Stress in Chronic Mitral Regurgitation Before and After Mitral Valve Repair
Desmond, John	Stanford OTL	Neuroimaging Investigations of Cognitive Impairment After Concussion Injury
Do, Huy	GE-AUR	Clinical Outcomes of Percutaneous Vertebroplasty for Patients with Osteoporotic Vertebral Body Compression Fractures
Fahrig, Rebecca	The Whitaker Foundation	Ultrafast Tomosynthesis for the Detection of Lung Cancer
Gold, Garry	The Whitaker Foundation	MR Imaging of Joints with Intra-Articular Coils
Gold, Garry	Interdisciplinary Initiatives Program	Modeling Muscles in Contact
Herfkens, Robert	National Marfan Association	Assessment of Mechanical Properties of the Aortic Arch in Patients with Marfan Syndrome by Means of Magnetic Resonance Imaging (MRI)
Ikeda, Debra	Susan G. Komen Breast Cancer Fdn	Do K21, Parametric Mapping or Tumor Morphology on Contrast-Enhanced Breast MRI Predict Tumor Response to Chemotherapy?
Kee, Stephen	CIRREF	The Dr. Ernest J. Ring Academic Development Grant
Pelc, Norbert	The Whitaker Foundation	Department of Bioengineering -Graduate and Postdoctoral Education

PROPOSALS UNDER CONSIDERATION

Birdwell, Robyn	NIH-SubCont	Differential Vasoactive Optical Mammography	R21
Blankenberg, Francis	NIH	Annexin V Imaging and Therapeutic Outcome in Lung Cancer	R01
Desmond, John	NIH	fMRI Analysis of Cognitive Function in Alcoholics	R01
Desmond, John	NIH	fMRI Analysis of Aging & Awareness in Conditioning	R01
Fahrig, Rebecca	NIH	Hybrid Biplane Xray/MR System	R21
Fahrig, Rebecca	NIH	Improved C-Arm CT for Interventional Procedures	R01
Gambhir, Sanjiv	DOE	MI of Stem Cell Survival, Apoptosis & Differentiation in Myocardium	
Gold, Garry	NIH	Biomechanical Modeling of Muscle Fx Following Tendon Transfer Surgery	
Ikeda, Debra	DOD	Automated 3-D Whole Brst US vs Real-Time Hand Held US in Preop Assessment of Breast Cancer Patients	
Ikeda, Debra	NIH	Automated 3D Whole Breast Ultrasound in CA Patients	R21
Illes, Judy	NIH	Ethical & Social Impact of Self-referred Body Imaging	R21
Rubin, Geoff	RSNA	Fellowship in Cardiovascular Imaging	
Sommer, Graham	NIH-Renew	MRI of Renal Anatomy & Function in Chronic Ischemia	R01-renew
Sze, Dan	CIRREF	The Mechanism of Anti-Tumor Activity of Adenovirus	

EDUCATION AND TRAINING

NCI Training Program in Cancer Imaging

Donna Cronister

Our eleventh year of training began on February 1, 2003. We have graduated 14 trainees from our program, Advanced Techniques in Cancer Imaging, thus far. Our trainees continue to be extremely productive and we often collaborate with them in their new positions both locally and throughout the country. Drs. Susan K. Hobbs completed her two year fellowship in 2003. Susan returned to finish her last two years of residency training at the University of Minnesota. Dr. Karl Vigen also completed his fellowship and has joined the Scientific Staff continuing his work in interventional MRI. Dr. Charles Liu graduated from the program effective June 2003 and has joined La Jolla Radiology. Dr. Jonathan Levin continues his second year of his fellowship. Daniel Margolis started July 1, 2003. He is currently doing a 6-month clinical rotation.

A total of 15 postdoctoral slots became available on February 1, 2003 with the approval of the NCI/NIH. We are also glad to announce that Sam Gambhir, M.D., Ph.D., Kim Butts, Ph.D., and Daniel Spielman, Ph.D. have joined the program as preceptors.

TRAINEES SUPPORTED ON NCI TRAINING GRANT

GRADUATED TRAINEES

John Strang, M.D.
09/01/93 - 08/31/95
from Harbor - UCLA, Los Angeles, CA
Robert Herfkens, M.D. - preceptor
Current Position: Assistant Professor
University of Rochester, Rochester, NY

Ian Ch'en, M.D.
07/1/94 - 06/30/96
from University of Colorado, Denver, CO
King Li, M.D.-preceptor
Current position: Staff Radiologist
Southwest Washington Medical Center
Vancouver, WA

Susan Lemieux, Ph.D.
10/16/93 - 08/31/96
from Siemens Gammasonics, Knoxville, KY
Gary H. Glover, Ph.D. - preceptor
Current position: Assistant Professor
Diagnostic Imaging, University of
Western Virginia

Bruce Daniel, M.D.
07/01/95 - 06/30/97
from University of Michigan
Robert Herfkens, M.D. - preceptor
Current position: Assistant Professor
Stanford University

Garry Gold, M.D.
07/01/95 - 06/30/97
from Stanford University
Albert Macovski, Ph.D. - preceptor
Current position: Assistant Professor:
Stanford University

Yi-Fen Yen, Ph.D.
09/01/95 - 08/31/97
from Los Alamos Nat'l Lab, Los Alamos, NM
Gary H. Glover, PhD - preceptor
Current position: Assistant Professor
University of Western Ontario, London , Ontario Canada

Esther Yuh, Ph.D.
05/01/97 - 09/30/98
from Heartport, Inc., San Mateo, CA
King Li, M.D. - preceptor
Sandy Napel, Ph.D. - preceptor
Current position: Medical Student
Stanford University

Roger Shifrin, M.D.
07/01/96 - 06/30/98
from Bowman Gray Univ., Winston-Salem, NC
Norbert J. Pelc, Sc.D. - preceptor
Robert Herfkens, M.D. - preceptor
Current position: Private Practice
Radiology Associates, Daytona Beach, FL

Steven G. Heiss, M.D.
07/01/97 - 06/30/99
from University of California, Los Angeles, CA
King Li, M.D. - preceptor
Current position: Radiology Imaging Associates
Denver, Colorado

Martin Blum, M.D.
07/01/98 - 06/30/2000
from The Cleveland Clinic
Brooke Jeffrey, M.D. - preceptor
Current Position: PET/Nuclear Med Research
Palo Alto VA Health Care System

Curtis Coulam, M.D.
07/01/99 - 06/30/01
from: Duke University
Graham Sommer, M.D. - preceptor
Research topic: Prostate cancer imaging
Current Position: Gems State Radiology Group
Boise, Idaho

Samira Guccione, Ph.D.
01/31/00 - 01/30/02
from: Johns Hopkins
Mark Bednarski, M.D., Ph.D. - preceptor
Research topic: Molecular Imaging
Current Position: Research Associate
Stanford University

Yishan Yang, Ph.D.
12/01/00 - 04/30/02
From: Stanford University
Mark Bednarski, M.D., Ph.D. - preceptor
Research topic: Molecular Imaging
Current Position: Research Associate
Stanford University

Lawrence Chow, M.D.
07/01/00 - 06/30/02
from: Stanford University
Graham Sommer, M.D. - preceptor
Research topics: Prostate cancer imaging
Current Position: Assistant Professor
Stanford University

CURRENT TRAINEES

Jonatha Levin, M.D.
07/01/02 - 06/30/04
from: Harbor-UCLA Medical Center
Robert Herfkens, M.D. - preceptor
Research topics: Cardiac motion imaging

Karl Vigen, Ph.D.
01/29/01 - 01/28/03
from: University of Wisconsin, Madison
R. Kim Butts, Ph.D. - preceptor
Research topic: Thermal treatment of cancer, liver
Current Position: Research Associate
Stanford University

Susan Hobbs, M.D., Ph.D.
02/12/01 - 02/11/03
from: University of Minnesota
Mark Bednarski, M.D., Ph.D. - preceptor
Research topic: Molecular Imaging
Current Position: Resident
University of Minnesota

Charles Liu, M.D.
07/01/01 - 06/30/03
from: University of San Diego
Robert Herfkens, M.D., Graham Sommer, M.D. - preceptors
Research Topic: Cardiac Function Analysis: Breath-Hold and
Free Breathing Techniques
Current Position: Radiologist
La Jolla Radiology

Daniel Margolis, M.D.
07/01/02 - 06/30/04
from: UCLA
Sam Gambhir, M.D., Ph.D. - preceptor
Research topics: Multimodality Molecular Imaging

Postgraduate Education

Susie Spielman

The Department's Continuing Medical Education program continues to thrive and has become the number one Radiology CME program in the country. We once again offered ten courses in 2003 and many factors helped to differentiate our program and lead to our sustained growth. These include:

- Premiere courses on new technologies
- New/fresh lectures
- Topics which meet accreditation needs of registrants
- Selection of world renowned faculty
- Strict criteria for selection of locations (cities, hotels) and timing of meetings
- Innovative features (e.g. interactive lectures, wireless access, hands on training, protocol CDs)
- Strategic Partnerships (Japan, Europe)
- Strength of Stanford brand

When our program first began we selected "resort" destinations with content covering broad topics. Today, we have added meetings which are singly focused and the first to educate the medical imaging community about impending transitions to new and emerging technologies.

It is also our priority to offer the highest quality experience for both the faculty and registrants. We have been experimenting with the best uses of technology for increasing the interactivity of our meetings and providing important tools to help enhance the overall educational experience.

Our international symposium on Multidetector Row CT (MDCT) is now in its fifth year and, with over 500 attendees and innovative content, has surpassed our earlier efforts. We have received feedback from registrants and industry alike that its reputation as the premier meeting on MDCT has again been validated.^o We heard repeatedly from our registrants that the meeting was excellent, comprehensive and useful to their practice.^o We are extremely pleased to offer a program with so many strengths and such a significant attendance.

The ability to include world renowned speakers has been a key element of differentiation and our collaboration with industry has enabled participation of the thought leaders in our field. We are now in the second year of our course on Clinical High Field MRI which builds upon the successful model of our MDCT effort.

Additionally, we have meetings that are co-hosted by strategic partners in Japan and Europe which build international relationships for our faculty and grow our international reach and reputation. Our course this year in Venice, Italy included 200 registrants from over 25 countries.

In FY 2003 Stanford's postgraduate program included an impressive 193 speakers and more than 2,200 registrants. We look forward to continued growth and success in the year ahead.

LUCAS CENTER UPDATES

MR Systems, Education and Systems Support

Anne Marie Sawyer-Glover

Systems

1.5 TESLA MAGNET

This year we installed the latest in gradient amplifiers (ACGD), on the 1.5 Tesla GE Medical Systems Echospeed LX CV/i MR Whole-Body Magnet and upgraded the software to the 9.1 systems revision. These enhancements keep the Lucas Center at the leading edge of functional brain imaging and the development of cardiovascular applications. ACGD allows faster imaging and shorter echo times, as well providing increased sensitivities for Diffusion Weighted Echo Planar Imaging, which is used for the detection and treatment of stroke. The maximum gradient strength is now 50 mT/m. The software upgrade adds imaging sequences and enhancements to existing acquisition capabilities, as well as providing faster scanning, greater coverage and higher temporal and spatial resolution. It also allows us to visualize white matter tracks in the central nervous system and obtain information on the molecular diffusion of biological tissues.

3.0 TESLA MAGNET

The ACGD gradient amplifiers were also installed on the 3.0 Tesla G.E. Medical Systems Echospeed LX NV/i MR Whole Body Magnet. System software was also upgraded to VH3 (M4). Multi-Nuclear Spectroscopy is now available and phosphorus imaging is currently under development.

3.0 T is an important tool in carrying out a multitude of functional brain imaging studies (fMRI) which investigate diseases, conditions and congenital disorders in adults and children. It is also advancing neuroscientific knowledge on basic brain function. Body and musculoskeletal imaging applications are also in development at the 3.0T including knee, ankle/foot, wrist, elbow, shoulder, breast, abdomen, pelvis, prostate, and cervical spine.



Romi Samra, MR Research Technologist, prepares a research subject for a 3.0T MR scan of the abdomen using the 4-channel torso phased array coil.

AREAS OF RESEARCH USING LUCAS CENTER 1.5T AND 3.0T MAGNETS

Aging	Fragile X Syndrome
AIDS and HIV	Kidney disease
Alcoholism	Memory and language disorders
Alzheimer's disease	Mental retardation
Attention deficit hyperactive disorder (ADHD)	Mood disorders
Autism	Muscle damage
Bipolar disorder	Obesity
Breast disease detection and characterization	Obsessive compulsive disease
Cancer of the head and neck	Post traumatic stress disorder
Cardiovascular disease	Prostate cancer
Cartilage of the knee	Psychotic disorders
Chronic and intractable pain	Schizophrenia
Concussion	Stroke
Cystic fibrosis	Uterine leiomyomata
Depression	Vision
Dyslexia	Williams syndrome

COILS

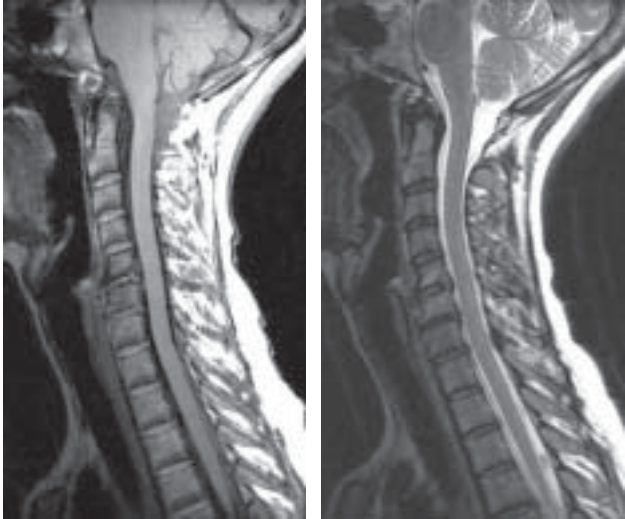
We continue to investigate and test new designs and concepts in RF imaging coils for use in MR imaging and spectroscopy at the Lucas Center whole body scanners, both 1.5 Tesla and 3.0 Tesla. A primary focus currently is the improved imaging of the knee, foot/ankle, wrist, breast, abdomen, and prostate at 3.0T. We are working with coil manufacturers and independent researchers building coils at the Lucas Center and at other academic research facilities.

NEW COILS FOR 3.0T



Cervical spine RF coil (P. Ledden, Nova Medical, Inc.) for functional imaging of the spinal cord to evaluate chronic and intractable pain (S. Mackey, Anesthesiology).

Two 3.0T cervical spine images acquired in the sagittal plane using the cervical spine coil: T1-weighted Spin Echo (left) and T2-weighted Fast Spin Echo (right).



3.0T Anterior neck coil (R. Hashoian, Clinical MR Solutions).

4-CHANNEL PHASED ARRAY COILS FOR THE 3.0T



Coil for abdomen, pelvis, and chest (G. E. Medical Systems).



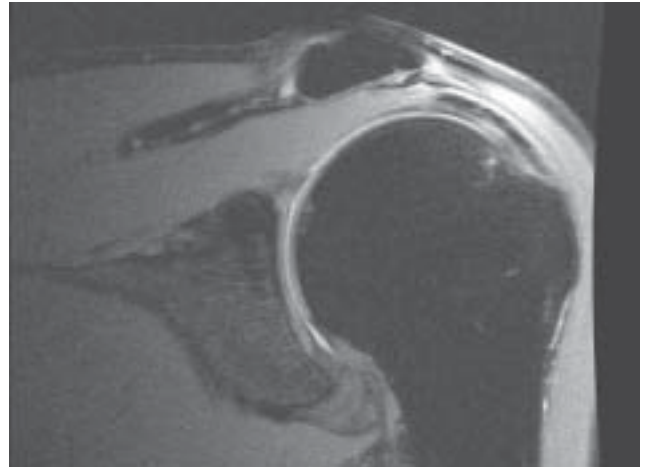
A 3D contrast-enhanced image acquired at the 3.0T using the 4-channel torso phased array coil to visualize the aorta and renal arteries (R. Herfkens, Director of MR, Stanford and G.E. Medical Systems collaboration).

4-CHANNEL PHASED ARRAY COILS FOR THE 3.0T (CONTINUED)



Shoulder coil (T. Schubert, MRI Devices, Inc.).

3.0T shoulder image acquired using a fast spin echo acquisition with fat suppression.



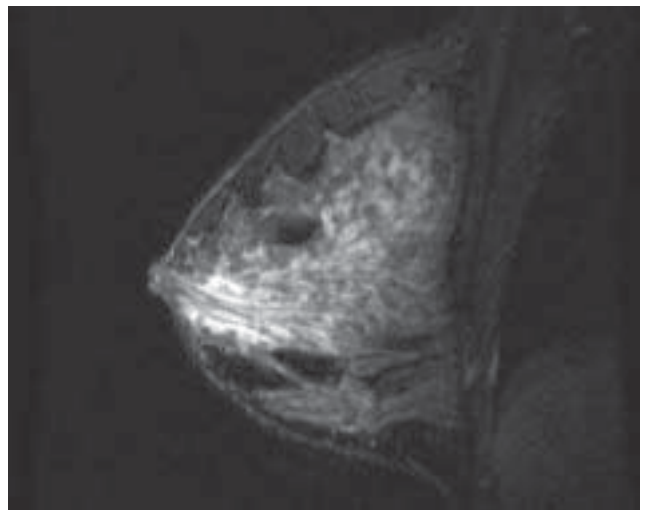
Wrist coil (T. Schubert, MRI Devices, Inc.).

T1-weighted spin echo wrist image acquired at 3.0T.



Breast coil (T. Schubert, MRI Devices, Inc.).

3.0T breast image acquired using a 3D spoiled gradient echo with fat selective inversion recovery.



PROSTATE COIL FOR THE 3.0T



RF coil for imaging of the prostate (C. Dumoulin and R. Watkins, G.E. Medical Systems Corporate Research and Development).



An axial prostate image acquired at the 3.0T using a fast spin echo sequence.

EQUIPMENT

New imaging devices and accessories have been added over the last year EEG (Neuroscan), an immobilization device for cervical spine functional imaging (B. Krasnow, Mag Concepts), and new video projectors and audio systems for fMRI studies. In current development is eye tracker for use at 3.0T for functional brain studies (B. Krasnow, Mag Concepts).



Scan subject in preparation for functional brain MR scan and electroencephalogram(EEG, Neuroscan).

Immobilization device for functional imaging of the cervical spine at 3.0T (B. Krasnow, Mag Concepts).



Eye tracker device in development for use at 3.0T (B. Krasnow, Mag Concepts).

Both monitoring systems have been upgraded to the latest software and hardware which addresses system noise that occurs as a result of faster imaging strategies. The monitoring systems provide heart rate, cardiac waveform, pulse oximetry (saturated oxygen), end-tidal carbon dioxide, and blood pressure (non-invasive and invasive). Monitoring systems can serve to synchronize the MR image acquisition to various types of motion generated by the subject such as breathing, the beating heart and blood flow. These improve image quality and improve the accuracy of collected MR data. These systems also serve to monitor the status of animal models while being imaged in the magnet under the affects of anesthesia and often on a respirator.

Safety Training and System Instruction

Safety training and system instruction have been provided to over 102 new researchers conducting experimental MR studies at the Lucas Center. Magnet safety training is provided twice a month and is a requirement for all researchers assisting or conducting studies on any of the magnet systems at the Lucas Center. Safety training is a yearly requirement for all researchers. A magnet safety refresher course is currently being provided to 134 researchers. This ensures that all users and assistants are qualified to operate the system and satisfies Lucas Center and University requirements for safety. System and safety support is provided to the researchers 7 days a week, 24 hours a day to ensure that research endeavors are successful, generate valuable data, and, above all, are safe for the researchers, the human subjects and the MR system and its components. Magnet safety is an on-going concern as the MR environment can be a potentially lethal setting without continuing education and persevering support. The research environment generates many new yet prototype designs in RF imaging coils, imaging accessories, monitoring and response devices such as button boxes, eye trackers, and electroencephalogram (EEG) recorders, and sensory devices. Evaluation of these new devices is on-going to ensure that neither the image data, the safety of the human subject, nor the integrity of the MR system is compromised by the presence of these devices in the magnet room, in the bore of the magnet, or in the presence of an RF coil.

MR Systems Support

Daily support is provided to all researchers including faculty, post-doctoral fellows, graduate students, and visiting scholars in the Lucas Center and Department of Radiology; researchers from other University departments such as Psychology, Psychiatry, Neurology, Neurosurgery, and Nephrology; and service center users from outside of the University.

MR research technologist, Romi Samra, provides scan support to the researchers conducting MR studies at the Lucas Center.

Scan support was provided for multiple research studies including:

- MR Spectroscopy of Breast Disease and Cancer
D. Ikeda, D. Spielman, E. Adalsteinsson, and L. Stables (Radiology)
- MR Imaging of Breast Disease and Cancer
R. Herfkens, B. Daniel, D. Ikeda, R. Birdwell, G. Glover, and L. Stables (Radiology)
- MRI/MRS of Prostate at 3.0T
B. Daniel, G. Sommer (Radiology)
- MRI of Renal Anatomy and Function in Chronic Ischemia
G. Sommer and N. Pelc (Radiology); B. Myers (Nephrology)
- A Model for Hypercortisolism for Major Depression
- Functional MRI of the Brain
D. Lyons and A. Schatzberg (Psychiatry)
- Computer Modeling and MRI of Hemodynamic Conditions in the Aorta
- Blood Flow in a Porcine Thoracic Aortic Bypass Graft Measured In Vivo using MR Imaging
- Hemodynamic Determinants of AAA Disease Following Spinal Cord Injury
C. Taylor, C. Zarins (Vascular Surgery); N. Pelc, R. Herfkens (Radiology)
- Cortical Processing of Visual Motion in Primates
W. Newsome (Neurobiology)
- Fat Redistribution and Metabolic Change in HIV
A. Zolopa (Infectious Diseases)
- Diabetes Therapy to Improve Muscle Mass and Clinical Status in Cystic Fibrosis Patients with Abnormal Glucose Tolerance
R. Moss (Pediatrics)
- Image Based Computational Blood Flow Modeling of the Pulmonary Tree as Applied to Problems in Congenital Heart Disease
J. Feinstein (Pediatric Cardiology), C. Taylor (Vascular Surgery)
- Cortical Processing of Arm Movements (Primates)
K. Shenoy (Neurobiology)

Experimental Model Management

Diane Howard, Wendy Baumgardner

In our continuing efforts to provide support to the Radiology investigative staff, we are entrusted with the responsibility of overseeing all animal protocols within our department and all other departments carrying on work at the Lucas Center. Two experienced California Licensed Veterinary Nurses each with over 20 years in the field, attend all animal studies making the health and welfare of the animals always our most important priority. Diligent care is taken during all procedures involving animal subjects; they are treated with the utmost respect, compassion, and professional care. Animal studies at the Lucas Center enhance both treatment and diagnostic abilities, and are never taken lightly.

We realize the necessity of living subjects in advancing our knowledge, and ensure proper respect for life is part of all protocols. Work at the Lucas Center produces advancement of invasive and non-invasive procedures such as magnetic resonance imaging, fluoroscopy, focused ultrasound, computed topography, as well as magnetic resonance therapy. In addition, studies currently being done involve the study of alcoholism, stroke, liver and prostate cancers, neuroimaging of the brain, and stent/graft implantation. The techniques currently being explored at the Lucas Center all contribute to more efficient and effective medical treatment for illness and disease.

CURRENT ACTIVE PROTOCOLS IN USE AT THE LUCAS CENTER

- Adenoviral Mediated Gene Delivery
- Blood Flow in a Thoracic Aortic Bypass Graft
- Catheter Based Cardiovascular Magnetic Resonance Imaging
- Characterization of a Novel Abdominal Aortic Aneurysm
- Control of Gene Expression Using Focused Ultrasound
- Controlled Release System for Low Dose Adenoviral-mediated GeneDelivery
- Coronary Artery Imaging using CT and Intravascular Contrast Agent PH-50
- Cortical Processing of Arm Movements
- Cortical Processing of Visual Motion
- CT Angiography Using PH-50 Delivery to the Arterial Wall in vivo
- Effects of Antioxidant Supplementation on the Aging Process
- Eudragit for Embolization of an AVM Model
- Evaluation of Endovascular Devices using Fluoroscopy
- Gene Expression Changes and Protein Profile Patterns
- Image Based Computational Blood Flow Modeling
- Imaging Apoptosis During Cancer Therapy Using Annexin
- Integrative Neuroscience Initiative on Alcoholism
- Magnetic Resonance Imaging Sequence Development
- Minimally Invasive MR-Guided Thermal Therapies
- Model of Hypercortisolism for Depression-Phase 2
- Molecular Imaging of Tumor and Vascular Receptors
- MR Guided Prostate Cryosurgery
- Prefrontal Brain Growth and Psychosocial Development
- Prostate Ablation Using Acoustic Applications and MRI
- Prostate Cancer and BPH Ablation with Acoustic Wavelengths
- Relationship of CT Dose to Scan Resolution
- Somatic Gene Therapy for Vascular Restenosis
- Stent Coatings to Decrease In-stent Restenosis
- Techniques of Stent/Graft Implantation and Liver Ablation

Neuroimaging

Spiral-in/out for fMRI: Comparison with spiral at 1.5T and 3T

Allison Preston¹, Moriah Thomason², Kevin Ochsner¹, Gary H. Glover³

²Department of Psychology¹, ²Neurosciences Program, ³Department of Radiology

INTRODUCTION

BOLD fMRI at 3.0T has been shown to provide increased signal in uniform brain regions compared with 1.5T (1, 2), but this is accompanied by increased signal dropout in regions compromised by air/tissue susceptibility interfaces. Spiral-in/out trajectories have been found to reduce the dropout and provide improved CNR in primary sensory and visual tasks (3). However, comparison of these spiral trajectories at both field strengths with high-order cognitive tasks has not yet been performed. The goal of this study was to examine this 2x2 comparison to determine whether spiral-in/out can overcome increased susceptibility effects at 3T and provide improved activation even in compromised regions at both fields.

METHODS AND MATERIALS

After giving informed consent, eight volunteers were scanned at 1.5T and 3T (GE Signa, Cv/Nv gradients) in contiguous sessions using a spiral-in/out sequence. Cognitive tasks included verbal working memory, novel vs. repeated pictures (episodic memory) and viewing emotional scenes, in order to activate respectively inferior frontal gyrus (IFG), medial temporal lobe (MTL) and amygdala. The acquisition parameters were 25 axial 4 mm slices, 22 cm FOV, 64x64 matrix, TE 40ms (1.5T) or 30ms (3T), TR 2000ms, 192 time frames, spectral-spatial RF excitation pulse. Task and scanner order were counter-balanced. The image time series were analyzed after weighted combination of the spiral-in and spiral-out data (3) as well as for the spiral out component alone using SPM99. ROIs were defined that included regions visible in all four activation maps for each subject. In addition, overall activation volumes were measured. Significant differences in activation volumes were tested using 2 way ANOVA with factors of field strength and pulse sequence.

RESULTS

The spiral-in/out technique generally provided substantially more activation both globally and in targeted ROIs (Figs. 1, 2), and exhibited greater signal recovery than the spiral-out method (Fig. 3). Critically, 3T in/out results showed significantly more activation than at 1.5T even in regions traditionally compromised by susceptibility dropout. For example, mean voxel counts in MTL were 114, 95, 204 and 165 for 1.5T-in/out, 1.5T-out, 3T-in/out and 3T-out, respectively ($F = 4.83$, field; 19.7, pulse sequence). Even though the dropout was larger at 3T with the spiral-out sequence, the spiral in/out sequence demonstrated recovery of signal comparable to that at 1.5T. Overall, the spiral in/out sequence resulted in increased global activation and improved signal in artifact prone areas at both 3T and 1.5T.

CONCLUSIONS

The spiral-in/out method demonstrated substantially increased activation volumes as compared to conventional spiral-out acquisitions, and improved BOLD signal in MTL and IFG regions at 3T compared with 1.5T. Thus, the spiral-in/out trajectory at 3T may provide substantial advantages in fMRI studies of higher cognitive function

REFERENCES

1. Kruger G, Kastrup A, Glover G. *Magn Reson Med* 2001; 45:594-604
2. Krasnow B, Tamm L, Grecius M, Yang T, Glover G, Reiss A, Menon V. *NeuroImage* 2003; 18:813-826
3. Glover G Law CS. *Magn Reson Med* 2001; 46:515-522.

Figure 1: Activation maps in episodic memory task

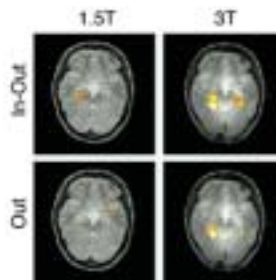


Figure 2: activation maps in VWM task

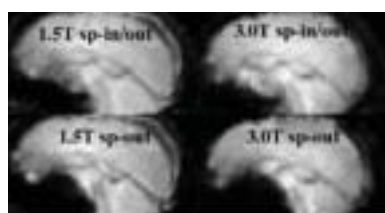
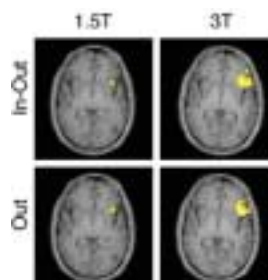


Figure 3 : T2* weighted images.

fMRI - Technology Development

Novel Spiral-In/Out Method for Reduced Susceptibility Artifacts in BOLD fMRI

Christine S. Law^{1,2}, Gary H. Glover²

Departments of ¹Electrical Engineering and ²Radiology

INTRODUCTION

Conventional BOLD fMRI suffers from signal dropout in frontal orbital and lateral parietal regions because of air/tissue susceptibility interfaces. Spiral-in/out trajectories [1] have been found to reduce the dropout and provide improved CNR in such regions [2], but artifacts remain because each image is acquired with a full k-space trajectory leading to a lengthy total readout time. We propose the use of a two-segment acquisition in which the two interleaves are gathered contiguously as a spiral-in/out trajectory.

METHODS AND MATERIALS

A two-interleaf design was used as the basis for the pulse sequence. The first interleaf is played out as a spiral-in trajectory ending with the k-space origin at TE, while the second interleaf begins immediately as a spiral-out acquisition. The entire readout thus comprises a complete k-space sampling. Figure 1 shows a conventional spiral-out trajectory and the new sequence. While the total readout durations are similar, the in-out trajectory extends about half as far beyond TE and was thus hypothesized to result in reduced susceptibility dropout.

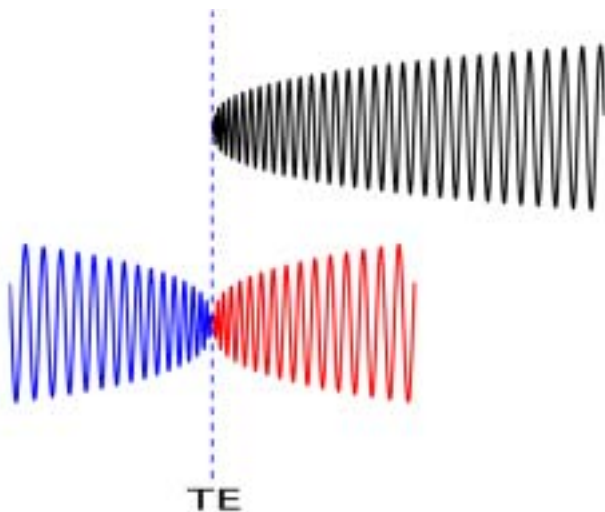


Figure 1: (top) Conventional spiral out, and (bottom) spiral-in/out gradients. The blue and red portions of the gradients indicate their corresponding k-space trajectory location in Figure 2.

Image quality depends heavily on the accuracy of the trajectory rendered by the scanner hardware. We found the accuracy inadequate, but it improved with precompensation for this particular application. That problem was corrected assuming a linear model for the gradients, and by developing a precompensation filter convolved with the designed (ideal) gradient trajectory. A very long finite impulse response filter was obtained from measurements of the trajectory [3] in comparison with the ideal trajectory using an exact inversion. The uncompensated and precompensated measurements are shown in Figure 2.

We compared the spiral-in/out sequence with the conventional spiral-out trajectory [4] on a normal subject using a 1.5 Tesla whole-body scanner (Signa, GE Medical Systems, Milwaukee, WI) having a conventional head-coil. Fourteen slices were chosen including the frontal orbital region (TR/TE/a/MAT/TH/FOV = 1s, 30ms, 90°, 64X64, 4mm, 20cm).

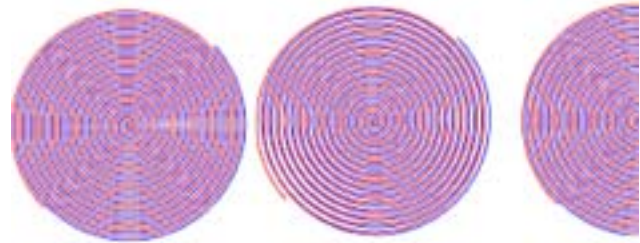


Figure 2: (left) Designed (ideal) spiral-in/out trajectory, (center) measurement of the designed trajectory without precompensation, and (right) measurement of precompensated trajectory. Without precompensation, k-space trajectory differs from the designed one, especially at the outer portion of k-space. With compensation, much of the trajectory errors can be corrected.

RESULTS

Figure 3 shows a comparison of imaging between the conventional and new spiral-in/out trajectories. Reduction in susceptibility dropout is significant using the in-out method. Some artifacts remain from trajectory errors that may be corrected with oversampling each segment near the k-space origin. T_2^* weighting differences between conjugate points in k-space do not produce significant artifacts.

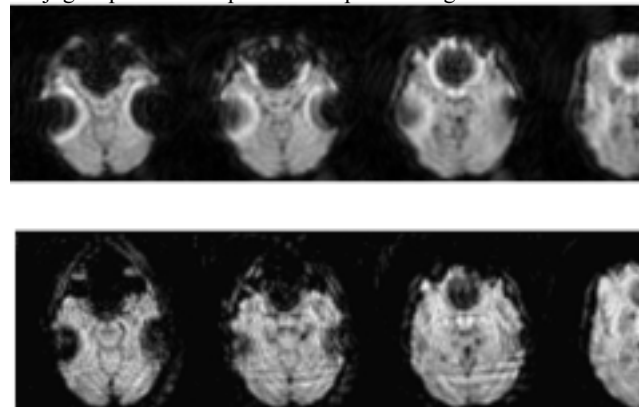


Figure 3: Images of the frontal orbital and lateral parietal regions using (top) conventional spiral-out and (bottom) spiral-in/out trajectories. . Susceptibility dropout is reduced with spiral-in/out sequence. Residual artifacts may be corrected with over-sampling at k-space origin.

CONCLUSIONS

We developed a novel spiral-in/out trajectory that reduces susceptibility artifacts without increasing scan time. We also demonstrated that precompensation filters ensure data acquisition at desired k-space locations. Both techniques are beneficial to magnetic resonance imaging in general and, in particular, to fMRI applications requiring fast imaging techniques and the need to explore the frontal orbital and lateral parietal regions. Greater image quality may accompany over-sampling around the k-space origin which contains much of the low spatial-frequency components.

REFERENCES

1. Glover GH, Law CS. *Magn Reson Med* 2001; 46:515-22
2. Thomason M, Preston A, Ochsner K, Glover GH. ISMRM Annual Meeting 2003 (submitted)
3. Duyn JH, Yang Y, Frank JA, van der Veen JW. *J Magn Reson* 1998; 132:150-3
4. Glover GH. *Magn Reson Me.* 1999; 42:412-5

Real-time Reconstruction and Analysis of fMRI Data

David Ress, Gary E. Glover

Department Of Radiology

INTRODUCTION

We have developed software package that reconstructs, analyzes, and displays fMRI results as they are acquired from the scanner with a latency of only a few seconds. This utility should be useful for a variety of purposes, including confirmation of experimental results from simple blocked designs, real-time monitoring of “resting-state” activity, and tracking subject head movement.

METHODS AND MATERIALS

Two separate programs implement the real-time functions. The reconstruction code is a C-language program that runs on the scanner host computer. The analysis code is an IDL program that runs on a dedicated real-time analysis computer, also in the scanner control suite. The reconstruction code acquires raw k -space data from the scanner, reconstructs each image, and writes the resulting data to a single large file in temporal order. The analysis code accesses this data file via a network connection, and processes it to create a variety of informational data overlays that are continuously updated as the scan proceeds. The analysis code can also read in and display anatomical images of the brain. Data processed from the functional time series can be overlaid upon these anatomical images, or directly upon a static set of functional slice images. A variety of analysis options are available. For all studies, the mean functional image and its standard deviation are calculated. For simple, AB-blocked studies, the code can calculate the correlation, amplitude, and phase for the best-fit sinusoid for each voxel's time series. For resting-state or event-related studies, the code can calculate the power in a particular passband. These calculated quantities can be displayed as a colored overlay upon the static anatomical images using either colormaps or false-color methods.

To illustrate the capabilities of the real-time code, we conducted a simple fMRI demonstration. A single subject engaged in a simple blocked task. During the 15-s active portion of each block, they viewed a large field-of-view flickering checkerboard, tapped their index fingers bilaterally in time with flickering display, and listened to a series of tone pips. During the 15-s inactive periods, the subjects simply rested. This 30-s alternation was repeated 8 times to create a 4-minute scan. This task was trivially known to produce substantial sensory and motor activations. Functional MR images were collected (GRE BOLD contrast, spiral PSD, $T_E = 30$ ms, flip-angle = 77° , eff. pixel size = 3.75 mm) every 2 s on 25 5-mm-thick axial slices covering most of the brain. On the same slices, a set of high-resolution (pixel size = 0.94 mm) T_2 -weighted images was also acquired as an anatomical reference.

RESULTS

To display the scan results with the real-time analysis system, we chose a false-color overlay displaying correlation on the red channel, time-series standard-deviation on the blue channel, and raw functional image signal magnitude on the opacity channel (Fig. 1). This color data, overlaid upon the gray-scale anatomical images, plainly shows the regions of task- or stimulus-correlated activity with a red color in motor, auditory, and visual cortex. Noisy regions, e.g., the optic nerve, are marked with a blue overlay color. The display is shown as it appears at the end of the 4-minute scan, but useful localization information becomes evident after 30–60 s of scanning.

CONCLUSION

This real-time analysis system will be a useful addition to fMRI analysis tools at the Lucas Center.

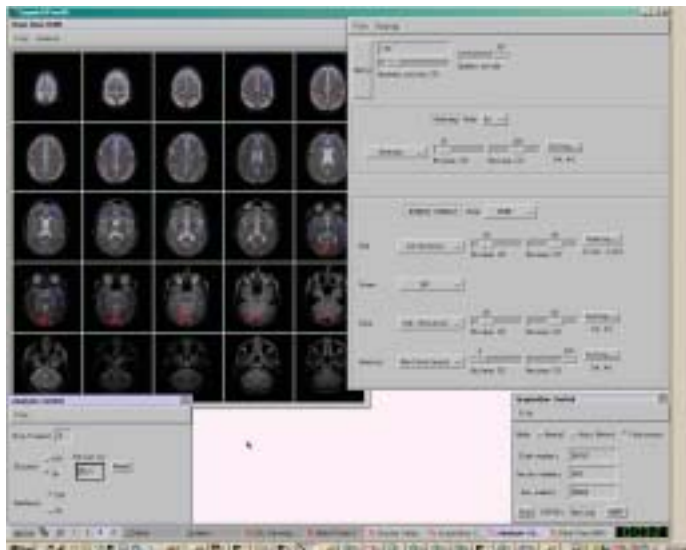


Figure 1: The real-time analysis system display. Upper left window shows slice display with grayscale anatomy images and color fMRI overlays. Upper right window shows display control panel. Lower windows controls image analysis functions (left), and reconstructed image acquisition (right).

fMRI - Technology Development

T1 and T2 Measurements of Breast Tissue at 0.5T, 1.5T, and 3T

Rebecca Rakow, Bruce Daniel, Karl Vigen, Anne Sawyer-Glover, Gary Glover

Department of Radiology

INTRODUCTION

In breast MR imaging, decreasing imaging time and optimizing the contrast to noise ratio may improve breast MRI's diagnostic potential. This study explored the utility of higher magnetic fields in achieving these goals. By better understanding relaxation times of breast tissue as a function of increasing magnetic fields, imaging parameters can be fine-tuned for maximal results. The purpose of this study serves to quantify T1 and T2 of fat and glandular tissue in breasts at different field strengths.

METHODS

In order to measure the effects of increasing magnetization on breast MRI, T1 and T2 images were calculated from measurements made on the right breasts of five healthy women ranging in age from 22-49 at three magnetic fields: 0.5T, 1.5T, and 3.0T. A spin-echo sequence was employed for T1 and T2 measurements. A 3-Point-Dixon sequence was also used to measure T1. Calculated T1 and T2 values for the regular spin-echo sequence were based respectively on three TR's: 3000, 800, 300 ms, and two TE's: 20, 100 ms. The TR's for the calculated T1 values for the Dixon sequence were: 1500, 800, 300 ms. In calculating T1 using the regular spin-echo and Dixon methods, a sampling of three ROI's in each fat and water, of the centermost images, per volunteer, provided the data for T1 calculation and analysis. For the T2 measurements, a sampling of ten ROI's in the centermost T2 calculated image (five ROI's in fat, and five in glandular tissue) provided the data for analysis. The average T1 and T2 of fat and glandular tissue (independently) per person were then collectively averaged for each magnetic field. To collect contrast to noise ratio(CNR) information, three specified ROI's (fat, glandular tissue, and outer noise) placed in the spin echo T1 images (TR 800) supplied the measured values. The difference between the signal (averaged over five volunteers) in the fat and glandular tissue divided by the outer noise rendered the calculated value.

RESULTS

Differences in T2 across fields proved insignificant compared to intrinsic tissue variability(Fig.1). T1 differences across fields in fat also proved insignificant. T1 measurements in glandular tissue, however, showed an upward trend with increasing field (Fig. 2,3). Specifically, data indicates that on average T1 of glandular tissue at 0.5T, 1.5T, and 3T are correspondingly 900, 1350 and 1550 ms. The glandular tissue (water images) for the Dixon results (Fig. 4) indicate similar results to the regular spin-echo values. Though, due to the admixture of lipid and water in breast fat, the Dixon fat T1's are significantly lower than the regular spin-echo fat T1 values. The CNR ratio in the regular spin echo T1 images between 1.5T and 0.5T is approximately 1.8. The CNR ratio between 3.0T and 1.5T is 3.3.

DISCUSSION

Results quantify the T1 dependence on magnetic field in breast glandular tissue. As magnetic field increases, T1 in breast glandular tissue increases. CNR calculations confirm that T1 data collected at a TR of 800 ms improve with increasing field strength. This enhancement more than compensates for any loss in saturation recovery due to higher magnetic fields. Diagnostic informa-

tion in breast MRI depends on differentiating between glandular tissue and mammary fat. Results support greater tissue contrast at 3.0T and set expectations for breast MRI at 3.0T to yield superior diagnostic information. These results differ from previous relaxation measurements made in breast tissue¹, and are in keeping with measurements made in other organs². 3-Point Dixon imaging indicates that separating water and fat when measuring T1 is recommended when interested in the lipid component of fat. Support thanks to NIH RR 09784, NIH GM 08294, Lucas Foundation and GEMS.

REFERENCES

- 1 Bolinger L, Cecil K, Englander S, Stolpen A. *Book of Abstracts, ISMRM Sixth Annual Meeting*, 1998; p. 232
- 2 de Bazelaire C, Duhamel G, Alsop D. *Book of Abstracts, ISMRM Tenth Annual Meeting*, 2002; p. 2292

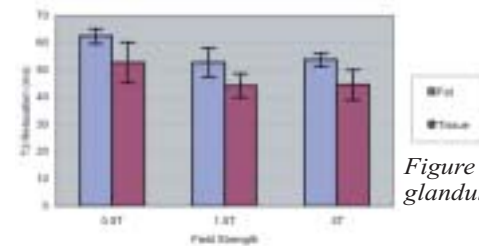


Figure 1: T2 of fat and glandular tissue.

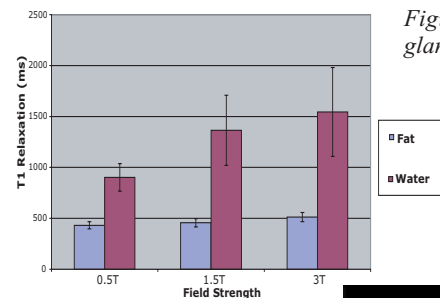


Figure 2: T1 of fat and glandular tissue.

Figure 3: T1 calculated image.

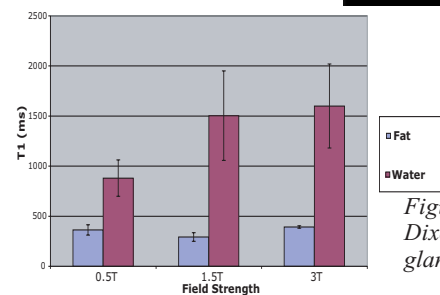
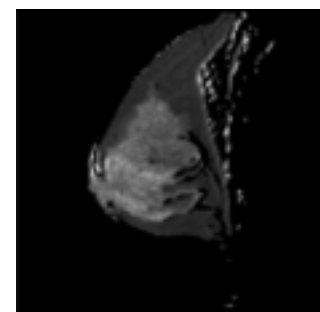


Figure 4: T1 of 3-Point Dixon results of fat and glandular tissue.

The Effect of the Concomitant Magnetic Field in Diffusion Weighted Imaging

Chunlei Liu^{1,2}, Roland Bammer², Michael E. Moseley²

Departments of ¹Electrical Engineering and ²Radiology

INTRODUCTION

Concomitant magnetic fields with non-linear spatial dependences arise where linear gradients are applied in order to satisfy Maxwell's equations. In this study, the effect of the concomitant field on diffusion weighted imaging is explored. Although spatial averaging over one voxel will not normally cause signal attenuation in the presence of the concomitant field, the spin's random movement will affect the signal intensity. Nevertheless, a simulation shows that the signal attenuation due to the concomitant field is negligible in diffusion experiments.

METHODS AND MATERIALS

It has been demonstrated that a pure linear gradient can not be produced without introducing extra non-linear spatial varying magnetic fields (1, 2). Let G_x , G_y , and G_z be the applied gradients along the x, y, and z directions respectively, then the magnitude of the magnetic field vector exceeds the sum of $B_0 + \mathbf{G} \cdot \mathbf{r}$ (\mathbf{r} is the position vector) by an amount of B_c (2), given by,

$$B_c(x, y, z) \cong \frac{1}{2B_0} \left[\left(G_x z - \frac{G_z x}{2} \right)^2 + \left(G_y z - \frac{G_z y}{2} \right)^2 \right] \quad [1]$$

Let ϕ be the accumulated phase of a spin at the echo time in a diffusion encoded spin echo sequence, then ϕ is given by,

$$\Phi = -\gamma \int_0^{TE/2} (\mathbf{G} \cdot \mathbf{r}(t) + B_c(\mathbf{r})) dt + \gamma \int_{TE/2}^{TE} (\mathbf{G} \cdot \mathbf{r}(t) + B_c(\mathbf{r})) dt \quad [2]$$

where $\mathbf{r}(t)$ is the spin's 3D random displacement over time t .

In principle, the presence of the concomitant field will introduce additional diffusion attenuation to the signal intensity on top of that caused by the linear gradient. The normalized MR signal can be expressed as the ensemble average over each voxel (3), as shown below,

$$S = \int_{-\infty}^{+\infty} \exp(j\Phi) P(\Phi) d\Phi \quad [3]$$

Here, $P(\phi)$ is the probability density function of the accumulated phase. ϕ is generally not Gaussian. As a consequence, the concomitant field will also introduce a phase shift in the signal.

Assuming a Gaussian distribution of the random spin displacement, simulation techniques were applied to evaluate the signal intensity given by Eq. [3]. The following parameters were used: $B_0 = 1.5T$, $\delta = 20.2ms$, $\Delta = 100.5ms$ and $D = 2.02 \times 10^{-3} \text{ mm}^2/s$. Seven diffusion gradient directions as given in table 1 were applied. At each direction the gradient strength was varied from 0 to 40 mT/m in 10 uni-

form steps. As a result, the largest b-value used was around 5000s/mm². Two signal decay curves were obtained with and without the consideration of the concomitant field. The effective b-value was computed as $b = -\ln(S/S_0)/D$ for both cases.

RESULTS

The average percentage increase of the effective b-value for each direction after considering the concomitant field is listed in Table 1. As shown in the table, the relative differences of the computed b-values are on the order of 10⁻⁶%, which are completely negligible. Simulation also demonstrates that there is no significant gradient orientational dependence as seen in Table 1.

Gradient Direction (x y z)	Relative b difference ($b_c - b$)/b (10 ⁻⁶ %)
(1 0 0)	6.60 ± 10.1
(0 1 0)	3.14 ± 7.43
(0 0 1)	2.93 ± 15.7
(1 1 0)	-3.50 ± 12.1
(1 0 1)	1.43 ± 28.7
(0 1 1)	3.05 ± 16.6
(1 1 1)	0.99 ± 15.4

Table 1: The differences of computed effective b-values with and without considering the concomitant field. b is the b-value when the concomitant field is neglected and b_c is the b-value when it is considered.

CONCLUSIONS

In principle, the effective b-value will increase in the presence of concomitant fields. This is a result of additional signal dephasing caused by the spatial dependent concomitant field. However, the concomitant field is usually very small due to the facts that $G \ll B_0$, and the mean square diffusion distance $\langle \mathbf{r}^2 \rangle$ is very small. As a result, the accumulated phase is not significant and the effect of the concomitant field can be neglected.

REFERENCES

1. Norris DG, et al. *Magn Reson Imaging* 1990; 8:33-37.
2. Bernstein MA. et al. *Magn Reson Med* 1998; 39:300-308.
3. Callaghan PT, *Principles of Nuclear Magnetic Resonance Microscopy*, Oxford Science Publication 1991.

INTRODUCTION

Diffusion tensor imaging (DTI) is known to have a limited capability of resolving multiple fiber orientations within one voxel. The angular distribution of the apparent diffusion coefficient is incapable of inferring the correct fiber orientations as demonstrated in this report. A new methodology is proposed by generalizing the Fick's law to a higher order partial differential equation and reconstructing the probability density function of the displacement using higher order cumulants.

METHODS AND MATERIALS

Fick's first law can be generalized as,

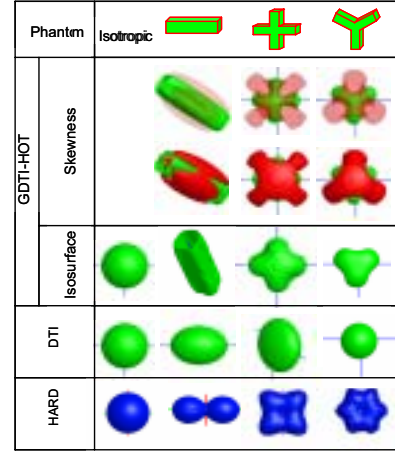
$$F_i = -D_{ij}^{(2)} \frac{\partial C}{\partial x_j} - D_{ijk}^{(3)} \frac{\partial^2 C}{\partial x_j \partial x_k} - D_{ijkl}^{(4)} \frac{\partial^3 C}{\partial x_j \partial x_k \partial x_l} - \dots \quad [1]$$

Here the coefficient is a n -th order diffusion tensor, F is the flux and C is concentration. Using Eq. [1], and following Torrey's derivation (1), the transverse magnetization is found to be,

$$m(b^{(n)}) = m(0) \exp \left(\sum_{n=2}^{\infty} (+j)^n D_{i_1 i_2 \dots i_n}^{(n)} b_{i_1 i_2 \dots i_n}^{(n)} \right) \quad [2]$$

where $m(0)$ is the transverse magnetization in the absence of diffusion gradient and $b^{(n)}$ is an n -th order tensor determined by diffusion gradients. The higher order tensors (HOT) can be estimated by combining a series of diffusion-weighted images. The higher order cumulants can then be calculated using these tensors. The probability density function (PDF) of the displacement can be reconstructed based on those cumulants by using Gram-Charlier series. Simulations were done on four synthetic phantoms: (i) an isotropic phantom, (ii) a single tube, (iii) two perpendicularly crossing tubes, and (iv) a Y-shaped tube. The following parameters were used: $\delta = 20.2\text{ms}$, $\Delta = 100.5\text{ms}$ and $D = 2.02 \times 10^{-3} \text{ mm}^2/\text{s}$. 200 diffusion gradient directions evenly distributed on the surface of a sphere were applied. At each orientation the gradient strength was varied from 0 to 40 mT/m in 10 uniform steps. The generalized diffusion tensors up to order 4 were estimated. The PDF of spin displacement was reconstructed by calculating its higher order cumulants. PDF iso-surface plot and skewness plot were used to visualize the reconstructed fiber structure. In the skewness map, green represents positive values and red represents negative values.

Figure 1: Comparison of HOT, DTI and HARD. For isotropic phantom, the skewness is too small to be significant. Hence they are not plotted here. In the PDF and diffusion ellipsoid plots, the blue lines are x and y axis; in the HARD image, red line is the y axis and green is the x axis.



RESULTS

The resultant PDF iso-surface plots and the skewness maps obtained from the four phantoms are plotted in Fig. 1. The diffusion ellipsoid determined by conventional DTI and the angular distribution of ADC determined by high angular resolution diffusion weighted imaging (HARD) method (2) are also shown in this figure. The skewness map is plotted in two ways: in the first plot, the negative part (red) is made transparent while the positive part (green) is solid; in the other plot, both parts are made solid. All those plots are 3D objects. The HOT method revealed the structure of the phantoms accurately as seen in the PDF plots. Neither DTI nor HARD can identify the crossing and Y-shaped structure correctly.

CONCLUSIONS

As demonstrated by the simulations, the HOT method can accurately reveal the underlying structure for all four phantoms, whereas DTI and HARD fail to identify the simulated intersecting fibers. Both DTI and HARD only utilize the first term on the left hand side of Eq. [1], hence will suffer from the unrecoverable information loss. HOT also has the potential to greatly improve tractography (3).

REFERENCES

1. Torrey HC, *Phys Rev* 1956; 104:563-565.
2. Tuch DS, et al. Proceedings of the 7th Annual Meeting of ISMRM, 1999, p321.
3. Basser PJ, et al. *Magn Reson Med* 2000; 44:625-632.

“Fiber-Tracking” - Tracing White Matter Connectivity

Burak Acar, Roland Bammer, Chunlei Liu, Michael Moseley

Departments of Electrical Engineering and Radiology

INTRODUCTION

Diffusion tensor imaging (DTI) is a promising new technique for the assessment of white matter (WM) structural integrity and connectivity. Tensors (a mathematical construct useful for describing multidimensional vector systems) are ideal for describing proton diffusion restricted by white matter tracts, by indicating the direction and the magnitude of restriction. This in turn offers an index of directional coherence of fiber tracts or integrity of cellular structure.

One of the more exciting methods to arise from the noninvasive mapping of white matter tracks is the potential of tracking the white matter fibers from one region of brain to another. This in essence, reveals the underlying “wiring” of the activated brain..

METHODS AND MATERIALS

Our diffusion tensor imaging protocol is performed using a spin echo EPI technique is as described earlier. The 4-minute exam yields a 39 slice dataset of vector maps. The vector maps hold the orientation of the fibers as well as the magnitude of the orientation. From the fiber maps, one can compose several general approaches to finding connectivity from fiber to fiber. Aside from regression and Monte Carlo methods, one of the most direct is to find the intervoxel connections that exist within a prescribed cone. We use presently a 50-degree angle cone to determine potential connections from voxel to voxel.

RESULTS

Our algorithm allows for real-time connectivity maps that can be generated from planting a seed in one white matter tract region. We have constructed software “phantoms” to check the algorithms for accuracy and reproducibility.

CONCLUSIONS

The overall aim of this project is to map the potential pathways of cognitive and motor activation. As such, fiber tracking would be an ideal adjunct to fMRI and spectroscopy.

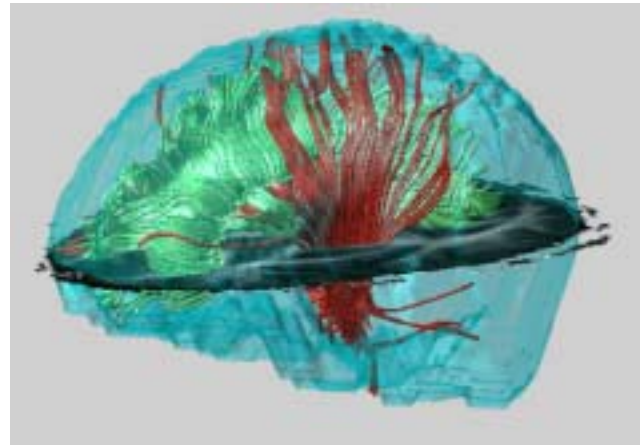
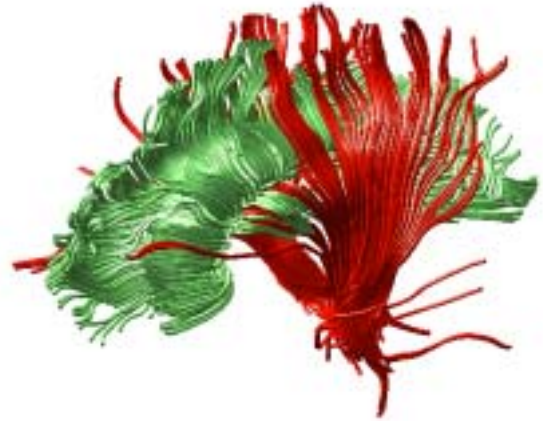


Figure 1: Vector maps through the corpus callosum in a volunteer showing the preferred orientation of white matter tracts from a DTI exam. Top: Vector maps of the entire corpus callosum in 3D space for rotational analyses. The bottom image is the composite of the raw data within the 3D space, the 3D volume of the entire head from a 3D volume acquisition, and the fiber rprojections.

DIFFUSION/PERFUSION WEIGHTED IMAGING

Comparative Assessment of DT-MRI Fiber Tractography Methods

Burak Acar, Roland Bammer, Michael E. Moseley
Department of Radiology

INTRODUCTION

Diffusion Tensor MRI (DT-MRI) fiber tractography refers to the reconstruction of the fibrous structure of brain based on in-vivo DT-MRI data. It is the unique in-vivo method to image the anisotropic structures. It has already been demonstrated several times that the fiber tractography results correlate well with the known anatomy. The underlying data is a tensor field representation of the diffusion of water molecules within tubular structures (the fibers). Despite its current popularity and the research efforts, no single methodology has been standardized yet. We have developed a software tool and implemented the most popular algorithms. A quantitative comparison of these methods was performed on phantom DT-MRI data with circular, twisting and kissing fiber geometries.

METHODS AND MATERIALS

Currently, the Matlab tool (Stanford University Fiber Tracking) includes the B-Spline interpolation, approximation filters [1], the linear interpolation filter for upsampling and the Euler and the 4th order Runge-Kutta methods for tracking (See Figure 1). Several other algorithms (both currently published and new) are under development. SUFiT has a graphical user interface to visualize the DT-MRI data, to select seed points / regions and to visualize the computed tracks.

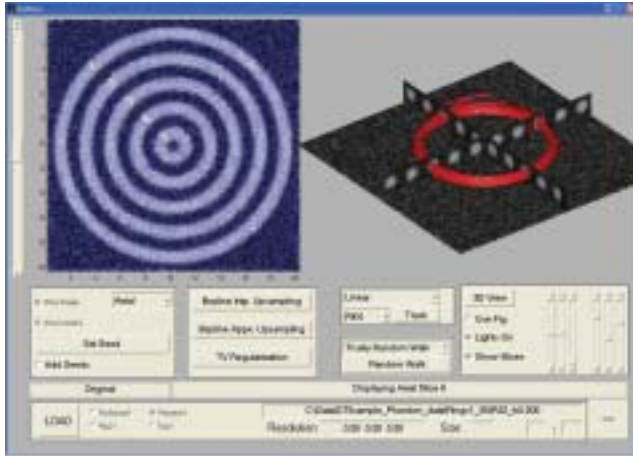


Figure 1: Sample SUFiT results: Resolution 0.2 Units, SNR = 32, RK4 w/Linear Interpolation

The phantom DT-MRI data was generated based on geometrical structures as shown in Figure 2. We sampled the data volume isotropically at $0.1 \times 0.1 \times 0.1$ unit³. The voxels inside the fibers were assigned diffusion tensors with $FA=0.82$ (oriented with the fiber's tangent) while the others were assigned randomly oriented tensors with $FA=0.13$. The simulated Diffusion Weighted MRI signals are corrupted with different levels of noise, re-sampled and final DT-MRI data was computed.



Figure 2: Fiber geometries used Rings Kissing Twisting

The above mentioned algorithms were evaluated at 0.2 and 0.8 unit isotropic resolution with $SNR=8, 32, 128$. We evaluated the tracking performance based on the mean Euclidean distance between the computed track and the center-axis of the corresponding fiber for different resolution and SNR values.

RESULTS & CONCLUSIONS

Our results can be summarized as follows:

- 1) Euler and RK4 have similar performances at small step sizes. RK4's advantage over Euler would be apparent at larger step sizes that will speed up the tracking that can be a limiting factor in large scale tracking problems.
- 2) The resolution and SNR can not be traded off. Tracking performance is satisfactory in neither "high resolution and low SNR" nor "low resolution and high SNR". The resolution (relative to the size of the structures of interest) should be higher than 80% and $SNR \geq 32$ for reliable tracking. $SNR > 32$ does not seem to lead to better tracking.
- 3) We did not observe significant differences between tracking and interpolation/approximation schemes considered here.
- 4) However, in general $\text{Error (B-Spline Approximation)} \leq \text{Error (B-Spline Interpolation)} \leq \text{Error (Linear Interpolation)}$.
- 5) RK4 had a noticeable difference in tracking quality only in 'Ring' phantoms at 0.2 unit resolution and $SNR=128$. Since the errors are already low in this case, the difference can not be considered as a significant performance improvement over the Euler method.
- 6) The tracking of twisting fibers is rather independent of the method, the resolution and the SNR as expected.

Ultrafast Diffusion Weighted Imaging of the Abdomen

Lawrence C. Chow, Roland Bammer, Mike Moseley, F. Graham Sommer

Department of Radiology

INTRODUCTION

Within the past decade, diffusion-weighted imaging (DWI) has seen rapid growth and development, quickly escalating it from an experimental tool to an established clinical methodology whose primary use has been for the evaluation of acute cerebral ischemia. Much like T1 and T2, diffusivity can be thought of as an intrinsic tissue property. Thus, it follows that DWI might be of utility in imaging extracranial organs, such as the solid organs within the abdomen. The ability to determine diffusion coefficients within the abdomen has great potential for furthering our understanding of normal and abnormal physiology, as well as for characterizing focal and diffuse disease within abdominal organs—particularly in the liver in kidneys where conventional imaging findings are frequently non-specific. Historically, bulk physiologic motion such as respiration and peristalsis, however, has hampered the application of DWI in the abdomen. We sought to generate breath-held diffusion-weighted images and corresponding isotropic $\langle D \rangle$ maps of the abdomen with high image quality and full organ coverage.

METHODS AND MATERIALS

DWI was performed in 11 healthy, young subjects between the ages of 20 and 35 with an asymmetric SE single-shot EPI readout on a high performance gradient (40 mT/m) system and a quadrature wrap-around body coil. The isotropic diffusion coefficient $\langle D \rangle$ was measured from $\langle D \rangle$ maps and SNR was determined for both diffusion weighted and reference images in the liver, spleen, pancreas and kidneys. In 6 patients, single-axis diffusion encoding (12 NEX) was employed to assess anisotropic diffusion in kidneys. Additionally, single breath hold scans with 12 b-values from 7-800 were performed in 5 patients.

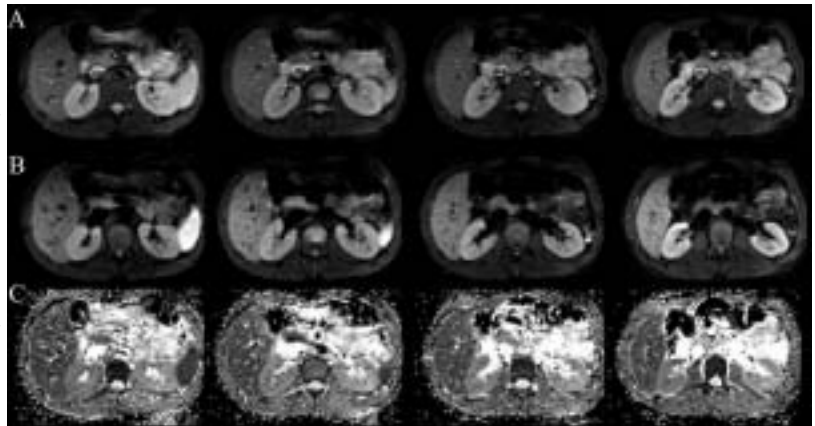
RESULTS

Because of the high gradient strength and asymmetric readout, TE was minimized, resulting in less image blurring, diminished susceptibility artifacts, more slices per TR and greater signal from short T2 tissues such as liver. This, in conjunction with the single-shot, breath-held technique which eliminates ghosting and respiratory mis-registration resulted in images of superior quality and resolution when compared to prior work. After magnitude averaging and Rayleigh noise correction, the SNR ranged from 27.0 in liver to 44.1 in kidneys for the diffusion-weighted images and from 19.6 in liver to 39.0 in kidneys in reference images. Renal cortico-medullary differentiation was possible in all patients. ADCs obtained in the renal medulla, renal cortex, liver, spleen, and pancreas were $(2091 \pm 55) \times 10^{-6}$, $(2580 \pm 53) \times 10^{-6}$, $(1697 \pm 52) \times 10^{-6}$, $(1047 \pm 82) \times 10^{-6}$, and $(2605 \pm 168) \times 10^{-6}$ mm²/s respectively (mean \pm SE). ADC in the renal medulla and cortex were significantly different by paired *t*-test ($p = 4.22 \times 10^{-10}$). Renal medulla and cortex yielded anisotropy indices (AI) of 0.129 and 0.067 respectively.

CONCLUSIONS

1. Single-shot SE EPI DWI with this technique provides high-quality images and $\langle D \rangle$ maps with full organ coverage within the abdomen in a single breath hold.
2. Diffusion within the renal medulla appears to be moderately anisotropic while that in renal cortex does not.
3. ADCs obtained in the renal medulla and cortex are significantly different.

Figure 1: Axial ssEPI images obtained through the upper abdomen in a 26 year-old, healthy volunteer, matrix 128 x 128. (A) Non-diffusion weighted ($b = 0$ s/mm², 2 averages) reference images demonstrate essentially T2-weighted contrast and good depiction of the regional anatomy. (B) Diffusion-weighted ($b = 300$ s/mm²) images demonstrate no loss of SNR when compared with reference images as two averages were performed for each of the four diffusion sensitizing gradients resulting in a total of eight averages. (C) The $\langle D \rangle$ maps allowed visualization of the parenchymal organs such as liver and kidneys with excellent image quality and with preserved depiction of cortico-medullary differentiation in the kidneys.



COGNITIVE IMAGING RESEARCH

Cerebro-Cerebellar Circuitry of Verbal Working Memory

S.H. Annabel Chen,² John E. Desmond^{1,2}

¹Neuroscience Program, ²Department of Radiology

INTRODUCTION

Anatomical, neuropsychological and neuroimaging studies have indicated cerebellar involvement in cognitive processing, in particular, tasks involving verbal working memory. An event-related (e) fMRI study, designed to tease apart the various phases of a Sternberg verbal working memory task in the cerebellum, showed right superior cerebellum activation during encoding which is in parallel with the articulatory process, and maintenance (rehearsal of letters) to involve more of the inferior cerebellum, which is thought to be related to the working memory and phonological processing of verbal information.¹ In the present efMRI study, we included cortical regions to complete our understanding of the circuitry.

METHODS AND MATERIALS

Subjects were presented a two alternative forced choice Sternberg paradigm (Figure 1). Functional data were acquired with a 3T (GE Signa Lx 8.3) using the following parameters: TE = 30ms, FOV = 240mm, one interleave, inplane resolution = 3.75mm, TR = 1000ms, 16 slices (axial prescription with 25degree rotation from AC-PC line to cover whole brain including the cerebellum), 7mm slice thickness (6mm skip 1mm), and spiral-in-and-out pulse sequence. Subjects were administered 5 sessions of verbal memory task in the scanner presented by Psyscope 1.2.5. SPM99 was used for functional data analyses. Each subject's own hemodynamic response function (hrf) in the right superior cerebellum and left motor cortex, obtained from a finger tapping task was convolved with the event times in the Sternberg task to generate regressors for the respective analyses (Figure 2).



Figure 1: Each trial consisted of an encoding phase of either 2-letters (easy) or 6-letters (hard) appearing simultaneously on the screen for 2 seconds followed by a maintenance phase of either 4 or 6 seconds and a retrieval phase of 1 probe letter that appeared for 1 second. The subject is expected to respond within 3 seconds.

RESULTS

Results from 15 subjects showed 94% accuracy for the easy and 88.5% accuracy for the hard conditions ($p < 0.0001$). Reaction time for responses were significantly faster for the easy condition ($p < 0.0004$). Functional activations were seen during the encoding phase in the cortical regions of the left inferior frontal gyrus extending to the supplementary motor cortex, superior anterior cingulate, bilateral hippocampus, and subcortical regions of the right superior/lateral and right pos-

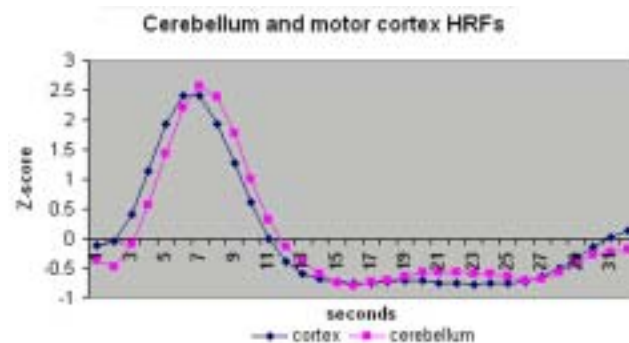


Figure 2: Averaged Hemodynamic Response Functions (HRFs) obtained from the motor cortex and superior right cerebellum from a finger-tapping task. Shape of the HRFs are similar; however, the cerebellum HRF peaked 1 second later than the motor cortex HRF.

terior inferior cerebellum. During the maintenance phase, cortical activations in the left parietal region corresponded with that seen in the right inferior cerebellum. In the retrieval phase, anterior cingulate and left inferior frontal gyrus, as well as, superior vermis activations were observed (Figure 3).

CONCLUSIONS

These findings indicate that the cerebellum is not solely involved with sensory acquisition during encoding, and that the right inferior cerebellum activates in tandem with cortical regions thought to be involved with phonological processing during maintenance.

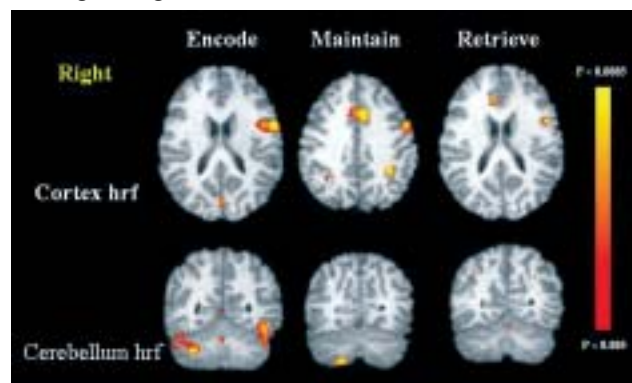


Figure 3: Averaged brain activation maps from 15 subjects obtained from the different phases of the task. Of note, activations during Encoding: left inferior frontal gyrus and right superior cerebellum; Maintenance: left parietal and right inferior cerebellum; Retrieval: left inferior frontal gyrus and superior mid-vermis.

REFERENCE:

1. Chen SHA, Pryor MR, Desmond JE. Cerebellar involvement in encoding, maintenance, and retrieval components of verbal working memory: An event-related fMRI study. Program No. 416.4. Abstract Viewer/Itinerary Planner. Washington, D.C.: Society for Neuroscience, 2002. CD-ROM

Supported by: NIMH (MH60234)

Load Dependent Increases in Cerebellar Activation During Verbal Working Memory: An fMRI Study

Matthew P. Kirschen, S.H. Annabel Chen, John E. Desmond

Department of Radiology and Neurosciences Program

INTRODUCTION

Verbal working memory (VWM) relies on a phonological store that is capable of holding verbal information for a few seconds, but must be periodically refreshed by articulatory rehearsal - the so called phonological loop. Neuroimaging studies have demonstrated cerebellar activation during VWM and correlated this activity with various neocortical structures. Classical VWM experiments show a linear increase in reaction time (RT) as the number of items in memory increases¹. Previous investigations of VWM have demonstrated monotonic increases in activation of dorsal lateral pre-frontal cortex and Broca's area with increasing memory load². Studies of cerebellar activation during verbal working memory, however, have focused on high versus low load comparisons³ and have not addressed whether increases in activation follow similar linear trends as a function of working memory load. The present study investigates whether cerebellar activation, as well as reaction time, are linearly related to load increases.

METHODS AND MATERIALS

Sixteen right-handed subjects (7 male, 9 female) were instructed to remember 2, 3, 4 or 6 consonants (list length) presented sequentially at 1 item per second in uppercase font. They were told to sub-vocally rehearse these letters during a 5 second retention interval. A lowercase probe letter was then presented and subjects indicated with a button press if this probe letter matched a remembered letter in the preceding list (yes - right index finger; no - right middle finger). Inter-trial-interval was 3 seconds. An equal number of probes and lures were used. The position of the probe/lure was counter-balanced over all presentation positions. Each subject completed 4 sessions. Each session consisted of 48 trials, presented in 2 trials per block and 6 blocks per list length. fMRI scanning was performed on the 3.0T GE Signa scanner with a gradient echo spiral pulse sequence (TR = 2000 ms, TE = 30 ms, flip = 75 deg). Whole brain functional scans (32 slices) were collected in the coronal plane with an inplane resolution of 3.75 mm and 6 mm slice thickness.

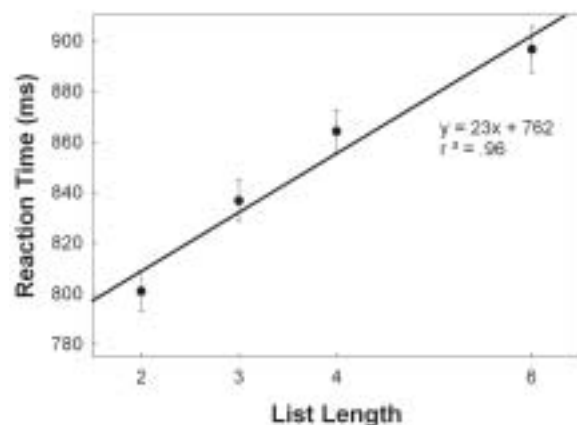


Figure 1: Plot of reaction time vs. memory load (list length).

RESULTS

Both reaction time (Fig. 1) and brain activation (Fig. 2) showed significant linear increases with increasing memory load. There was an overall significant increase in RT with increasing memory load ($F(3,45)=28.06, p<.001$). The parametric increase in memory load had a highly significant linear component ($F(1,15)=71.68, p<.001$) and a non-significant quadratic trend ($F(1,15)=.097, NS$). The average accuracy for each memory load were: load 2=96%, load 3=94%, load 4=95% and load 6=88% ($F(2,30)=0.73, NS$). ROI analysis of specific sub-regions indicate mainly linear increases in activation with parametrically increasing memory load in inf. frontal (BA 47) and inf. parietal (BA 40) regions bilaterally, and in the right superior (HVI/sup HVIIA) and inferior (HVIIB) cerebellum.

CONCLUSIONS

Both reaction time and cerebellar activations increased linearly with VWM load. Analysis of linear and quadratic trends revealed significant linear trends in activations of inferior frontal, inferior parietal, and superior and inferior regions of the cerebellum. Although purely quadratic increases were absent, some regions showed combined linear and quadratic increases with load. Activation in right temporal and frontal regions decreased as subjects became more proficient at the task. Similar load-dependent activation trends in cerebellar, frontal, and parietal regions are consistent with the cerebro-cerebellar model of verbal working memory.

REFERENCES

1. Sternberg S. High-speed scanning in human memory. *Science* 1996; 153:652-4
2. Braver et al. A parametric study of pre-frontal cortex involvement in human working memory. *Neuroimage* 1997; 5:49-62
3. Desmond et al. Lobular patterns of cerebellar activation in verbal working-memory and finger-tapping tasks as revealed by functional MRI. *J Neurosci* 1997; 17:9675-9685.

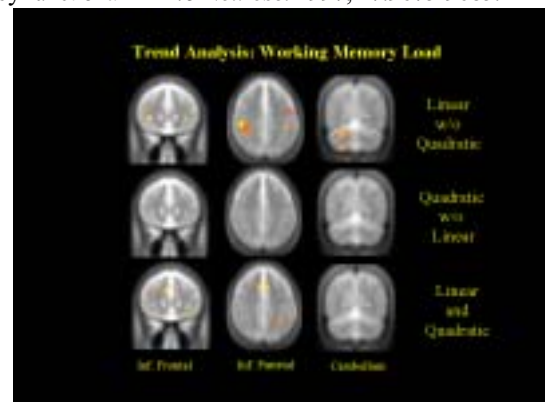


Figure 2: The 3 panels represent conjunction analyses at the $p<.05$ level, followed by thresholding at $p<.001$, to identify regions where linear alone, quadratic alone, and combined linear and quadratic trends are present. The regions containing the most significant clusters are listed below each column.

COGNITIVE IMAGING RESEARCH

From Bench to Bedside: Bringing fMRI to the Clinic at Stanford

John Desmond and Jenea Boshart

Department of Radiology

INTRODUCTION

fMRI holds great promise for use in a clinical setting where this non-invasive technique can be used to inform pre-surgical planning and diagnose and track disease. Translating fMRI research into the clinical domain, however, has challenges, some inherent in the technique, some arising out of differences between clinical and research goals and approaches. Both kinds of challenges must be met for fMRI to be successful in the clinic.

CLINICAL OPPORTUNITIES

fMRI has great potential in a clinical setting. For example, fMRI can be effectively combined with traditional neurological testing in pre-surgical planning, such as helping to determine language lateralization for tumor or epilepsy patients, ensuring that patients will not lose their language abilities post-operatively (Figure 1). Similarly, fMRI can be used to characterize and track disease.

TECHNICAL CHALLENGES

While fMRI lends itself well to clinical practice, there are technical challenges that must be overcome before the full benefit can be achieved. Statistical comparison is at the heart of the technique, and effect sizes are small. It is therefore necessary to design tasks that are robust and yield the maximum possible signal. Furthermore, because many patients may be cognitively or motor impaired, passive tasks, e.g., listening to language, or receiving tactile stimulation from an external device, rather than tasks that require active movement or response, may be optimal. Furthermore, while researchers want to avoid Type I statistical errors (representing false activations), Type II errors (false *lack* of activation) can be more problematic for the neurosurgeon who may need to be conservative about what parts of the brain are deemed non-essential for functioning.

IMPLEMENTATION AT STANFORD

In the Blake Wilbur clinic at Stanford we have had considerable initial success in implementing fMRI protocols. Several tasks are available that help define somatosensory areas and determine language lateralization. Tasks and analysis have been streamlined as much as possible to reduce the amount of fMRI expertise required from the MR technologists while at the same time ensuring uniformly administered tasks. We have developed a one-click data analysis tool that automatically completes all necessary pre- and post-processing including motion correction and 3D image rendering. MR technologists have been trained in the administration of these tasks, and a radiology resident has been trained in our lab in order to be a liaison between our lab and clinicians who may be interested in using fMRI with their patients.

CONCLUSIONS

The capability to perform fMRI on patients has successfully been implemented at the Blake Wilbur clinic at Stanford. The full potential of this methodology for surgical planning and diagnostic purposes has yet to be fully explored, and there will no doubt continue to be challenges that will need to be addressed. For example, the goals and methods of clinicians and researchers differ significantly, and these differences must be taken into account when translating fMRI methods directly to the clinic. Furthermore, while fMRI makes it possible to measure individual activations, interpretation of these activations must occur in the context of comparisons with others, and therefore, norms must be developed for standardized tasks across various populations. However, despite these challenges, fMRI will continue to develop as a clinical tool to improve health care.

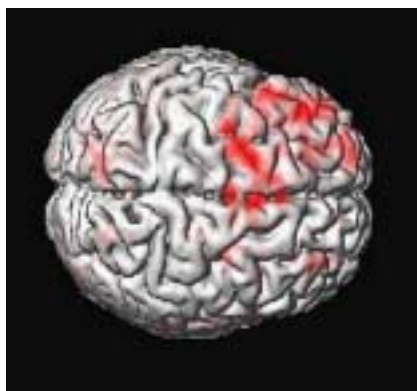


Figure 1: Case Study.

Patient: Epilepsy patient who suffered a seizure during her Wada tests, resulting in inconclusive results. Epileptic focus likely in the left MTL.

Goal: Determine memory lateralization with fMRI to guide decisions about surgery.

Results: Memory was strongly lateralized on left. As a consequence of these results coupled with results from traditional tests, surgery is unlikely.

A Magnetic Resonance Imaging Compatible Intravenous Drip

H.Z. Adriaan van der Loos¹, H.F. Machiel Van der Loos², Gary H. Glover⁴, Robert J. Herfkens⁴

¹Kehillah High School, San Jose, ²Palo Alto VA Health Care System, ³Departments of Surgery, and ⁴Radiology, Stanford University

INTRODUCTION

The purpose of this device is to provide a flow-regulated intravenous (IV) feed of medication to a patient receiving a scan in a Magnetic Resonance Imaging (MRI) suite, without affecting the quality of the images. Due to the high magnetic field present in an MRI suite, there are severe restrictions on materials and types of equipment, like electric motors, that can be used. Conventional regulated IV pumps cannot be used. The only commercially available syringe pumps that can be used in an MR suite must be kept more than three meters away from the bore of the magnet for safety. Gravity-fed IV drips with non-metallic components, while routinely used, are not accurate enough for some patients on critical medication regimens. With the regulated IV drip we have invented, there are no restrictions on location and proximity to the bore and no materials issues that may distort the MR images.

DEVELOPMENT

A drop-counting sensor located with the patient in the MRI suite sends a signal through the perforation panel to the IV controller in the MRI control room. A pump inside the MRI control room creates a flow of low-pressure air or water through a flexible tube that passes through the controller and then loops back up to the reservoir of the pump. The controller uses a solenoid to squeeze off this tube intermittently, compressing the fluid in the portion of the tube coming from the pump. There is a "T" in this portion of the loop. A separate, 10m long, flexible hose comes off the "T" and leads through the perforation panel that separates the MRI control room from the MRI suite, terminating at the "Remote Drip Regulator" (RDR) next to the patient inside the MRI suite. The RDR, which contains a bellows and piston connected to the flexible hose, regulates the flow of medication in the

patient's IV drip line; this results in a steady number of drops per minute going to the patient.

RESULTS

DRIP REPRODUCIBILITY

We tested the device by setting an IVAC drip meter to various number of micro-drops/min, and then visually counted how many drops actually dropped in one minute. We did this inside and outside of the MRI suite to prove that the device was not only accurate, but was also not affected by the strong magnetic field of the MRI scanner. Results demonstrate its performance reliability to within 3 micro drops/minute of the setting.

IMAGE QUALITY

The IV drip was also tested for MR compatibility by taking pictures of a phantom with the system on and off. No artifacts or image distortion could be detected (Figure 1).

CONCLUSION

The lack of an MR compatible IV drip has compromised the best care for patients needing ongoing medication and scans for further diagnosis. This new device responds to this important medical problem. *Patent disclosure in progress (3/10/03).*

REFERENCES

1. <http://www.encyclopedia.com/html/m1/magresim.asp>
2. <http://www.howstuffworks.com/mri.htm>
3. <http://www.cis.rit.edu/htbooks/mri/inside.htm>
4. <http://www.cis.rit.edu/htbooks/mri/chap-1/chap-1.htm>
5. <http://www.erads.com/mrimod.htm>
6. <http://216.239.53.100/search?q=cache:D5JMvH4WleIC:www.bme.umich.edu/~dnoll/primer2.pdf+MRI+primer&hl=en&ie=UTF>

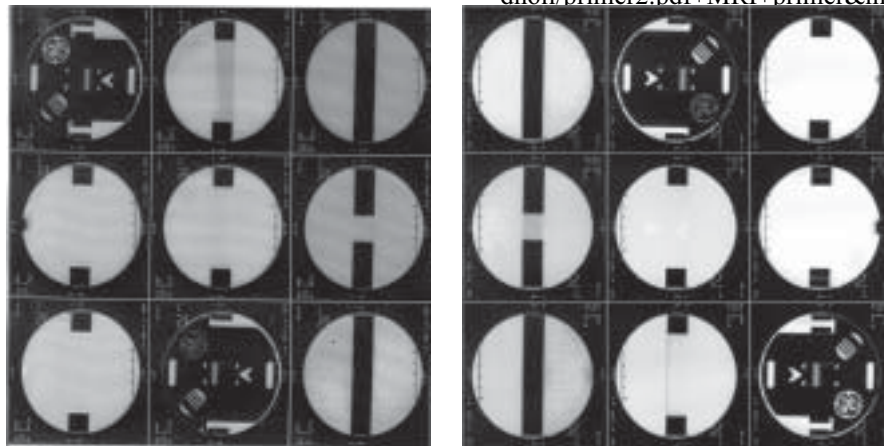


Figure 1: Pictures of Phantom without the IV drip on Pictures of Phantom with the IV drip on. As you can see, there is no difference between when the IV drip is on and when it is off in the MRI suite.

STANFORD CENTER FOR BIOMEDICAL ETHICS
Discovery and Disclosure of Incidental Findings on Brain MRI

Judy Illes^{1,2,3}, Megan Kelly¹, Arnold Saha¹, Matthew P. Kirschen^{1,2,4}, John E. Desmond², Thomas A. Raffin³, Gary H. Glover², Scott W. Atlas^{2,5}

¹Stanford Center for Biomedical Ethics, Departments of ²Radiology and ³Medicine, ⁴Program in Neurosciences, ⁵Hoover Institution, Stanford University

INTRODUCTION

Incidental findings on brain MRI – i.e., brain abnormalities discovered in subjects recruited to research studies as healthy controls or unexpected findings in patients – have garnered significant attention in the literature recently [e.g., 1-4]. Suspicious brain abnormalities have been reported to occur in as many as 40% of research participants, with clinically significant findings occurring in 2-8% of children and adults.

METHODS AND MATERIALS

We surveyed members of the MRI research community to document protocols used for discovering and disclosing such findings in research subjects recruited to studies as healthy controls. The cohort comprised investigators who conduct both structural and functional MRI studies.

RESULTS

Of the investigators (N=31 to date) who have responded to the survey at the time of this writing, 84% reported discoveries of incidental findings on their studies. Findings ranged in severity from those requiring routine follow-up to those requiring immediate or urgent follow-up, and were detected by both MD-trained and non-MD-trained research personnel, including PhD investigators, professional laboratory personnel, and students. Of the respondents providing information about their specific protocols, 59% reported having standardized procedures for detecting incidental findings and communicating with research participants in whom findings are discovered; 41% proceed on an *ad hoc*, case-by-case basis. Review of research scans by a neuroradiologist is a current IRB requirement for only 17% (5/30) reporting. Lag time between scan acquisition and neuroradiologist readings, when applicable and reported, was 3-7 days in 75% (15/20), same day in 10%, and within or longer than one month in 15%. Data collection for the study continues.

CONCLUSIONS

Informed consent is essential to respecting the autonomy of parties participating in any medical procedure, whether they are research participants, prospective donors of blood or tissue, or patients, as is understanding of their underlying motivation to participate. The issue of autonomy becomes complicated, however, when pathology is uncovered in someone who has not asked to be screened for his or her own immediate benefit. Informed consent and human subjects protocols generated on an institution-by-institution may not be adequately responsive to the problem of incidental findings given the apparent ubiquity of such findings in pediatric and adult medical imaging research, whether they occur in the central nervous system or elsewhere. We believe that discussion and debate of broad standards that can then be adopted universally in medical imaging and across other medical subspecialties, perhaps developed at the level of the major professional associations and the NIH, are needed to ensure the protection of subjects, third parties on whom results may be imputed, providers and investigators, as well as of the overall integrity of medical research and care.

REFERENCES

1. Katzman GL, Dagher AP, Patronas NJ. Incidental findings on brain magnetic resonance imaging from 1000 asymptomatic volunteers. *JAMA* 1999; 282:36-9
2. Kim BS, Illes J, Kaplan RT, Reiss A, Atlas SW. Neurologic findings in healthy children on pediatric fMRI: incidence and significance. *AJNR* 2002;23:1-4
3. Illes J, Desmond J, Huang LF, et al. Ethical and practical considerations in managing incidental neurologic findings in fMRI. *Brain and Cognition*. 2002;50:358-65
4. Illes J, Rosen A, Huang L, Goldstein RA, Raffin TA, Swan G, Atlas SW. Incidental findings on adult brain MRI: Age-related double dissociation and ethical considerations. *New England Journal of Medicine* (Under review)

Learned Regulation of Spatially Localized Brain Activation Using Real-Time fMRI

R. Christopher deCharms¹, Kalina Christoff², Gary H. Glover^{3,4}, John M. Pauly⁴, Susan Whitfield¹, John D. E. Gabrieli¹
Departments of ¹Psychology, ³Radiology and ⁴Electrical Engineering, Stanford University; ²MRC Cognition and Brain Sciences Unit, Cambridge, UK

Brain activation correlates with anatomically localized processes that underlie cognitive function. It has previously been shown that subjects can be trained to regulate global measures of brain function such as EEG. However, it has not previously been determined whether subjects can learn volitional control over the level of activation taking place in anatomically localized regions of the brain involved in more specific neural functions. If subjects can be trained to control the level of activation in localized brain regions, this has implications for the extent to which top-down processes can regulate activation during the performance of tasks. Training-induced alterations in the level of activation in localized brain regions may also impact behavioral performance and learning or plasticity in normal individuals or in disease remediation.

We have shown that subjects are able to learn to voluntarily increase task-specific activation in the somatomotor cortex during an imagined manual action task using information derived in real-time from functional magnetic resonance imaging (fMRI) [1-3]. During training conducted inside the scanner, subjects were continuously presented with activation information from a target region of interest, and were instructed to alternately increase and decrease the activation in this region while performing imagined manual actions in the absence of actual movement. Increases in activation measured in somatomotor cortex grew with practice and were anatomically specific. Comparable increases did not occur as a result of training in the absence of real-time fMRI information, and thus were not an effect of conventional, practice-based neural plasticity alone. The training-induced increases led to robust fMRI activation in the somatomotor cortex during imagined manual action, similar to levels observed during actual manual action. After training, subjects were able to increase localized brain activation in the absence of observed muscle tensing as measured using EMG, and when continued access to real-time fMRI information was no longer provided. Thus, humans are able to learn to consciously regulate activation in an anatomically-targeted brain region, surpassing task-driven activation observed prior to training.

REFERENCES

1. Posse S, et al. A new approach to measure single-event related brain activity using real-time fMRI: feasibility of sensory, motor, and higher cognitive tasks. *Hum Brain Mapp* 2001; 121:25-41.
2. Cox RW, Jesmanowicz A, Hyde JS, Real-time functional magnetic resonance imaging. *Magn Reson Med*, 1995; 33:230-6.
3. Weiskopf N, et al. Feedback of cortical activity using real-time functional magnetic resonance imaging (fMRI). *Human Brain Mapping*. 2002. Sendai, Japan.

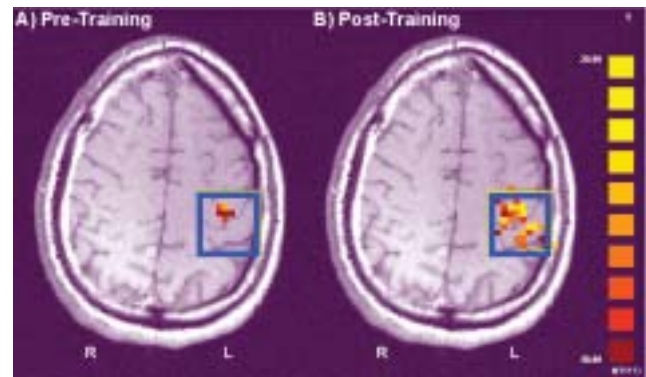


Figure 1: Somatomotor activation before and after training. BOLD activation during a right-hand imagined-action task (A) before and (B) after training. Statistically significant activation pattern is superimposed upon a T1-weighted anatomical image. The blue box designates the selected region of interest used in training the subject. The scale designates the corrected t value.

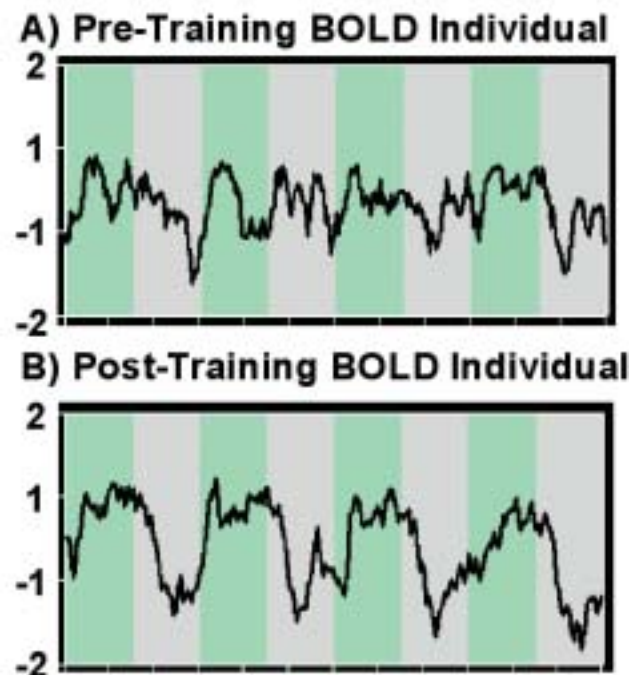


Figure 2: Temporal progression of activation during imagined action task before and after training. (A) Average value within the ROI for a single subject at successive measurement points (TRs), expressed as a percent change from the mean for the entire period before training, and (B) after training. No spatial or temporal averaging or filtering was used.

Cognitively Decreasing or Increasing Emotion Engages Common Prefrontal Systems that Differentially Modulate the Amygdala

Kevin N. Ochsner, Rebecca D. Ray, James J. Gross, & John D. E. Gabrieli

Department of Psychology, Stanford University

INTRODUCTION

Reappraisal is a cognitive form of emotion regulation that can alter emotional responses.

In prior work, the use of reappraisal to decrease negative emotion activated regions of left lateralized prefrontal cortex implicated in cognitive control and modulated emotion processing systems such as the amygdala. The use of reappraisal to up-regulate, or increase, emotional responses has yet to be investigated, even though it may play an essential regulatory role. The present study sought to extend initial findings by determining whether reappraisal used to *increase* as opposed to *decrease negative emotion* will involve substantially *similar prefrontal control systems that divergently up- or down-regulate amygdala activity*.

METHODS AND MATERIALS

Participants: 24 healthy adult females

Scan Parameters: 25 4mm axial slices (1 mm skip) on 3T GE Scanner; Spiral pulse sequence, TR 2; Pre-processing and random effects analysis w/SPM99; beta weights extracted from functional ROIs

Stimuli: 3 sets of 27 neutral and 3 sets of 27 negative images selected from the IAPS (Lang et al, 1993).

Different pre-stimulus cues on 3 intermixed trial types:

Increase: Think about negative image in such a way that you feel MORE negative in response to it.

Decrease: Think about negative image in such a way that you feel LESS negative in response to it.

Look: Look at image and respond naturally.

RESULTS

As shown in Figure 1, results provided support for our hypothesis that these two uses of reappraisal should involve some common and some distinct control systems. Both up and down regulating negative emotion engaged left lateral prefrontal control systems implicated in verbal strategic processes such as the maintenance and manipulation of verbal information in working memory-processes essential to reappraisal.

Regions unique to each form of reappraisal were identified by directly comparing activation on increase and decrease trials. In keeping with predictions, up regulating negative affect uniquely recruited a region of left rostral lateral prefrontal cortex previously implicated in self generating negative words to emotional category cues whereas down regulating negative affect recruited right lateral prefrontal and lateral orbitofrontal regions previously implicated in inhibiting prepotent responses and altering emotional associations. Up or down regulating negative affect resulted in increases or decreases in amygdala activation, respectively. Furthermore, as shown in Figure 2, the extent to which amygdala activation increased or decreased was correlated with activation in prefrontal cortex. When up regulating negative affect, prefrontal activation correlated positively with amygdala activation, and when down regulating negative affect, prefrontal activation correlated negatively with amygdala activation.

CONCLUSIONS

Question: When using reappraisal to increase vs. decrease negative emotion are similar prefrontal systems differentially modulating the amygdala?

Answer: Yes.

1. Increasing and decreasing recruited common left lateral PFC systems supporting verbal strategic processing.
2. Increasing uniquely recruited left rostral LPFC whereas decreasing uniquely recruited right PFC.
3. Increasing boosted left and right amygdala whereas decreasing diminished right (and to a lesser extent left) amygdala activation.
4. Bilateral changes in amygdala activation predicted reappraisal success (i.e. task-appropriate increases or decreases in affect).

REFERENCES

1. Gross JJ. Antecedent- and response-focused emotion regulation: Divergent consequences for experience, expression, and physiology. *Journal of Personality & Social Psychology* 1998; 74:224-237
2. Ochsner KN, Bunge SA, Gross JJ, Gabrieli JDE. Rethinking feelings: An fMRI study of the cognitive regulation of emotion. *Journal of Cognitive Neuroscience* 2002; 14:8

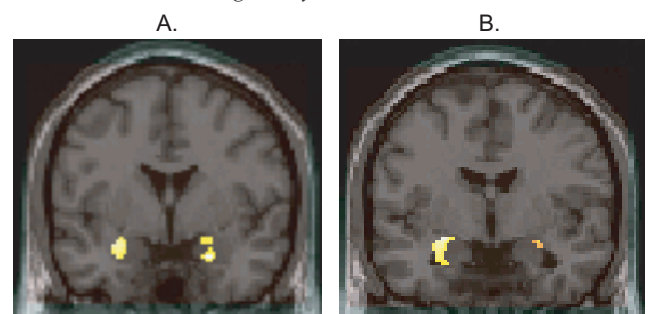
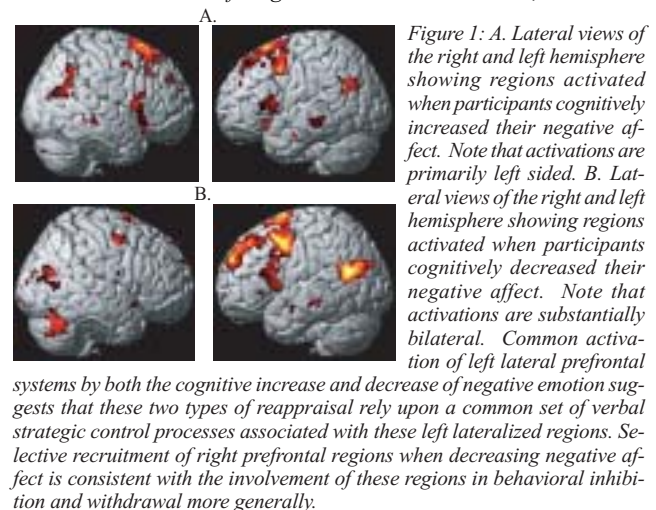


Figure 2: Panel A - Amygdala regions whose de-activation on decrease trials correlates with decreases in self-reported affect. Panel B - Amygdala regions whose activation on increase trials correlates with increases in self-reported affect.

An Event-Related fMRI Study of Word Regularity and Frequency Effects

Wai Ting Siok¹, Gayle Deutsch¹, Bob Dougherty², Gary Glover², John Gabrieli^{1,2}

¹*Departments of Psychology and* ²*Radiology*

INTRODUCTION

English has an opaque orthography that follows quasi-regular grapheme-phoneme correspondence rules. While visually similar words tend to have analogous pronunciations (e.g., SAVE, GAVE, CAVE), exceptions do occur (e.g., HAVE). Response times are longer for words that follow unusual letter-sound mappings relative to words that follow usual letter-sound correspondences. In addition, regularity effects are typically more salient for low frequency words compared to high-frequency words. This interaction may reflect a trade-off between two cognitive processes: An assembled route that derives the pronunciation of a word form by using a rule-based process (grapheme-to-phoneme conversion rules), and a direct route that retrieves the phonological form appropriate to a particular word form from the long term memory [1]. Recent neuroimaging studies have identified several brain regions that show effects of regularity, including left inferior frontal gyrus [2,3], left superior temporal cortex [4], right inferior frontal areas [5] and bilateral motor cortex [3]. These studies used a block design, in which regular and irregular words were presented in alternate blocks. Regularity effects obtained in this type of design could be confounded with strategic effects due to processing words imposed by the different conditions of stimulus presentation. In the current study, we used event-related functional magnetic resonance imaging (ER-fMRI) to investigate naming for words that were systematically manipulated in frequency and regularity. ER-fMRI permitted us to randomize the presentation of various stimulus types and hence examine the neural substrate relevant to automatic processing of sublexical phonological information.

METHODS AND MATERIALS

Whole-brain imaging data were acquired on a 3T Signa LX (GE Medical Systems) using T2*-sensitive gradient echo spiral pulse sequence [6] (1 interleave; TE=30 ms; TR=6 s; flip angle=90; field of view=24 cm). Thirty-one noncontiguous axial planes (3-mm thickness, 1-mm skip) parallel to the AC-PC line were collected over 2000 ms in a clustered acquisition sequence. This sequence allowed overt verbal responses to be made in the absence of scanner noise.

The subject was shown a series of words that were systematically manipulated in frequency (high vs. low) and regularity (regular vs. irregular). There were 20 items per condition. Each word was presented for 500 ms and ISI was 18s. The subject was instructed to read aloud the viewed word.

RESULTS

Our preliminary data with 9 subjects indicated that the left inferior frontal regions showed effects of both word regularity and word frequency. Specifically, irregular words produced stronger activation in left inferior frontal regions than regular words, with low frequency irregular words yielding significantly stronger activation than the other word conditions. The same regions also showed effects of word frequency, with low frequency words producing stronger activation than high frequency words.

CONCLUSIONS

Left inferior frontal regions show stronger activation to irregular words than to regular words, even when block-design strategy effects are removed, suggesting their role in grapheme-to-phoneme conversion. The stronger activations observed in these areas for irregular words might result from the competition of phonological codes and/or articulatory gestures derived from the direct route and the assembled route.

REFERENCES

1. Coltheart M, Curtis B, Atkins P, Haller M. Models of reading aloud: Dual route and parallel-distributed-processing approaches. *Psych Rev* 1993; 100:589-608
2. Herbster AN, Mintun MA, Nebes RD et al. *Hum Brain Mapp* 1997; 5:84-92
3. Fiez JA, Balota D, Raichle M et al. *Neuron* 1999; 24:205-218
4. Rumsey JM, Horwitz B, Donohue C et al. *Brain* 1997; 119:739-759
5. Pugh KR, Shaywitz BA, Shaywitz SE et al. *J Exp Psychol Hum Percept Perform* 1997; 23:299-318
6. Glover GH, Lai S. *Magn Reson Med* 1998; 39:361-368

Amygdala Responses to Arousing Stimuli Measured in Older and Younger Adults by fMRI

M. Mather¹, T. Canli², T. English,³ S. Whitfield³, P. Wais³, K. Ochsner³, J. Gabrieli,³ L. Carstensen³¹University of California, Santa Cruz ² State University of New York, Stonybrook; ³ Stanford University

INTRODUCTION

Older adults experience less negative affect than younger adults (in both cross-sectional and longitudinal studies) and appear to be better able to regulate their emotions (1). The improved affective experience and regulation seen in old age stand in sharp contrast to the many physical and cognitive declines associated with aging. This improved ability to regulate emotion appears to be motivated and may involve changes in the way emotional information is initially processed and later remembered.

It is unknown what neural mechanisms might be associated with these changes; however, because of its central role in emotional attention and memory, the amygdala is a region of particular interest (2,3). Older adults' increased focus on emotion regulation suggests that with age the amygdala may show less reactivity to negative information while maintaining or increasing its reactivity to positive information. We proposed to examine these phenomena by measuring the amygdala responses of older and younger adults while they were presented with arousing stimuli and then comparing these results to the participants' subsequent tests for recognition for these same stimuli.

METHOD

Participants and fMRI Data Acquisition. Seventeen younger adults between the ages of 18 and 29 years ($M = 23.41$, $SD = 3.24$; eight female and nine male) and 17 older adults between the ages of 70 and 90 years ($M = 78.41$, $SD = 4.86$; eight female and nine male) were paid for their participation. Anatomical and functional imaging data were acquired on a 3-Tesla MRI Signa LX Horizon Echospeed scanner (G. E. Medical Systems) in 16 contiguous 7-mm axial slices using a gradient echo T2*-weighted spiral scan (1000 ms TR; 30 ms TE; 60° flip angle; 24 cm field of view).

Procedure. Participants were scanned using event-related functional magnetic resonance imaging (fMRI) while they viewed randomly-ordered positive, negative, and neutral emotional pictures (Lang, Bradley, & Cuthbert, 1995). While they saw 64 pictures of each valence for three seconds each, participants rated their subjective emotional arousal to each picture on a scale of 1-4 on a 4-button device, with 4 being most arousing.

RESULTS

Older and younger adults revealed different activation patterns in the amygdala. A valence (negative, positive) X laterality (left, right) X age (younger, older) ANOVA revealed a significant interaction of age and valence, $F(1,32) = 5.08$, $MSe = .00$, $p < .05$. For older adults, average signal change in the amygdala for positive pictures ($M = .020$, $SE = .009$) was greater than for negative pictures ($M = -.012$, $SE = .012$), $F(1,16) = 4.47$, $MSe = .02$, $p = .05$ (Fig. 1). In contrast, younger adults' average signal change for positive pictures ($M = .009$, $SE = .009$) and negative pictures ($M = .022$, $SE = .012$) did not significantly differ. Direct comparisons between young and old for negative pictures revealed greater signal change among younger than older adults, $F(1,32) = 4.25$, $MSe = .00$, $p < .05$, but comparisons for positive pictures revealed no significant age differences.

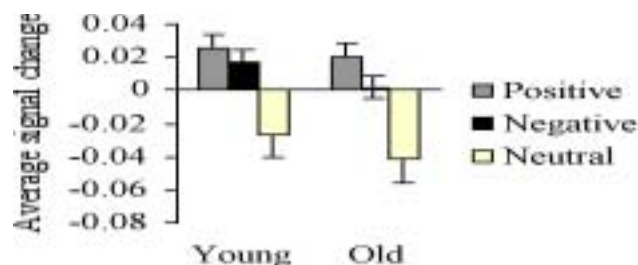


Figure 1.

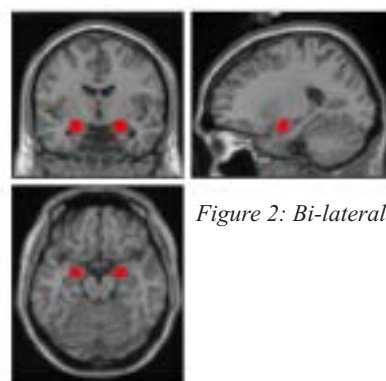


Figure 2: Bi-lateral Amygdala ROI

CONCLUSIONS

The present findings indicate that older adults diminish their encoding of negative emotional experience during the first moments of that experience. This was evident in the reduced arousal ratings and the reduced amygdala response for negative pictures that occurred during the encoding of the pictures. For younger adults, amygdala activation during picture encoding is associated with superior memory for emotional (positive and negative) but not neutral information (2,3). This suggests that older adults' on-line reductions in response to negative pictures should lead to disproportionately diminished later memory for negative information as has been found in behavioural studies with the elderly (Mather & Carstensen, in press). These findings demonstrate how changes in priorities across the life span may be related to changes in the neural substrates of emotion.

REFERENCES

- 1 Carstensen, L. L., Pasupathi, M., Mayr, U., & Nesselroade, J. R. (2000). Emotional experience in everyday life across the adult life span. *Journal of Personality and Social Psychology*, 79, 644-655.
- 2 Canli, T., Zhao, Z., Brewer, J. B., Gabrieli, J. D. E., & Cahill, L. (2000). Event-related activation in the human amygdala associates with later memory for individual emotional response. *Journal of Neuroscience*, 20, RC99.
- 3 Cahill, L., Haier, R. J., Fallon, J., Alkire, M. T., Tang, C., Keator, D., et al. (1996). Amygdala activity at encoding correlated with long-term, free recall of emotional information. *Proceedings of the National Academy of Sciences of the United States of America*, 93, 8016-8021.

Diffusion Tensor Imaging Measurements Predict Reading Performance in Children and Adults

G.K Deutsch¹, R. Dougherty¹, W.T. Siok¹, R. Bammer², J.D.E. Gabrieli¹, B.A. Wandell¹

¹Departments of Psychology and ²Radiology

INTRODUCTION

Diffusion Tensor Imaging (DTI), a form of magnetic resonance imaging (MRI), allows in-vivo examination of white matter microstructure. Fractional anisotropy (FA) estimates the magnitude of diffusion anisotropy within a voxel. Coherence index (CI) estimates consistency of axonal direction across a neighborhood of voxels. FA has been found to correlate with reading ability in adults (Klingberg et al., 2000). We investigated the microstructural integrity of white matter in children (n=14) and adults (n=12) with a wide range of reading performance levels using DTI.

METHODS AND MATERIALS

The current study used whole-brain DTI (1.5T GE Scanner) to measure FA and CI. The DTI protocol involved four three-minute whole-brain scans that were averaged. The pulse sequence was a diffusion-weighted single-shot spin-echo, echo planar imaging sequence (TE=63ms; TR=12s; FOV=260 mm with 128 x 128 matrix size = ~ 2 x 2 mm voxels, bandwidth=±110kHz, partial k-space acquisition). Thirty-eight axial, 3 mm thick slice (no skip) were measured for two b-values, b=0 and b=~800 s/mm² (Bammer et al., 2002) in both dyslexic and control children (mean age = 10.7; n = 14) as well as adults (mean age 23.2; n = 12). All participants underwent a battery of reading, phonological awareness, and spelling tests.

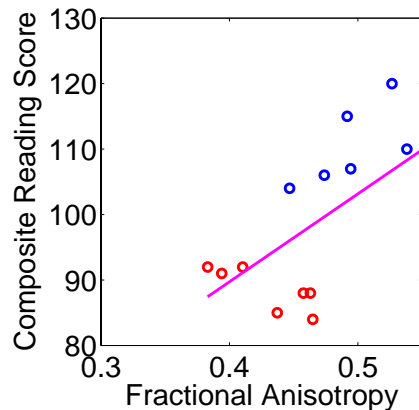


Figure 1: Scatter plot showing the correlation between the mean FA, across 14 voxels, and the Basic Reading Composite score from the Woodcock-Johnson-III ($r = 0.62$, $p = 0.019$) in children.

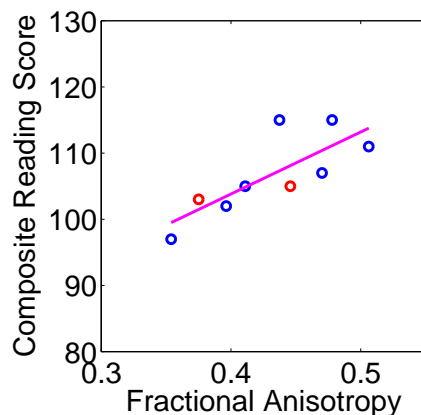


Figure 2: Scatter plot showing the correlation between the mean FA, across 14 voxels, and the Basic Reading Composite score from the Woodcock-Johnson-III ($r = 0.64$, $p = 0.025$) in adults.

RESULTS

Significant group differences in FA and CI were found in a small region around the superior temporal gyrus in children. Both FA and CI in this region were correlated with reading performance: The FA values significantly correlated with oral reading of single words and pseudowords ($r = .62$, $p = .019$; see Figure 1). FA values, in this same region were also found to correlate with reading performance in adults ($r = .64$, $p = .025$; see Figure 2). The principal diffusion direction, presumably indicative of the primary axonal orientation (Mori et al., 2002), was computed from the DTI data for normal and poor reading groups of children (see Figure 3). Across all subjects, 78% of the voxels in the significant cluster (91% normal reading children; 64% poor reading children) were oriented in the inferior-superior direction.

CONCLUSIONS

The results support the hypothesis that the microstructural integrity of left temporo-parietal neural pathways is a significant component of the neural system needed to develop fluent reading.

REFERENCES

1. Bammer et al. Diffusion tensor imaging using single-shot sense-epi. *Magnetic Resonance in Medicine* 2002; 48:128-36
2. Klingberg et al. Microstructure of temporal-parietal white matter as a basis for reading ability: Evidence from diffusion tensor magnetic resonance imaging. *Neuron*, 2000; 25:493-500
3. Mori et. al. Imaging Cortical Association tracts in the Human Brain Using Diffusion-Tensor-Based Axonal Tracking. *Magnetic Resonance in Medicine* 2002; 47:215-223

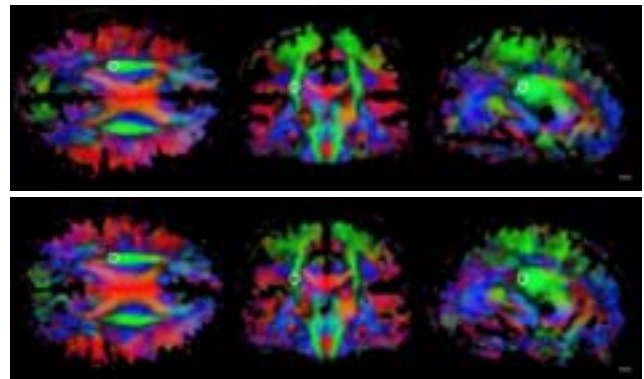


Figure 3: Color maps indicating the principal diffusion direction in three orthogonal slices in the control group (A) and the dyslexic group (B) of children. The white circle indicates the center of the cluster of voxels that was correlated with reading. In this representation, voxels with a principal diffusion direction oriented left-right are red, those with an anterior-posterior orientation are blue and those oriented inferior-superior are green. Voxels with intermediate directions are represented by intermediate colors (e.g., a voxel intermediate between anterior-posterior and inferior-superior are green + blue = cyan). The axial slice (left) is at Talairach Z = 24 mm, the coronal slice (center) is at Talairach Y = -26 mm and the sagittal slice (right) is at Talairach X = -28 mm. The scale bar is 1 cm.

The Effects of Long-Term Deprivation on Visual Perception and Visual Cortex

I. Fine¹, Alex R. Wade², Alyssa A. Brewer³, Michael G. May⁴, Daniel F. Goodman⁵, Geoffrey M. Boynton⁶, Donald I.A. MacLeod¹, Brian A. Wandell^{2,3}

¹Department of Psychology, University of California, San Diego, Departments of ²Neuroscience and ³Psychology, Stanford University, ⁴Sendero Group, LLC, Concord, California, ⁵California Pacific Medical Center, San Francisco, ⁶The Salk Institute, La Jolla, California

INTRODUCTION

Though the first clinical study of recovery after long-term blindness was carried out in 1793, only a few cases have been studied since then^{1,2}. Our study combined psychophysical and neuroimaging techniques to characterize the effects of long-term visual deprivation on human cortex.

MM lost one eye and was blinded in the other after chemical and thermal damage to his corneal tissue at the age of 3½. Damage to his limbal epithelium prevented successful replacement of MM's cornea for 40 years, during which he had some light perception, but no experience of contrast or form. One unsuccessful attempt was made to replace MM's cornea during his childhood, but he reported no visual memories or imagery. In March 2000, at 43 years of age, MM underwent a successful corneal and limbal stem cell transplant in his right eye.

METHODS AND MATERIALS

Functional images were acquired with a spiral k-space sampling sequence on a 3T GE Signa system. fMRI response was quantified as the phase and amplitude of the sinusoid that best fit the average time-series of voxel responses averaged across a given cortical region of interest and projected onto a unit vector with an angle representing the hemodynamic delay. We measured MM's fMRI response to low frequency gratings and objects and face images using a block design.

RESULTS

Functional magnetic resonance imaging (fMRI) BOLD responses to low-frequency gratings were about half those of control observers in motion selective cortex (MT+) and about 1/5th those of controls in the area we defined as V1. Unlike normal observers, MM's fMRI responses within V1 and MT and his visual evoked potential responses (VEP) fell off rapidly with increasing spatial frequency with little or no fMRI or VEP response above 1 cpd. At 3 years of age MM's acuity should have been at least 25 cpd. As shown in the Figure, we found little or no significant activation within MM's lingual and fusiform gyri in response to the face images and only small amounts of activation to the object images, whereas control observers had strong responses in these areas. These same stimuli did evoke responses within occipital regions near calcarine cortex. MM saw these images, but he had difficulties interpreting them as objects and the cortical areas associated with face and object processing were inactive.

CONCLUSIONS

Together, these measurements suggest that prolonged deprivation degrades the spatial resolution of early visual cortex and areas involved in object interpretation.

REFERENCES

1. Cheselden W. *Phil. Trans.* 1728; **402**:447-50
2. Gregory RL & Wallace JG. (Heffer and Sons, Cambridge, 1963).

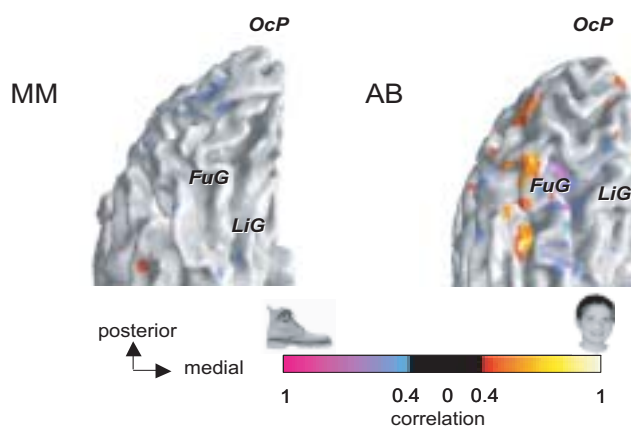


Figure 1: Left hemisphere activation in response to faces vs. object stimuli. Regions responding at a coherence value above 0.4 are shown, and the color-coding represents the phase preference of each voxel. Red-orange coloring indicates regions that responded preferentially to the face stimuli. Green-blue coloring indicates regions that responded preferentially to object stimuli. Control observer AAB showed a typical pattern of activation, with large contiguous regions that responded preferentially either to faces or objects near the fusiform gyrus (FuG) and lingual gyrus (LiG). In contrast, MM showed only a very small amount of activity in response to objects, and little or no activity to faces.

Functional Brain Imaging of Olfactory Processing in Monkeys

J. M. Boyett-Anderson,¹ D. M. Lyons¹, A. L. Reiss,^{1,2,3} A. F. Schatzberg,^{1,3} V. Menon^{1,2,3}¹Department of Psychiatry and Behavioral Sciences, ²Program in Neuroscience, ³Stanford Brain Research Institute

INTRODUCTION

Current understanding of olfactory neural processing comes primarily from electrophysiological, anatomical, biochemical, and lesion studies in animals (1-4) and brain lesion studies in humans (5). Such studies have elucidated the involvement of the olfactory bulb, piriform cortex, and entorhinal cortex in olfaction. Recently, this picture of olfactory processing has been broadened by imaging studies designed to explore the linked neural substrates of olfaction in healthy alert conscious humans. PET, SPECT, and fMRI studies of human olfaction have discerned the involvement of piriform and entorhinal cortex, as well as other brain regions that play less obvious functional roles, i.e., orbitofrontal cortex and the cerebellum. Despite the striking similarity of the human and animal literature, no single research modality has been used to tie together the region-specific findings from electrophysiological, neuroanatomical, biochemical, and lesion studies in animals with the more global picture emerging from imaging studies of humans. fMRI studies of olfactory processing have typically examined alert conscious humans (6). Here, we report fMRI techniques for investigating olfaction in sedated squirrel monkeys.

METHODS AND MATERIALS

Six sedated adult male squirrel monkeys (*Saimiri sciureus*) served as subjects in this study. All procedures were conducted in accord with and as required by the Animal Welfare Act, and were approved by Stanford University's Administrative Panel on Laboratory Animal Care. High-resolution fMRI images at 3T with 1.25x1.25x1.2 mm³ voxels were obtained covering the whole brain using an 8-cm diameter birdcage coil and a gradient-echo spiral pulse sequence. Data were acquired using a standard block design in which three increasing concentra-

tions of acetic acid were presented to the monkey for 40 sec followed by no odorant control (distilled water). All fMRI data were spatially normalized to a common template, and analyzed at the individual and group-wise levels with statistical parametric and non-parametric methods.

RESULTS

The regions of interest (ROI) that were identified on the squirrel monkey template are shown in Figure 1, upper panel. The distributed network of BOLD activations evoked by odorants in sedated squirrel monkeys included the orbitofrontal cortex, cerebellum, and, to a lesser extent, hippocampus and piriform cortex, as shown in Figure 1, lower panel. BOLD signal activation was not detected in the entorhinal cortex. This undoubtedly reflects the high susceptibility of this region to dropout artifacts. The entorhinal ROI was therefore excluded from further analysis. Increased BOLD signal intensities in representative voxels from olfactory brain regions were time-locked with the odorant presentations. In the spectral analysis, clear peaks were discerned at the task frequency for olfactory regions, but not in the visual cortex which served as a control region. Overall, 1592, or 14.5%, of the voxels examined throughout the brain showed significant activation. Consistent with human data, no stimulus intensity effects were observed in any of these regions. Average signal changes in these regions exceeded 0.6%, more than three times the expected signal change based on human fMRI studies of olfaction adjusting for differences in voxel size.

CONCLUSIONS

These results demonstrate the feasibility of studying olfaction in sedated monkeys with 3T MRI techniques commonly in humans, and help to promote direct comparisons between humans and nonhuman primates. Our findings support the hypothesis that the cerebellum is involved in sensory acquisition. More broadly, this study suggests that olfactory processing in sedated monkeys and non-sedated humans share similar neural substrates both within and beyond the primary olfactory system.

REFERENCES

- Doty RL. Olfaction. *Annu Rev Psychol* 2001; 52:423-452
- Hildebrand JG, Shepherd GM. Mechanisms of olfactory discrimination: converging evidence for common principles across phyla. *Annu Rev Neurosci* 1997; 20:595-631
- Kauer JS, White J. Imaging and coding in the olfactory system. *Annu Rev Neurosci* 2001; 24:963-979
- Shipley MT, Ennis M. Functional organization of olfactory system. *J Neurobiol* 1996; 30:123-176
- West SE, Doty RL. Influence of epilepsy and temporal lobe resection on olfactory function. *Epilepsia* 1995; 36:531-542
- Zald DH, Pardo JV. Functional neuroimaging of the olfactory system in humans. *Int J Psychophysiol* 2000; 36:165-181

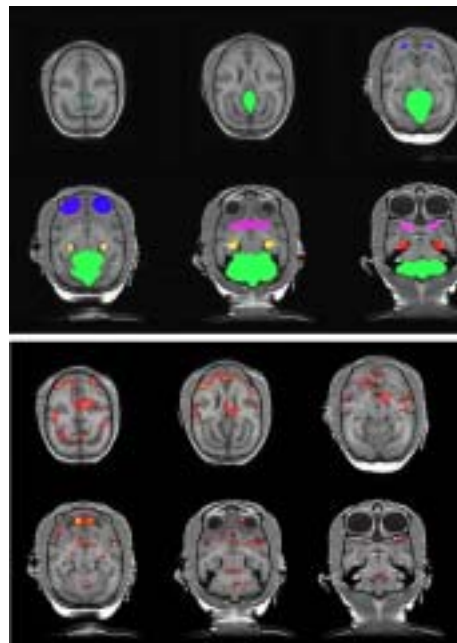


Figure 1:
Top panel: Regions of interest presented on the squirrel monkey brain template. Orbitofrontal cortex - blue, cerebellum - green, hippocampus - yellow, entorhinal cortex - red, piriform cortex - purple.
Bottom panel: fMRI activation evoked by odorant presentation compared to clean air with a fixed-effects analysis depicted for six monkeys combined.

Naama Barnea-Goraly¹, Stephan Eliez¹, Maj Hedehus², Vinod Menon¹, Christopher D. White¹, Michael Moseley², Allan L. Reiss¹

Departments of ¹Psychiatry & Behavioral Sciences, ²Radiology

INTRODUCTION

Fragile X syndrome, the most common form of hereditary developmental disability, causes disruption in the development of dendrites and synapses, the targets for axonal growth in the central nervous system. This disruption could potentially affect the development, wiring, and targeting of axons. The current study used diffusion tensor imaging (DTI) to investigate whether white matter tract integrity and connectivity are altered in fragile X syndrome. Based on previous neuroimaging research involving individuals with fragile X that indicated dysfunction of frontal-subcortical circuits (1), and the finding of an enlarged caudate nucleus in fragile X (2), we hypothesized that there would be white matter differences between subjects with fragile X and controls in pathways connecting the corpus striatum and the frontal lobe.

METHODS AND MATERIALS

Ten females with a diagnosis of fragile X syndrome and 10, age matched, female control subjects underwent diffusion weighted MRI scans. In the current study, fractional anisotropy (FA) was the variable of interest. Fractional anisotropy is an intravoxel measure that yields values indicating levels of isotropic diffusion and anisotropic diffusion. A whole brain analysis of FA values was performed using statistical parametric mapping (SPM). A follow-up, regions-of-interest analysis also was conducted.

RESULTS

Relative to controls, females with fragile X exhibited lower FA values in white matter in fronto-striatal pathways, as well as in parietal sensory-motor tracts (Figures 1 and 2). One cluster was observed in left frontal-caudate white matter tracts, extending between the head of the caudate towards the prefrontal cortex. In addition, two well-defined clusters were observed along the corona radiata and centrum semiovale corresponding to sensory-motor areas bilaterally. A small cluster of increased fractional anisotropy in subjects with fragile X when compared with controls was seen in the posterior part of the superior temporal gyrus.

CONCLUSIONS

This preliminary study suggests that regionally specific alterations of white matter integrity occur in females with fragile X. Aberrant white matter connectivity in these regions is consistent with the profile of cognitive and behavioral features of fragile X syndrome, and potentially provide additional insight into the detrimental effects of suboptimal levels of FMRP in the developing brain.

REFERENCES

1. Hjalgrim H, Jacobsen TB, et al. Frontal-subcortical hypofunction in the fragile X syndrome [letter]. *Am J Med Genet* 1999; 83:140-1
2. Reiss AL, Abrams MT, et al. Neurodevelopmental effects of the FMR-1 full mutation in humans. *Nat Med* 1995; 1:159-67

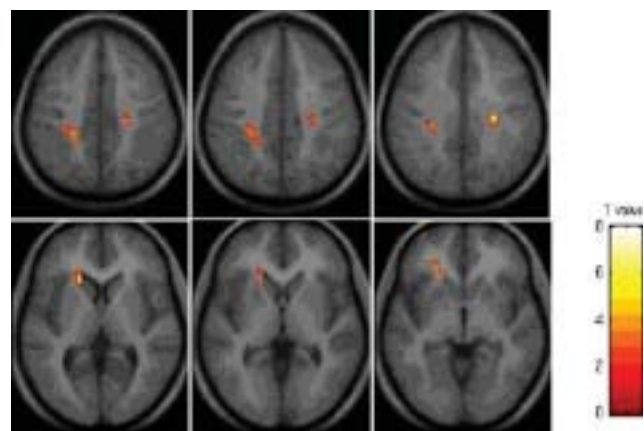


Figure 1. Voxels that showed significant reduction in white matter fractional anisotropy in fragile X compared to control subjects, mapped onto an average T1 weighted image of control and fragile X brains.



Figure 2. A 3-dimensional representation of the aberrant white matter tracts (shown in yellow) in relation to the caudate nucleus (shown in red), as drawn from the average image of all subjects. 2A, anterior-sagittal view; 2B, superior view.

Here's Looking At You Kid: Neural Systems Underlying Face and Gaze Processing in Fragile X Syndrome

Amy S. Garrett, Vinod Menon, Katie MacKenzie, Allan L. Reiss

*Stanford Psychiatry Neuroimaging Laboratory and Behavioral Neurogenetics Research Center (SPNL-BNRC), Department of Psychiatry and Behavioral Sciences***INTRODUCTION**

Children with the fragile X syndrome (fraX) are at risk for manifesting abnormalities in social function that overlap with features of both autism and social anxiety disorder. One hallmark of fraX is the propensity to avoid eye contact and turn away during a social greeting, even while offering a handshake or socially acceptable remark (1). The neural basis of responses to social information in fraX is unknown. In this study, we analyzed brain activation associated with the presentation of face and gaze stimuli to better understand neural functioning associated with social perception in fraX.

METHODS AND MATERIALS

Eleven females with fraX, ages 10-22, were compared with 11 age-matched female control subjects. Photographs of both forward-facing and angled faces, each having direct and averted gaze (4 types of stimuli) were presented in an event-

related design during functional Magnetic Resonance Imaging (fMRI). Subjects were instructed to determine the direction of gaze for each photograph. Between-group differences in brain activation related to the presentation of forward faces (minus angled faces) and direct gaze (minus averted gaze) were determined.

RESULTS

FraX subjects were less accurate than controls when determining direction of gaze. ROI analysis of the FG revealed a significant interaction between diagnostic group and face orientation. Specifically, control subjects had greater FG activation to forward faces than to angled faces, but fraX subjects had no difference in FG activation to forward and angled faces (Figure 1). ROI analyses also showed that fraX subjects had significantly lower STS activation to both direct and averted gaze stimuli when compared to controls (Figure 2).

CONCLUSIONS

The results suggest that individuals with fraX, unlike controls, have similar FG responsiveness to faces regardless of orientation; fraX subjects also showed decreased STS activation to direct gaze stimuli compared to controls. These results may be related to gaze avoidance in fraX and may reflect a decreased capacity to process information about gaze. This is the first study to examine functional brain responses to face and gaze stimuli in a homogeneous group of individuals with a verified diagnosis of fraX, and thus represents a unique opportunity to study social information processing in these individuals.

REFERENCES

1. Wolff PH, Gardner J, Paccla J, Lappen J. The greeting behavior of fragile X males. *Am J Ment Retard* 1989; 93:406-11.

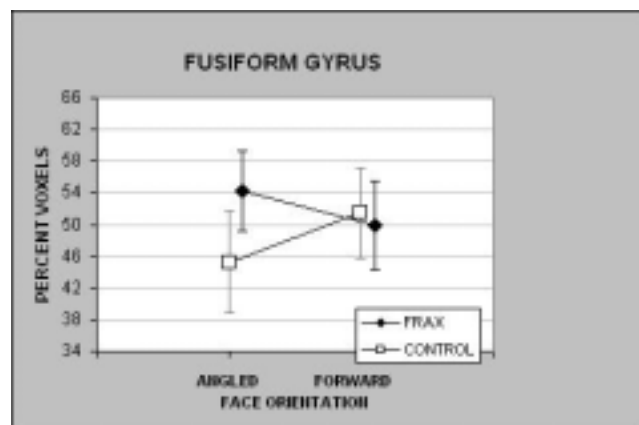


Figure 1: Fusiform gyrus ROI: significant interaction between group and face orientation ($F(1,20)=9.2, p=.007$). Control subjects show significantly greater FG activation for forward faces than for angled faces, while fraX subjects show no difference between forward and angled faces.

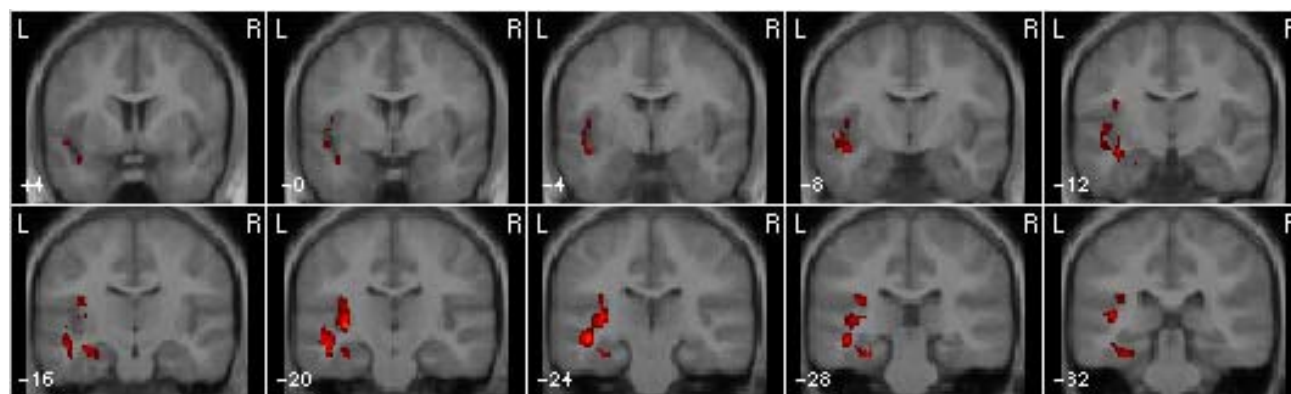


Figure 2: Illustration of significantly greater activation in control compared to fraX subjects in the whole brain analysis of direct versus averted gaze (both having forward face orientation) in addition to other significant differences. The control group has significantly greater STS activation compared with the fraX group.

DEPARTMENT OF PSYCHIATRY AND BEHAVIORAL SCIENCES

Brain Function in Children and Adolescents with Posttraumatic Stress Disorder

Victor Carrion, Allan Reiss

Department of Psychiatry

Together with the Stanford Psychiatry Neuroimaging Laboratory (SPNL), we are establishing new methods to understand the link between the neurobiological underpinnings of early life stress and brain development. The main goal of the Early Life Stress Research Program (ELS RP) is to elucidate how an individual's "stress load" interacts with his or her biological proclivity. In other words, how genetic predisposition to stress vulnerability gets affected by stressors in life. The understanding of this interaction will lead to more focused and targeted interventions of psychiatric disorders (decreased prevalence) and to the development of preventive measures early in life (decreased incidence).

60 children (20 with PTSD, 20 with history of trauma but no PTSD and 20 controls) will be evaluated. Tasks performed during functional imaging include 1) responses to affective stimuli, including facial expressions of fear, anger, sadness, and happiness; 2) response inhibition using a Go-NoGo task; 3) verbal-declarative memory encoding and subsequent incidental recall. Statistical analyses will evaluate the relationship between activation and behavioral and clinical data using SPM99 and Region of Interest techniques.

FUNDING: Brain Function in Pediatric PTSD NIMH K23 MH63893-01

REFERENCES

1. Carrion VG, Weems CF, Eliez S, Patwardan AJ, Brown W, Ray RD, Reiss AL. Attenuation of frontal asymmetry in pediatric posttraumatic stress disorder. *Biological Psychiatry* 2001; 50: 943-951.
2. Understanding the Effects of Early Life Stress on Brain Development. University of California, San Francisco Annual Attachment and Trauma in Child Development Conference: New Directions in Research, Intervention, and Public Policy. February 7, 2003.
3. Carrion V (Chair), Garrett A, Karchemskiy A, MacKenzie K: MRI studies of brain structure and function in pediatric PTSD. 49th Annual Meeting of the American Academy of Child and Adolescent Psychiatry 2002; 18:45-46.
4. Karchemskiy A, Carrion V, Weems C, Reiss A. Longitudinal MRI findings of brain morphology in pediatric PTSD. 49th Annual Meeting of the American Academy of Child and Adolescent Psychiatry 2002; 18:46.
5. Garrett A, Carrion V, Pageler N, Menon V, Mackenzie K, Saltzman K, Reiss A. Alterations in fMRI response of facial expression in adolescent PTSD. 49th Annual Meeting of the American Academy of Child and Adolescent Psychiatry 2002; 18:46.
6. Carrion V, Weems C, Eliez S, Schmitt J, Liu Y, Menon V, Reiss A. Morphological abnormalities of the prefrontal cortex in pediatric PTSD. 49th Annual Meeting of the American Academy of Child and Adolescent Psychiatry 2002; 18:46.
7. Mackenzie K, Carrion V, Garrett A, Saltzman K, Pageler N, Menon V. Frontostriatal deficits in PTSD. 49th Annual Meeting of the American Academy of Child and Adolescent Psychiatry 2002; 18:46.
8. Schreier, H (Chair), Terr, L, Carrion, V, Hardy, L. Methodological issues in research, and results by age, type of trauma, and type. 49th Annual Meeting of the American Academy of Child and Adolescent Psychiatry 2002; 18:28-29.

Brain White Matter Correlates of Cognitive Aging and Stress Neurobiology

David M. Lyons, Chou Yang, Allan R. Reiss, Alan F. Schatzberg

Department of Psychiatry and Behavioral Sciences

INTRODUCTION

Brain white matter volumes continue to increase in humans throughout the first five decades of life, but the functional significance of white matter expansion during brain aging is unknown. Here, we examine relationships between age-related differences in cognitive control, baseline and stress-levels of plasma cortisol and adrenocorticotrophic hormone (ACTH), and white matter volumes determined in vivo by high-resolution magnetic resonance imaging in healthy adult female squirrel monkeys between 5-17 years of age. This period of life span development corresponds to years 20-65 in humans.

METHODS AND MATERIALS

Brain images were acquired on a General Electric Signa 3T scanner at the Lucas Center. The first scan was acquired in the sagittal plane with a 2D sequential radio frequency spoiled gradient echo (SPGR) pulse sequence using the following parameters: TR = 18 msec, TE = 4 msec, flip angle = 30°, NEX = 1, matrix = 256 x 128, FOV = 8 cm, voxel size = 0.5 x 1.0 x 4.0 mm, slice thickness = 4 mm. This initial localizer scan was used to standardize head tilt and rotation by assuring that two external markers (vitamin E capsules in the meatus of each ear) were aligned in the coronal and axial planes. The head was re-positioned as required, and another sagittal localizer scan was performed. Head pitch was then standardized against the midsagittal image, and the final scan used for volumetric analysis was acquired in the coronal plane with a 3D volumetric inversion recovery-prepared fast SPGR pulse sequence: TR = 12 msec, TE = 3 msec, TI = 300 msec, flip angle = 15°, NEX = 4, matrix = 256 x 256, FOV = 8 cm, voxel size = 0.31 x 0.31 x 1.00 mm, slice thickness = 1 mm, gap = 0 mm, total scan time = 17 minutes. Inversion recovery-prepared SPGR protocols provide maximum gray versus white matter contrast currently available with MRI, and thereby improve identification and quantification of white matter brain tissue.

RESULTS

Older adult monkeys responded to stress with larger increases in cortisol and ACTH relative to young adults. Sensitivity to glucocorticoid negative-feedback determined by hydrocortisone administration was also diminished in the older adults. Cognitive performance did not differ with age during initial tests of learning and memory, but older adults more often failed to inhibit the initial learned response after spatial reversals. Impaired response inhibition and diminished sensitivity to glucocorticoid negative-feedback correlated with age-related global expansion of white matter volumes.

CONCLUSIONS

These results provide the first indication that white matter changes during brain aging are linked with diminished regulation of neuroendocrine responses to stress in adults, and concur with reports that myelin de-compaction contributes to cognitive decline.

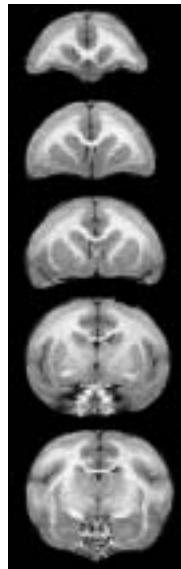


Figure 1: Representative squirrel monkey brain images.

Judith M. Ford¹, Max Gray¹, Susan L. Whitfield², U. Turken², Gary Glover³, Daniel H. Mathalon⁴

Departments of ¹Psychiatry & Behavioral Sciences, ²Psychology, and ³Radiology, Stanford University;

⁴Department of Psychiatry, Yale University

INTRODUCTION

Schizophrenia is associated with deficits in using context to establish pre-potent responses in complex paradigms and failures to inhibit pre-potent responses once established. We sought to assess pre-potent response establishment and inhibition in schizophrenia patients using a simple NoGo task. Subjects performed the task in both event-related brain potentials (ERP) and functional magnetic resonance imaging (fMRI) environments so that we could use the higher temporal resolution of the NoGo P300 ERP component to focus on fMRI activations associated with the brief (~200 ms) moment of context updating.

METHODS AND MATERIALS

DSM-IV schizophrenia patients (n=11) recruited from the community and the VA hospital, and sex- and age-matched healthy control subjects (n=11) recruited from the community participated in the study. They performed a NoGo task requiring a speedy button press to Xs (p=.88) but none to Ks (p=.12) on two occasions: once while ERPs were recorded and once while fMRI activations were recorded.

RESULTS

Behavioral accuracy, P300 amplitudes and latencies, and fMRI activations suggested that patients did not establish as strong a pre-potent tendency to respond to the Go stimulus as healthy subjects. In healthy subjects, NoGo P300 was related to activations in (1) anterior cingulate cortex, (2) dorsal lateral prefrontal cortex, and (3) right inferior parietal lobule and caudate nucleus, perhaps reflecting (1) conflict experienced when withholding a response, (2) control needed to inhibit a response, and (3) stopping a response-in-action, respectively. In patients, NoGo P300 was modestly related to activations in anterior cingulate cortex, consistent with experiencing conflict.

CONCLUSIONS

The difference in ERP and fMRI responses to Go and NoGo stimuli suggested that inhibiting a response was less effortful for patients than for healthy subjects. Correlations of P300 and fMRI data suggested that patients and healthy subjects used different neural structures to inhibit responses, with healthy subjects using a more complex system.

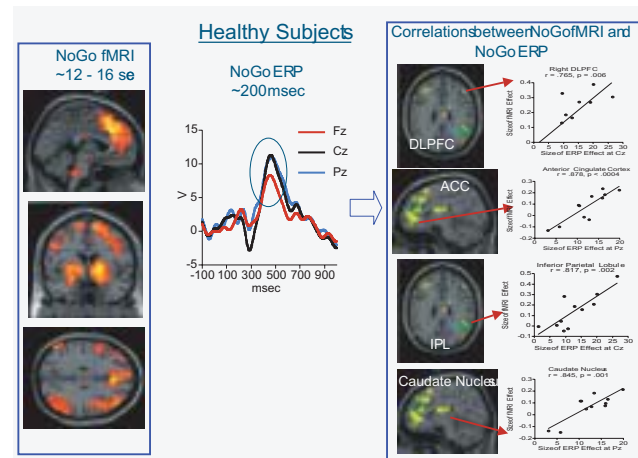


Figure 1: Control subjects. The NoGo fMRI beta image (left). NoGo ERPs with NoGo P300 circled (middle). Image of fMRI activations ($p < .01$ uncorrected, contiguous voxels = 6) that correlated with P300 amplitudes recorded at Fz [red], Cz [green], and Pz [yellow] and scatter plots of average activation for that region and P300 amplitudes (right).

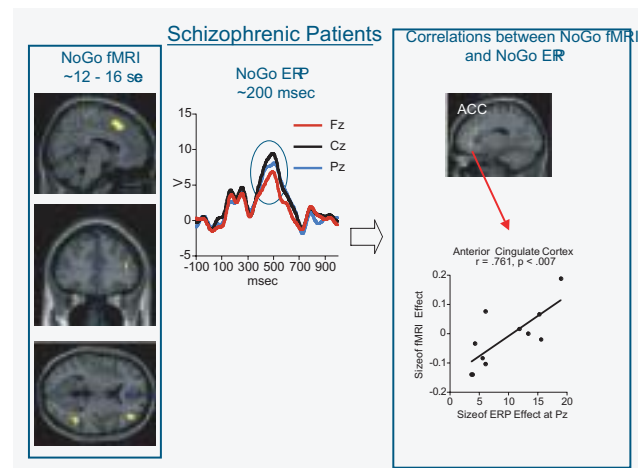


Figure 2: Same as in Figure 1, for schizophrenic patients

Anatomy of an Error: ERPs and fMRI

Judith M. Ford¹, Susan L. Whitfield², Gary Glover³ and Daniel H. Mathalon⁴

Departments of ¹Psychiatry & Behavioral Sciences, ²Psychology, and ³Radiology, Stanford University;

⁴Department of Psychiatry, Yale University

INTRODUCTION

Successful inhibition of pre-potent responses involves only conflict monitoring, while failed inhibition involves not only conflict monitoring but also recognition of error. Functional magnetic resonance imaging (fMRI) data reveal similar frontal lobe activations during both successful and failed inhibitions. By contrast, event-related brain potential (ERP) data reveal an N2 component associated with *successful* inhibition, but an error-related negativity (ERN) associated with *failed* inhibition. While these two components are closely related, they are only moderately correlated, suggesting that they contain both shared and unique sources of variance. Their shared variance reflects conflict processing common to both successful and failed response inhibition, while residual ERN activity remaining after removing variance shared with N2 reflects activity uniquely associated with error processing. We used ERP recordings to help identify fMRI brain activations uniquely associated with error monitoring and conflict monitoring.

METHODS AND MATERIALS

In separate sessions, ERP and event-related fMRI data were collected while 10 healthy subjects, spanning the adult age range of 26-55 years, performed a NoGo task requiring speedy button presses to Xs ($p=.88$) but none to Ks ($p=.12$). The following ERP components were measured: ERNs to false alarms, correct-related negativities (CRNs) to correct responses (hits), NoGo N2 to correctly inhibited responses (correct rejections), and Go N2 to correct responses (hits). ERP contrast scores were derived (ERN-CRN; NoGoN2-GoN2). Both ERN and N2 were corrected for the effects of age, and the CRN was corrected for effects of conflict, as reflected in the N2 contrast score, using regression analysis. These relatively “conflict-free” and “age-free” physiological signals were then used to identify the fMRI error-related and conflict monitoring brain activation contrasts (False Alarms-Hits; Correct Rejections-Hits) specifically associated with them.

RESULTS

The ERN measure correlated with fMRI activations in rostral anterior cingulate cortex (ACC), while the N2 measure correlated with fMRI activations in caudal ACC, as well as executive control regions of the brain such as dorsolateral prefrontal cortex.

CONCLUSIONS

This finding suggests error monitoring and conflict monitoring may be subserved by different regions of ACC.

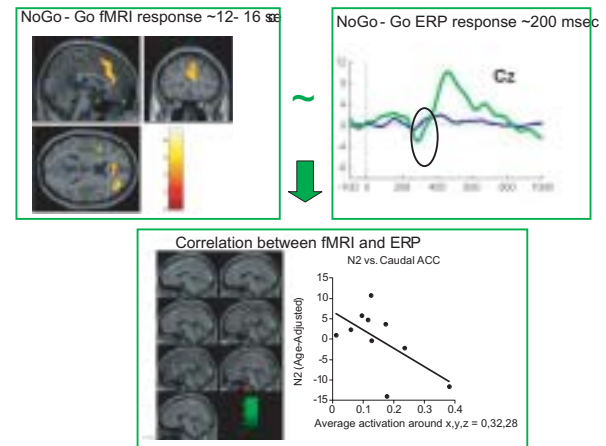


Figure 1: fMRI, ERP, and fMRI/ERP correlations for Correct Rejections (NoGo) – Hits (Go) comparisons. Three-planar view for fMRI ($p<.001$, uncorrected) (upper left), ERPs overlaid Correct Rejections and Hits from Cz (upper right), fMRI and ERP correlations ERP correlations ($p<.05$, uncorrected, extent 6) focussing on ACC (lower left), scatter plot showing that subjects with larger Age-Adjusted N2 scores have greater caudal ACC activation.

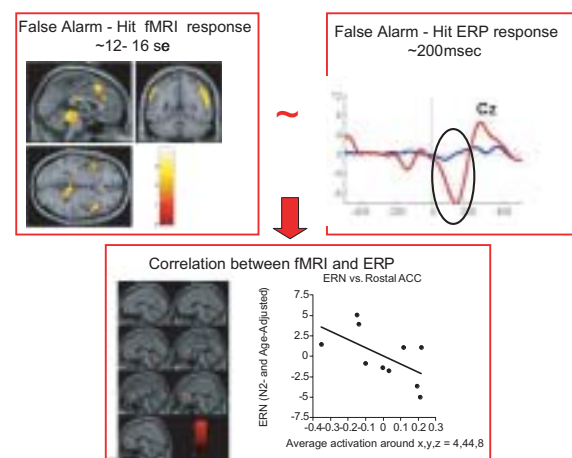


Figure 2: fMRI, ERP, and fMRI/ERP correlations for False Alarms (NoGo) – Hits (Go) comparisons. Three-planar view for fMRI ($p<.05$, uncorrected) (upper left), ERPs overlaid False Alarms and Hits from Cz (upper right), fMRI and ERP correlations ERP correlations ($p<.05$, uncorrected, extent 6) focussing on ACC (lower left), scatter plot showing that subjects with larger N2 and Age-Adjusted ERN scores have greater rostral ACC activation.

¹Edith V. Sullivan, ^{1,2}Margaret J. Rosenbloom, ²Kathleen L. Serventi, ^{1,2}Adolf Pfefferbaum.

¹Department of Psychiatry and Behavioral Sciences, Stanford University, ²Neuroscience Program, SRI International

INTRODUCTION

The pons and thalamus are both critical nodes in circuits linking the cerebellum and basal ganglia to motor and sensory cortices as well as frontal and prefrontal cortex that subserve higher-order behavior. To date, no report has covered normal aging effects or sex differences on both pons and thalamus in the same sample or examined whether age effects or sex differences for these subcortical gray and white matter structures parallel those found for cortical gray and white matter.

METHODS AND MATERIALS

Thalamus and pons were measured on 3D T1-weighted images obtained from a sample of 51 men and 49 women. Cortical gray and white matter volumes were measured from dual-echo axial image sequences obtained on a different occasion from 95 men (33 of whom were in the 3D scan data set) and 48 women (47 of whom were in the 3D dataset). All subjects had been recruited from the community to participate in studies of normal aging and to serve as healthy comparison groups for patient populations.

The most lateral boundaries of pons and thalamus were first estimated by marking the limits on coronal and axial views of the 3D scan. Each structure was then manually traced following visible borders on every third 1 mm thick sagittal slice with the medial slice at the mid-sagittal plane. All measurements were completed twice, and the volume was the mean of the two measurements. The left and right thalami were randomly reversed in orientation to prevent measurement bias. Cortical gray and white matter volume was estimated by counting segmented gray and white matter pixels falling in the outer 45% of seven consecutive sections on axial scans beginning at an index section (the most inferior section above the level of the orbits, where the anterior horns of the lateral ventricles could be seen bilaterally) and proceeding superiorly. Intracranial volume (ICV) was estimated for each scan type by modeling the head as a sphere.

RESULTS

Thalamic, pontine, and cortical white matter volumes did not differ between men and women once ICV differences were taken into account, but men had more cortical gray matter than women even after accounting for ICV. Thalamic volume declined linearly with age at a similar rate in both men and women, whereas cortical gray matter volume declined more steeply with age in men than women. Both pontine and cortical white matter volumes remained stable across the age span in both men and women.

CONCLUSIONS

Changes in the thalamus and pons over the adult age span parallel global changes in cortical gray and white matter volume. Gender differences in ICV-corrected volumes of pons and thalamus were not apparent, but men had more cortical gray matter than women, even after accounting for ICV and cortical gray matter volume declined more steeply with age in men than women.

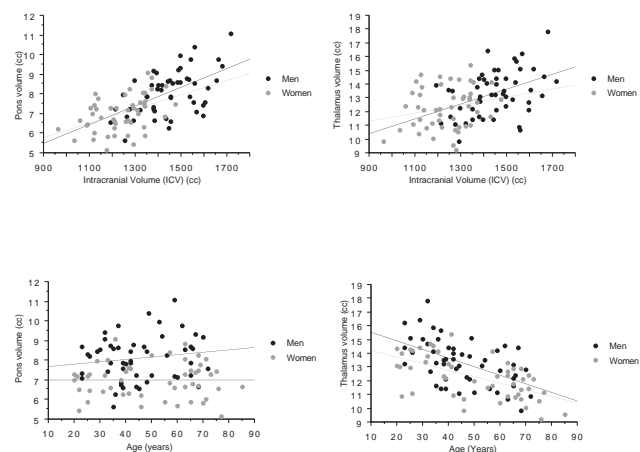


Figure 1: Volumes for thalamus and pons plotted as a function of ICV (upper row) and age (lower row) for 51 men and 49 women.

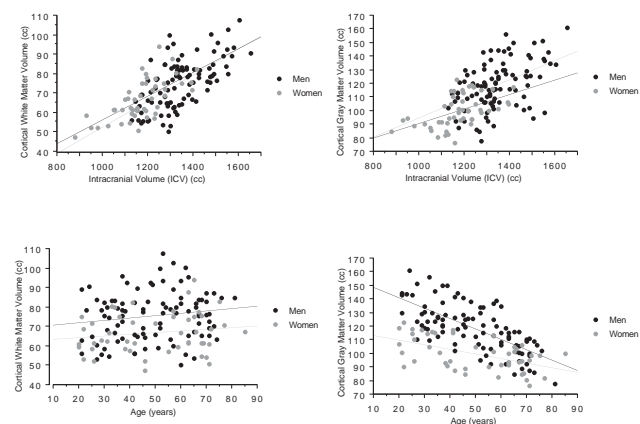


Figure 2: Volumes of cortical gray and white matter plotted as a function of ICV (upper row) and age (lower row) in 48 women and 95 men.

Effects of Alcoholism-Schizophrenia Comorbidity on Volumes of the Thalamus and Pons

¹Edith V. Sullivan, ^{1,2}Margaret J. Rosenbloom, ²Kathleen L. Serventi, ²Anjali Deshmukh, ^{1,2}Adolf Pfefferbaum.

¹Department of Psychiatry and Behavioral Sciences, Stanford University, ²Neuroscience Program, SRI International

INTRODUCTION

Postmortem and in vivo brain imaging studies have identified abnormalities in the thalamus and the pons in both schizophrenia and alcoholism. Alcohol abuse and dependence occur with high prevalence in schizophrenia and pose exceptional risks of brain damage to patients with schizophrenia, especially in regions vulnerable to the toxic effects of alcohol. Typical neuroleptic treatments for schizophrenia increase thalamic volume, while atypical neuroleptics do not. We sought to determine whether patients with both diseases would manifest exaggerated volume deficits in either thalamus or pons and whether these effects may be mitigated by type of antipsychotic medication.

METHODS AND MATERIALS

Volumetric measures of left and right thalamus and pons were derived from MRI scans obtained from 27 schizophrenics, 19 schizophrenics comorbid for alcoholism, 25 alcoholics, and 51 healthy comparison subjects.

RESULTS

Patients with alcoholism had significant volume deficits in both thalami and the pons. Patients with schizophrenia had preservation of the thalamus, whether or not they were comorbid for alcoholism. However, among patients with schizophrenia, with or without alcoholism comorbidity, those on atypical antipsychotic medications had bilateral thalamic deficits whereas those on typical neuroleptics did not. Patients with schizophrenia had pontine shrinkage only if they were comorbid for alcoholism.

CONCLUSIONS

Patients with schizophrenia comorbid for alcoholism are at risk for alcohol-related reduction of pontine structures not necessarily affected by schizophrenia per se. Nonetheless, the effect of alcoholism on the thalamus in schizophrenic patients may be mitigated by type of neuroleptic medication.

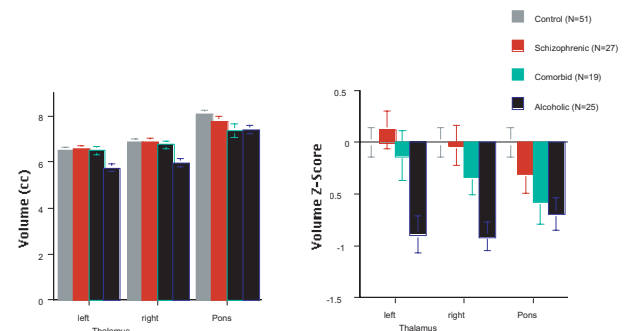


Figure 1: Outlines of thalamus and pons on five medial slices from the 12 sagittal slices used for delineating these structures. Subject is a 46 year old alcoholic man.

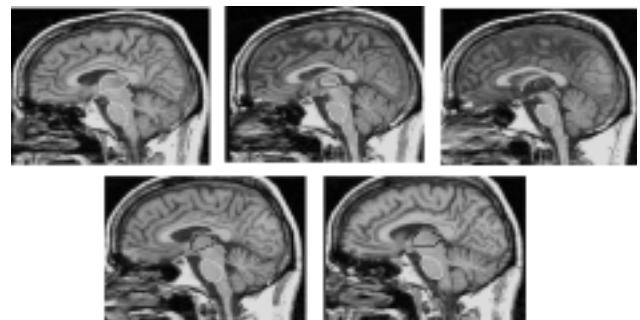


Figure 2: Absolute volume in cc (left) and as a Z-score reflecting deviation from age and headsize norms (right) for left and right thalamus and pons from healthy comparison subjects, schizophrenic patients, comorbid patients and alcoholic patients.

^{1,2}Adolf Pfefferbaum, ³Elfar Adalsteinsson, ²Edith V. Sullivan

¹Neuroscience Program, SRI International, ²Departments of Psychiatry and Behavioral Sciences and ³Radiology, Stanford University

INTRODUCTION

Diffusion tensor imaging (DTI) provides a safe, noninvasive, in vivo neuroimaging tool that is being used to track the course of normal aging as well as neurodegenerative diseases of white matter and may provide a sensitive measure of improved microstructural integrity with pharmacological therapy. To examine the stability of DTI as a tool to measure change with advancing age, disease progression, or intervention for single and multi site studies, we assessed within and between scan measurement reliability of two commonly used DTI metrics: trace and fractional anisotropy (FA).

METHODS AND MATERIALS

Ten young healthy adults were scanned on three separate days on 1.5T GE systems at the Lucas Imaging Center and at the GE ASL-West facility at SRI International. One scan was acquired at one site, and two scans were acquired on two different occasions on another scanner at another site. Three levels of analysis were used to compare the DTI metrics: 1) a voxel-by-voxel analysis of all supratentorial brain (gray matter + white matter + cerebrospinal fluid) and of supratentorial white matter; 2) a slice-by-slice analysis of supratentorial white matter; and 3) a single-region analysis of the corpus callosum. Data for all subjects were placed in a coordinate system where the origin was chosen as the manually identified anterior commissure (AC). Furthermore, each

exam was rotated around the AC to place the data in a standard orientation. This procedure differs from atlas-based methods where all subjects are warped to a standard reference.

RESULTS

The voxel-by-voxel analysis of all supratentorial brain found that FA and trace measures and correlations were equivalently and significantly higher within than across scanners. For supratentorial white matter, FA was similar within and across scanners, whereas trace demonstrated across scanner bias. A similar pattern was observed for the slice-by-slice comparison. For the single-region analysis of the corpus callosum, within-scanner FA and trace measures were highly reproducible for FA (CV=1.9%) and trace (CV=2.6%), but both DTI measures showed a systematic mean bias across scanners (CV=4.5% for FA and CV=7.5% for trace).

CONCLUSIONS

These estimates of measurement variation and scanner bias can be used to predict effect sizes for longitudinal and multi-site studies using diffusion tensor imaging. Across platforms, FA was more replicable than trace, perhaps due to variation in gradient subsystems. Corrections for gradient nonlinearity on diffusion measurements may reduce non-target variability between scan sessions or scanners.

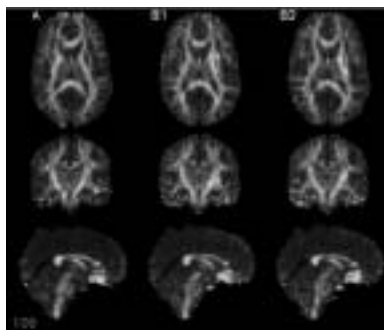


Figure 1: A representative example of FA, displayed in three orthogonal sections from one subject scanned once on scanner A, and twice on scanner B.

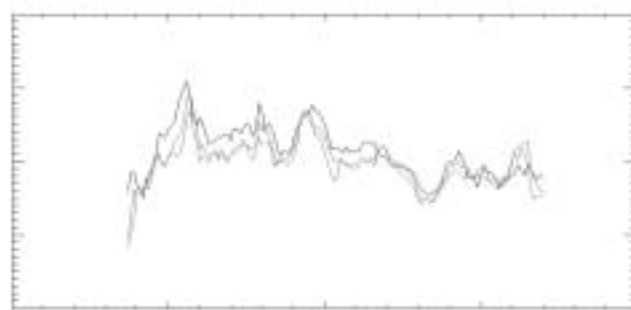


Figure 2: An example of data from the slice-by-slice comparison. The black line shows the FA on a slice-by-slice basis, posterior to anterior for one subject acquired on scanner A. The gray lines show the same data for two separate acquisitions on scanner B.

Morphological Changes in Aging Brain Structures Are Differentially Affected by Time-Linked Environmental Influences Despite Strong Genetic Stability

^{1,2}Adolf Pfefferbaum, ¹Edith V. Sullivan, ²Dorit Carmelli

¹Department of Psychiatry and Behavioral Sciences, Stanford University, ²Neuroscience Program, SRI International

INTRODUCTION

Most studies of the role of genes in determining the ultimate dimension of somatic structure have focused on early development. However, there is evidence that turn-on/turn-off genes operate at different times over the life-span. These potential breaches in genetic continuity may be discerned by applying the twin model to longitudinal data on brain size and shape. Genetic statistical modeling uses differences between brain size and shape between monozygotic (MZ) and dizygotic (DZ) twin pairs for estimating separate contributions of genes and the environment. Longitudinal study of twins can identify whether new genetic or environmental factors emerge that contribute to stability or change in morphometric characteristics of particular brain structures.

METHODS AND MATERIALS

MRI scans were obtained twice, 4-years apart, from 34 monozygotic (MZ) and 37 dizygotic (DZ) elderly male twin pairs from the NHLBI Twin Study. The corpus callosum was measured on a sagittal midline slice and total cross-sectional area, regional areas, and height were quantified. Lateral ventricles were outlined by semi-automated edge identification on three slices of a proton-density weighted coronal scan. The area on each slice summed to estimate volume.

RESULTS

Genetic factors accounted for a substantial portion of individual differences in the size of the corpus callosum and its substructures and of lateral ventricular size. Longitudinal genetic analyses revealed no significant change in the heritability of these structures and no evidence for new genetic variance at time 2 not present at time 1. However, both the callosal and ventricular measures showed evidence for new environmental variance at time 2 not present at time 1. Confirming a previously posed hypothesis, the phenotypic correlation between absolute change in height of the corpus callosum and absolute change in ventricular volume was significant. Bivariate genetic analysis estimated a significant genetic correlation between the changes in these two structures and the genetic variance in the change of callosal height was due entirely to genes involved in the expansion of ventricles..

CONCLUSIONS

Genetic stability was present even in old age when brain and other morphological changes can be rapid and highly variable across individuals, inconsistent with an hypothesis that random DNA damage is the cause of aging.

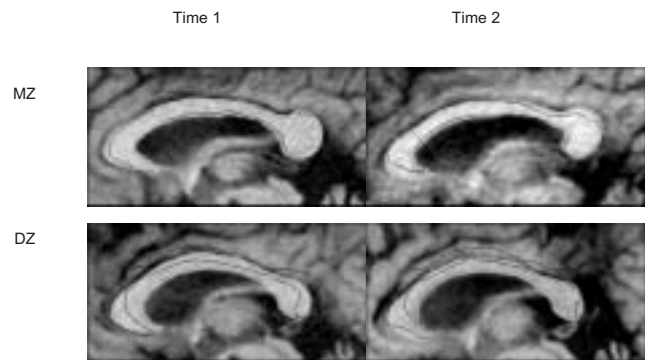


Figure 1: Midsagittal MR brain images of the corpus callosum from 2 individuals (one MZ twin and one DZ twin) at Time 1 and Time 2. The corpus callosum profile of each twin is outlined in white and the profile from his brother is superimposed in black. Note the similarity in the shape of the corpus callosum in the MZ twin and his brother at both times versus that of the DZ pair.

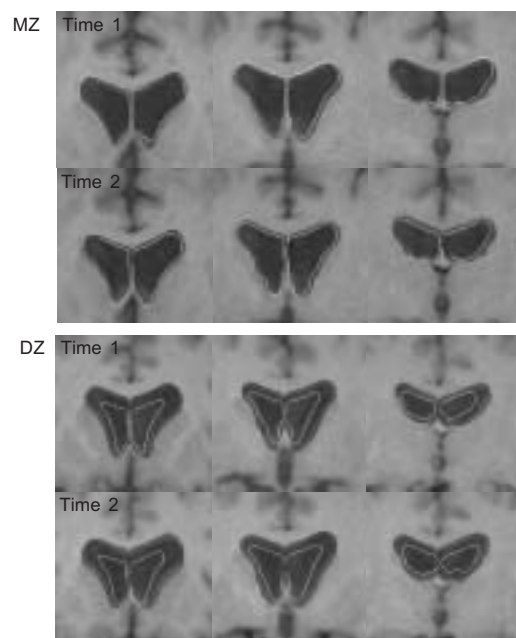


Figure 2: Three coronal MR brain images through the lateral ventricles from 2 individuals (one MZ twin and one DZ twin) at Time 1 and Time 2. The ventricle profile of each twin is outlined in black and the profile from his brother is superimposed in white. Note the similarity in the size and shape of the ventricles in the MZ twin and his brother at both times versus that of the DZ pair.

ANESTHESIA

fMRI Activation in the Human Cervical Spinal Cord to Noxious Thermal Stimulation

Sean Mackey, David Ludlow, Kyle Knierim, Josh Hanelin, Tara Ramachandra, Gary Glover

Departments of Anesthesia and Radiology

INTRODUCTION

Functional magnetic resonance imaging (fMRI) has been a valuable tool in elucidating the neural circuitry of pain processing within the human brain. But significant processing of noxious stimuli and neural plasticity also occur at the level of the spinal cord. Despite difficulties in the past, research has shown that fMRI can reliably detect blood oxygen level dependent (BOLD) signal changes due to neural activity within the cervical spinal cord on a 3 Tesla (3T) magnet. To date, however, there is no published data on the uses of fMRI for studying nociceptive processing within the cervical spine on a 3T magnet. The present study, therefore, sought to extend initial neuroimaging findings by defining patterns of activation in the human cervical spine to noxious thermal stimuli.

METHODS

Conventional and functional magnetic resonance imaging data was collected on a 3T scanner (GE Lx rev VH3-M3.8, Milwaukee, WI) while a thermal stimulator applied heat to 7 healthy female subjects in the following areas: left and right lateral forearm in a C6 dermatomal distribution, and left and right deltoid in a C5-C4 distribution (see Figure 1). Alternating 30 second blocks of noxious heat (45-50C) and warmth stimuli (38C) were applied to each of these areas. Images were acquired using a gradient echo single-shot spiral acquisition with 14 contiguous axial 4 mm slices of cervical levels C3 to C7 (see Figure 2). We used a 16 cm FOV, a 2000 ms TR, a 30 ms TE, and a matrix of 128x128. Physiological motion correction from cardiac and respiratory effects was corrected for in preprocessing. Additional motion correction and statistical analysis was performed using AFNI.



Figure 1: Example placement of the Peltier thermode on the left deltoid during noxious thermal stimulation. Also shown is the sagittal slice prescription for the fourteen axial slices taken from the middle of C3 to the bottom of C6.

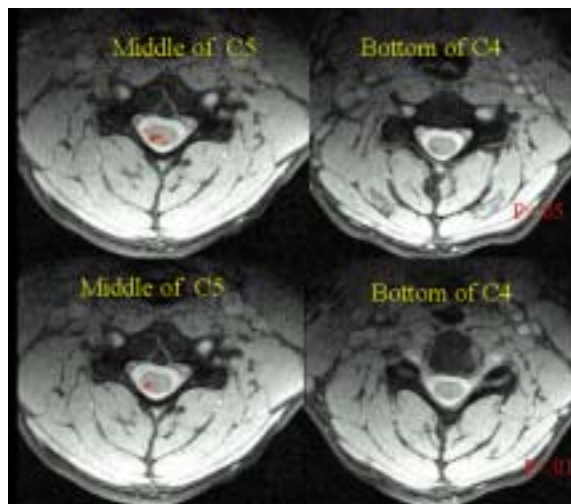


Figure 2: BOLD response to thermal stimulation of the right lateral forearm in the cervical spine. At $p < .05$ multiple activations are seen in the ipsilateral and contralateral dorsal horn. As the p-value become more stringent ($p < .01$), the contralateral activations disappear, and the remaining activations center around the bottom of C5.

RESULTS

Simple regression ($p < 0.05$) analyses defined statistically significant voxels of activation within the ipsilateral dorsal horn of the cervical spinal cord. The most densely activated regions corresponded to the correct dermatomal distribution within the cervical spine for the left and right deltoid tasks (C5-C4 region), but was higher than expected for the left and right lateral forearm stimulation (around the bottom of C5). Contralateral activations were also apparent at all levels although not as robustly as ipsilateral activation, and as the p-value became more stringent the contralateral activation began to disappear.

CONCLUSION

The data provides evidence for using fMRI to map the spinal cord in healthy subjects and investigate the changes that occur with chronic pain.

REFERENCES

1. Stroman PW, Nance PW, Ryner LN. BOLD MRI of the human cervical spinal cord at 3 tesla. *Magn Reson Med* 1999;42:571-6
2. Madi S, Flanders AE, Vinitski S, Herbison GJ, Nissanov J. Functional MR imaging of the human cervical spinal cord. *AJNR Am J Neuroradiol* 2001; 22:1768-74

Do I Feel What You Feel? A Functional Imaging Study of Empathy of Pain

Kevin Ochsner, David Ludlow, Josh Hanelin, Kyle Knierim, Tara Ramachandra, Gary Glover, Sean Mackey

Departments of Anesthesia, Psychology, Radiology

INTRODUCTION

Prior functional neuroimaging studies have implicated areas such as the anterior cingulate cortex, the primary and secondary somatosensory cortex, the insular cortex, and the amygdala in the nociceptive processing of pain for one's own body. Similarly, prior functional neuroimaging studies have shown that some of the same regions involved in processing pain also respond to observing negatively valenced stimuli in the environment. It is not yet clear, however, whether the same systems implicated in the experience of pain applied to one's own body also are involved in the perception of another individual who is experiencing pain. The present study, therefore, sought to determine the common and distinct regions of activation to pain when it is inflicted on one-self versus when it is perceived in others.

METHODS

Fourteen participants completed two tasks in counterbalanced order while whole-brain conventional and functional magnetic resonance imaging data was collected on a 3T scanner (GE Lx rev VH3-M3.8, Milwaukee, WI). In the noxious thermal task a thermal stimulator (TSA II, Medoc, Inc.) applied heat to the subject's left lateral forearm in alternating blocks of painful heat (45-50°C) and warmth stimuli (38°C). In the pain video task, participants viewed a short video clip that showed individuals suffering injuries in sporting events (e.g. a leg break in a soccer match) or vehicular accidents (e.g. a car crash).



Figure 1: Example placement of the peltier thermode during the noxious thermal task. Also shown here is an example of a video clip projected into the scanner showing a leg break.

RESULTS

A conjunction analyses revealed a network of commonly activated regions involved in the perception of pain in one's self as well as in others. These regions included the cingulate cortex, bilateral insular cortex, and bilateral somatosensory cortex. In contrast to this, the noxious thermal task showed greater activation than the pain video in the medial orbitofrontal cortex, a region implicated in the perception of reinforcing stimuli and the experience of emotion, and also in the middle frontal gyrus, a region implicated in the cognitive interpretation and reappraisal of emotional stimuli. Finally, the pain video induced greater activation in the right posterior insular cortex, a region implicated in viscerosensory processing, and in the superior temporal sulcus, a region implicated in the perception of nonverbal social cues.

CONCLUSIONS

These findings have implications for theories of the neural matrix for pain perception as well as the study of empathy.

REFERENCES

1. Allison T, Puce A., McCarthy G. Social perception from visual cues: role of the STS region. *Trends Cogn Sci* 2000; 4:267-278
2. Ochsner KN, Bunge SA, Gross JJ, Gabrieli JD. Rethinking feelings: an fMRI study of the cognitive regulation of emotion. *Cogn Neurosci* 2002; 14:1215-29
3. Hofbauer RK, Rainville P, Duncan GH, Bushnell MC. Cortical representation of sensory dimension of pain. *J Neurophysiol* 2001; 86:402-11

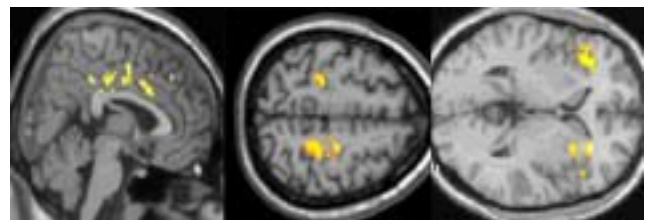


Figure 2: Shown above are the areas of common activation between the noxious thermal task and the pain video. On the left is a sagittal view of cingulate activation; in the middle is an axial view of bilateral insular cortex activation; on the right is an axial view of somatosensory cortex activation.

Chien-Chung Chen^{1,2}, Christopher W. Tyler¹ and Heidi A. Baseler¹

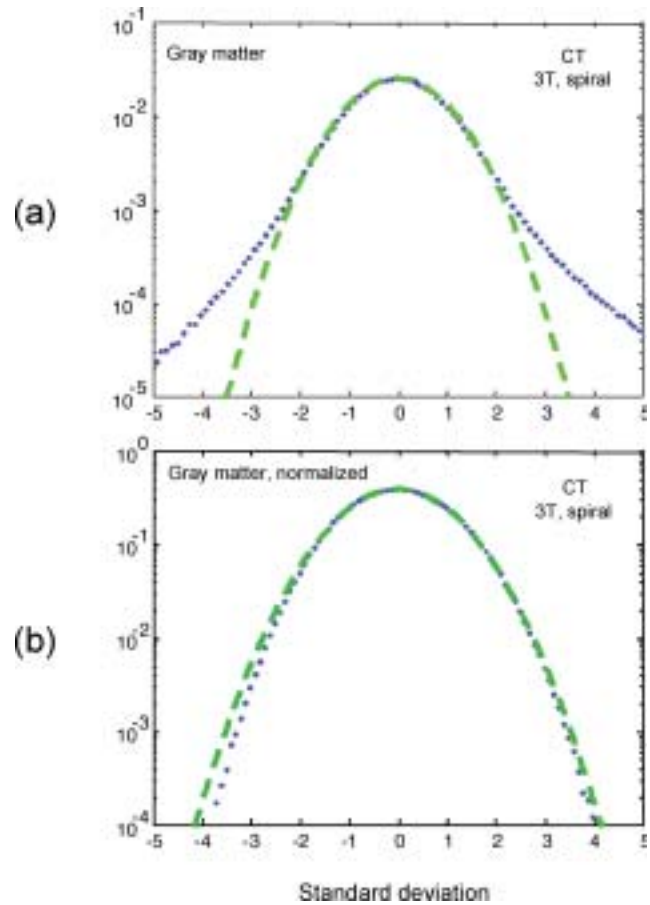
¹The Smith-Kettlewell Eye Research Institute, San Francisco, CA ²National Taiwan University, Taipei, Taiwan

We investigated the random variability of BOLD (blood oxygen level dependent) activation during rest, or null-hypothesis, conditions in which the observers were neither receiving controlled sensory stimuli nor performing cognitive tasks. The data indicate that the distributions for the BOLD variation across space are skewed, with highly non-Gaussian tails, while the distributions for the temporal variation within individual voxels are predominantly Gaussian.

The figure shows the data for a typical cortical recording. The cortex was segmented with the mrGray software package. The dotted curve in panel (a) shows the probability distribution of BOLD variation pooled from all voxels and time points within the segmented gray matter of one subject in the data set. The distribution includes both temporal and spatial variation. Compared with the best-fit Gaussian density function (dashed curve), the empirical distribution shows extended tails on both sides. This form of distribution is problematic for statistical analysis because it violates the Gaussian assumption for the probability of outliers (false alarms).

We find, however, that scaling each plotted amplitude by the standard deviation of the respective voxel can effectively remove the spatial effect. The dotted curve in panel (b) is the empirical normalized distribution and the dashed curve, the Gaussian density function. Thus, the resulting probability distribution becomes accurately Gaussian, implying that the temporal variation in the resting brain is purely Gaussian.

The proportion of voxels that show non-Gaussian properties is highly correlated with the magnitude of head movement of the observers. In all observers, the white matter shows less variability than the gray matter. The distributions for the spatial and the temporal variations are robust across observers despite differences in the data acquisition methods (EPI vs. spiral) and magnetic field strength (1.5 vs. 3T).



Functional Imaging of Cortical Areas Responding to Stereoscopic Depth

C.W.Tyler, L.Kontsevich, L.Likova, A.R.Wade

Smith Kettlewell Eye Research Institute, San Francisco, CA

INTRODUCTION

The human visual system can detect the distance or depth of an object by comparing the relative displacements of the images that it produces on the two retinas. The computation of this 'stereoscopic' depth is a multi-step process that must begin in early visual cortex but which also involves many higher-level mechanisms. In this study, we used dynamic random dot autostereograms to produce stimuli with well-controlled stereoscopic depth or 3-dimensional slant and analyzed the resulting responses in early and mid-level visual cortex.

METHODS AND MATERIALS

We acquired functional data on a 3T GE Signa scanner with a custom posterior surface coil to maximize signal to noise. High contrast dynamic random dot autostereograms (refresh rate 1Hz, density 5%) were projected onto a ground glass projection screen and viewed by the subjects through a mirror. Subjects were experts in viewing autostereograms and reported no difficulty in fusing the stimuli to generate a strong depth percept. In half the scans, subjects performed a fixation task unrelated to the depth modulation in order to control for attentional effects. An A-B block design stimuli was used. Each cycle lasted 18 seconds with 10 total cycles per scan. Stimulus 'A' consisted of pairs of intersecting slanted 3-D flat planes (with the vertical intersection line bisecting the fixation point). The planes had a high relative slant (and therefore, large depth and disparity contrast gradients). Stimulus 'B' was identical to stimulus 'A' except with one quarter the relative slant. The number of planes, the overall form of the stimulus and the stereoscopic depth of the fixation point were all constant over time and the only parameter that changed was the magnitude of the depth contrast between the planes.

RESULTS

As well as an activation in a retinotopic region described in a previous study¹ we find significant responses in an extrastriate and weakly-retinotopic region previously thought to respond mainly to kinetic motion boundaries.² This area lies on the dorso-lateral surface of occipital cortex between V3A and human MT complex and, in these studies, is active only when subjects report the perception of depth modulation.

CONCLUSIONS

It is possible that this dorso-lateral region responds to a broader class of object boundaries than previously described.³ Alternatively, it is possible that this area has a strong specialization for depth form. Many of the stimuli that have been used so far used to probe this area may have had significant depth structure leading to a mis-categorization of its functional specificity. The strong dependence of the signal we find on attentional state and the correlation with conscious percept suggests that it is critical to control for these factors during fMRI analysis of this region.

REFERENCES

1. Backus BT, Fleet DJ, et al. Human cortical activity correlates with stereoscopic depth perception. *J Neurophysiol* 2001; 86:2054-68
2. Oostende SV, Sunaert S, et al. The kinetic occipital (KO) region in man: an fMRI study. *Cereb Cortex* 1997; 7:690-701
3. Zeki S, Perry RJ, et al. (2003). The processing of kinetic contours in the brain. *Cereb Cortex* 2003; 13:189-202

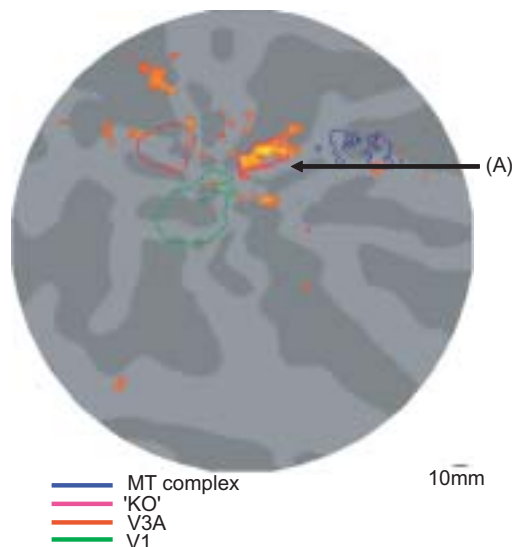


Figure 1: Areas responding to high vs low stereo depth stimuli. The boundaries of visual areas V1, V3A, MT complex and putative KO (defined from separate retinotopic mapping and localizer scans) are marked. Note that the main stereo activation lies almost entirely within putative 'KO'.

Mitigation of susceptibility-induced signal loss in neuroimaging using localized shim coil

Jung-Jiin (Jason) Hsu, Gary H. Glover

Department of Radiology

INTRODUCTION

In MRI, the Zeeman magnetic field (B_0) in the human inferior frontal cortex (IFC) is seriously distorted due to the geometrical shape and the change of the magnetic susceptibility across boundaries of the brain, the nasal cavity, and sinuses (see Ref. [1] and references therein). Consequently, brain fMRI and NMR spectroscopic studies interested in the IFC using, in particular, fast non-spin-echo pulse sequences suffer from signal loss associated with the field inhomogeneity. Recently, signal recovery is found possible by counteracting the magnetic field inhomogeneity through the use of pyrolytic graphite, a highly diamagnetic material [2], held in the mouth of the subject [3,4]. While such passive shimming scheme provides a quick solution, a shimming device with adjustable parameters is desirable. In this work, active shimming using magnetic fields produced by variable free electric currents is being explored.

METHODS AND MATERIALS

Because of the presence of the air cavities, which are 9 ppm less diamagnetic than the tissue, the Zeeman field in the IFC is higher than the rest part the brain. In the present implementation, a shim coil is placed in the mouth of the subject so that they produces negative magnetic field in the IFC. For the image presented below, the shim coil contained two circular, concentric, independent coils (diameter 2.5 cm, 50 turns; 1.7 cm, 80 turns; both wound with 32-gauge magnet wire), which were sandwiched between thermal and electrical insulating thin plastic plates. The shim coil is held naturally between the tongue and the mouth roof, ~3 cm deep from the front teeth. Three B_0 maps were acquired using a spiral pulse sequence [5]: first one with no input current, then one for each coil with a test current. From these maps, the magnetic field generated by unit current of each coil was calculated. The shim currents were then calculated by least-linear-square fitting (SVD) to cancel the first B_0 map.

RESULTS

Figure 1 shows transverse brain images and the associated B_0 maps at the IFC of a healthy volunteer (Zeeman field 1.5 T, echo time 40 ms, slice thickness 5 mm). Notice that, with the mouth shim, the artifact around the cavity is reduced and some signal near the cavity is recovered. In addition, the B_0 field in the brain is much more uniform with the mouth shim.

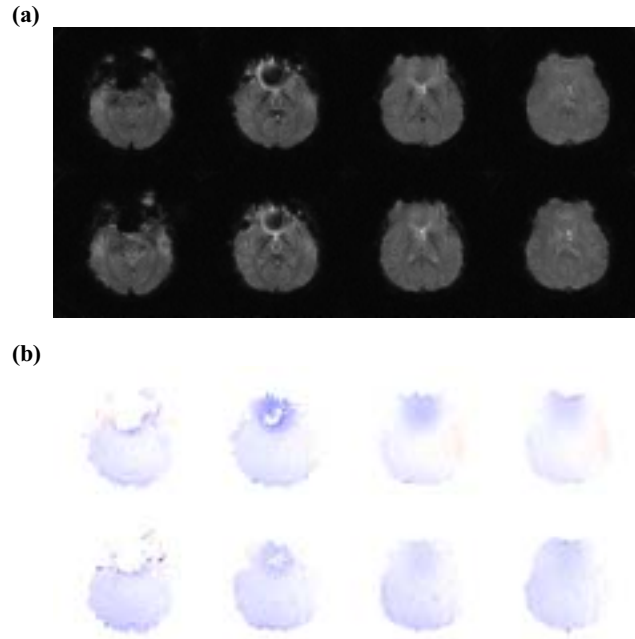


Figure 1: Transverse images (a) and B_0 maps (b) at the human brain IFC without (top row) and with (bottom row) the mouth shim.

CONCLUSIONS

The present active shimming is simple, economical, and effective. The shimming currents can be successfully determined by the proposed algorithm. Computational analysis of the current distribution for optimal shimming as well as testing on fMRI are now in progress.

REFERENCES

1. S. Li, *et al.*, Magn. Reson. Med. **34**, 268 (1995); S. Li, *et al.*, *ibid.* **36**, 705 (1996).
2. M.D. Simon, *et al.*, Am. J. Phys. **69**, 702 (2001).
3. J.L. Wilson, *et al.*, Magn Reson Med **48**, 906 (2002).
4. N. Sobel, personal communication.
5. G.H. Glover and S. Lai, Magn. Reson. Med. **39** (1998).

Cardiovascular **Imaging**

Multi-Coil Cardiac CINE Imaging with “Dixon” Fat-Water Separation and Steady-State Free Precession

Scott B. Reeder, Michael Markl, Jeff C. Hellinger, Huanzhou Yu, Robert J. Herfkens, Norbert J. Pelc

Department of Radiology

PURPOSE

To combine a novel “Dixon” water-fat decomposition technique with CINE steady-state free precession (SSFP) cardiac imaging, to obtain uniform water-fat separation.

MATERIALS AND METHODS:

SSFP is a rapid imaging technique with high SNR and excellent contrast between blood and myocardium, and has gained recent widespread use for cardiac CINE imaging. SSFP is limited by the fact that water and fat both appear bright and are difficult to distinguish, possibly obscuring underlying pathology. Current fat suppression techniques used with cardiac imaging and SSFP are relatively sensitive to B_0 field heterogeneities.

Typical “Dixon” water-fat decomposition techniques[1, 2] are relatively insensitive to field heterogeneities, however, implementation with SSFP cardiac imaging presents several challenges. Short repetition times (TR) are necessary to prevent image degradation resulting from field heterogeneities, as well as “freeze” cardiac motion – these factors limit echo time (TE) increments to small values not used with typical “Dixon” techniques.

To address these challenges, water and fat CINE movies were decomposed with a novel iterative least-squares algorithm that was formulated for fitting data from images acquired at arbitrary (short) TE values. This algorithm requires no phase unwrapping and lends naturally to multi-coil reconstruction.

Image acquisition was performed on a GE 1.5T CVI scanner with a retrospectively ECG-gated CINE SSFP sequence that sequentially obtains sets of CINE images at 3–4 TEs. A phased

array torso coil was used, and imaging parameters were: TE=0.8, 1.7, 2.6ms; TR=4.7–5.0ms; FOV=32cm; slice=8mm; BW=+/-125kHz; $N_x=224$ (partial echo); $N_y=128$; views per segment=16, temporal resolution=16TR=75–80ms. 20 CINE phases were retrospectively reconstructed and breath-hold time was 20s per slice.

RESULTS

CINE water, fat and source movies were obtained in different imaging planes (short axis, axial, 3 and 4 chamber views) from 2 normal volunteers and 4 patients. Excellent fat-water separation was obtained in all images, and distinction between pericardial fat and fluid was well demonstrated in all studies, as was fatty infiltration of the atrial septum of 1 patient.

CONCLUSION

Multi-coil “Dixon” techniques using an iterative least-squares fitting algorithm can be combined with SSFP cardiac CINE imaging to obtain water and fat movies with excellent fat-water separation. This facilitates improved visualization of water and fat structures within and around the heart while retaining the high CNR of SSFP imaging, and has potential for clinical applications that require uniform water-fat separation.

1. Dixon W. Simple proton spectroscopic imaging. *Radiology* 1984;153:189-194
2. Glover G. Multipoint Dixon technique for water and fat proton and susceptibility imaging. *J Magn Reson Imag* 1991; 1:521-530

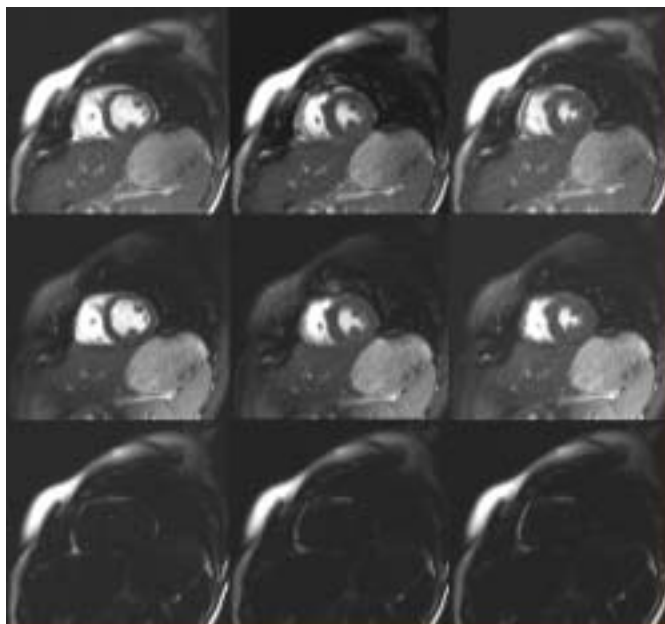


Figure 1: Short axis CINE SSFP cardiac images acquired with torso phased array coil. Source images (top row), calculated water images (middle row) and calculated fat images (bottom row) are shown at three (of 20) phases at end-diastole (left column), mid-systole (middle column), and end-diastole (right column). Uniform fat-water separation was consistently achieved in all slices and phases. Three source images were acquired (TE=0.9, 1.9, 2.9ms) and TR=5.2ms. Image matrix size was 224x128, and bandwidth was ± 125 kHz.

Zhifei Wen¹, Scott Reeder², Angel R. Pineda², Norbert J. Pelc²

Departments of ¹Physics and ²Radiology

INTRODUCTION

In the so-called “Dixon” method for the decomposition of multi-echo data into fat and water, multiple images are acquired at different echo times. Combinations of these images produce fat selective and water selective images. Most typically, three measurements are used to allow calculation of fat and water as well as the local resonance offset. The method can be relatively insensitive to magnetic field inhomogeneities by including the resonance offset in the reconstruction model. An important issue is how it performs in the presence of noise, an aspect that was studied previously only for the case in which only fat or only water was present^[1]. As we show here, this is incomplete since the noise is strongly dependent on the water/fat ratio.

THEORIES AND METHODS

For the symmetric three-point Dixon method (3PD)^[1], the three images are acquired at three evenly spaced time points:

$$S_{-1} = (\rho_1 + \rho_2 e^{-i\theta})e^{-i(\phi-\phi_0)}, S_0 = (\rho_1 + \rho_2)e^{-i\phi_0}, S_1 = (\rho_1 + \rho_2 e^{i\theta})e^{i(\phi-\phi_0)},$$

where ρ_1 and ρ_2 are the water and fat signals, respectively, $\theta = \Delta\omega \cdot \Delta TE$ (water-fat phase incremental angle between two echoes, $\Delta\omega$: water-fat resonance frequency difference, ΔTE : time interval between two echoes), $\phi - \psi \cdot \Delta TE$, (ψ : resonance offset). The analytical solution to the set of equations is given by

$$\rho_{1,2} = S_2' \pm 1/2 \sqrt{S_0'^2 - 2(S_0'^2 - S_1'S_{-1}')/(1 - \cos\theta)} \quad [1]$$

where $S_n' = S_n e^{-i\phi}$. The variance of ρ_1 and ρ_2 can be expressed in terms of σ_0^2 , the variance of the uncorrelated three images, as $\sigma_{\rho_{1,2}}^2 = [(\frac{\partial \rho_{1,2}}{\partial S_{-1}})^2 + (\frac{\partial \rho_{1,2}}{\partial S_0})^2 + (\frac{\partial \rho_{1,2}}{\partial S_1})^2] \sigma_0^2$. The noise performance is described by an SNR-equivalent number of

signals averaged (NSA) as $NSA_{\rho_{1,2}} = \frac{\sigma_0^2}{\sigma_{\rho_{1,2}}^2}$

$$= 4 \{ 1 + [(3 \cos^2 \theta + 2 \cos \theta + 1) \rho_{1,2}^2 + (\cos^2 \theta + 6 \cos \theta + 1) \rho_1 \rho_2 + (-\cos^2 \theta + 2 \cos \theta + 5) \rho_{2,1}^2] / [(\rho_1 - \rho_2)^2 (1 - \cos \theta)^2] \}^{-1}. \quad \{\text{Eqn. 1}\}$$

The dependence of NSA on water and fat contents is evident. NSA vs. q curves from this formula were plotted at different water/fat ratios and compared with Monte-Carlo simulations (Fig. 1). In the simulations, Gaussian noise was added to both (real and imaginary) channels of the signals, which were then sent to the analytic solution for the water and fat densities. This was repeated 10,000 times for each choice of parameters. NSA was calculated as the ratio of the noise variance to the variance of ρ_1 and ρ_2 . A high NSA indicates lower noise and efficient extraction of fat and water information.

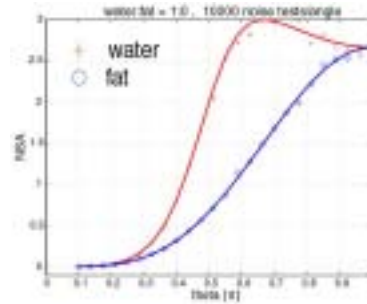


Figure 1: NSA vs. q curves at water: fat = 1:0, 1:0.5 and 1:1.

RESULTS

The simulated NSA agreed quite well with the theoretical predictions from Eqn. 1. The NSA not only depends on the phase incremental angle θ but also on the water/fat ratio. Further, the noise in the fat image is different from that in the water image, with the more dominant species having a higher NSA, especially at smaller θ . If there was only one species (ρ_1), its NSA expression could be simplified to

$$NSA_{\rho_1} = \frac{2(1 - \cos \theta)^2}{1 + 2 \cos^2 \theta}, \text{ in agreement with previous reports}^{[1]}. \text{ In}$$

that case, the maximum NSA occurred at $\theta = 2\pi/3$, uniform spacing of 3 echoes around the full circle. The NSA for both materials decreases as the object becomes less “pure”. An extreme case happens when the amount of water and fat are equal. For any θ not close to π , the NSA approaches zero, while at $\theta = \pi$, the NSA is about 2.7 regardless of the water/fat ratio.

CONCLUSIONS

We’ve shown that the noise in fat and water images computed using the 3PD method can depend strongly on the relative amounts of the species.

REFERENCES

1. Glover. *JMRI* 1991; 1:521-530

Dixon Imaging for Polymethylmethacralate During a Percutaneous Vertebroplasty Procedure

Huanzhou Yu^{1,2}, Rebecca Fahrig², Kim Butts², Arundhuti Ganguly², Elfar Adalsteinsson², Dirk Mayer², Norbert J. Pelc²

Departments of ¹Electrical Engineering and ²Radiology

INTRODUCTION

Percutaneous vertebroplasty (PV) has been found to provide relief from vertebrogenic pain resulting from vertebral compression fracture, where acrylic cement (polymethylmethacralate [PMMA]) is injected into a diseased vertebral body. PV is generally guided using x-ray imaging; however, PMMA is difficult to visualize with x-rays, and MR imaging of PMMA in a hybrid system could improve the guidance of PV. The goal of this work is to develop techniques to depict PMMA in MRI with high sensitivity, so MRI could be used to guide PV.

METHODS AND MATERIALS

Our approach is to use the unique NMR spectrum of PMMA to develop a “Dixon” strategy for PMMA-specific imaging. Similar to Reeder [1], the signal S_n acquired at echo times TE_n in a pixel is modeled as:

$$S_n = (\rho_w + \rho_f e^{i2\pi\Delta f_f TE_n} + \rho_p p(TE_n)) e^{i2\pi\psi TE_n} \quad [1]$$

where, ρ_w , ρ_f , ρ_p are the density of water, fat and PMMA in that pixel, Δf_f is the frequency offset of fat with respect to water, ψ is the local off-resonance frequency of the pixel. Since PMMA has a complex spectrum, we include this in Eqn. 1 in the term $p(t)$, the Fourier Transform of the PMMA spectrum.

ψ will be determined prior to the PMMA injection using an iterative solution to the nonlinear Eqn. 1, and y can be reasonably assumed to be slowly varying over the time. With y known, the signals S_n can be demodulated ($S'_n = S_n / e^{i2\pi\psi TE_n}$) and the problem of estimating ρ_w , ρ_f , ρ_p from signals of three echoes becomes linear and can be written as:

$$\mathbf{S}' = \begin{bmatrix} S'_1 \\ S'_2 \\ S'_3 \end{bmatrix} = \begin{bmatrix} 1 \\ 1 \\ 1 \end{bmatrix} \begin{bmatrix} e^{i2\pi\Delta f_f TE_1} \\ e^{i2\pi\Delta f_f TE_2} \\ e^{i2\pi\Delta f_f TE_3} \end{bmatrix} \begin{bmatrix} p(TE_1) \\ p(TE_2) \\ p(TE_3) \end{bmatrix} \begin{bmatrix} \rho_w \\ \rho_f \\ \rho_p \end{bmatrix} = \mathbf{A}(\mathbf{TE}) \cdot \boldsymbol{\rho} \quad [2]$$

where $\boldsymbol{\rho}$ is a vector containing the unknown densities. When the noise of the images (denoted by \mathbf{n}) is included, the estimated density of the three materials is given by:

$$\hat{\boldsymbol{\rho}} = \mathbf{A}^{-1}(\mathbf{TE}) \cdot (\mathbf{S}' + \mathbf{n}) = \boldsymbol{\rho} + \mathbf{A}^{-1}(\mathbf{TE}) \cdot \mathbf{n} \quad [3]$$

The term $\mathbf{A}^{-1}(\mathbf{TE}) \cdot \mathbf{n}$ represents the error in the estimated $\hat{\boldsymbol{\rho}}$, which is dependent on \mathbf{TE} (the vector of selected echo times

$[TE_1, TE_2, TE_3]$). The relative norm error: $\frac{\|\mathbf{A}^{-1}(\mathbf{TE}) \cdot \mathbf{n}\|}{\|\boldsymbol{\rho}\|} / \frac{\|\mathbf{n}\|}{\|\mathbf{S}'\|}$

is bounded by the condition number of matrix \mathbf{A} [2], represented by $\kappa(\mathbf{A}(\mathbf{TE}))$. An additional consideration is that a short \mathbf{TE} is preferred. Therefore, the optimization problem can be formulated as

$$\text{minimizing: } C(\mathbf{TE}) = \kappa(\mathbf{A}(\mathbf{TE})) + \beta \cdot TE_3$$

subject to: \mathbf{TE} being practically implementable.

Here, $C(\mathbf{TE})$ is the total cost function, TE_3 is the longest echo time, and β controls any possible tradeoff between optimizing SNR and minimizing TE_3 .

We used a global search to find the minimum $C(\mathbf{TE})$. To illustrate the idea, consider the case where the three echoes are equally spaced

so there are two degrees of freedom, the first echo time TE_1 and the increment DTE (this constraint can be easily removed). Fig. 2 shows a plot $1/C(\mathbf{TE})$ vs. TE_1 and ΔTE for $\beta=0.1$, a value gives $\kappa(\mathbf{A}(\mathbf{TE}))$ and TE_3 comparable weight.

The effect of \mathbf{TE} on the quality of the density estimates was studied with computer simulations. Simulated images had Gaussian noise such that the SNR in water, fat and PMMA was 10, 11 and 8 respectively.

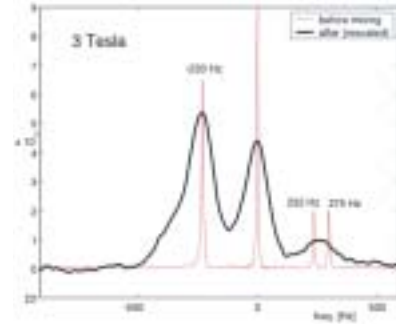


Figure 1: Spectra obtained before and after mixing, demonstrating that the location of the spectral peaks do not change after mixing. This data is shown with respect to water.

RESULTS

Spectra, as well as the T1 and T2, of the PMMA were obtained at 3 Tesla before and after mixing, as shown in Fig 1.

The optimal \mathbf{TE} read from Fig 2 is [13.25, 22.75, 32.25] ms. The phantom and its separation with this optimal \mathbf{TE} and a “bad” \mathbf{TE} are shown in Fig 3. The difference in the separation quality is clearly seen.

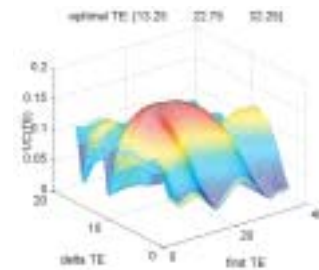


Figure 2: $1/C(\mathbf{TE})$ vs. first echo time and delta TE in the case of $\beta=0.1$. $1/C(\mathbf{TE})$ has a maximum when echo times are 13.25ms, 22.75ms, and 32.25ms

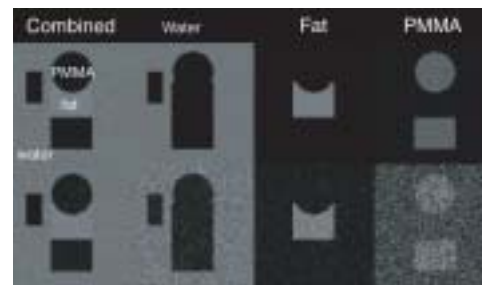


Figure 3: Simulation demonstrating excellent separation results (top row) when optimal echo times of 13.25 ms, 22.75ms, and 32.25ms are used. The second row shows poor separation results with suboptimal echo times of 36ms, 40ms, and 44ms.

CONCLUSIONS

We have shown a modified 3-point Dixon method to image PMMA during a PV procedure. A cost function is formulated, and optimal TEs can be selected with flexible tradeoff between short TE and SNR. With this method, we should be able to achieve a repetition time of 30ms.

REFERENCES

1. Reeder SB, et al. RSNA 2002; *Radiology*; 225(P):284
2. Leon SJ. *Linear Algebra with Applications* (3rd Edition) Macmillan Publishing Company. 1990; 350-354

INTRODUCTION

Some MRI sequences such as perfusion imaging collect data when the magnetization is not in the steady state, causing the signal to vary during acquisition. GRASS EPI sequences exhibit ghosting artifacts in the phase-encoded direction due to the effect of these transients in k-space. We examined these effects using simulations and experiments in sequences with centric phase-encoding order. The artifacts depend on the flip angle, TR, and T1/T2. Furthermore, at high flip angles, the ghost pattern has modulation bands. Phantom experiments verified that, especially at high flip angles, significant artifacts could be observed.

METHODS AND RESULTS

We start by looking at the transient behavior of the transverse magnetization for different values of flip angle, T1, and T2, using the signal equations. GRASS was simulated by averaging the SSFP response over residual phases from 0 to 2 π for flip angles of 8 and 40 degrees, and for different materials. Figure 1 shows the centric k-space acquisition pattern used in both simulations and experiments. The impulse response in the phase-encoded direction was simulated by assigning each measured point an intensity dependent on the RF pulse number (or shot) during which it was acquired. Thus, the signal in each segment varies due to the transient (non steady state) effects. The simulations ignored T2* signal loss during the echo train, i.e. all echoes in each simulated TR had equal signal intensity, but possibly different phase due to off-resonance effects.

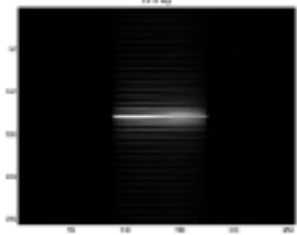


Figure 1: Centric order acquisition scheme.

Experiments were performed on an 18cm diameter spherical phantom using a 1.5T scanner (GE Signa, 40mT/m, 150 mT/m/ms gradients). A conventional fast gradient-echo echo-planar imaging sequence was used with 4 echoes per TR and a 256x256 matrix. (FOV=30cm, BW=125kHz, TR=12ms, TE=1.8ms, 5mm slice). The simulated impulse response was compared to images collected with phase-encoding turned off. 2D images were also collected. Measurements were made on a GE 1.5 T system (40 mT/m, 150 mT/m/ms gradients). A 256x128 matrix with 20cm field of view, 5mm slices, and flip angle of 25° were used. 4 echoes per shot with a 125kHz readout bandwidth and 2.2ms TE were used. TR's of 27 and 54ms were used to evaluate the effects of the doubling.

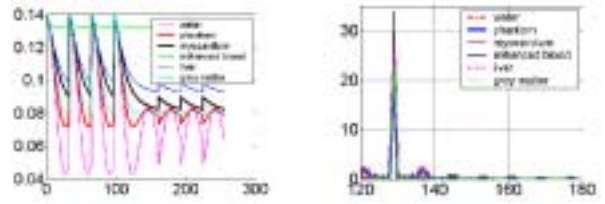


Figure 2. FA=8 deg a) k-space b) impulse response

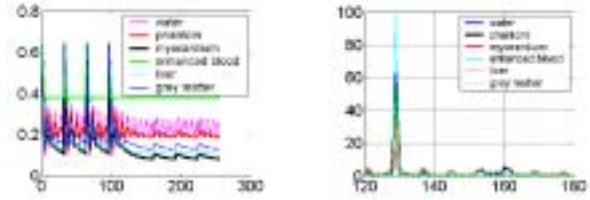


Figure 3. FA=40 deg a) k-space b) impulse response

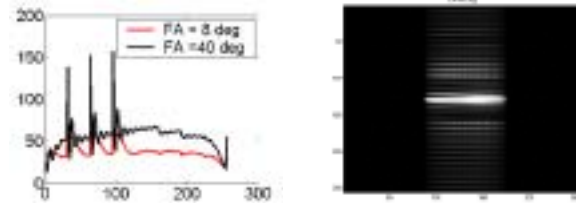


Figure 4. Measured results for FA=8 and 40 deg a) k-space b) images

The simulated impulse response for 4 echoes for different T1's and T2's (figs. 2 and 3) predicts ghosts in the phase-encode direction 8 pixels apart. For longer T1's and T2's, the amplitudes of these ghosts increase due to the faster decay of the transverse signal with pulse number for longer T1's, which leads to larger signal variation in the phase-encode direction. The impulse response is blurred due to signal variation between the positive and negative k-space of the centric phase-encoding order. With the higher flip angle (40 deg), the k-space signal varies more noticeably, and the location of the brightest ghosts is shifted in phase-encode direction. Predicted impulse responses were validated with phantom experiments with phase encoding turned off (fig 4). Good agreement was found.

CONCLUSIONS

The amplitude weighting of the transient response causes ghosts in the phase-encoding direction for multi-shot GRASS EPI. The dynamic nature of these transients, as function of flip angle, T1/T2, and TR, determine the amplitude of these ghosts. Furthermore, a high flip angle modulates the k-space weighting and causes the ghosts to shift in the image. Images of practical sizes with high flip angles readily show the artifacts. Future work should explore other k-space filling patterns to see if the effects can be reduced.

Investigating UNFOLD with Factors Greater Than 2

Calvin Lew^{1,2}, Frandics Chan¹, and Norbert J. Pelc¹

Departments of ¹Radiology and ²Electrical Engineering

INTRODUCTION

In cardiovascular imaging applications, such as perfusion or flow imaging, it is often needed to acquire data at high temporal resolution. UNFOLD can produce an increase in temporal resolution of almost a factor of 2 if half the FOV is known to be less dynamic than the other half. UNFOLD can be extended to a factor $n > 2$ by acquiring $1/n$ of the normal data set in each time frame and shifting the k-space lines from frame to frame. Fig 1 and 2 show UNFOLD at $n=3$ and $n=4$. Note that we expect the central peak to have high temporal dynamics. UNFOLD at these larger factors is difficult because these spectral peaks fall within the spectrum of the ROI. The aliased signal needs to be removed with minimal impact on the dynamic depiction of the unaliased signal. For UNFOLDx4, we must prove 1) UNFOLD x2 with lower temporal resolution is inadequate 2) UNFOLD x4 achieves good suppression of aliased signal and better temporal resolution. We show here that UNFOLD with $n=3$ or $n=4$ follows the high temporal dynamics better than standard UNFOLD at lower temporal resolution but introduce aliasing when the aliased signal dynamics are too great.

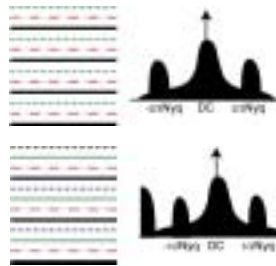


Figure 1. UNFOLD at $n=3$

Figure 2. UNFOLD at $n=4$

METHODS AND RESULTS

A multi-shot gradient-echo echo-planar imaging sequence was used to image perfusion in a patient with no breath holding. The patient was injected with 20cc of gadolinium contrast, and cardiac short-axis slices were collected using 1.5T scanners (GE Signa, 40mT/m, 150 mT/m/ms gradients). 4 echoes were collected per TR using a 256x128 matrix. (FOV=40cm, BW=125kHz, TR=6.6ms, TE=1.2ms, 10mm slice, FA=25 deg). These data were resampled to model acquisitions with reduced FOV or reduced temporal sampling. The cases modeled were 1) UNFOLD x2 with 2x temporal resolution loss, 2) UNFOLD x4 at the original temporal resolution, 3) UNFOLD x3 at the original temporal resolution. The sequence of images for each case was compared to each other and to the original images. The temporal filter passbands were chosen based on the dynamics of an area in the right ventricle. The cutoff frequencies were chosen by iteratively evaluating the image quality at different cutoff points and choosing the “best one”.

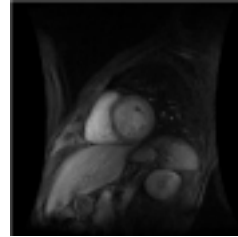


Figure 3. Original image



Figure 4. UNFOLDx3 and difference



Figure 5. UNFOLDx4 and difference

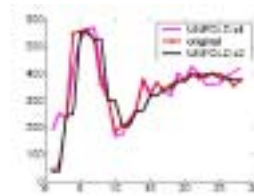


Figure 6. Comparison of UNFOLDx4, Original, and UNFOLD

Fig 3-5 show images of the original, UNFOLDx3 and x4, and difference images. It is observed that, with UNFOLDx4, signals from the edges of the liver and stomach have high temporal dynamics that alias into the center of the FOV, probably due to respiratory effects. However, UNFOLDx4 follows the frame-to-frame movement of the organs better than UNFOLDx2 at half the temporal resolution. A plot of the temporal dynamics for the ROI (fig 6) shows, that in the central part of the dynamics, the x4 case follows the high frequency fluctuations of the ROI better, although there is still ringing at the temporal edges. The x3 case is a balance between the x4 case and UNFOLDx2 at half the temporal resolution. The aliased signal is not as noticeable as in the x4 case.

CONCLUSIONS

UNFOLD with factors of 3 and 4 is feasible and can provide improved temporal dynamics over a limited FOV, but it is not as robust in removing temporal high frequencies of the aliased signal. The clinical areas in which this trade-off may be useful still need to be explored. The aliased signal may be less dynamic in respiratory-held acquisitions.

CARDIOVASCULAR IMAGING

Time Resolved Three Dimensional Phase Contrast MRI (4D-Flow): Visualization of Three-Directional Blood Flow in Healthy Volunteers and Patients

M. Markl¹, F.P. Chan¹, M.T. Alley¹, M.T. Draney², R.J. Herfkens¹, N.J. Pelc¹

Departments of ¹Radiology and ²Mechanical Engineering

INTRODUCTION

Results of examinations with a 4D phase contrast technique that permits spatial and temporal coverage of an entire 3D volume are presented. Visualization of time-resolved three-directional blood flow in healthy volunteers and in clinical applications permits the qualitative and quantitative assessment of blood flow in the aortic outflow tract as well as ascending and descending aorta within a single 4D data set.

METHODS AND MATERIALS

The pulse sequence for 4D-Flow data acquisition consisted of a rf-spoiled gradient echo sequence with velocity encoding along all three spatial directions and a flexible trade-off between temporal resolution and total acquisition time [1]. Time-resolved, three-dimensional anatomical images are generated simultaneously with three directional velocity fields. Measurements were respiratory compensated and retrospectively gated to the ECG cycle in order to generate a CINE series of 3D data sets. The 4D-flow scan was typically performed directly after a MR-Angio to benefit from the contrast agent remaining in the blood pool.

Post processing of the acquired data included fully automated noise filtering and eddy current correction [2]. Noise filtering was based on thresholding the pixel-wise standard deviation of the velocities (std_v) along the temporal domain. Phase offsets due to eddy currents were removed by using std_v to identify static tissue and subtracting offsets determined by a magnitude weighted least square fit of a plane to those regions. In a second step the entire time resolved 3D data set including magnitude and velocity images was loaded into a software package (EnSight, CEI) which offers a variety of image processing options such as magnitude and velocity multi-planar reformation, vector field plots mapped onto selected planes of interest, stream-lines and particle traces [3].

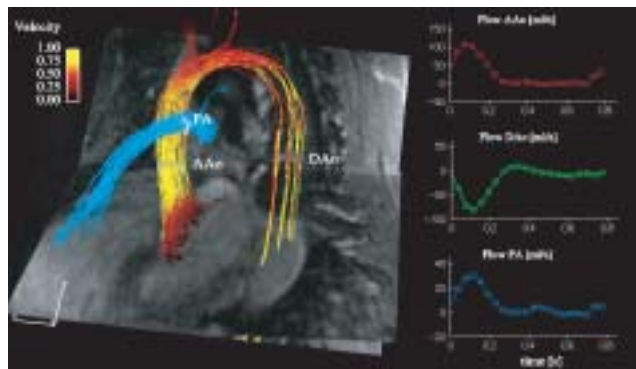


Figure 1: Systolic Stream-lines outlining the aortic outflow tract and the ascending (AAo) and descending aorta (DAo) in a healthy volunteer. The color-coding corresponds to the magnitude of the local systolic blood flow velocity. The pulmonary artery (PA) is depicted by stream-lines with constant color. Time resolved flow rates as a function of cardiac phase within the RR-interval (graphs on the right) were evaluated at different levels in the aorta and pulmonary artery.

Figure 2: Blood flow visualization in a patient with an ascending aortic aneurysm. A: Aortic stream-lines in the entire aorta. The color-coding corresponds to the magnitude of the local systolic blood flow velocity B: Systolic velocity vector fields color coded according to their z-velocity component. Length and orientation of the vectors correspond to magnitude and direction of the local systolic blood flow velocities. For both visualization techniques the zoomed regions demonstrates reverse and circular flow fields within the ascending aortic aneurysm.

RESULTS

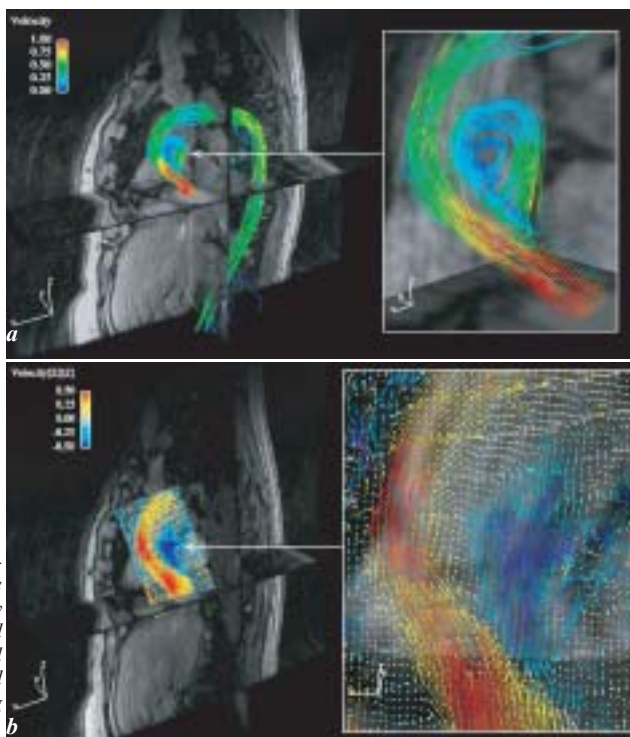
Figure 1 and 2 show exemplary results of processing and visualization strategies in a healthy volunteer and a patient with ascending aortic aneurysm which illustrate the advantage of the complete temporal and spatial coverage available in the 4D data sets. Figure 1 displays blood flow velocities in the entire ascending aorta and large part of the descending aorta which are visualized by stream-lines that reflect traces along the instantaneous velocity vector field in a systolic time frame. In addition, the vessel geometry outlined by the stream-lines could be used to define regions of interest for flow quantification in the ascending aorta, descending aorta and pulmonary artery. The resulting graphs demonstrate typical flow waveforms over the cardiac cycle. Figure 2a displays systolic stream-lines which exhibit reverse and circular flow features within the ascending aortic aneurysm but otherwise normal flow in the aortic arch and descending aorta. Similar features are also visible in systolic color-coded velocity vector fields, reformatted onto a plane transecting the aortic root and ascending aorta (figure 2b)

CONCLUSIONS

The 4D-Flow technique was successfully applied in human studies, covering a true time resolved 3D volume, with flexible control of temporal resolution and scan time. To handle the large number of images and to navigate within the time resolves 3D-volume, advanced data processing and display methods are necessary. Computer-aided analysis tools could successfully be used for efficient data extraction, visualization of normal and pathological blood flow within large parts of the aorta and quantitative analysis of the 4D data sets.

REFERENCES

1. Markl M, et al. *J Magn Reson Imaging* 2003;17:499-506
2. Walker PG, et al. *J Magn Reson Imaging* 1993; 3:521-30
3. Wigstrom L, et al. *Magn Reson Med* 1999; 41:793-9



Generalized Reconstruction of Phase Contrast MRI: Analysis and Correction of the Effect of Gradient Field Distortions

M. Markl¹, R. Bammer¹, M.T. Alley¹, C.J. Elkins², M.T. Draney², M.E. Moseley¹, G. H. Glover¹, N.J. Pelc¹

Departments of ¹Radiology and ²Mechanical Engineering

INTRODUCTION

A generalized model to characterize gradient field non-uniformities and their effect on phase contrast (PC) MRI [1] is presented. Gradient fields deviate not only in nominal strength but also orientation and can introduce errors in strength and direction of velocity encoding. Resulting errors in the measured phase shifts used for velocity quantification can therefore cause significant deviations in velocity quantification. The true magnitude and direction of the velocities can be recovered by a generalized PC reconstruction which requires the acquisition of the full 3-directional velocity information.

METHODS AND MATERIALS

To model spatial imperfections of the magnetic field $B_{z,model}^{(i)}(\mathbf{r})$ produced by the gradient coils along nominal directions $i = x, y, z$ a polynomial model based on a spherical harmonic expansion (using scanner specific parameters) is employed [1,2]. Based on the model local magnetic field gradients $G_{ij,model}(\mathbf{r})$ can be calculated. In this context, As a result the true gradient field demonstrates not only deviations from the nominal gradient strength but also from the nominal gradient direction (figure 1). To account for the deviation of the ideal (spatially constant) gradient field $G_{i,ideal}$ from the actual (modeled) field strength $G_{ij,model}(\mathbf{r})$, relative field deviations $\lambda_{ij}(\mathbf{r}) = G_{ij,model}(\mathbf{r})/G_{i,ideal}$ are introduced. These relative field deviations $\lambda_{ij}(\mathbf{r})$ result in a relative error in the first moments and therefore encoded velocity induced phase shift in phase contrast MRI.

With the ideal first moment \mathbf{M}_1^{ideal} for an ideal arbitrary gradient $\mathbf{G}_{ideal}(\tau)$ the true first moment $\mathbf{M}_1(\mathbf{r})$ can be calculated using the matrix $\mathbf{\Lambda}(\mathbf{r})$ which contains the relative field deviations $\lambda_{ij}(\mathbf{r})$:

$$\mathbf{M}_1(\mathbf{r}) = \int_0^{TE} \mathbf{\Lambda}(\mathbf{r}) \mathbf{G}_{ideal}(\tau) d\tau = \int_0^{TE} \begin{pmatrix} \lambda_{xx}(\mathbf{r}) & \lambda_{xy}(\mathbf{r}) & \lambda_{xz}(\mathbf{r}) \\ \lambda_{yx}(\mathbf{r}) & \lambda_{yy}(\mathbf{r}) & \lambda_{yz}(\mathbf{r}) \\ \lambda_{zx}(\mathbf{r}) & \lambda_{zy}(\mathbf{r}) & \lambda_{zz}(\mathbf{r}) \end{pmatrix} \mathbf{G}_{i,ideal}(\tau) d\tau = \mathbf{\Lambda}(\mathbf{r}) \mathbf{M}_1^{ideal} \quad (1)$$

For a typical phase contrast experiment a phase difference vector $\Delta\Phi(\mathbf{r}) = (\Delta\phi_1(\mathbf{r}), \Delta\phi_2(\mathbf{r}), \dots, \Delta\phi_N(\mathbf{r}))^T$ resulting from velocity encoding along N different directions with nominal velocity sensitivities combined in the encoding matrix $\Omega = (\Delta\mathbf{M}_1^{ideal}, \Delta\mathbf{M}_2^{ideal}, \dots, \Delta\mathbf{M}_N^{ideal})$ can be written as $\Delta\Phi(\mathbf{r}) = \gamma[\mathbf{\Lambda}(\mathbf{r})\Omega]^T \mathbf{v}(\mathbf{r})$. The true velocities can be recovered from the measured phase differences by inverting $[\mathbf{\Lambda}(\mathbf{r})\Omega]^T$ and solving for $\mathbf{v}(\mathbf{r})$:

$$\mathbf{v}(\mathbf{r}) = \frac{1}{\gamma} [\mathbf{\Lambda}(\mathbf{r})\Omega]^{-T} \Delta\Phi(\mathbf{r}). \quad (2)$$

In the general case, the true velocity vector can only be recovered from the phase difference data if at least three-directional velocity encoding ($N=3$) was performed.

For single-direction velocity encoding along \mathbf{n} it is impossible to exactly reconstruct the velocity in the presence of gradient field inhomogeneity. However, an approximate solution may be useful in some cases when the direction error is small or if it can be assumed that the true flow is predominantly along \mathbf{n} :

$$v_n(\mathbf{r}) = \frac{\Delta\phi_1(\mathbf{r})}{\gamma \Delta M_{1,ideal}^{(1)} \sum n_i n_j \Lambda_{ij}} \quad (3)$$

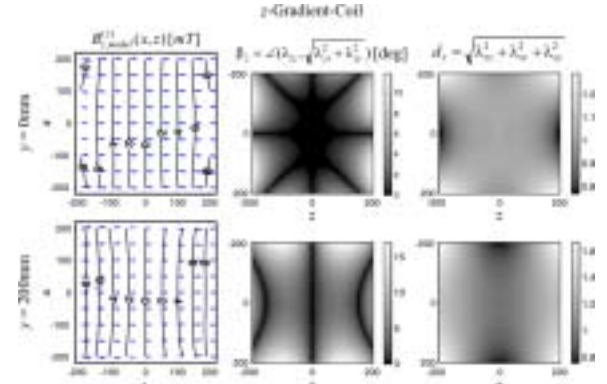


Figure 1: Simulated iso-contours [mT] for the magnetic field $B_{z,model}^{(i)}(x, z)$ generated by the z-gradient coil in coronal planes (FOV=400mm) at $y=0$ mm and 200mm (left column). The overlaid vector fields represent the orientation and strength of the local magnetic field gradients. Angular deviations $q_z(x, z)$ and relative strength variation $d_z(x, z)$ from the nominal gradient field are displayed as gray-scaled images.

RESULTS

Comparisons of standard and generalized reconstruction of 3-directional PC data demonstrate that a gradient field model can be used to compensate for magnitude and angular deviations in first gradient moments and thus velocity encoding (figure 2). The effect on the magnitude strongly depends on the off center location and can be as large as 65% within a (400mm)³ volume. Angular deviations can result in encoding direction errors up to 45°.

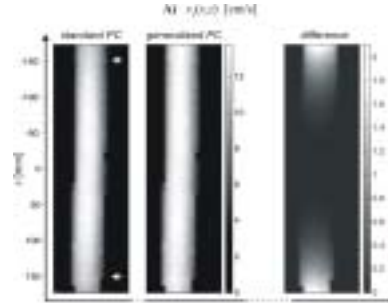


Figure 2: 3D phase contrast MRI with three-directional velocity encoding: Two dimensional intensity plots reflecting velocity profiles in the coronal (x - z) plane for velocities encoded along z . The images show velocity profiles for standard (left, standard PC) and generalized phase contrast reconstruction (middle, generalized PC) as well as the difference between both methods (right).

reconstruction (middle, generalized PC) as well as the difference between both methods (right).

CONCLUSIONS

This study of the effect of gradient field imperfections on strength and orientation of velocity encoding demonstrate the necessity for a more generalized reconstruction of PC-MRI data. In general, accurate reconstruction of magnitude and direction of velocities can be achieved if 3-directional velocity encoding is performed and an appropriate correction that includes the direction error is applied (Eqn. 2). Even though not all gradient field deviations are accounted for by the approximate correction (Eqn. 3) and some encoding error remains, significant improvement can be achieved if compared to the uncorrected data.

REFERENCES

1. Pelc NJ, et al. *Magn Reson Q* 1991; 7:229-54
2. Romeo F, et al. *Magn Reson Med* 1984; 1:44-65
3. Glover GH, Pelc NJ. Method for correcting image distortions due to gradient nonuniformity. U.S. patent 4.591.789. 1996

INTRODUCTION

An analysis of the effect of flow on 2D fully balanced Steady State Free Precession (SSFP) [1] imaging was performed. Transient and steady-state SSFP signal intensities in the presence of steady and pulsatile flow were simulated and compared to phantom measurements. For accurate modeling of SSFP signal intensities it is crucial to include properties such as imperfect slice profiles (i.e. non-constant flip angles across the slice) and, more importantly, ‘out-of-slice’ contributions to the signal. Both simulations and experiments show that there can be considerable flow related changes in SSFP signal intensity resulting from frequency-dependent signal contributions from flowing spins that have already left the slice but still influence the SSFP signal.

METHODS AND MATERIALS

SSFP signal intensities were simulated using a matrix formalism based on the Bloch equations [2,3]. Modeling of in-flow was performed by subdividing the imaging slice into thin sub-slices and, for each TR, shifting the magnetization vectors according to spin motion. The total SSFP signal intensity in each TR was calculated by forming the complex sum over all sub-slices. Flow phantom experiments with a purposely misbalanced gradient axis (to create spatially dependent frequency offsets) were performed to analyze the sensitivity of the SSFP signal to in-flow effects as a function of off-resonance (figure 1).

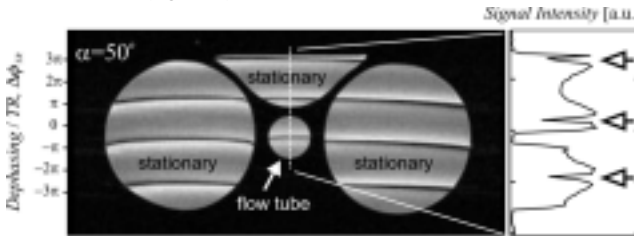


Figure 1: SSFP images of the experimental setup. The flow tube in the center (solid arrow) is surrounded by static objects. Purposely introduced frequency offsets result in equally spaced banding artifacts (signal drop-off, open arrows) corresponding to dephasing/TR of odd multiples of p .

RESULTS

Simulations and experiments showed significant (up to five fold) flow related changes in SSFP signal near banding artifacts while on-resonance regions exhibited only slight changes.

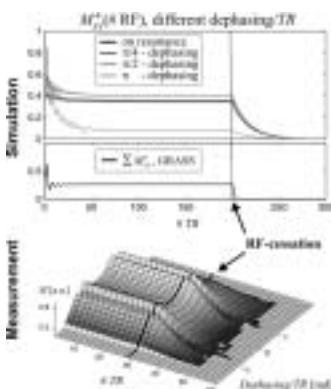


Figure 2: Simulated and measured SSFP signal evolution for RF-cessation and continued gradient activity

To investigate the origin of those signal changes the evolution of magnetization in a static object with paused rf-excitation but continued gradient activity was analyzed (figure 2). For standard sequences the signal is expected to cease once rf-excitation ends. With SSFP this is not the case and a T2*-dependent persistence of the SSFP signal even after rf-cessation was observed. On the other hand, GRASS type pulse sequences decay much faster since complex averaging of spins with different phases quickly reduces signal contributions after suspended RF-excitation. Similarly, spins flowing out of the slice do not experience additional rf-excitation, but gradient activity is not confined to the region of excitations. Remaining transversal ‘out-of-slice’ magnetization can thus still contribute to the total SSFP signal, effectively by broadening the slice thickness.

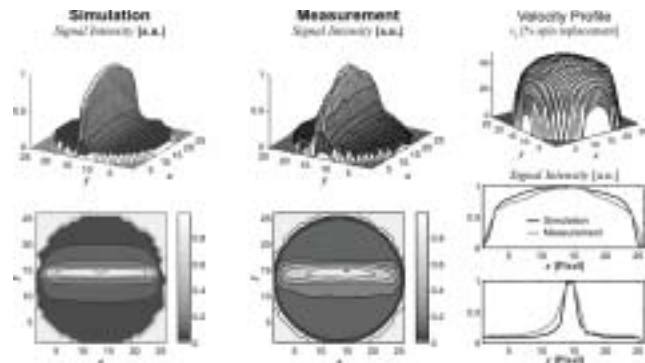


Figure 3: Comparison of measured and simulated signal intensities in the flow tube for steady flow. Top right: measured velocity profile used for simulations. Note the strong signal enhancement at the tube center.

To validate the simulation, detailed comparisons for pixel wise signal intensities (figure 3) were performed. and characteristic features of the signal enhancement patterns could be reproduced by the simulations with high accuracy. By contrast, simulations that exclude the ‘out-of-slice’ phenomenon were unable to reproduce signal variations observed in the experiments. In addition, excellent agreement was seen for pulsatile flow. On-resonance spins mostly remain in a steady state while signal originating from regions at or near the band demonstrate large cyclic signal changes with the same periodicity as the in-flow waveform.

CONCLUSIONS

Excellent agreement between theory and measurement validate the computer simulations and assumptions of the factors that contribute to the in-flow effects of SSFP and verify that SSFP imaging has considerable flow related signal changes which are strongly dependent on off-resonance effects. It is essential to include ‘out-of-slice’ contribution into the simulation process to permit a correct description of the influence of flow onto the SSFP signal. These contributions effectively increase slice thickness non-uniformly as a function of local through plane velocity and frequency offset. Implications for SSFP imaging in humans therefore include frequency offset dependent in-flow enhancement with a concomitant sensitivity to flow artifacts

REFERENCES

1. Carr HY. *Physical Review* 1958;112:1693-1701,
2. Scheffler K. *Concepts in Magnetic Resonance* 1999;11:291-304
3. Hargreaves BA, et al. *Magn Reson Med* 2001; 46:149-58

A Method For MR Eddy Current Characterization And Compensation

M. T. Alley, A. R. Pineda, R. Bammer, M. Markl, N. J. Pelc

Department of Radiology

INTRODUCTION

Magnetic Resonance (MR) imaging systems produce unwanted residual fields during normal operation. Usually referred to as eddy currents, these induced fields cause unintended phase effects that can increase dramatically with the strength and slew rate of the active gradients.¹ In phase contrast imaging, eddy currents produce a spatially varying background phase that affects the accuracy of velocity and flow measurements. While many systems are equipped with compensation mechanisms, it is generally not possible to eliminate all residual phase effects from the subsequent eddy current activity. Using an impulse-response formalism, we show that it is possible to characterize the system so that given the appropriate timing parameters of a particular sequence the resulting eddy current effects can be greatly reduced.

METHODS AND MATERIALS

The characterization procedure consists of three steps. In the first step the eddy current characteristics of a particular scanner are measured through the use of a sequence with a known gradient stimulus. In the second step the collected data are used to produce a mathematical characterization of the eddy current activity. This is done by modeling the field produced by the gradient impulse as $B(t, \mathbf{x}) = i(t) * h(t, \mathbf{x})$, where $i(t)$ represents the gradient input and $h(t, \mathbf{x})$ is the impulse response kernel. The function $h(t, \mathbf{x})$ is expressed as a sum of Laguerre polynomials in the time domain with coefficients comprised of sums of solid spherical harmonics in the spatial domain. The accumulated phase $f(t, \mathbf{x})$ is then the time integral of the field $B(t, \mathbf{x})$. The coefficients of $h(t, \mathbf{x})$ are determined through a least-squares fit of $f(t, \mathbf{x})$. The final step in the process involves using the kernel $h(t, \mathbf{x})$ to predict the eddy current activity of an arbitrary sequence given the parameters of the gradients used within that sequence.

As a test of the predictive ability of this technique, 2D phase contrast data were acquired from a stationary phantom using a commercial sequence and a velocity-encoding value of 10 cm/s, 43 days after acquisition of the impulse response data. The eddy current induced phase was predicted from the modeled $h(t, \mathbf{x})$ and the timing and amplitude of the velocity encoding gradients and then removed on a pixel by pixel basis.

RESULTS

The image on the left in Figure 1 shows the typical shading from the residual eddy currents in a phase contrast sequence. The predicted phase map from the model is shown in the center, and the final corrected image is shown on the right. For this particular image the correction has reduced the absolute value of the residual phase (expressed in terms of the velocity encoding value) from 3.6 ± 2.9 cm/s to 0.36 ± 0.31 cm/s

CONCLUSIONS

Because the approach described here can address non-linear eddy currents it is amenable to corrections that are not possible using gradient pre-emphasis filters alone. Once the model coefficients are determined the correction can be fully automated, thus eliminating the need for baseline scans prior to individual studies.

REFERENCES

1. Ahn CB, Cho ZH, *Magn Reson Med* 1991; 17:149-163



Figure 1: The correction process involves subtracting the predicted phase map (center image) from the uncompensated phase contrast image (left). The final result (right) shows very little shading in the signal.

Comparison of Flow Patterns from CFD and MRI in a Bypass Graft Model

Joy P. Ku¹, Christopher J. Elkins², Michael Markl³, Charles A. Taylor^{2,4}

¹Department of Electrical Engineering, ²Department of Mechanical Engineering, ³Department of Radiology,

⁴Department of Surgery

INTRODUCTION

Taylor, *et al.* have described the use of computational fluid dynamics (CFD) in a simulation-based medical planning system that enables the preoperative assessment of alternate treatment plans for vascular disease [1]. In order to apply these computational methods, they must be validated against direct experimental measurements. No studies have validated the flow patterns predicted by these methods for the more complex geometry of a stenotic vessel with a bypass graft under conditions that are suitable for surgical planning purposes. This *in vitro* study undertakes this task, comparing the flow patterns predicted by the numerical simulations against those measured using magnetic resonance imaging (MRI) for this more complex geometry.

METHODS AND MATERIALS

A phantom model was constructed using stereolithography [2]. The model consisted of a host vessel with a 75% stenosis and a bypass graft attached both proximally and distally to the stenosis [3], as shown in Figure 1. The fluid used in this experiment was a mixture of glycerol, distilled water, and gadolinium, and a custom blood flow pump was used to generate a pulsatile flow waveform at the inlet of the model.

The phantom was placed inside of a head coil. Magnetic resonance angiography (MRA) provided the volumetric data for the numerical simulations, while a two-dimensional (2D) cine phase-contrast magnetic resonance imaging (PC-MRI) sequence, customized to shorten TR values by improving gradient heating calculations and allowing for a variable bandwidth for a given spatial resolution, was used to measure the three components of velocity at the planes indicated in Figure 1. The grad-warp corrected MRA data [4] was used to construct a solid model and finite element mesh, as described in [5], and the PC-MRI measured velocities were mapped onto the mesh inlet [6].

A no-slip boundary condition was applied to the walls and the outlet pressure was set to zero. The fluid was modeled as incompressible and Newtonian with a viscosity of 0.036 dynes-s/cm² and a density of 1.1 g/mL, matching the measured values. The walls were assumed to be rigid. Under these boundary conditions and assumptions, pulsatile flow was computed for 25 cycles using a previously validated finite element method [7]. The numerically computed velocities were then temporally averaged over cycles 16 to 23 and spatially averaged over 5 slices that spanned a distance of 5 mm, matching the thickness of the PC-MRI slice.

RESULTS

The temporally and spatially averaged velocities from the simulations were compared against the PC-MRI-acquired velocities at three locations, as indicated in Figure 1: in the aorta (B), outlet (C), and graft (D). Figure 2 shows isocontours of the through-plane velocities at these locations at time points corresponding to the maximum and minimum flows. The Womersley number was 17.0, and based on the average inlet velocity, the Reynolds' number (Re) was 766. The magnitudes and shapes of the isocontours at these locations were similar, with the best agreement occurring in the aorta.

CONCLUSIONS

This experiment demonstrated that averaging of the simulation results was needed in order to fairly compare them against PC-MRI measurements, which represent data from multiple cycles and from a finite volume. With the post-processing, good agreement was obtained between the velocity patterns measured using PC-MRI and those generated by the CFD methods. The results presented in this investigation

are promising, and future work would extend these comparisons to *in vivo* experiments.

ACKNOWLEDGEMENTS

Many thanks to Gilbert Palafox and Dr. Ryan Wicker (University of Texas at El Paso) for constructing the phantom model. Research support was provided by an American Heart Association Predoctoral Fellowship (Ku), NSF ACI-0205741, the Lucas Foundation and NIH P41RR09784.

REFERENCES

1. Taylor CA, et al. *Computer Aided Surgery* 1999; 4: 231-247
2. Elkins CJ, Eaton JK, Wicker RB. *Proceedings, 4th ASME / JSME Joint Fluids Engineering Conference*, Honolulu, Hawai'i, 2003
3. Palafox GN, Wicker RB, Elkins CJ. *Proceedings, 2003 ASME Summer Bioengineering Meeting*, Key Biscayne, Florida
4. Draney MT, et al. *Proceedings, International Society for Magnetic Resonance in Medicine (ISMRM) Tenth Scientific Meeting and Exhibition, ISMRM*, Honolulu, Hawai'i, 2002; 3:151
5. Ku JP, et al. *Annals of Biomedical Engineering* 2002; 30:743-752
6. Wilson NM. *Geometric Algorithms and Software Architecture for Computational Prototyping: Applications in Vascular Surgery and MEMS*. Ph.D. thesis, Stanford University, 2002
7. Taylor CA, Hughes TJR, Zarins CK. *Computer Methods in Applied Mechanics and Engineering* 1998; 158:155-196

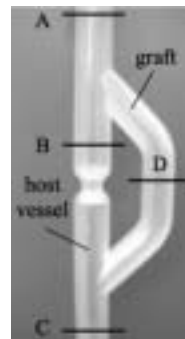


Figure 1: Phantom model used in the experiment. Inlet velocities are prescribed upstream (A) and comparisons of flow patterns are made at planes B (aorta), C (outlet), and D (graft).

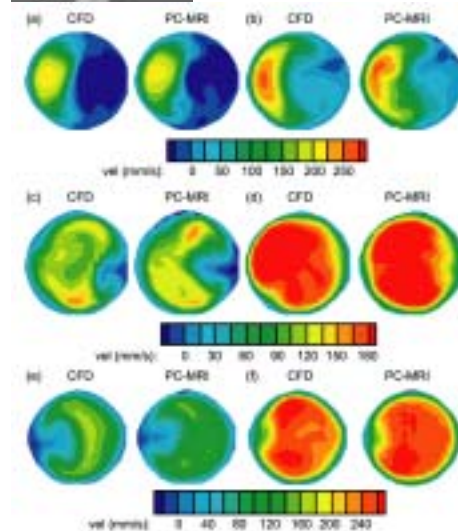


Figure 2: Comparison of isocontours of through-plane velocities in the aorta (plane B) at (a) minimum flow and at (b) maximum flow. (c) and (d) compare results in the bypass (plane D) at the minimum and maximum flow time points respectively, while (e) and (f) are comparisons at the outlet (plane C) at the minimum and maximum flow time points respectively.

Image-Based Computational Blood Flow Modeling as Applied to Unilateral Pulmonary Arterial Stenosis

Ryan L. Spilker¹, Mary T. Draney¹, Michael Markl², Robert J. Herfkens², Jeffrey A. Feinstein³, and Charles A. Taylor^{1,4}

Departments of ¹Mechanical Engineering, ²Radiology, ³Pediatrics, and ⁴Surgery

INTRODUCTION

Computational blood flow modeling holds great promise for the planning of treatments for congenital and acquired cardiovascular diseases [1]. Accurate prediction of changes in hemodynamic conditions including flow distribution with simulated interventions will enable evaluation of alternative treatments and lead to better-informed decisions. The goal of our research is to simulate blood flow in subject-specific models of the pulmonary arteries that consist of a one-dimensional finite element model of the proximal pulmonary arteries created from MRA data and calculation of the terminal impedance of the branch vessels included in the 1D finite element model using morphometric data. We have developed an experiment to apply this approach to the case of acute unilateral pulmonary arterial stenosis in a porcine model.

METHODS AND MATERIALS

Anatomic data for the porcine pulmonary arteries is obtained using contrast-enhanced magnetic resonance angiography with a 1.5 T MRI system. Cine phase contrast MRI (4D-Flow) is used to obtain velocity information throughout the cardiac cycle for a volume including the MPA, RPA, and LPA [2]. These data are supplemented, in some cases, by through-plane cine phase-contrast MRI. A geometric model of the resolvable pulmonary arterial anatomy is created from each set of MRA data using custom image segmentation and geometric modeling procedures. A set of human pulmonary morphometric data, based on the diameter-defined Strahler ordering system, is used to generate a downstream arterial tree for each outlet of the geometric model [3]. An impedance boundary condition for each outlet of the finite element model is computed from each of these trees using the characteristic impedance from Womersley's solution for pulsatile flow in an elastic tube. The flow calculations and pressure measurements, at the locations shown in figure 1, are performed both with and without an acutely created unilateral pulmonary stenosis.

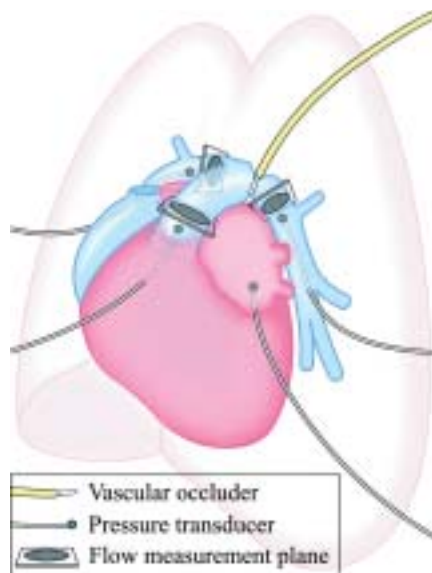


Figure 1: Experimental protocol for porcine validation study.

RESULTS

A geometric model of the proximal pulmonary arteries for one pig is shown in figure 2, along with a morphometry-based arterial tree. In the blood flow simulation, flow, measured with PC-MRI when no stenosis was present, was prescribed at the MPA and morphometry-based impedance was prescribed at each outlet. 4D-Flow showed that the left lung received 57% of the pulmonary blood flow when the RPA was left in its original state and 85% when a stenosis was induced. The simulations predicted values of 58% and 84%, respectively. Predicted pressures exceeded measured pressures and could be corrected by tuning the morphometry-based trees for the measured preoperative pressures in a surgical planning situation.

CONCLUSIONS

The ability of magnetic resonance imaging to noninvasively acquire vascular anatomy and time-resolved blood velocity has enabled its union with computational fluid dynamics for predictive medicine. The goal of this ongoing study is to develop techniques to use patient-specific diagnostic imaging data for simulation-based treatment planning, leveraging the advances in both MRI and CFD. Preliminary results from our model and experiment indicate that outlet boundary conditions from morphometry-based trees provide an appropriate representation of the pulmonary arteries that cannot be resolved from MRA.

REFERENCES

1. Taylor CA, et al. *Comput Aided Surg* 1999; 4:231-247
2. Markl M, et al. *J Magn Reson Imag* 2003; 17:499-506
3. Huang W, et al. *J Appl Physiol* 1996; 81:2123-33

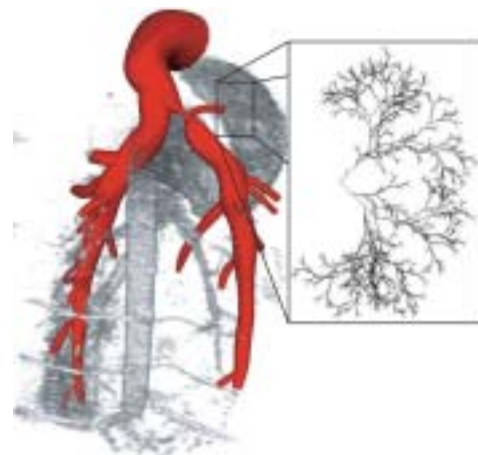


Figure 2: Geometric model of the porcine pulmonary arteries with volume-rendered CE-MRA data and a diagram of 6 generations of a morphometry-based tree.

MR Spectroscopy

Novel Spectral-Spatial RF Pulse Designs for *in vivo* Measurement of Extraction Fraction (EF) and Single-Kidney GFR (skGFR)

Yakir Levin^{1,2}, Daniel Spielman¹, Lawrence Chow², F. Graham Sommer²

¹Departments of Electrical Engineering and ²Radiology

INTRODUCTION

Determination of glomerular filtration rate (GFR) is very helpful in the diagnosis and evaluation of renal disease by providing information about kidney function, which may be impaired even if other measurements, such as fluid and electrolyte balance obtained from a urine test, are normal¹. Current methods for GFR estimation suffer from one or more of the following limitations: consistent overestimation or underestimation of the actual value; duration and expense of the test; invasiveness of the measurement procedure; measurement of composite GFR of both kidneys, not skGFR². We have investigated a method for determining skGFR rate using Gadolinium-DTPA (Gd-DTPA) as a filtration marker is presented. T_1 measurements in blood both before and after filtration by the kidney allow for determination of Gd concentrations in the blood and therefore filtration fraction^{2,3}. Subsequent measurement of renal blood flow and hematocrit allow for determination of skGFR. While initial patient studies were quite promising, additional improvements are needed to develop a more accurate and robust clinical tool. One important improvement is the use of flow-compensated RF pulses to minimize vascular flow artifacts.

METHODS AND MATERIALS

Using the analysis tools developed by Fredrickson et al³, we designed first-order flow-compensated spectral spatial pulses by playing RF only during the positive lobes of the slice-selection gradient while doubling the gradient modulation frequency in order to maintain the spectral bandwidth necessary for retaining good fat suppression properties. While this flow-compensated design is very effective in eliminating signal losses arising from constant velocity blood flow, signal losses from higher order moments (e.g. acceleration, jerk, etc), are not corrected. As has been shown repeatedly in MR angiography, the most effective method of minimizing higher order moments is to reduce the echo time; this

can be achieved using minimum phase pulses⁵. We thus implemented both linear and minimum phase spectral-spatial RF pulses for use in a renal function MR examination.

RESULTS

Fig 1 shows RF and gradient waveforms corresponding to the new spectral-spatial pulses. All spectral-spatial pulses were designed to achieve a minimum slice thickness ≤ 5 mm with TE's ranging from 4 to 8.5 msec. for the uncompensated linear phase, flow compensated linear phase, uncompensated minimum phase, and flow compensated minimum phase designs respectively.

CONCLUSIONS

Both linear and minimum phase flow-compensated RF pulses were successfully designed. In general, minimum phase pulse designs tradeoff a short echo time for some signal loss due to a slightly nonlinear through-slice phase profile. Whether this signal loss is compensated by the gain associated with the decreased TE and flow compensation depends on the blood flow patterns in the particular vessels of interest. Thus, validation and optimization studies on normal volunteers and patients suffering from chronic renal ischemia are ongoing.

REFERENCES

1. Rose BD. *Clinical Physiology of Acid-Base and Electrolyte Disorders*. McGraw-Hill, Inc. 1994 pp. 47-58
2. Niendorf ER, et al. *Radiology* 206:3 791-798.
3. Dumoulin CL, et al. *Mag Res Med* 32:3 370-378.
4. Fredrickson JO, Meyer C, Pelc NJ. Flow effects of spectral spatial excitation. ISMRM. 1997. Vancouver, B.C.
5. Pauly JM, et al. Parameter relations for the Shinnar-LeRoux selective excitation pulse design algorithm. *IEEE Trans. Medical Imaging* 1991; 10:53-65.

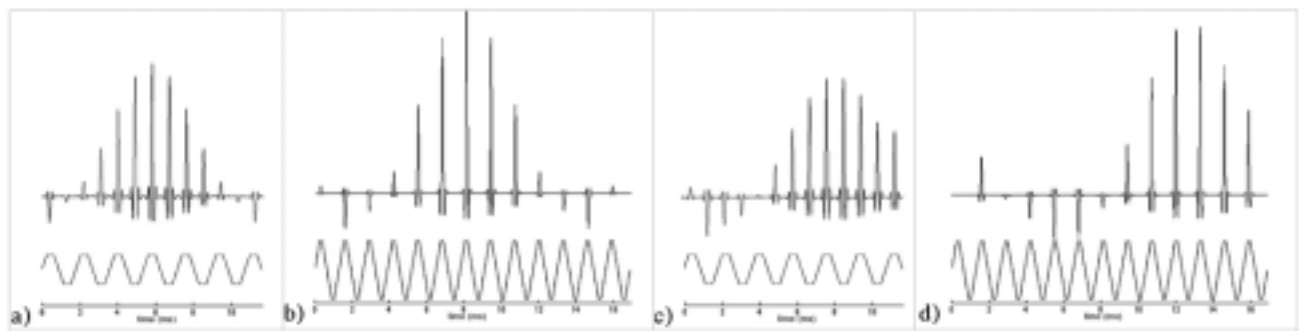


Figure 1: Various spectral-spatial RF pulse designs. (a) linear phase design, (b) flow-compensated linear phase design, (c) minimum phase design, and (d) flow-compensated minimum phase design. All pulses are designed for 5mm slices and have minimum TEs of 5.9 ms, 8.5 ms, 4.0 ms, and 4.5 ms respectively.

INTRODUCTION

Two-dimensional correlation spectroscopy improves the spectral information and signal separation, but is time consuming, especially if combined with 2D spectroscopic imaging (SI) to correlation peak imaging (CPI) [1]. One remedy is to use fast SI techniques, e.g., echo planar based sequences [2] or spectroscopic U-FLARE [3]. The latter allows for effective homonuclear decoupling in both frequency domains, but has an inherent loss in signal-to-noise ratio (SNR) due to the occurrence of two echo families within the train of RF refocused echoes.

The purpose of this work was to combine 2D correlation spectroscopy with spectroscopic RARE [4] as the total transverse magnetization is detected in this recently proposed sequence while complete effective decoupling is still possible. Circularly reduced chemical shift (CS) encoding was used to reduce the minimum total measurement time (T_{\min}).

METHODS AND MATERIALS

All measurements were performed on a 4.7 T/40 cm Bruker Biospec system and anaesthetized female Wistar rats were used for *in vivo* experiments.

In the implemented pulse sequence [exc. - $(t_{c1} - t_1)/2$ - 180° - $(t_{c1} + t_1)/2$ - 90° - $(t_{c2} - t_2)/2$ - 180° - $(t_{c2} + t_2)/2$ - RARE] the signal excitation was performed by a CS selective hard pulse sequence 1-2 τ -5.4- τ -5.4-2 τ -1 with $\tau = 1.25$ ms ($\alpha_{\text{exc}} \approx 79^\circ$). As the first refocusing pulse was also frequency selective (FWHM = 500 Hz) the spectral width in f_1 was 449.5 Hz while it was 899 Hz in f_2 . In circular CS encoding the encoding steps are restricted to: $(t_1^2 + t_2^2)^{0.5} \leq t_{\max}$. With $t_{\max} = 16.68$ ms the total number of CS encoding steps was 1407. Complete effective decoupling is achieved by keeping the time intervals between excitation and mixing (t_{c1}) and between mixing and start of the imaging sequence (t_{c2}) constant. The evolution times t_{c1} (100 ms) and t_{c2} (50 ms) were optimized according to the spin systems of *myo*-inositol (Ins) and taurine (Tau). Within the RARE module for localization in the *xy*-plane 4 \times 16 echoes were acquired within a train of rectangular 180° -pulses (140 μ s) using a four-step phase cycle (xyxy) to compensate for B_1 inhomogeneities. Hence, each four consecutive echoes were phase encoded uniformly (FOV_{PE} = 48 mm). Localization in the third spatial dimension was carried out by the mixing pulse which selected a 5 mm slice in *z* leading to a nominal resolution of 3 \times 3 \times 5 mm³. Total measurement time was 35 min (TR = 1.5 s).

RESULTS

The correlation map (Fig. 1a) from a single voxel of a spherical Ins phantom shows the effect of complete effective decoupling as both diagonal and cross peaks from [2]CH and [5]CH resonances are detected as single lines. The CPI image obtained by evaluation of the cross peak at (3.28, 3.62) ppm is shown in Fig 1b. The contour plot (Fig. 2a) from a single voxel of the healthy rat brain demonstrates the improved spectral resolution of correlation spectroscopy as cross peak signals of Ins and Tau are clearly separated. The spatial distribution of Tau (cross peak at (3.27, 3.44) ppm) in the brain is shown in Fig. 2b. Only the central 24 \times 24 mm² of the FOV are displayed.

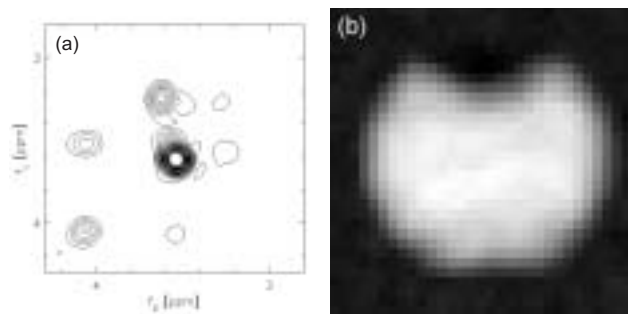


Figure 1: (a) Correlation map from a single voxel and (b) CPI image (Ins cross peak at (3.28, 3.62) ppm) of a spherical phantom.

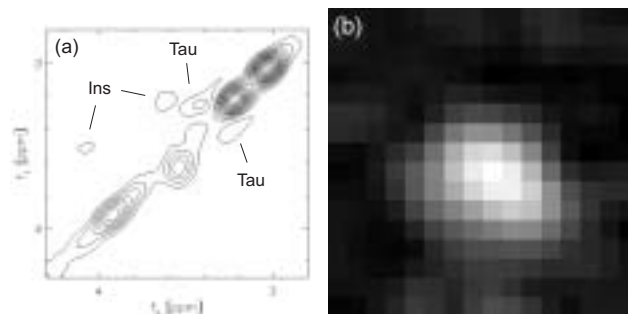


Figure 2: (a) Correlation map from a single voxel and (b) CPI image Tau cross peak at (3.27, 3.43) ppm) of a healthy rat brain.

CONCLUSIONS

The presented data show the feasibility of the combination of 2D correlation spectroscopy and fast spectroscopic RARE. In the *in vivo* application of the method it was possible to separate cross peak signals from Ins and Tau within 35 min.

REFERENCES

1. Metzler A et al. *PNAS USA* 1995; 92:11912-11915
2. Mayer D et al. *Magn Reson Med* 2000; 44:23-28
3. Mayer D et al. *Magn Reson Med* 2003; 49:810-816
4. Dreher W, Leibfritz D. *Magn Reson Med* 2002; 47:523-528

RF Refocused Echo Amplitudes of J-Coupled Spin Systems: Effects on RARE-Based Spectroscopic Imaging Sequences

Dirk Mayer¹, Wolfgang Dreher², Dieter Leibfritz², Daniel M. Spielman¹¹Department of Radiology, ²Department of Biology/Chemistry, University of Bremen, Germany

INTRODUCTION

It has been shown that the signal modulation due to J-coupling in rapid acquisition with relaxation enhancement (RARE) experiments is suppressed by a rapid series of 180°-pulses if the inverse of the pulse interval (Δt_p) is large compared to both the chemical shift difference ($\Delta\delta$) of the coupled spins and the coupling constant ("fast pulse regime") [1,2]. The fact that there is no apparent difference in the spatial impulse response in read-out and phase encoding (PE) directions in spectroscopic ultrafast low-angle RARE (U-FLARE) experiments on phantoms even if $\Delta\delta$ is larger than $1/\Delta t_p$ (cf. Fig. 2b), indicates a completely different signal behavior. In this work, the echo amplitudes for complex spin systems in a series of RF refocused echoes are calculated and the dependence on the flip angles and pulse interval are examined.

METHODS AND MATERIALS

The echo amplitudes (pulse sequence: $\alpha_{exc} - (TE/2 - \alpha_{ref} - TE/2 - echo)^n$) were calculated using the GAMMA NMR simulation library [3]. To simulate the effect of pathway-selection gradient pulses, the calculated signal is averaged over a number of spin systems with different B_0 offsets. Simulations have been performed for spin systems of metabolites detectable in the brain. No relaxation effects have been taken into account. The simulations were complemented by measurements carried out on a 4.7 T Bruker Biospec system.

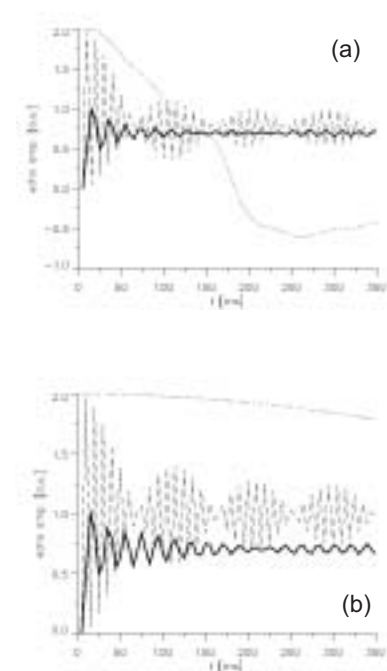


Figure 1: (a) Echo amplitudes for Glu (⁴CH₂) with an α_{ref} of 90° (solid), 170° (dashed), and 180° (dotted). (b) Same as (a) but for Tau (¹CH₂).

RESULTS

Figure 1 shows the real part of the first 70 echo amplitudes ($TE = 5$ ms) simulated for both the ⁴CH₂ resonance of glutamate (Glu) and the ¹CH₂ resonance of taurine (Tau) with an α_{ref} of 90° and 170°, respectively. Also shown are the echo amplitudes for a RARE experiment with $\alpha_{ref} = 180^\circ$. For lower flip angles ($\alpha_{ref} < 180^\circ$) the signal oscillates around a constant value > 0 . The mean value and amplitude of the oscillation depend on α_{ref} and TE.

A similar signal behavior can be seen in the echo amplitudes calculated for the ³CH₃ resonance of alanine (Ala) in Fig. 2a. The $\Delta\delta$ of 460 Hz is larger than $(5\text{ms})^{-1}$ and the RARE signal is clearly J-modulated. As slice selective Gaussian RF pulses are usually used for refocusing in the implementation of spectroscopic U-FLARE, there is a flip angle distribution over the measured slice. The solid line in Fig. 2a was calculated by integrating over a Gaussian distribution of flip angles (3 mm FWHM, 31 points between ± 3.4 mm, $\alpha_{max} = 135^\circ$). The metabolic image of the Ala phantom in Fig. 2b (spectroscopic U-FLARE, $\alpha_{ref} = 135^\circ$) has the same spatial resolution in read-out and PE direction. This demonstrates in agreement with the simulated data that the spatial impulse response in PE direction is not affected by the signal modulation caused by J-coupling although $\Delta\delta > 1/TE$.

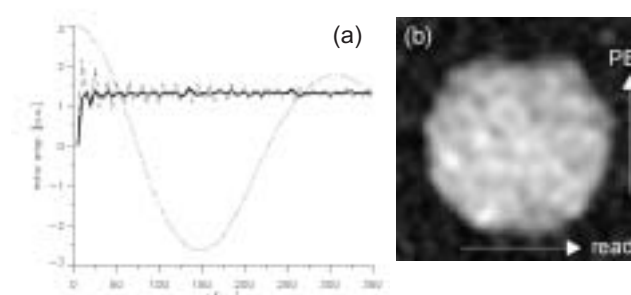


Figure 2: (a) Echo amplitudes for Ala (³CH₃) with $\alpha_{ref} = 135^\circ$ (dashed), 180° (dotted), and integrated over a Gaussian distribution of flip angles with a maximum α_{ref} of 135° (solid). (b) Metabolic image of the central slice from a spherical Ala phantom acquired with spectroscopic U-FLARE.

CONCLUSIONS

The presented data show that for $\alpha_{ref} < 180^\circ$ the echo amplitudes oscillate around a constant value > 0 even if $\Delta\delta > 1/TE$. Therefore, when the pulse interval falls short of the fast pulse rate regime, spectroscopic U-FLARE provides an improved spatial impulse response in PE direction compared to spectroscopic RARE.

REFERENCES

1. Allerhand A. *J Chem Phys* 1966; 44:1
2. Stables LA et al. *J Magn Reson* 1999; 140:305
3. Smith SA et al. *J Magn Reson A*, 1994; 106:75

MR SPECTROSCOPY

Quantitation of 3D Chemical Shift Data: Nonlinear Least-Squares Spectral Estimation Using a Water Reference and A Priori Knowledge

David B. Clayton, Elfar Adalsteinsson, Daniel M. Spielman

Department of Radiology

INTRODUCTION

Spectra acquired in vivo by chemical shift imaging (CSI) suffer from inherently low signal-to-noise ratio (SNR), poor frequency resolution, and are extremely sensitive to perturbations in the main field (B_0). To quantitate these spectra, a robust estimation algorithm is necessary. Incorporating information from a high-SNR water signal can greatly enhance the accuracy of fitting CSI data (1-3) by compensating for T_2^* effects, RF pulse imperfections and spatial inhomogeneity, eddy current distortions, and phase-encoding point spread functions. The goal of this work is to demonstrate the efficacy of a nonlinear least-squares (NLS) estimation routine that uses a water reference and minimal a priori knowledge about the metabolite signals to fit CSI spectra.

METHODS AND MATERIALS

All data acquisitions were performed using a 1.5 T GE Signa whole-body scanner and standard birdcage coil. A 3D variable-density spiral CSI sequence (4) was used (144-ms TE, 2-s TR, 24-cm FOV, 36-pixel diameter, 7 mm slice thickness) to acquire spectra from a 2.7 L spherical phantom (12.5 mM NAA, 10 mM Cre, and 3 mM Cho in solution) and a normal volunteer. Higher-order shimming (5) was performed and an IR pulse was used for lipid suppression in vivo. Solvent suppression was achieved by shifting the center frequency so that the water resonance was outside the passband of the spectral-spatial RF excitation. 3 sets of phantom scans were acquired: (A) with an optimized shim ($\Delta B_0 = 2$ Hz), (B) with a linear gradient in x such that ΔB_0 was 7 Hz, and (C) similar to (B) but with $\Delta B_0 = 12$ Hz.

The fitting algorithm is a modified version of that described by Sundin (6). A basis set of 3 normalized echo signals is constructed by modulating the frequency and T_2 of the water signal by a priori values for NAA, Cre, and Cho. This reduces the number of nonlinear parameters to 2 (B_0 shift and T_2 correction) which are estimated using a standard simplex method to minimize the NLS estimator from which the linear parameters (signal amplitudes) have been removed; the latter are then found by a matrix pseudoinversion. The initial estimate for the T_2 term is found by fitting the decay portion of the water echo to a Voigt model, and the initial estimate for the frequency shift is determined by the deviation of the reference signal from the center frequency.

RESULTS AND CONCLUSION

Representative fits to phantom and in vivo spectra are shown in Fig 1 and demonstrate good agreement with the acquired data even in the presence of poor SNR and degraded B_0 homogeneity. Figure 2 summarizes the amplitude estimates from the center 4,400 voxels in each of the 3 phantom experiments with varied shim. The fitting method does not

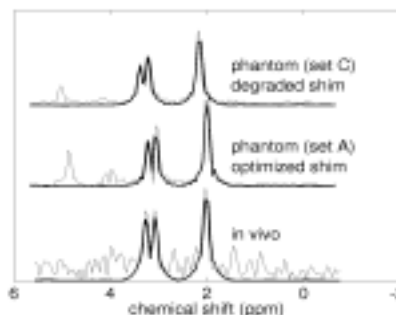


Figure 1: Sample fits (in bold) to spectra (shown in magnitude mode) in 3D CSI data sets acquired from a phantom and in vivo.

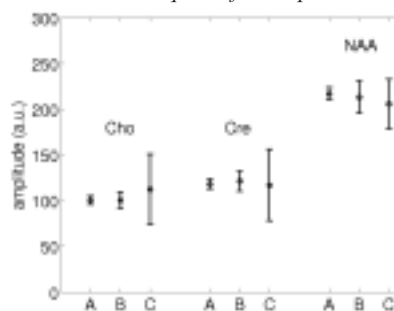


Figure 2: Amplitude estimates for NAA, Cre, and Cho averaged over the center 4,400 voxels inside the phantom for acquisitions with a good shim (A) and with the shim spoiled by an x-gradient applied so that ΔB_0 across the ROI was 7 Hz (B) and 12 Hz (C).

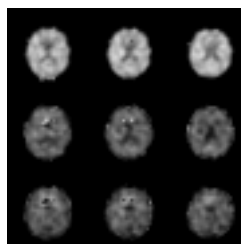


Figure 3: Center slices of the metabolic images formed from the amplitude estimates found by the NLS fit to in vivo spectra in a 3D CSI acquisition.

appear to introduce bias as homogeneity decreases, however the variance in the estimates does increase as expected. Figure 3 shows 3 center slices of the metabolic images formed from the amplitude estimates returned by the fitting algorithm. Only 23 of the 26,093 in vivo voxels (fits) failed to converge. These voxels were in regions of poor homogeneity (tissue boundaries) and are therefore a challenge to any fitting method because of severely degraded spectral quality.

REFERENCES

1. Spielman DS, et al. *Magn Reson Med* 1989;12:38-49
2. Webb P, et al. *Magn Reson Med* 1992;23:1-11
3. Maudsley AA, et al. *Magn Reson Med* 1994;31:589-95
4. Adalsteinsson E, et al. *Magn Reson Med* 1999;42:314-23
5. Kim D-H, et al. *Magn Reson Med* 2002;48:715-22
6. Sundin T. *Uppsala Dissertations from the Faculty of Science and Technology* 29; 2001

High Resolution Spiral PRESS at 3T

DongHyun Kim¹, Napapom Sailasuta², Ralph Hurd², Elfar Adalsteinsson³, Dan Spielman³

¹Electrical Engineering, ²General Electric Medical Systems, ³Radiology

INTRODUCTION

Chemical shift imaging (CSI) at a field strength of $B_0=3T$ has the benefit of increased signal to noise ratio (SNR) and improved spectral separation. The increase in SNR allows flexible tradeoffs to be made in the CSI data acquisition stage. For example, higher resolution acquisitions can be obtained without any scan time increase for fixed SNR. In this case, due to the limitation of phase-encoded CSI where at least one repetition time period (TR) is required for each resolved voxel, spiral based readout trajectory [1] offers an efficient sampling scheme for CSI acquisitions. The tradeoff can further be optimized by acquiring data with surface/phased array coils which give better SNR compared to conventional head coils.

Unwanted chemical shift resonances can be better suppressed with spectral-spatial (SS) RF pulses [2]. SS pulses have increased spatial bandwidth compared to conventional PRESS sequence, which reduces spatial displacements induced by chemical shifts. SS pulses are also more robust to B1 scaling errors than conventional CHESS (CHEMical Shift selective Saturation) pulses, which can be problematic at high B_0 field. Finally, spatial suppression of signals can be accomplished by using VSS (Very Selective Saturation) pulses [3]. Restricting the volume also allows a better field homogeneity to be obtained over the region of interest.

We thus implemented a PRESS based sequence for 3T using VSS pulses for spatial saturation, SS pulses for chemical shift selectivity, spiral based readouts for efficient k-space coverage, and acquired data with a surface coil targeting high resolution ($\approx 0.5cc$) CSI applications.

METHODS AND MATERIALS

We demonstrate the high resolution spiral PRESS CSI by collecting late-echo (TE/TR=144/2000 ms) metabolite data from a normal volunteer and a spectro phantom using a 5 inch surface coil. VSS pulses were placed at the edge of the brain to eliminate signals coming from subcutaneous fat. SS 180° pulses with a spectral passband of 390 Hz (3 ppm) were used to pass signals from NAA, Cre, and Cho while partially suppressing water and lipids. Spirals were designed using an analytic solution which enables on the fly design [4]. For this study, a spatial matrix covering a $32 \times 32 \times 8$ region over a $20 \times 20 \times 10$ cm FOV was used which resulted in 0.49 cc voxel size. The readout time was 350 ms long. The whole k-space coverage was obtained by interleaving the spirals in the spatial domain by rotating each readout gradients by 30°. The total acquisition time was 6:40 seconds (12 interleaves \times 2 sec TR \times 8 phase encodes \times 2 avgs). The spectral bandwidth was 800 Hz. Higher order shimming over the region of interest preceded spiral CSI. The reconstruction included gridding, FFT, and line broadening with a 5Hz Gaussian filter.

RESULTS

Figure 1 shows metabolite spectra obtained from a spectro phantom overlaid on the image. The middle slice from the 8 resolved slices are shown. Places where the VSS pulses were located are also shown. Representative spectra taken from the slice are also shown. Good spatial and spectral suppression (eg, water) are demonstrated from the phantom data.

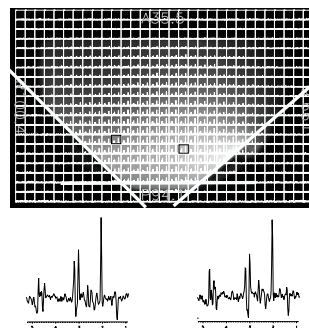


Figure 1: Metabolite spectra (zoomed in from Naa to Cho region) overlaid on the excited portion of the phantom. VSS pulse positions are also depicted. Representative spectra taken are shown on the right side.

Figure 2 shows metabolite spectra from the center of eight slices obtained from an in vivo brain study overlaid on the excited image. Representative spectra taken from the reconstructed data are also given. The PRESS box was selected to eliminate subcutaneous lipids. VSS pulses were also placed diagonally at the corners near the surface coil. Regions where the surface coil sensitivity profile is adequate demonstrated good spectral quality.

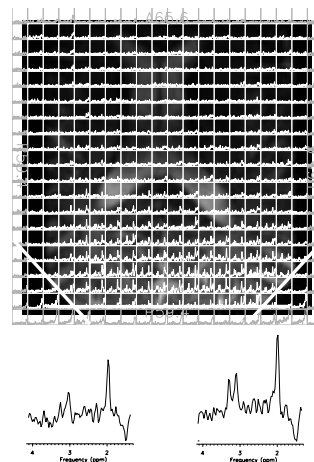


Figure 2: Metabolite spectra from in vivo scan. The PRESS box region and VSS saturation are depicted on the underlayered image.

CONCLUSIONS

We have demonstrated high resolution CSI at 3T by integrating VSS pulses, SS pulses, and spiral based readout gradients on a PRESS sequence using a surface coil.

REFERENCES

1. Adalsteinsson E, et al. *Magn Reson Med* 1998; 39:889-898
2. Meyer CH, et al. *Magn Reson Med* 1990; 15:287-304
3. Tran TC, et al. *Magn Reson Med* 2000; 43:23-33
4. Glover G, *Magn Reson Med* 1999; 42:412

MR SPECTROSCOPY

Spiral-out Spiral-in Chemical Shift Imaging

DongHyun Kim¹, Elfar Adalsteinsson², Dan Spielman²

¹Electrical Engineering, ²Radiology

INTRODUCTION

CSI (Chemical Shift Imaging) studies outside of the head are prone to motion effects. The long scan time required for adequate signal to noise ratio (SNR) can affect brain exams as well due to small movements. Spiral based CSI [1] has the advantage of covering the required k-space in less time than normal phase encoded CSI. This enables multiple acquisitions of the same k-space trajectory, which can be used to diminish motion effects by simple averaging and phasing techniques [2]. However, since gradients are played during the readout, unwanted phase can be accrued from motion proportional to the gradient moments, forming artifacts in the form of spatial/spectral blurring/ringing. In this work, spiral out-in [3] trajectories, which decreases the gradient moments in both directions, were used to minimize phase accrual due to motion during the readout.

Conventional spiral based CSI requires each spiral lobe to be connected via rewinding gradients which brings the k-space trajectory back to its origin ($k_x=k_y=0$) during the readout. Figure 1(a) illustrates one spiral lobe used for CSI readouts with its rewinders. In the presence of motion, the phase accrued by the moving object will be proportional to the moment of the gradients. Figure 1(c) shows the corresponding first order gradient moment of the trajectory for one spiral lobe (* corresponds to when the trajectory returns to its origin). Since many spiral lobes are played out during the readout for spiral CSI, the amount of phase accrual can be considerable. Moment compensated spirals can be built in a out-in fashion. Figure 1(b) illustrates the k-space sampling scheme of an out-in spiral. Due to the symmetry of the out- and in- portions, the trajectory has negligible first order gradient moment compared to normal phase encoded CSI and conventional spiral CSI with rewinders (fig 1(d)).

METHODS AND MATERIALS

Spiral out-in trajectories were designed and compared with normal phase encoded CSI and conventional rewriter based spiral CSI. Experiments were performed by gently rocking a spectro phantom similar to respiratory motion. To demonstrate the reduced ghosting artifacts, 16x16 pixel spiral out-in trajectory were compared with normal phase encoding readouts (20cm FOV with 10cm PRESS box). For comparison with conventional rewriter based CSI, 32x32 pixel spiral trajectories were used for both cases. Simulations

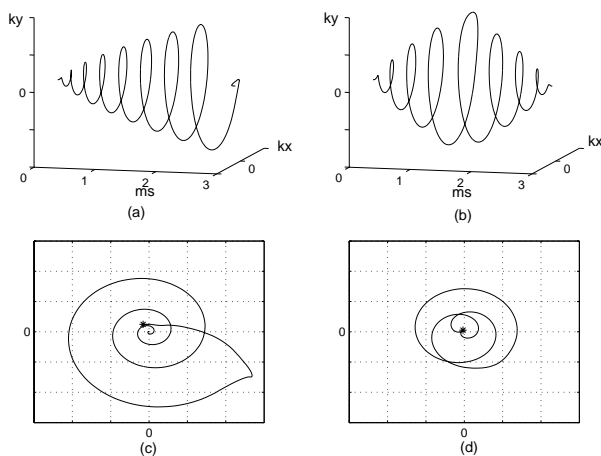


Figure 1

were performed to estimate the amount of spectral ringing. Data were also collected with and without motion induced to a spectro phantom to evaluate the performance of each trajectory. The readout length was .5 sec with 2 minute scan time (TE/TR = 144/1500 ms, 30cm FOV with 10cm PRESS box).

RESULTS

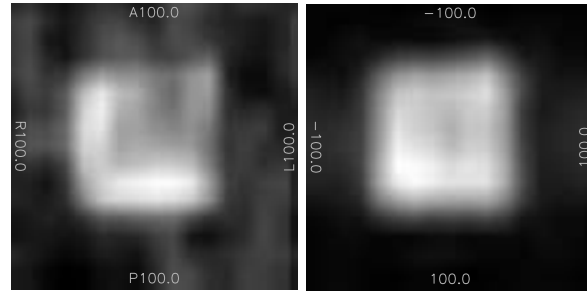


Figure 2: Reconstructed water images from normal phase encoded CSI (left) vs. moment compensated spiral CSI (right).

Figure 2 shows the water image from the reconstructed spectra and the corresponding PRESS box selected. Ghosting artifacts appear for the normal phase encoded CSI sequence with motion present. These artifacts can warp into the PRESS box selected region with insufficient FOV. The spiral out-in trajectory shows reduced artifacts.

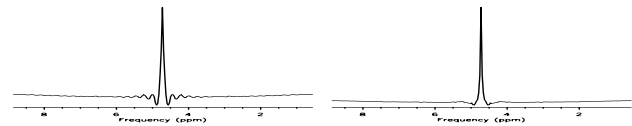


Figure 3: Simulated point spread function using rewriter based spiral CSI (left) vs. moment compensated spiral CSI (right).

Figure 3 compares simulated results of the spectra from the two spiral CSI sampling schemes. An impulsive object was located at the origin moving in the Y direction at a velocity of 1cm/sec during each readout. With the moment compensated sampling scheme, spectral ringing is reduced compared to rewriter based CSI.

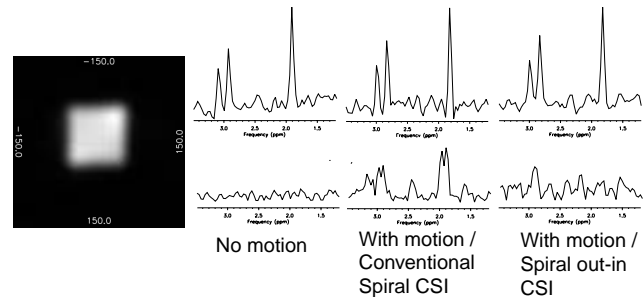


Figure 4: Representative metabolite spectra from phantom experiment. Spectra from within the excited PRESS box (top row). Spectra from the edge of the excited region (bottom row).

Figure 4 shows representative spectra without motion, with motion using rewinders, and with motion using moment compensating gradients from two areas of the phantom. The top row spectra illustrate the spectral ringing in the rewriter based CSI. The bottom row spectra show blurring effect at the edge of the excited PRESS box. Our method decreases the affect of blurring as can be seen.

CONCLUSIONS

Spiral out-in trajectory, which has the characteristic of gradient moment nulling, has been used to minimize motion effects for CSI.

REFERENCES

- [1] E. Adalsteinsson, et al., MRM, 39, 889-898, 1998.
- [2] D.H. Kim, et al., ISMRM 2002, 532, 2002.
- [3] G.H. Glover, et al., MRM, 46, 515-522, 2001.

A Dual-Tuned Volume Coil for ^{31}P and ^1H MR Spectroscopic Imaging of Mitochondrial Metabolism at 3 Tesla

Chardonnay J. Vance¹, David B. Clayton², Bruce N. Ames¹, Daniel M. Spielman², Gary H. Glover²

¹*Division of Biochemistry and Molecular Biology, University of California at Berkeley,* ²*Department of Radiology, Stanford Medical School*

INTRODUCTION

Accumulation of oxidative damage to mitochondria in tissues and organs, including the human brain, can impair the cellular processes of detoxification, DNA replication and repair, osmotic balance, and the capacity to generate ATP. Current research in the Ames lab (1,2) has shown that age-related mitochondrial decay, metabolic dysfunction, and memory loss in old rats can be partially reversed by the administration of specific antioxidants and mitochondrial metabolites. The goal of this study is to create a protocol for in vivo, non-invasive assessment of mitochondrial metabolism in the human brain as it is affected by this antioxidant/metabolite supplementation. Since phosphorous (^{31}P) is an integral part of cellular metabolic pathways, we plan to monitor naturally abundant ^{31}P compounds using MR spectroscopic imaging. A preliminary study will be conducted using an animal model for which it is necessary to design, construct, and test a suitable RF coil.

METHODS AND MATERIALS

We built a dual-tuned low-pass quadrature birdcage coil (Fig 1) for acquiring spectroscopic images from the rat brain. The coil consists of eight equally-spaced struts (0.8 cm wide, 7.9 cm long) and two end rings of etched copper sheeting fixed to a plexiglass tube (7 cm diameter). For tuning to the ^{31}P frequency (51.7 MHz), capacitors were used to join one end ring to each of the struts while tank circuits (parallel capacitors and inductors) were used to join each strut to the opposite end ring to allow for separate tuning to the proton (^1H) frequency (127.7 MHz). Four quarter-wavelength cables with traps were attached to the coil: 2 were grounded to the end ring with the ^{31}P tuning capacitors and connected to struts (separated axially by 90°) using series capacitance for matching the impedance to $50\ \Omega$; the other 2 cables were grounded to the ^1H end ring and connected with series capacitance to struts opposite to the ^{31}P cables. Spatial homogeneity of the two resonances was refined by adjusting the capacitance on each strut to reduce any shift in frequency observed in the inductive coupling between the coil and the pick-up loop of a network analyzer (reflection coefficient) as a function of axial orientation.



Figure 1: The ^1H - ^{31}P dual-tuned birdcage coil.

RESULTS AND CONCLUSION

Each channel of the coil was tuned to within 50 kHz and matched to approximately $50\ \Omega$ with minimal reactance. ^1H images and ^{31}P spectra were acquired from a phantom containing 150 mM phosphoric acid. Currently we are investigating methods of mapping the B_1 field of the entire volume of the coil. The dual-tuned coil design (3,4) will provide the ability to obtain ^1H -decoupled ^{31}P spectra and to acquire high-resolution ^1H images and ^{31}P spectroscopic images without repositioning the subject which enables more accurate spatial registration.

REFERENCES

1. Liu J, Killilea DW, Ames BN. *PNAS* 2002; 99:1876-81
2. Liu J, et al. *PNAS* 2002; 99:2356-61
3. Schnall MD, et al. *JMR* 1985; 65:122-9
4. Shen GX, Wu JF, Boada FE, Thulborn KR. *MRM* 1999; 41:268-75

Including Metabolic Uncertainty into Proton MR Spectroscopic Imaging (MRSI)-Guided Inverse Treatment Planning

Jun Lian¹, Daniel Spielman², Cristian Cotrut¹, Sandeep Hunjan¹, Elfar Adalsteinsson², Christopher King¹, Gary Luxton¹, Arthur Boyer¹, Bruce Daniel², and Lei Xing

¹Departments of Radiation Oncology and ²Radiology, Stanford University

INTRODUCTION

With the development of functional imaging techniques and intensity modulated radiation therapy (IMRT), there is growing interest in image-guided IMRT to produce customized 3D dose distributions in accordance with the patient specific biological requirements. MRSI is one of the most promising functional imaging modalities and has been applied to brain, breast, and prostate cancer imaging. In practice, however, the MRSI data do not always accurately reflect the actual metabolic level over the entire imaging volume due to our limited ability to shim near air-filled cavities and/or the strong dependence of the surface coil SNR on spatial location. In this work, we provide an algorithm to numerically incorporate the spectral uncertainties into MRSI-guided IMRT treatment planning.

METHODS AND MATERIALS

Assuming that the fluctuation of the spectral activity of the prescribed dose $EUD_0(n)$ at voxel n is specified by a probability distribution $P_n(EUD_0)$, we treat $P_n(EUD_0)$ as an *a priori* variable distribution and construct an objective function based on the statistical inference technique. The algorithm is used to plan a brain tumor treatment with incorporation of MRSI and the corresponding confidence map.

RESULTS

The method was applied to generate a hypothetical IMRT treatment plan of a malignant glioma. The target metabolic map was discretized into three levels (Fig 1A) based on the choline/NAA ratio. In a conventional plan, the inner region

with the highest abnormality (target 1) was prescribed 64 Gy, the middle region (target 2) 54 Gy, and the external region (target 3) 44 Gy. Because the measurement of choline/NAA has uncertainty, we replaced the fixed value desired dose with a probability density based dose prescription, and a dose distribution is shown in Fig 1B when three targets are all prescribed with a Gaussian type distribution. The objective functions are lower than those of the conventional plan (Fig 1C). The corresponding DVH shows this type of distribution could result in slight under dose (Fig 1D), suggesting a higher dose prescription may be needed when measurement uncertainty is of a Gaussian form. Overall, the resultant DVHs were significantly different from those of a conventional plan (Fig 1E).

CONCLUSIONS

The results indicate that the proposed technique is capable of producing deliberately non-uniform dose distributions consistent with the MRSI and its spatial uncertainty distribution. Considering that currently available functional image data are not completely reliable and that missing spectral data may frequently occur, the proposed technique provides us with an effective tool to minimize the effect and generate statistically optimal treatment plans.

REFERENCES

1. L Xing, C Cortuz, S Hunjan, A Boyer, E Adalsteinsson, and D Spielman, Inverse planning for functional image-guided intensity-modulated radiation therapy, Phys. Med. Biol. 47 (2002) 1-12.

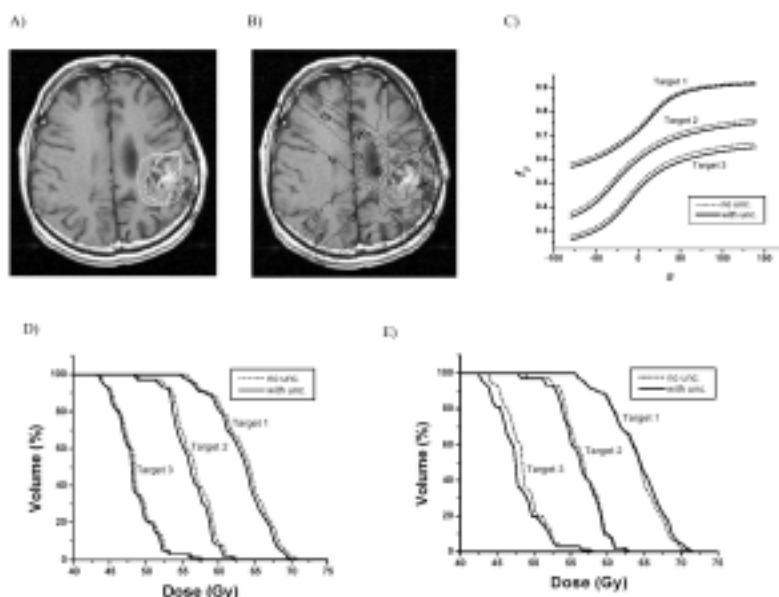


Figure 1: (A) Three targets with different MRSI-derived abnormality indices. (B) Dose distribution with inclusion of Gaussian-type uncertainty. (C) Target objective functions. (D) and (E) Target DVHs under different probability distributions.

Gray Matter Deficits in Secondary Progressive but not Relapsing Remitting Multiple Sclerosis

Elfar Adalsteinsson¹, Annette Langer-Gould², Ronald J. Homer¹, Archana Rao¹, Edith V. Sullivan³, Adolf Pfefferbaum^{3,4}, Scott W. Atlas¹

Department of ¹Radiology, ²Neurology, ³Psychiatry and Behavioral Sciences; ⁴Neuroscience Program, SRI International Menlo Park CA, USA

INTRODUCTION

Multiple sclerosis (MS) is a neurodegenerative disease with characteristic lesions in brain white matter. As a progressive disorder, MS-related symptoms exacerbate with time but the course of functional decline can vary across patients [1]. Over 80% of patients with MS begin with a relapsing-remitting form of the illness (RRMS). However, 5 to 20 years after disease onset, most RRMS patients enter the progressive phase of disease, called secondary progressive MS (SPMS). This progressive phase is marked by unrelenting physical and cognitive decline, implicating neuronal damage.

Presently, there are no reliable tests to predict who of the RRMS type will develop SPMS and when they will develop it. Similarly, determination of when transition from the relapsing-remitting phase to the progressive phase occurs can be accomplished only retrospectively. A quantitative test that could accurately classify or predict MS clinical subtypes could make a significant contribution to patient management decisions and provide an outcome measure in MS clinical trials

METHODS AND MATERIALS

The subject groups comprised 5 RRMS (all women), 5 SPMS (1 man, 4 women), and 9 controls (1 man, 8 women). Each patient met Poser criteria for clinically definite multiple sclerosis.

Volumetric, variable-density spiral MRSI [2] was used together with high resolution MRI to derive absolute measures of metabolite concentrations separately in normal-appearing supratentorial cerebral gray matter and white matter in RRMS patients, SPMS patients, and age-matched controls. Structural MR images were segmented into compartments of gray matter, white matter, cerebrospinal fluid, and lesions, and metabolite signals per unit of tissue volume were calculated for gray matter and white matter separately [3].

RESULTS

Only the SPMS group had significantly lower N-acetyl-aspartate (NAA) concentrations in normal appearing gray matter compared with controls. NAA in normal-appearing white matter was equally reduced in RRMS and SPMS patients. The functional relevance of this brain metabolite measure was supported by the observed modest correlation between higher disability scores on the Expanded Disability Status Scale and lower gray matter NAA concentrations.

CONCLUSIONS

The otherwise occult abnormality in supratentorial gray matter in SPMS but not RRMS may explain the more severe physical and cognitive impairments afflicting patients with SPMS that do not correlate well with visible lesion burden.

As a safe and noninvasive technique, quantitative gray matter NAA measurements in serial volumetric MR spectroscopic imaging may be an effective way to distinguish RRMS from early SPMS patients both before and after treatment. Further, these findings suggest that decreased gray matter NAA concentrations may be predictive of a poor outcome in MS.

REFERENCES

1. Confavreux C, Vukusic S, Moreau T, Adeleine P. Relapses and progression of disability in multiple sclerosis. *New Eng J Med* 2000; 343: 1430-1438.
2. Adalsteinsson E, StarLack J, Meyer C, Spielman D. Reduced spatial side lobes in chemical-shift imaging. *Magn Reson Med* 1999; 42: 314-323.

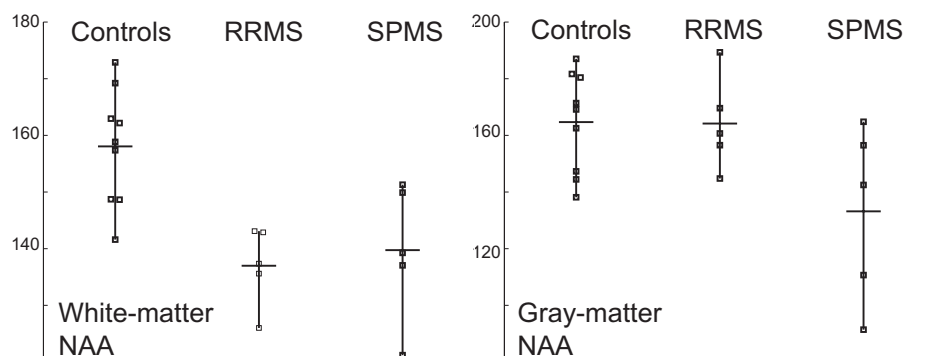


Figure 1: Group means and individual data of NAA concentrations in GM and WM in controls, RRMS, and SPMS.

Effect of Forced Diving in Seals on Muscle Phosphate Metabolites: A ^{31}P -MRS Study

Shelia Thorton¹, Daniel Spielman², Norbert Pelc², Daniel Crocker³, Daniel Costa⁴, Burney LeBoeuf⁴, Peter Hochachka¹

¹Department of Zoology, University of British Columbia, ²Department of Radiology, Stanford University,

³Department Biology, Sonoma State University, ⁴Department of Biology, UC Santa Cruz

INTRODUCTION

Diving seals exhibit an extraordinary tolerance for extended periods of submergence. As has been known for over 60 years, forced diving elicits the so-called diving response, involving apnea, bradycardia, and hypometabolism associated with vasoconstricted peripheral tissues. While central organs, especially the brain, enjoy normal perfusion, peripheral tissues experience variable degrees of ischaemia. Studies have shown that seal muscle myoglobin stores are sufficient to support active contraction for approximately 4 minutes. However, the process by which peripheral tissues, such as muscles, are able to function for long dive periods (upto 1 hr for elephant seals) is not fully understood. We used non-invasive ^{31}P Magnetic Resonance Spectroscopy (MRS) for real-time evaluation of metabolic status in northern elephant seal locomotor muscle during forced diving.

METHODS AND MATERIALS

Seven ten-month-old northern elephant seals were collected from Ano Nuevo, CA and held at the Long Marine Lab, UC Santa Cruz for the duration of their captivity. On the day of the experiment, animals were transported to the Stanford Lucas Center, then manually restrained while 4 ECG electrodes were attached to the ventral surface. The animals were then placed in a conical nylon jacket and strapped to a restraining board in a prone position. The board was then listed into a PVC half pipe and placed in the 1.5T MR scanner. The seals were subjected to five sequential forced dives (ave duration = 8 min 21 s) using a water-filled custom design helmet. The following data was collected for each animal: ^{31}P MRS include PCr and intracellular pH, heart rate, and respiratory rate. Blood lactate samples could not be achieved in the MR unit as the caudal end of the animal was not accessible during MRS acquisition. Consequently, five animals were restrained and forcibly dived at Long Marine Lab using the same protocol employed during MRS. Blood samples were drawn from the extradural intervertebral vein during pre-dive, dive, and post-dive periods. All animals were released at the site of capture at the conclusion of the experiment.

RESULTS

End dive phosphocreatine (PCr) values from individual dives ranged from 36.27-116.63% of pre-dive values. In 4 animals, PCr declined continuously during the dive; PCr signal intensity was significantly correlated with pH. Overall lactate formation (peak washout value – pre-dive value) was 0.7 mmol/l, and blood lactate concentration did not vary significantly at any point throughout the experiment (ANOVA, $F_{(10,43)}=2.3$, $p=0.028$).

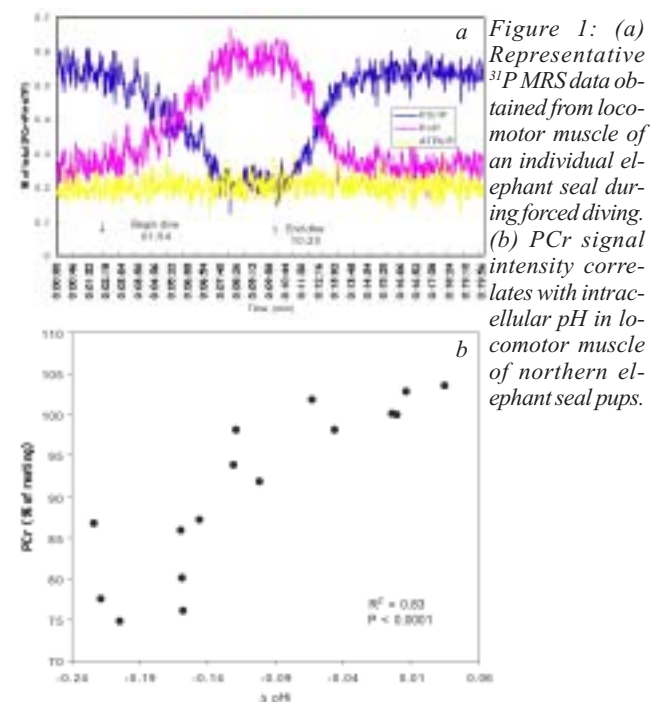
cantly at any point throughout the experiment (ANOVA, $F_{(10,43)}=2.3$, $p=0.028$).

CONCLUSIONS

These data are interpreted to indicate that significant PCr utilization and lactate-associated H^+ production occur prior to oxygen depletion in the ischemic muscle of seals during forced diving and suggest that even under aerobic conditions, a substantial portion of ATP production is supplied through anaerobic means.

REFERENCES

1. P Hochachka (2000). Pinniped diving response mechanism and evolution: A window on the paradigm of comparative biochemistry and physiology. *Comp. Physiol. and Biochem.*, 126A, 435-458.
2. M Castellini and G Somero (1981). Buffering capacity of vertebrate muscle: correlations with potentials for anaerobic function. *J. Comp. Physiology* 143, 191-198.
3. Kantous, 1999
4. M Castellini, G Kooyman, and P. Ponganis (1992). Metabolic rates of freely diving Weddell seals: correlations with oxygen stores, swim velocity, and diving duration. *J. Exp. Bio.* 165, 181-194.
5. G Guyton, K Stanek, R Schneider, et al (1995). Myoglobin saturation in free-diving Weddell seals. *J. Appl. Physiology* 79, 1148-1155.



MRS in Relation to Hippocampal Volume in the Oldest Old

David Spencer¹, Tracy Zitzelberger¹, Daniel Spielman², Jeffery Kaye¹

¹Department of Neurology, Oregon Health and Science University, ²Department of Radiology, Stanford University,

INTRODUCTION

At short-echo time, in vivo ¹H MRS can reliably detect brain metabolite peaks corresponding to myo-Inositol (mI), choline containing compounds (Cho), creatine and phosphocreatine (Cr), and N-acetylaspartate (NAA). NAA, localized predominately to neurons, has been used as a marker of neuronal integrity. MRS studies of probably and pathologically proved Alzheimer's Disease (AD) have almost uniformly shown decreases in NAA and increases in mI compared with age-matched controls. In contrast, most studies of healthy aging have reported stability of NAA and mI with advancing age. The oldest old (age ≥ 85 yrs) are the fastest growing segment of the US population, and are at high risk of developing dementia, with estimated conversion rates of up to 12% per year. We used ¹H MRS to examine brain metabolites in a cohort of healthy subjects ≥ 85 yrs of age. The objectives of the study were to establish normative values in this previously unstudied population and to examine the relationship between brain MRS measures and possible predictors of progression to dementia.

METHODS AND MATERIALS

60 healthy adults ≥ 85 yrs of age were studied. Inclusion criteria included functional independence, adequate vision and hearing, and no subjective memory impairment. Folstein Mini-Mental State Examination (MMSE) score >23, Clinical Dementia scale score of 0, and a normal score on the education-adjusted logical memory subscale of the Wechsler Memory Scale-Revised (WMS-R). Exclusion criteria included presence of any disease associated with dementia, substance abuse, major psychiatric disease, major systemic illness, or use of psychoactive medications. APOE genotype was also determined in all subjects.

MRS and MRI studies were performed on a 1.5T GE scanner. Structural MRI included a multiecho coronal sequence with 4 mm slices. Image analysis was performed using manual tracing. Single voxel

¹H MRS use an automated software package (PROBE/SV) with TR/TE=30/1500ms, 128 averages. Three volumes of interest were studied in the parietal and left and right medial temporal regions (8 cc voxels). Primary measures were hippocampal volume and ratios of NAA/CR and NAA/mI.

RESULTS

Ratios of both NAA/CR and NAA/mI were higher in parietal than temporal lobes with no significant left/right differences. Because 10% of the subjects were considered to be at high risk of progression to dementia within a year, MRS mea-

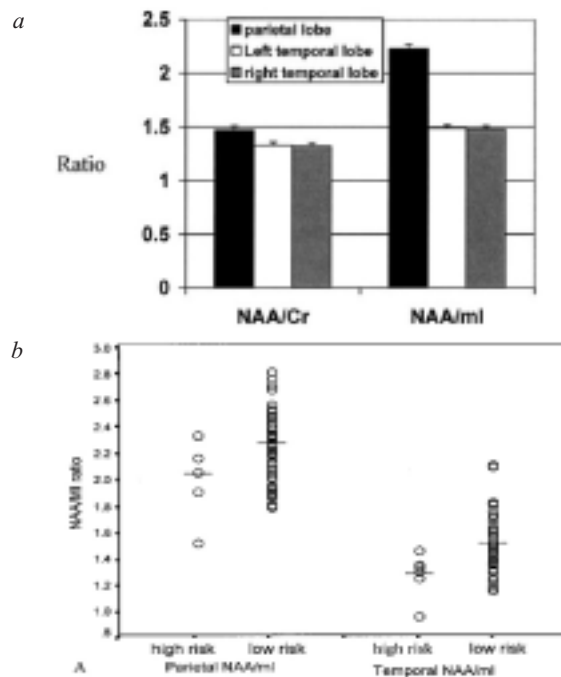


Figure 1: (a) Mean ¹H MRS metabolite ratios. (b) MRS ratios comparison between groups at high and low risk for dementia in the next year (horizontal line represents mean).

asures were compared between the lowest 10th percentile (high risk) and the remainder of the group (low risk). Subjects with small hippocampal volumes, a putative risk for dementia (high risk), had significantly lower NAA/mI in parietal and temporal lobes compared to low risk subjects ($p < 0.03$, $p < 0.01$). Neuropsychological tests and APOE genotype did not correlate with MRS ratios.

CONCLUSIONS

Short TE ¹H MRS measures are candidate biomarkers for dementia risk.

REFERENCES

1. D Spencer, T Zitzelberger, D Spielman, and J Kaye, MRS in relation to hippocampal volume in the oldest old, *Neurology* 2003;60:1194-1196.
2. M Valenzuela, and P Sachdev, Magnetic Resonance Spectroscopy in AD, *Neurology* 2001;56:592-598.
3. A Pfefferbaum, E Adalsteinsson, D Spielman, E Sullivan, and K Lim, In vivo spectroscopic quantification of the N-acetyl moiety, creatine, and choline from large volumes of gray and white matter: effects of normal aging. *Magn. Res. Med.* 1999; 41:276-284.

Interventional

MRI

In Vivo Comparison of Realtime Triggered, Navigated, Multi-baseline Thermometry with Conventional Respiratory Triggered PRF Thermometry for Monitoring Liver Ablation

Karl Vigen¹, Bruce Daniel¹, John Pauly², and Kim Butts¹

Departments of ¹Radiology and ²Electrical Engineering

INTRODUCTION

Quantitative MRI temperature mapping using the proton resonance frequency (PRF) shift method¹ requires phase-subtraction of a pre-treatment baseline image from images acquired during treatment. When respiratory motion occurs, artifacts can appear in the temperature map due to non-uniform alteration of the magnetic field due to organ motion, and variability in motion between respiratory cycles if only local anesthesia is used. This work compares an *in vivo* PRF temperature mapping strategy² during extended, variable respiration with conventional respiratory triggered methods using a single baseline image.

METHODS AND MATERIALS

The pulse sequence with two echoes per TR was implemented on a 0.5T interventional MRI scanner (Signa SP, GE Medical Systems, Milwaukee WI). The second echo is used to acquire 256x128 resolution images for temperature imaging. The first echo is used as a navigator echo to determine diaphragm position³. Images and navigator profiles were displayed in real-time on an offline workstation.

Imaging was divided into four sections. In the first section, imaging was performed without respiratory triggering to select navigator and phase-drift correction ROIs. In the second section, respiratory triggering with the bellows began data acquisition at approximately the same position in each respiratory cycle. Multiple baseline images were acquired, with the trigger delay increased for each image in order cover a range of diaphragm positions. Due to respiratory variability, some diaphragm positions might not be represented, and the third section reacquires baseline images at trigger delays determined by user feedback. After baseline images over a range of diaphragm positions were acquired, temperature sensitive images were acquired during heating.

During treatment, a composite baseline reference image was formed, with each k-space line selected by finding the baseline and treatment image k-space line pairs with the minimum diaphragm position difference. The measured displacements were also used to correct for displacement induced phase shifts in k-space. Phase-difference subtraction was performed, and temperature maps were displayed in real-time.

Seven laser ablations were performed in the livers of four pigs with the triggered, navigated, multi-baseline method. Temperature maps were also reconstructed using respiratory triggering only (just one baseline image), and respiratory triggering with navigator phase correction. One ablation was also performed in each animal and imaged without any respiratory triggering, but with navigator phase correction. Heating was performed for 10 min., with the laser tip kept at 95°C. Ventilation was performed manually to simulate free-breathing.

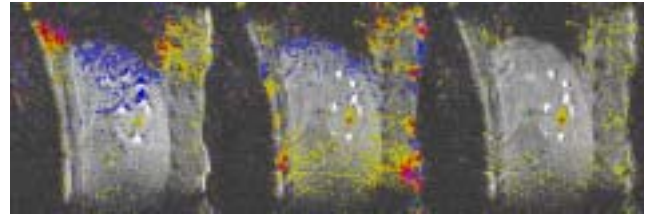


Figure 1: One representative time frame for images reconstructed with (a) respiratory triggering, (b) triggering with navigator correction, and (c) the triggered, navigated, multibaseline method.

RESULTS

Figure 1 shows a comparison of the three reconstruction methods. For each acquisition, a 10x10 region-of-interest (ROI) was selected in a uniform, unheated region of liver. The mean temperature of the ROI was averaged over the first 40 time frames acquired during heating, and the standard deviation of this mean was used as the variation in background temperature during heating. Figure 2 shows the results for each experiment, and taken over all 7 experiments (280 total time frames).

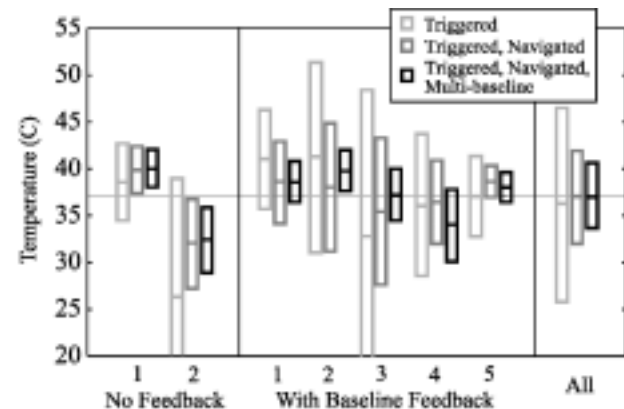


Figure 2: The mean ROI temperature averaged over all time frames; with the standard deviation (bars) showing the variation of the mean ROI temperature over all reconstructed time frames.

CONCLUSIONS

Images acquired with the triggered, navigated multi-baseline method showed suppression of temperature map artifacts seen in the other reconstruction methods. The measured temperature in a background ROI also showed less variation for the triggered, navigated, multi-baseline method.

REFERENCES

1. De Poorter J, et al. *Magn Reson Med* 1995; 33:74
2. Vigen K, Daniel B, Butts K, et al. *Proc. 10th ISMRM*, 2227 (2002).
3. Ehman RL, Felmlee J. *Radiology* 1989; 173:255

INTERVENTIONAL MRI

Simultaneous MR Temperature Mapping and Radiofrequency (RF) Ablation

Karl Vigen¹, Jerry Jarrard³, Vince Sullivan⁴, James Culp⁴, Viola Rieke², Bruce Daniel¹, Kim Butts¹

Departments of ¹Radiology and ²Electrical Engineering, Stanford University; ³Boston Scientific Corporation, San Jose; ⁴Stellartech Research Corporation, Sunnyvale

INTRODUCTION

Radio-frequency (RF) ablation techniques are widely used for the treatment of malignancies, usually under CT and/or ultrasound guidance. The use of magnetic resonance imaging is desirable for its ability to visualize soft tissue changes and monitor tissue temperature during treatment. However, imaging is often complicated by interference from the RF generator. MR imaging is often only performed prior to and immediately following treatment, or intermittently as treatment is stopped during the procedure. Investigators have previously used filtering^{1,2} as a means of suppressing interference, but at low RF power (up to 15W)². A custom-built switching device has also been used which multiplexes MR imaging with the RF generator operation³. The purpose of this work is to describe a system which allows the use of RF ablation at high RF generator power simultaneously with continuous MR imaging and temperature mapping in an *ex vivo* liver phantom.

METHODS AND MATERIALS

Magnetic resonance imaging and radio-frequency (RF) ablation tests were performed on a 0.5T interventional MR system (Signa SP, GE Medical Systems, Milwaukee WI), which was fully RF-shielded. A radio-frequency generator (RF3000, Boston Scientific Corporation, San Jose CA) was placed outside the room, and modified to eliminate interference at frequencies near those detected in imaging. The output of the RF source from the generator was passed through a filter network, which can be approximated as a low-pass LC filter with a cutoff frequency at 1.5 MHz (Fig. 1). The signal is then sent to a filter and isolation network in a shielding box firmly attached to the RF shielding pass-through panel of the MRI suite. The band-pass filter in this shielded box has a pass frequency at 460 kHz, which is the frequency of the RF generator. An umbrella-shaped needle electrode (LeVeen, Boston Scientific Corporation, San Jose CA) was attached to the output of the filter/isolation network inside the magnet room, and inserted into an *ex vivo* bovine liver phantom. Although just one path is shown in the simplified circuit of Figure 1, four paths are actually used with the four return electrodes connected to a conductive plate on the bottom of the tissue sample.

MR imaging was performed with a 2D gradient-echo sequence (TR/TE/BW = 67ms/27ms/±16kHz) with temperature maps calculated by the proton resonance frequency (PRF) method and displayed in real-time on an offline workstation. Imaging was performed with an unmodified RF generator switched on (i.e. without the isolation and filter network); and switched on with the isolation/filter network in place at 75W for 15 min.

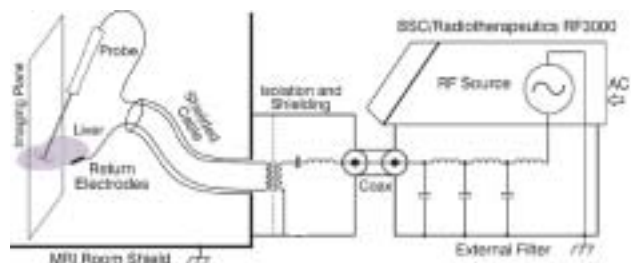


Figure 1: Simplified diagram of RF generator modified with external filter, and filtering and isolation network inside shielding box.

RESULTS

Images acquired with the unmodified RF generator were dominated by interference at frequencies within the acquisition bandwidth, and were uninterpretable. Temperature maps acquired during the application of RF generator power with the filtering and isolation network in place are shown in Figure 2 prior to heating, and at 3.5 min., 6.0 min., and 7.5 min. after the beginning of heating. No noticeable interference was observed in any images during the application of RF generator power.

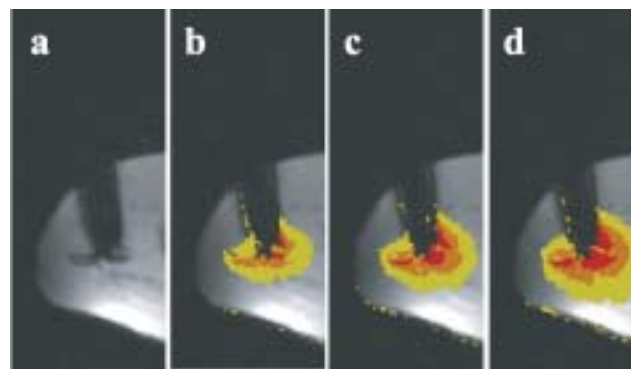


Figure 2: Temperature maps acquired (a) prior to heating, and at (b) 3.5, (c) 6.0, and (d) 7.5 minutes after heating begins. Yellow, orange and red represent temperature increases of +10°C, +20°C, and +30°C, respectively, above baseline.

CONCLUSIONS

A filtering and isolation network was added to a radio-frequency generator used for RF ablative techniques. RF generator interference in the MR images was essentially eliminated with this system, compared with the use of a standard unfiltered RF generator.

REFERENCES

1. Daniel BL et al. *Radiology* 1997; 205:1555
2. Oshiro T et al. *J. Comput Assist Tomogr* 2002; 26:308
3. Zhang Q et al. *J Magn Reson Imaging* 1998; 8:110

Referenceless PRF Shift Thermometry

Viola Rieke^{1,2}, Karl Vigen¹, Graham Sommer¹, John Pauly², Kim Butts¹

Departments of ¹Radiology and ²Electrical Engineering

INTRODUCTION

Minimally invasive thermal therapy is promising for the treatment of a variety of cancers. Temperature monitoring of these procedures using magnetic resonance proton resonance frequency (PRF) thermometry can be used to guide the treatment in real-time. In conventional PRF thermometry, phase images acquired previous to heating, called baseline images, are subtracted from phase images acquired during heating. With motion, images will not be registered to the baseline images, resulting in erroneous baseline phase elimination. We propose a new method where the baseline phase is estimated from the acquired phase image itself, so that a separate reference scan is not required. We call this method referenceless PRF thermometry. Estimating the baseline phase from each temperature map itself eliminates the mis-registration of images with the baseline data.

METHODS AND MATERIALS

An annular region of interest (ROI) is selected around the area to be heated as seen in Fig. 1a. The inner border is outside the anticipated heating region. The outer border is well within the object. The unwrapped phase within the annular ROI is weighted by the image magnitude squared [1] and approximated by a polynomial. The extrapolation of the fitted phase to locations within the inner ROI border serves as an estimation of the baseline phase. Before heating, the order of the polynomial (2nd to 6th order) is chosen that minimizes the variance of the difference between the estimated phase and the initial phase. Once ROI and polynomial order are determined, the background phase is estimated in every image during thermal treatment and subtracted from the actual phase. The temperature rise is then calculated from the remaining phase.

Images were acquired on a 0.5T Signa SP and 1.5T Signa MRI scanner (GE Medical Systems, Milwaukee WI). Laser heating was performed on a tofu phantom. Liver images of three normal human volunteers, acquired in a single breath-hold scan with and without flow compensation, were used to determine the accuracy of a zero degree temperature rise. Prostate ablation was studied in a canine model using a transurethral ultrasound transducer [2]. In all three cases the temperature maps acquired with the referenceless method were compared to images obtained with the conventional phase difference method.

RESULTS

Figure 1(a) shows a phantom heated with a laser fiber. Magnified temperature maps of the phantom during heating are shown: one with referenceless (b) and one with conventional (c) processing; the temperature images are essentially identical. A plot of the temperature along a vertical profile is also plotted (d), showing little difference between the two methods in the heated area.

The *in vivo* liver images were evaluated by comparing the variance of the temperature maps acquired with both methods. With flow compensation, the variance of the referenceless images decreased by 10-20% compared to baseline subtraction. The improvement was even greater in images where the subtraction was degraded by a higher order phase drift. Without flow compensation, the variance of the referenceless images was 60-80% higher, because phase

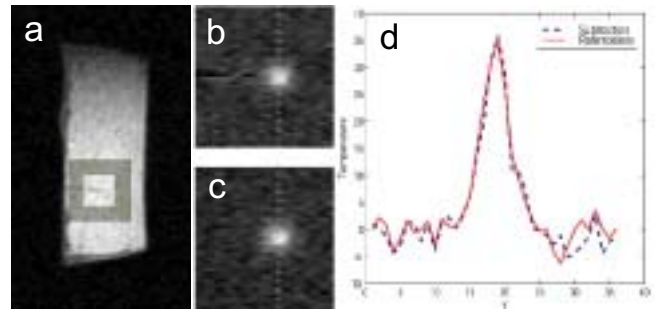


Figure 1: Magnitude image of a phantom with a laser fiber (a), showing the annular ROI. Referenceless (a) and conventional (b) temperature maps are qualitatively similar. A vertical profile through the heated area (d) demonstrates excellent agreement.

shifts due to flow are detected by the referenceless method and interpreted as temperature shifts. It shows that flow compensation is necessary for the referenceless method to work reliably.

Figure 2 shows temperature maps of a single time frame during canine prostate ablation reconstructed with conventional (a) and referenceless (b) methods. A good correlation between the two methods was found during the course of treatment. Motion of the urethra of approximately 2 mm occurred after acquisition of the baseline image, explaining differences in the temperature images.

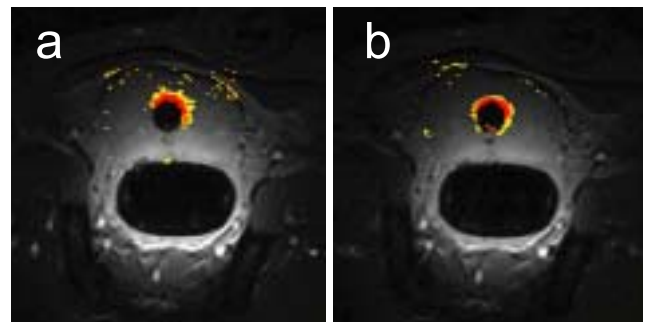


Figure 2: In the canine prostate, temperature overlay comparing conventional (a) and referenceless (b) methods demonstrate similar temperature maps with fewer artifacts in the prostate border in (b). Color overlay: yellow=44°, orange=48°, red=52°C.

CONCLUSIONS

We developed a new method for temperature mapping that does not rely on baseline images. The method is insensitive to changes in the background phase or to motion during thermal treatment. This work will benefit thermal therapy applications such as prostate and liver cancer therapy where swelling and respiratory motion during the treatment results in misregistration of the baseline phase image.

REFERENCES

1. Conturo TE et al. *MRM* 1990; 15:420-437
2. Sommer G et al. *Proc. ISMRM* 2002.

INTERVENTIONAL MRI

Phased Array PRF Thermometry in Canine Prostate

Viola Rieke^{1,2}, Roland Bammer¹, Graham Sommer¹, Bruce Daniel¹, Kim Butts¹

Departments of ¹Radiology and ²Electrical Engineering

INTRODUCTION

Minimally invasive thermal therapy is promising for the treatment of a variety of cancers, including prostate cancer. Temperature monitoring using magnetic resonance proton resonance frequency (PRF) thermometry can be used to guide these treatments in real-time. Since the temperature uncertainty σ_T in the acquired temperature maps is inversely proportional to the SNR of the corresponding magnitude images [1], it is important to achieve the best possible SNR over the treatment area.

Therefore, we combined an endorectal coil with an anterior surface coil in a phased array (PA) and developed a reconstruction algorithm for phased array thermometry. Conventional PA reconstruction typically discards the phase information with the use of a sum of squares algorithm [2]. However, for PRF thermometry, the phase information must be retained and the inherent location-dependent phase of each coil has to be taken into account.

METHODS AND MATERIALS

In PRF shift thermometry, phase images acquired previous to heating, called baseline images, are typically subtracted from phase images acquired during heating and corrected for background phase drift. When this correction is performed for the individual coils before the images are combined, the spatially dependent phase of each coil is also removed. The temperature data from each coil is then combined with a magnitude squared weighting. This weighting minimizes the variance of the resulting phase and is used in phased array phase contrast imaging [3].

A square anterior surface coil (12 cm diameter) was constructed and combined with an endorectal coil on the phased array port of a 0.5T interventional MRI scanner (Signa SP, GE Medical Systems, Milwaukee, WI). The phased array coils were tested in a canine model undergoing thermal ablation with a transurethral ultrasound applicator [4]. A cooling balloon was placed around the endorectal coil to protect the rectal wall.

For comparison, images were acquired before thermal treatment with the surface coil on the anterior abdominal wall of the animal and again with it outside the magnet. During thermal treatment, imaging was performed with the phased array pair. Temperature maps reconstructed with the phased array pair were compared to temperature maps reconstructed with the endorectal coil only. Measurement of the temperature uncertainty σ_T , which is defined as the standard deviation of the temperature, was used to evaluate the performance of both methods.



Figure 1: Magnitude images acquired using the endorectal coil alone (a) and in combination with an anterior surface coil (b).

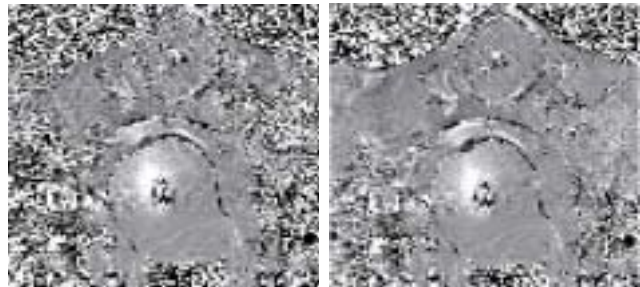


Figure 2: Temperature images reconstructed from the endorectal coil (a) and the phased array pair (b).

RESULTS

Figure 1 shows magnitude images reconstructed with the endorectal only (surface coil outside the magnet) (a) and in combination with the anterior surface coil (b). The phased array combination achieved an SNR gain of approximately 50% in the anterior part of the prostate.

Figure 2 shows temperature maps of endorectal coil (a) and phased array (b) during thermal treatment. Unlike the previous SNR measurement, both coils were used for imaging during the thermotherapy experiment. Comparing the temperature maps of the endorectal coil alone and the phased array shows an improvement in temperature uncertainty σ_T in the anterior part of the prostate by approximately 40%. The full 50% improvement is not reached in this comparison due to residual coupling between the two coils.

CONCLUSIONS

Combination of the anterior surface coil with the endorectal coil in a phased array provided a significant gain in SNR of 40-50% in the anterior portion of the prostate. We demonstrated a reconstruction algorithm that allows the use of this phased array pair for PRF shift thermometry.

REFERENCES

1. Conturo TE et al. *MRM* 1990; 15:420-437
2. Roemer PB et al. *MRM* 1990; 16:192-225
3. Bernstein MA et al. *MRM* 1994; 32:330-334
4. Sommer G et al. *Proc. ISMRM* 2002

Feasibility of Proton Density for Fat Thermometry

Jing Chen^{1,2}, Bruce L. Daniel², Kim Butts²

Departments of ¹Electrical Engineering and ²Radiology

INTRODUCTION

With the recent generation of open MRI systems, interest in MRI-guided local therapy of various cancers including breast cancer¹ is increasing. Methods for monitoring thermal therapy include the tissue proton resonant frequency², diffusion coefficient³, and relaxation times^{4,5,6}. The PRF method appears to be the most promising for water-based tissues, but adipose tissue does not exhibit a resonant frequency shift with temperature. The proton density (PD) is an additional tissue parameter that may be possible to relate to temperature⁷. Our purpose is to investigate the feasibility of apparent proton density (APD) method for fat thermometry.

METHODS AND MATERIALS

The APD is linearly dependent on $1/T$, with the resulting signal change being related to temperature by approximately $0.3\%/^{\circ}\text{C}$. To validate this, ex vivo experiments were performed with a 0.5T GE Signa SP interventional MRI scanner (MRT). In the first experiment, previously frozen and thawed bovine adipose tissue samples were heated in a water bath at successively constant temperatures from 20°C to 76°C , and then back to 28°C . Spin echo images ($\text{TR}/\text{TE} = 4\text{s}/19,38\text{ms}$) were obtained. From each pair of images, the T2 of the two tissues and the APD extrapolated back to an echo time of 0 were calculated. The APD was measured in an ROI completely within the sample and normalized to the value at 26°C . Then, the percentage change in APD, relative to its value at room temperature, was calculated with a linear regression analysis. In the second experiment ($\text{TE} = 11,30\text{ms}$), we adopted fresh porcine fat sample, and scanned it within 3hr of excision and the result was normalized relative to the value at 30°C .

RESULTS

The calculated APD of bovine adipose tissue is plotted as a function of temperature in Figure 1. The arrows show the direction of temperature change. The APD of frozen and thawed fat increases with temperature until $\sim 50^{\circ}\text{C}$. This is due to a change in the solid-liquid ratio, with short T2 species becoming visible at the echo times used in this study, as the fat liquefies. An early study used a related method to quantify the solid fat content in partially crystallized fats⁸. The APD in paths b and c demonstrate a $1/T$ dependence (slope = $0.3 \pm 0.035\%/^{\circ}\text{C}$). The APD measurements from the fresh fat samples are shown in Fig.2. The slope is $0.32 \pm 0.021\%/^{\circ}\text{C}$, proving the feasibility of PD for fat thermometry

CONCLUSIONS

This is the first experiment on PD thermometry for fat, and the result is encouraging. However, there are some inherent problems, like sensitivity to noise and low contrast to noise

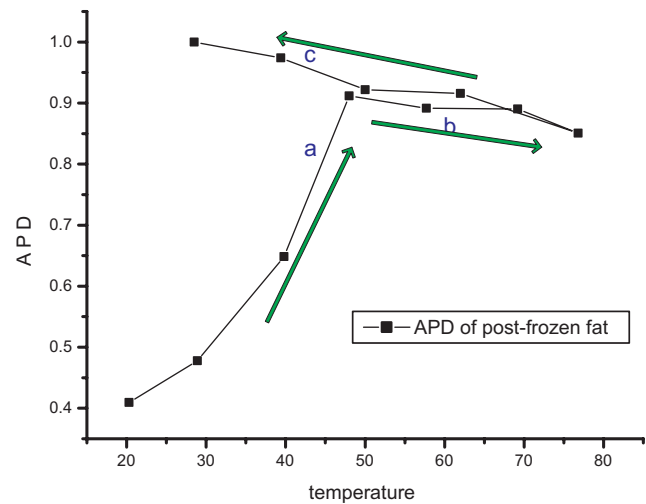


Figure 1: $\text{TR} = 4\text{s}$, $\text{TE} = 19,38\text{ms}$, post-frozen bovine adipose

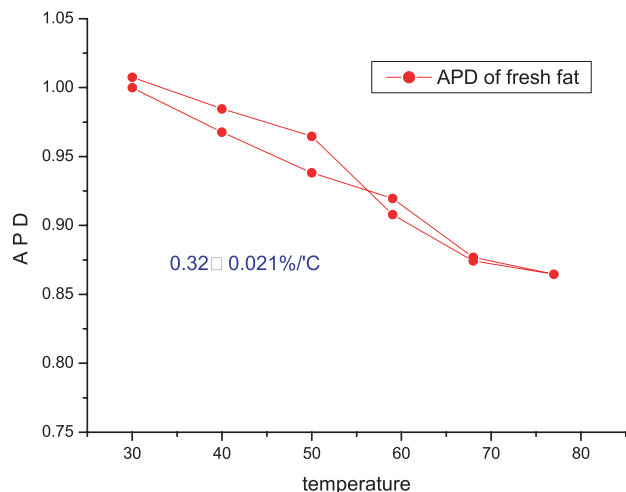


Figure 2: $\text{TR} = 4\text{s}$, $\text{TE} = 11,30\text{ms}$, fresh porcine fat

ratio. Our further investigation includes optimizations of this method, and fast PD weighted imaging technique, which is essential for real-time monitoring of thermal therapy.

REFERENCES

1. Cline HE, et al. *MRM* 1993; 30:9-106
2. De Poorter, et al. *MRM* 1995; 34:359-367
3. Zhang Y, et al. *Intl Journal of Hyperthermia* 1992; 8:263-274
4. Gandhi S, Daniel BL, Butts K, *5th ISMRM*, 1998; p 701
5. Hynymen K, et al. *MRM* 2000; 43:901-904
6. Graham SJ, Bronskill MJ, Henkelman RM. *MRM* 1998; 39:198-203
7. Young IR et.al. *MRM* 1994; 31:342-345
8. van Putte KPAM, van den Enden J. *J Physics E: Scientific Instruments* 1973; 6:910-12

Molecular **Imaging**

Genomic Profile of Vascular Permeable Regions of Patients with Glioblastoma Multiforme for Identification of Blood Markers for Disease

Samira Guccione¹, Yi-Shan Yang¹, Ron J. Homer¹, Steven Chang², Griff R. Harsh², Scott W. Atlas¹, Mark D. Bednarski¹

¹Departments of Radiology and ²Neurosurgery

INTRODUCTION

Contrast enhanced magnetic resonance imaging (MRI) using the contrast agent Gd(DTPA) can reveal imaging features associated with increased vascular permeability, vessel density, and areas of fluid accumulation and necrosis. Genomic analysis of solid tumors, like Glioblastoma multiforme (GBM), is difficult due to morphological heterogeneity. We hypothesized that contrast enhanced MRI can be used to guide sample acquisition for genomic analysis with more information about the characteristics of the sampled area than would be obtained without such image-based tissue sampling. Specifically, the comparison of genomic array information from contrast enhancing areas (CE) of GBM relative to areas that do not take up contrast (non-enhancing areas, NE) within the same tumor can reveal important molecular targets for the development of new diagnostic and therapeutic agents.

METHODS AND MATERIALS

Patients presenting with GBM, without any prior surgical, chemotherapy, or radiation interventions were recruited for tissue sampling at the time of their surgical resection. All patient were scanned on a clinical 1.5T GE MRI scanner using standard T1 and T2-weighted sequences, with Magnevist (Berlex) as contrast agent. Samples from CE and NE areas were obtained from each patient and used for genomic profiling using oligonucleotide microarray analysis (Figure1).

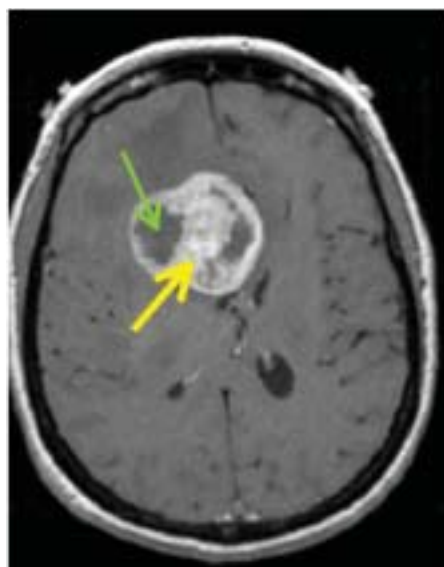


Figure 1: Contrast-enhanced MRI of a patient with GBM. Green arrow indicates an area within the tumor that is not enhancing (NE), yellow arrow indicates a contrast enhancing area (CE).

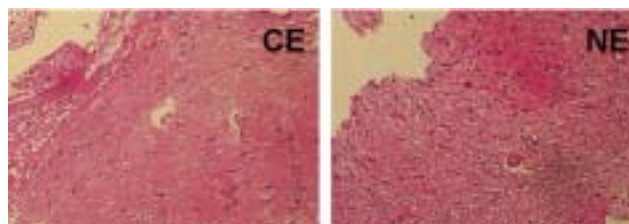


Figure 2: Hematoxylin and Hematoxylin and eosin (H&E) stained tissue samples obtained from marked areas on Figure 1.



Figure 3: Immunohistochemical staining of aFGF (a growth factor involved in angiogenesis). The upregulation of aFGF mRNA from the genomic analysis correlates with the upregulation of this gene product in the CE area of the tumor vasculature as compared with the vessels in the NE area.

Immunohistological staining was used to confirm the upregulation of the protein products of these genomic targets.

RESULTS

Results from 6 patients indicate that genes upregulated in the contrast enhancing areas are mostly related to angiogenesis, cell adhesion, and cell motility. Immunohistological staining confirmed the upregulation of the protein products of some of these genomic targets. Since these proteins are being produced in regions with high vascular permeability, we are currently evaluating their presence in the blood, urine, and CSF of GBM patients.

CONCLUSIONS

The evaluation of genomic data using imaging to sample areas of vascular permeability to identify targets for the detection of blood markers and development of therapeutics is a new approach for the use of genomic data for target identification.

MOLECULAR IMAGING

Magnetic Resonance Image Guided Proteomics of Human Glioblastoma Multiforme

Gongyi Shi, Susan K. Hobbs, Samira Guccione, Mark D. Bednarski

Department of Radiology

INTRODUCTION

Currently, proteomic expression profiles of cancer patients are being correlated with clinical presentation patterns, surrogate markers of disease, and pathological evaluations (1). The goal of these studies is to identify new cancer targets to make definitive diagnosis and to ultimately understand and track mechanistic events during disease progression and response to therapy. Imaging is a diagnostic tool that can play an important role in correlating molecular pathophysiology and the clinical management of disease. Contrast-enhanced MRI is an imaging modality that can provide high spatial resolution and molecular signatures of both normal and diseased tissue in solid tumors (2). It has been demonstrated that malignant tumors tend to have faster and higher levels of contrast enhancement when compared to normal surrounding tissues. Glioblastoma multiforme (GBM) is the most common primary and malignant brain tumor in humans. Here we describe the first use of magnetic resonance imaging (MRI) to guide proteomic analysis in human GBM.

METHODS AND MATERIALS

Images were acquired with a 1.5-T MRI scanner (GE Medical Systems). After the administration of a single dose (0.1 mmol/kg) gadopentate dimeglumine, spin echo T1-weighted images were obtained. Sites for tissue sampling were determined on the basis of the post-contrast T1-weighted images. The tissue samples were obtained at the time of surgical resection guided by the MR images and snap-frozen on dry ice. Samples were stored at -80°C until further analysis. Four individuals with confirmed diagnosis of GBM and MR images were studied and all samples were analyzed in triplicate. Protein profiles for this study were performed on an immobilized copper ProteinChip (IMAC-Cu+) due to its reproducibility and high protein capacity as observed in this study. Crude protein extracts were analyzed on the Protein Biology System time-of-flight (TOF) mass spectrometer (CiphaGen Biosystems, developed for mass spectral protein detection and proteomic analysis.

RESULTS

CONTRAST ENHANCING (CE) VS. NON-ENHANCING (NE) REGIONAL DIFFERENCES WITHIN INDIVIDUALS

Based on the contrast enhancement pattern, a comparison was made between tissue samples from NE and CE regions. Figure 1A shows a representative comparison of the protein profiles obtained from the corresponding regions on the MR image. Certain proteins appear to be common to all individuals in both CE and NE regions, as indicated by the arrows, and these were used as internal controls. The presence of small molecular weight proteins, high number of species is in accordance with the hypothesis that the CE region is the site of proteolysis. This is in agreement with the destruction of the basement membrane, presence of matrix metalloproteases (MMPs), increased vascular density and permeability associated with angiogenesis. Both regions in all individuals were confirmed to contain histological features of GBM as illustrated in Figure 1B.

CE VS. NE REGIONAL DIFFERENCES ACROSS INDIVIDUALS

To investigate the potential of determining if a characteristic protein profile of GBM could be obtained on the basis of contrast enhancement parameter, all NE regions and all CE regions from the 4 individuals were compared (Figure 2). The NE regions across the different tumors did not vary significantly, and thus could be used as a characteristic protein profile for GBM. On the other hand, the CE regions were extremely dissimilar and as was noted they varied even within the same patient. These regions also have more protein species than the NE regions. Certain peaks are present in all tumors and within all regions of

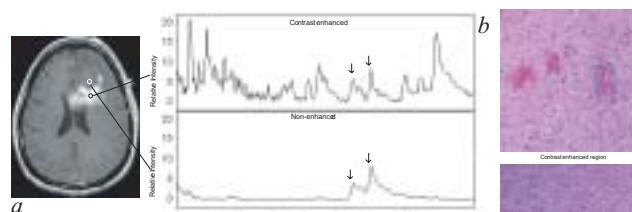


Figure 1: A) T1-weighted MRI of GBM and the protein expression profile of CE and NE regions. The circles highlight the areas where the protein profiles came from. The arrows indicate common proteins found in both regions. B) Hematoxylin and Hematoxylin and eosin (H&E) stained CE and NE regions.

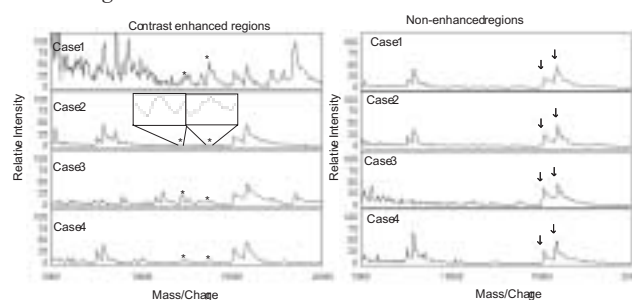


Figure 2: Protein expression profile of CE and NE regions from different patients. Asterisks indicate common proteins in the CE regions and arrows indicate common proteins in the NE region.

the tumor permitting the use of these protein peaks as internal controls for sample-to-sample comparison. Asterisks indicate peaks that were clearly demonstrated to be present in all CE regions as compared to the NE regions. Thus, characteristic proteins exist between individuals in the CE region but the variability in this region is high. In contrast many characteristic peaks are observed between individuals in the NE regions.

CONCLUSIONS

Using T1-weighted MRI to guide tissue biopsies, we examined the protein expression profile from contrast-enhancing and non-enhancing regions within a single tumor mass. We found that 1) there are unique protein profiles that correlate with contrast enhancement patterns, 2) NE region protein profiles are conserved within the same patient, 3) CE region protein profiles are heterogeneous within a patient, and 4) NE region protein profiles are conserved across individuals. We feel, therefore, that contrast enhanced MRI can serve as a powerful tool for characterizing different regions of tumors for proteomic analysis. Results from this investigation clearly show the existence of protein profile differences that correlate to regions of MR contrast enhancement. This study demonstrates that MRI can serve as a powerful, non-invasive tool for deciphering molecular processes that give rise to macroscopic phenomenon such as contrast enhancement in tumors. New MR imaging techniques can provide further discrimination of tissue samples for proteomic analysis.

REFERENCES

1. Ferrari L, Seraglia R, Rossi C, et al. Protein profiles in sera of patients with malignant cutaneous melanoma. *Rapid Communications in Mass Spectrometry* 2000; 14:1149-1154
2. Tynneninen O, Aronen H, Ruhala M, et al. MRI enhancement and microvascular density in gliomas. *Investigative Radiology* 1999; 34:427-434

Comparing Genomic and Histological Correlations to Radiographic Changes in Tumors: A Murine SCC VII Model Study

Yi-Shan Yang, Samira Guccione, Mark D. Bednarski

Department of Radiology

INTRODUCTION

Histological analysis has been widely used for tumor characterization and categorization and often provides the “gold standard” when characterizing tissues that show different imaging characteristics. Alternatively, functional genomic analysis has recently been used to classify new subclasses of cancer that were not defined using histological evaluation. In this paper we report the first use of clinical contrast-enhanced MRI (CE-MRI) to define temporal changes in tumor progression and compare genomic and histological analysis as it correlates to radiographic changes using a mouse tumor model for human head and neck cancers. We performed both functional genomic and histological evaluation at different stages of tumor growth. In many cases, changes in CE-MRI occur with distinct changes in gene expression profiles, while no significant change is observed in histological analysis.

METHODS AND MATERIALS

The squamous cell carcinoma (SCC VII) cell line was used to initiate subcutaneous tumors in mice. This mouse model has been used as a model for human head and neck carcinomas. A total of 20 animals were imaged using CE-MRI in a clinical 3.0T GE Signa MR Scanner with a custom designed quadrature high-pass birdcage coil tuned to 127 MHz for signal reception. T1- and T2-weighted MR images were obtained using standard spin-echo (SE) and fast spin-echo (FSE) pulse sequences, respectively. Different stages of tumor growth were defined based on changes in the T1 and T2-weighted MR imaging patterns. The contrast enhancing (CE) and non enhancing (NE) regions of the tumors were marked and biopsied for oligonucleotide microarray and histological analysis. Tumors with no differential contrast enhancement were used as controls.

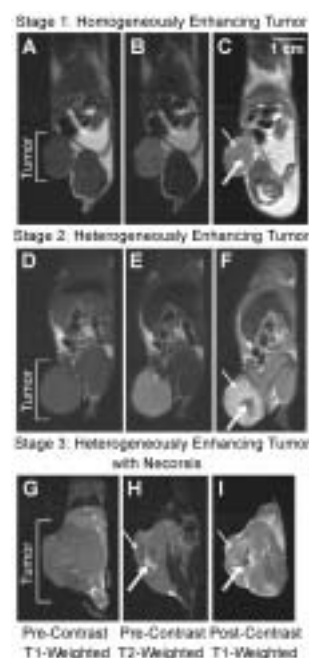


Figure 1: MRI of C3H/K mice with implanted subcutaneous squamous cell carcinoma VII tumors. Images A, D, G: pre-contrast T1-weighted, images B, E, H: pre-contrast T2-weighted, images C, F, I: contrast-enhanced T1-weighted images. The early stage of tumor growth (Stage 1): images A-C, tumors were homogeneously enhanced. The more advanced stage of tumor growth (Stage 2): images D-F, tumors were heterogeneously enhanced. The late stage of tumor growth (Stage 3): images G-I, tumors were heterogeneously enhanced with necrosis. The thick and thin arrows in images C and F indicate the central and peripheral regions of the tumors where the tissue samples were harvested for analysis. The thick and thin arrows in images H and I indicate regions with different T2-weighted MRI characteristics that were also obtained for tissue analysis. Scale bar=1 cm (—).

RESULTS

Distinct temporal stages of tumor progression can be defined using both T1- and T2-weighted CE-MRI and microarray analysis. The early stage tumors show a homogeneous contrast enhancement pattern in the T1- and T2-weighted images (Figure 1A-C) with no significant differential gene expression from the center and periphery of the tumor. The more advanced tumors that show discrete regions of contrast enhancement in the post contrast T1-weighted MR images (Figure 1D-F) and tissues from the CE and NE regions show distinctly differential gene expression profiles. Histological analysis (H&E) showed that the samples obtained from the periphery and center of the early stage tumors (Figure 2A-B), and the CE and NE regions from these more advanced tumors were similar (Figure 2C-D). The gene expression profiles of late stage tumors that showed change in T2-weighted MR signal intensity (Figure 1G-I) was consistent with tissue degradation in the NE region, which also showed characteristic signs of tissue necrosis in histological analysis (Figure 2E-F).

CONCLUSIONS

In the present study we demonstrate that distinct stages of tumor progression can be defined by T1- and T2-weighted MR imaging patterns, and the gene expression profiles obtained for each stage of tumor growth correlated with changes in MRI patterns are unique and significantly different. Histological analysis failed to reveal changes in tissue characteristics at advancing stages of tumor progression (Stage 2), but did confirm regions of necrosis determined by enhancement of the T2-weighted MR image for late stage of tumors (Stage 3). Genomic analysis with image guidance is critical as the gene expression profiles can be significantly different spatially and temporally, and standard histological analysis may not be sufficient to distinguish these differences. This is especially important when relating changes in imaging patterns with pathophysiology and tissue morphology. In conclusion, genomics analysis can reveal a more detailed picture of what occurs at the cellular level when correlating radiographic changes with morphological changes in tissues.

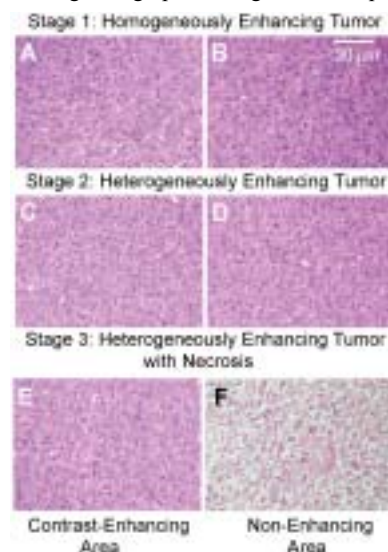


Figure 2: Hematoxylin and eosin (H&E) stained tissue samples obtained as marked by the arrows on Figure 1. Figure 2A is the peripheral and B the center areas of Stage 1 tumors. Figure 2C is the contrast enhancing and D the non-enhancing areas of Stage 2 tumors. Figure 2E is the contrast enhancing and F the non-enhancing areas of Stage 3 tumors. Figure 2A-E show viable tumor cells. Figure 2F shows characteristics that are indicative of necrosis. Scale bar=50 cm (—).

3D Imaging

A Theoretical Stochastic Model of Anatomy: Analysis of a Computer Aided Diagnosis Algorithm

David S. Paik, Sandy Napel

Department of Radiology

INTRODUCTION

Numerous computer-aided diagnosis (CAD) algorithms have been developed for a variety of radiological interpretation tasks. Often, however, the algorithms are developed in an *ad hoc* manner without a solid theoretical model of the anatomy being analyzed. Because shape is such a nebulous concept and anatomic variability is even harder to quantify, few satisfying models of anatomic shape have been developed. We have developed a simple, yet powerful, stochastic shape model that models the surface characteristics of both lung and colon anatomy.

METHODS AND MATERIALS

The model has three steps. It begins by treating each specific type of anatomy as a quadratic surface (e.g. lung nodules as spheres, pulmonary vessels as cylinders, colonic polyps as hemispheres, and haustral folds as half-cylinders). Then, each infinitesimal surface patch is then allowed to move inward or outward by a distance that follows a Gaussian distribution. Finally, the direction surface normal is allowed to deviate from its nominal direction following a Rayleigh distribution (often used to model the 2D spatial distribution of randomly thrown darts with a 2D Gaussian distribution).

We have then validated the model by estimating the distributions from chest CT and CT colonography data and comparing to theoretical prediction. To do this, we used a Canny edge detector to find and isolate the surface normals corresponding to a given anatomic feature. A least squares fit of the appropriate quadratic surface was performed and then the radial and directional variations from the quadratic surface were computed directly by simple geometric analysis.

RESULTS

An example of the empirically measured radial and directional variation histograms is compared to the theoretical model for a cylindrical pulmonary vessel and shown in Figure 1.

CONCLUSIONS

We have developed a novel stochastic model of anatomic shape that models the surface characteristics. The theoretical model matches empirical distributions well and is currently being used to provide a non-trivial theoretical analysis of a CAD algorithm that we have developed for detecting both lung nodules and colonic polyps from Computed Tomography.

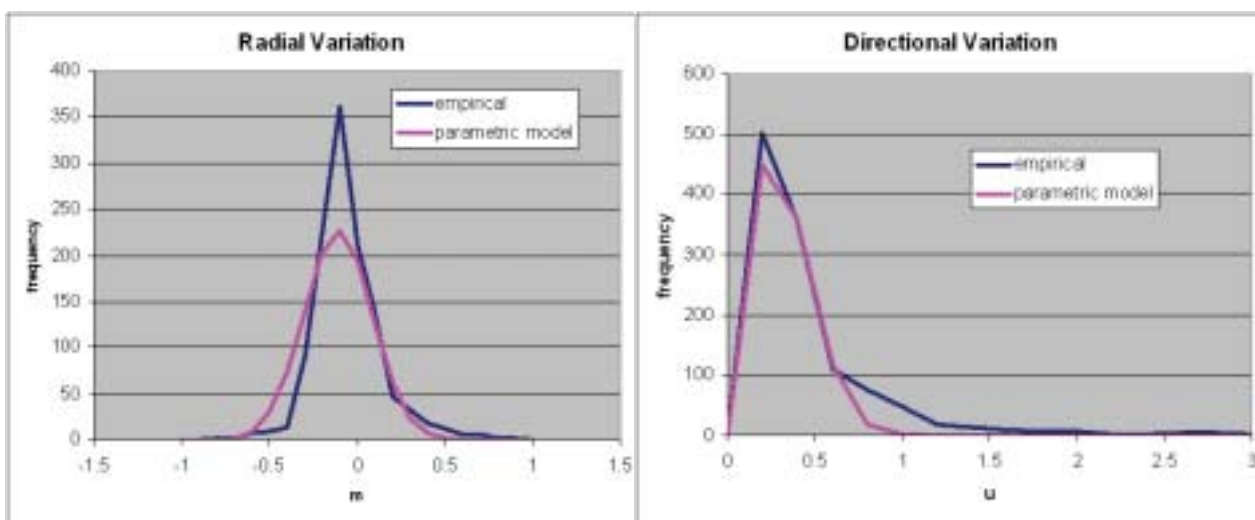


Figure 1: An example of the match between empirical measurements and the theoretical model for a pulmonary vessel.

3D IMAGING

Computer Aided Diagnosis of Lung Nodules in a Pediatric Population

David Paik, Sabrina Flunker, Geoffrey D. Rubin, Sandy Napel

Department of Radiology

INTRODUCTION

Early detection of lung nodules is an important task. While detection of lung nodules in helical computed Tomography (CT) is more sensitive than chest X-ray, interpretation of these large datasets can be daunting due to the large number of axial slices. Identifying lung nodules specifically in pediatric populations is also an important task, especially pulmonary metastases from Wilm's tumors, osteosarcoma, Ewing sarcoma, rhabdomyosarcoma, fibrosarcoma, lymphoma, and germ cell tumors. We have developed and are in the midst of evaluating a computer-aided diagnosis (CAD) system for detecting lung nodules in pediatric chest CT.

METHODS AND MATERIALS

We have developed a CAD method called Surface Normal Overlap that we have successfully applied to both detecting colonic polyps and lung nodules in adult populations. There were several factors that required adapting the algorithm for a pediatric population including increased motion and breathing artifacts, reduced inspiration volume, and anterior-posterior gradients in lung parenchyma density. After developing adaptive algorithms to handle these factors, we have applied the algorithm to a dataset of 21 patients ranging in age from 9 months to 18 years old. The patient cohort included a wide variety of diseases including those listed in the Introduction, as well as non-specific nodular densities.

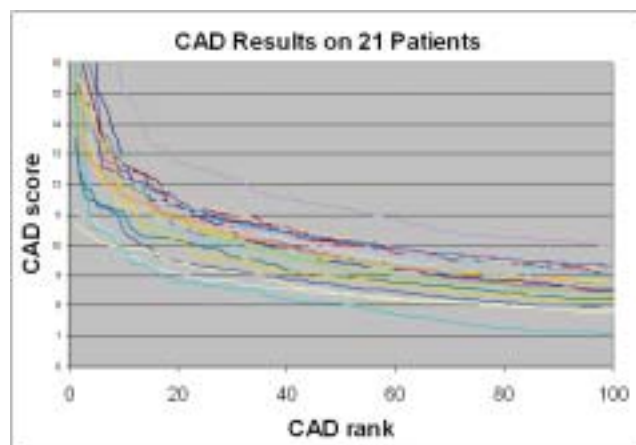


Figure 1: The lung nodule CAD scores of 21 pediatric patients (each colored line represents one patient) as a function of CAD rank.

RESULTS

The algorithm has been applied to all 21 patients and the resulting CAD scores are shown in Figure 1 as a function of CAD rank. The reference standard (i.e., the "truth") is currently being set by a consensus panel of 2 radiologists who are carefully reviewing the original data, findings from 3

unaided readers, and the findings from the CAD algorithm using both 2D MPR views as well as a 3D volume rendered view. In addition, we are also comparing the accuracy and efficiency of human interpretation with and without help from CAD. For reading with help from CAD, all algorithm detections above a threshold are indicated on a second set of images and presented to the reader, as illustrated by Figure 2.



Figure 2: An example of a Lung CT image with CAD markup (circle plus rank text).

CONCLUSIONS

We have developed a CAD system for detecting lung nodules in pediatric populations that will be used to aid in both the accuracy and efficiency of interpreting these large CT datasets.

Calcium Quantification in the Aortoiliac Arteries: Interscan Variability of Agatston Scoring vs. Automated Mass Quantification in Non-Contrast and Contrast-Enhanced Scans

Bhargav Raman¹, Raghav Raman¹, Mercedes Carnethon², Stephen P. Fortmann², Sandy Napel¹, Geoffrey D. Rubin¹.

¹Department of Radiology, ²Stanford Center for Research in Disease Prevention

INTRODUCTION

Traditionally, quantification of the extent of arterial calcification has been accomplished using the Agatston score, originally developed for the assessment of coronary calcifications. However, this score is arbitrary and has suffered from a high variability, decreasing its accuracy and making it difficult to use for patient follow-up. In contrast-enhanced scans, this problem was accentuated by variability in the level of contrast enhancement achieved in each scan. We had previously developed an automated mass quantification algorithm for quantifying the actual mass and distribution of dystrophic vascular calcification as detected on CT Angiograms acquired using multi-detector CT scanners that corrects for contrast enhancement. We aimed to compare the interscan variability of aortoiliac calcium quantification using traditional Agatston scoring (AS) to mass quantification with contrast correction using our algorithm.

METHODS AND MATERIALS

We scanned 22 patients (11 male, 11 female, 11 with cardiovascular disease) from the mid neck to the termination of the popliteal arteries in the lower legs. Scans were acquired using a 16-row multi-detector CT scanner at 120kV, 200mA, 0.5s rotation and 1.25 mm slice thickness with 50% overlap, using non-contrast and contrast-enhanced scanning protocols. To assess interscan variability, the contrast scan was repeated in 10 patients and the non-contrast scan was repeated in 12 patients. The amount of contrast injected was targeted to achieve arterial attenuation of approximately 100 HU (25-45 ml). Median centerline paths were calculated from the aortic root to the termination of both popliteal arteries. The Agatston score and the mass of mural calcium fragments were then automatically quantified by a previously developed algorithm that uses a conversion factor derived from standards of known calcium density included in the scan field. Absolute interscan variability (v) was measured per scan and per fragment. Percentage interscan variabilities were compared using two-tailed paired t-tests.

RESULTS

Patients had an average Agatston score of 2064.4 ± 2453.7 , with an average mass of 355.4 ± 425.9 mg of calcium. Non-contrast scans had an v of 6.9 ± 6.7 mg ($5.3\% \pm 4.8\%$) per scan; Agatston scores had a significantly higher v of 140.7 ± 190.9 units ($12.2\% \pm 8.2\%$, $p < 0.01$) per scan. Per fragment v in non-contrast scans was 2.3 ± 1.2 mg ($14.91\% \pm 4.9\%$) for mass; Agatston scores had a significantly higher v of 22.2 ± 18.1 units ($23.6\% \pm 13.6\%$, $p < 0.05$). Contrast scans had a v of 9.3 ± 8.4 mg ($8.5\% \pm 6.4\%$) while Agatston scores had a significantly higher v of 261.5 ± 292.4 units ($26.5\% \pm 20.4\%$, $p < 0.05$) per scan. Per-fragment v in contrast scans was 2.9 ± 1.5 mg ($16.2\% \pm 5.3\%$) for mass; Agatston scores had a significantly higher v of 43.7 ± 29.8 units ($32.5\% \pm 16.4\%$, $p < 0.05$). There was no significant difference in v of mass between contrast and non-contrast scans per scan ($p = 0.743$), and per fragment ($p = 0.329$) while v of Agatston scores was significantly higher in contrast versus non-contrast scans per scan ($p < 0.05$) and per fragment ($p < 0.05$).

CONCLUSIONS

We have shown that automated calcium mass quantification with contrast correction has a lower interscan variability than traditional Agatston scoring in both non-contrast and contrast scans. Additionally, the variability of mass quantification is not adversely affected by the contrast enhancement level of the arteries, due to the contrast correction applied. This potentially allows more accurate calcium quantification in contrast-enhanced scans. Changes in the level of contrast enhancement along a vessel can be taken into account using this algorithm. Contrast correction also enables serial scans with varying contrast enhancement to be used for patient follow-up. The quantification of calcium mass has the potential to replace Agatston scoring as the preferred measure of the extent of dystrophic vascular calcification.



Figure 1: Our algorithm allows automated output of a surface calcium map that displays the density and distribution of calcium on the vessel surface from the aortic root (AR) to the left popliteal artery (POP). AA-aortic arch. CA-celiac artery branchpoint. IR-Inferior (right) renal artery branchpoint. AB-aortic bifurcation. IB-left iliac bifurcation. FEM-commencement of left femoral artery.

3D IMAGING

Optimization of CT Scanning Protocol for Calcium Quantification in the Systemic Arteries using Multi-Detector CT

Raghav Raman, Bhargav Raman, Sandy Napel, Geoffrey D. Rubin

Department of Radiology

INTRODUCTION

We performed a comprehensive optimization of the multi-detector CT scanning protocols to maximize accuracy and reproducibility of our automated algorithm for quantification of the mass and distribution of calcium in the arteries of the body.

METHODS AND MATERIALS

28 calcium fragments (0.3-40 mg of elemental calcium) were prepared from three standard materials (calcium density 0.1-0.3 mg/mm³) and placed in four physical vessel phantoms. These phantoms were scanned using a 16-slice CT scanner at 80kV/200mAs, 100kV/210mAs and 120kV/220mAs (high dose) and 100kV/100mAs and 120kV/60mAs (low dose). Slice thicknesses (ST) of 0.625-2.5 mm each with 0% and 50% slice overlap and iodinated contrast at concentrations of 0%-2% were used. Scans were repeated with identical protocols to assess interscan variability. The Brightness-Volume Product (BVP) of each fragment was measured at multiple thresholds. From the linear series thus obtained, a best-fit line is calculated and extrapolated to calculate the BVP that would be obtained if a threshold of 0 HU (corresponding to water) was used (BVP0). True fragment mass is calculated from BVP0 using a conversion factor derived from standards of known calcium density from 0 mg/ml (water intensity) to 200 mg/ml included in the scan field. The mass of each fragment was quantified in each scan and the error in measurement was recorded as the difference between the measured and actual mass. Statistical significance was assessed using two-tailed t-tests.

RESULTS

The CT Dose Index (CTDI) ranged between 3.21 and 14.44. For all scans, the signed error was not significantly different from zero. Average absolute errors (AE) ranged between 0.74 mg and 3.15 mg (5.6-29.4%). In noncontrast scans, the lowest AE was 0.74 mg (5.6%, $p < 0.05$) achieved with 80kV/200mAs, 0.6 mm ST and 0.3 mm slice spacing (CTDI 4.07), though increasing the ST to 1.25 mm with 50% overlap (CTDI of 3.21) did not have a significantly higher AE (0.81 mg, 6.3%). Scans at 100kV and 120kV had significantly higher AE. Contrast enhancement ranged from 222-383HU. AE in contrast scans was significantly higher than in noncontrast scans ($p < 0.01$). The lowest AE was 1.60 mg (16.9%) at 120kV/220mAs, 1.25 mm ST and 50% overlap (CTDI 11.64). An ST of 2.5 mm with 50% overlap at 120kV/220 mAs (CTDI 9.38) did not have a significantly higher AE (1.85 mg, 19.5%). Low dose contrast scans at 120kV/60mAs (CTDI 3.21) had a significantly higher AE of 2.07 mg (21.8%, $p < 0.05$). All scans at 80 and 100kV had significantly higher AEs (2.14-3.15mg, 20.1-29.4%, $p < 0.05$). Interscan variability in noncontrast scans was 0.27 mg (1.8%), which was not significantly different from that in contrast scans (0.38 mg, 2.8%, $p = 0.24$) or in low dose scans (0.35 mg, 2.6%, $p = 0.27$).

CONCLUSIONS

Protocol optimization allows very high accuracy to be achieved in noncontrast scans. In contrast scans, absolute error can be limited to 1.6mg in high dose and 2.1mg in low dose scans with no increase in interscan variability. An optimized CT scanning protocol can increase the potential for systemic calcium quantification to be used as a tool for risk factor measurement, epidemiological studies and patient follow-up.

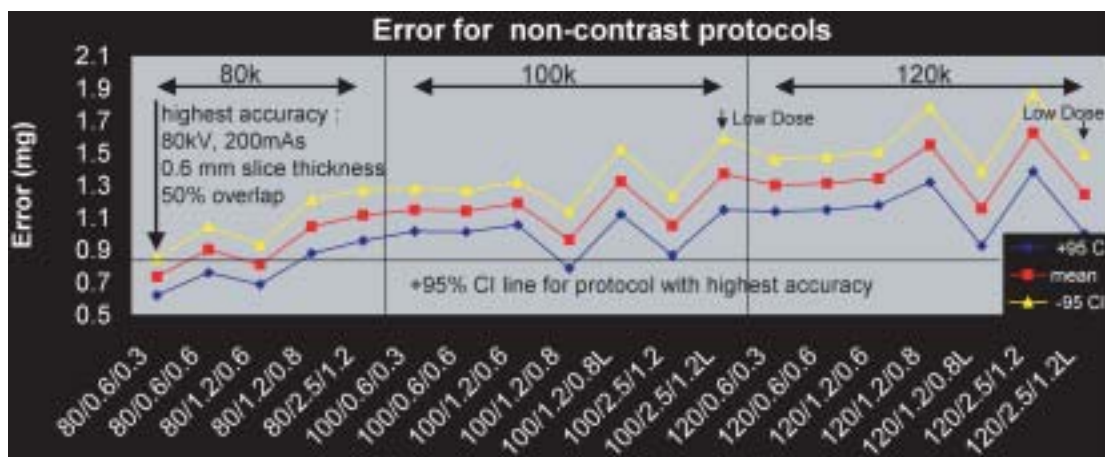


Figure 1: Noncontrast scans had the highest accuracy (lowest error). Almost all scans at 100kV and 120kV had a higher error than the best 80kV scan, except for one scan which had a very small overlap of confidence intervals (100kV, 1.2mm slice thickness, 0.8mm slice spacing). All low dose scans had a higher error, but the 80kV scans all had the same CTDI as the low dose scans, making 80kV the best choice for non-contrast scans.

Lung Nodule Evaluation Program (LNEP)

Anthony Sherbondy¹, Geoffrey Rubin², Sandy Napel^{1,2}

¹Departments of Electrical Engineering and ²Radiology

INTRODUCTION

We present a Lung Nodule Evaluation Program (LNEP) that uniquely combines advanced volume visualization algorithms for the purpose of detecting and characterizing lung nodules.

METHODS AND MATERIALS

The LNEP allows the evaluator to explore a scalar volume, currently obtained by CT, with multi-planar reformatted slices of the volume, Sliding Thin Slab Maximum Intensity Projections [1], a freely rotating oblique view known as the Cartwheel slice, nodule size measurement tools, a 3D texture mapped volume rendering, and a nodule management window. The management window lists candidate detections made by humans and/or Computer-Aided Detection (CAD) algorithms. All visualization tools are synchronized with the nodule management window so the operator may efficiently peruse suspect locations in the data set. Most of the image processing tools presented in the LNEP take advantage of programmable commodity video cards, originally developed for computer gaming programs, in order to maintain a fast and responsive interface. Figure 1 demonstrates the LNEP on CT images from a patient with pulmonary nodules.

RESULTS

Three radiologists have used the LNEP to evaluate over 4000 candidate sites identified from 43 patients. Candidate detections arose from our developing CAD algorithm [2,] as well as from other radiologists using traditional PACS viewing stations. Studies are undergoing to evaluate the LNEP's influence in the accuracy and efficiency of diagnostic radiology in the setting of pulmonary nodule detection.

CONCLUSIONS

Incipient results and communication with current users indicates that the LNEP is a promising method for enhanced nodule assessment, especially when paired with a CAD algorithm such as described in [2].

REFERENCES

1. Napel S, Rubin GD, Jeffrey RB Jr. STS-MIP: A new reconstruction technique for CT of the chest. *J Comput Assist Tomogr* 1993; 17:832-838
2. Paik DS, Beaulieu CF, Jeffrey RB, Karadi CA, Napel S. detection of polyps in CT colonography: a comparison of a computer aided detection algorithm to 3D visualization methods. Radiological Society of North America 85th Scientific Sessions, Chicago, IL, November 1999. *Radiology* 213(P):197

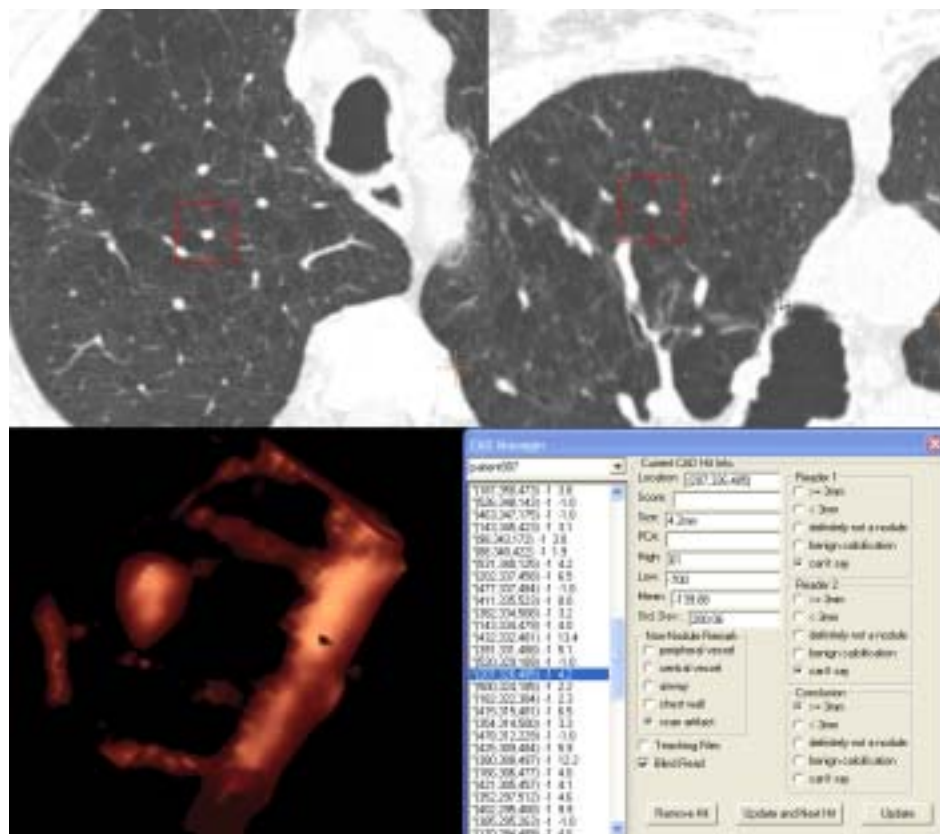


Figure 1: The top half of the LNEP interface is dedicated to the cross-sectional views of the volume data. The top half is split between an axial reformatted image and a coronal reformatted image. The red box in the image planes denotes the current nodule as chosen in the nodule manager in the lower right corner. The axial and coronal windows can also show cartwheel views, which are invoked by clicking and dragging on the edge of the red box to rotate the cutting plane through arbitrary angles, as well as sliding thin slab maximum intensity projections. The lower left corner is dedicated to a 3D texture mapped volume rendering, which can be rotated and scaled at will, of the cube of data denoted by the red box.

INTRODUCTION

We propose a fast segmentation method that leverages the computational power of modern programmable graphics hardware to combine some of the successful components of automated algorithms efficiently with real-time animation of the segmentation's progress [1]. This algorithm is unique in that it utilizes sophisticated functionality recently exposed in graphics hardware (*i.e.*, floating point precision, render to texture, fragment programming and Z culling for computational masking) to enable fast segmentation and interactive visualization.

METHODS AND MATERIALS

The segmentation algorithm is based on seeded region growing with the merging criteria based on intensity and gradient values, and with the gradient sensitivity scaled using nonlinear diffusion. The implementation of this algorithm consists of four stages: seed selection, segmentation evolution, optional image smoothing, and computational masking. Figure 1 shows a block diagram of the algorithm.

The user is able to paint seeds into voxels in the volume using a paintbrush metaphor. The user can scroll to the section of interest and paint on a cutting plane that reveals some of the desired structure. As the user draws with the cursor on the cutting plane, spherical seed populations are placed into the scene. The seeds are then evolved using a Perona-Malik nonlinear diffusion metric to grow across regions of low gradient and stop growing across edges. Figure 2 shows an example of the use of the program.

We also propose a solution to the common problem of sparse field computation on graphics processor units (GPUs), by utilizing the Z

culling capability of the GPU to limit computation of the segmentation evolution to a one-voxel dilation around voxels that have a seed population greater than zero. Figure 1 shows a slice of the computation mask during the segmentation of an aortic aneurysm.

RESULTS

All results were collected using an ATI Radeon 9800 Pro with 128MB of onboard memory on a 2.4GHz Pentium 4 with a 533MHz front side bus. We utilized a 128x128x128 volume of 16-bit intensity data from a CT scan for all presented results.

Each execution of the segmentation fragment program requires 0.22 ms and is one of the more costly components of our algorithm. Just doing the 3D texture lookup from within a fragment program takes 0.09 ms of that time. To perform any computation, we need to flip-flop textures, which costs an additional 0.04 ms. This gives a total time of 0.26 ms for each slice of the volume, or 33 ms per full volume iteration. Without considering the savings from computational masking, the segmentation algorithm is capable of sustaining 3.5 GFlops and processing 64 MVoxels/s, or 128 MB/s, of volume data. With the computational masking enabled we are able to more efficiently process voxels that only contribute to the segmentation. When compared to an SSE optimized version of the same algorithm run on the CPU, of the machine, the proposed GPU algorithm runs 10-20x faster.

CONCLUSIONS

Our segmentation method allows interactive visualization and control because of its computation speed and coordination with a hardware accelerated volume renderer. In addition, using the GPU for general computation will become even more advantageous as graphics processors continue to outpace the performance of CPUs. Also, through the use of computational masking we are able to use the computational resources of modern graphics hardware more effectively. These advances will allow much more efficient and accurate viewing of large volumetric datasets.

REFERENCES

1. Sherbondy A, Houston M, Napel S. In Press *IEEE Visualization*

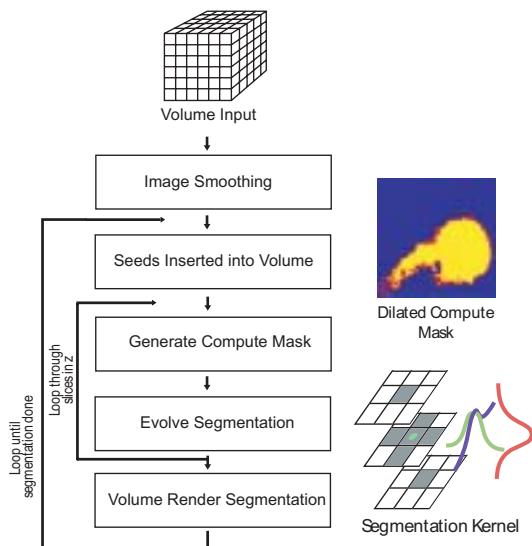


Figure 1: Simplified implementation of our segmentation algorithm. The image smoothing stage is optional and only included for noisy images. The dilated compute mask inset to the right shows the current seeds in yellow, the six-neighbor dilation in red, and the masked out portion in blue. The segmentation inset describes the explicit diffusion kernel in which the six neighbors are weighted by scaled Gaussians that differ in shape based on each neighbor's direction to calculate the value of the current pixel. Note that the computation renders to sections of the 3D texture and therefore must iterate through all sections in the z direction before a complete volume iteration has been computed.

Figure 2: Current interface to the interactive segmentation program. The user is able to browse the volume data with the tomogram or axial cutting plane. The user can then draw on the cutting plane with the mouse as the volume rendering shows what the user is drawing, while the segmentation algorithm evolves the drawn seeds according to a diffusion metric.

3D Coronary Artery Center Path Detection in MDCT Angiography using a 2D Cross-correlation Filter

Weite Lin, Frandics P. Chan, Sandy Napel

Department of Radiology

INTRODUCTION

Accurate depiction of coronary arteries in medical images is important for quantitative diagnosis and surgical planning. It is challenging due to small artery size, noisy image acquisition, low spatial and temporal resolution, and cardiac motion. One technique, Curved planar reformation (CPR), has been shown to be useful for the display for blood vessels, but creating a CPR requires extraction of the vascular centerline and is usually labor intensive. Although automated algorithms have been developed to generate the centerlines, accurate extraction relies on proper segmentation of the vascular structures, and it performs poorly for small vessels of low contrast-to-noise ratio. We developed a fast and robust algorithm based on a 2D normalized cross-correlation pattern matching filter to automatically detect and enhance the centerline of a blood vessel. Our approach reduces the 3D problem to 2D one, which dramatically reduces the computational load.

METHODS AND MATERIALS

Normalized cross-correlation is computed between a template (designed to detect a tubular structure, e.g., a blood vessel) and the test image at many different vessel orientations. The output indicates the possibility of a voxel being part of a vessel, and the closeness of the voxel to its centerline. We tested our method using data from six patient examinations using multidetector CT to image their hearts. We then used an existing computer program to generate the coronary centerlines from the output of the cross-correlation. We compared the output of this program to centerlines manually generated by a cardiac radiologist. Errors were computed as the average distance between the automatically- and manually-generated centerlines.

RESULTS

Figure 1 shows one slice of a CT volume of the heart, and the filtered output, showing that the artery has been enhanced by its high correlation value and can be segmented easily. Figure 2a shows that the accuracy of the paths generated after 2D cross-correlation are comparable to 3D cross-correlation; both are more accurate than paths generated without any processing. Another plot Fig. 2b shows that it is also easier to segment and obtain accurate paths with using our method. For a test that uses three template sizes, the computation for the 2D matching is at least 100 times faster than the 3D matching.

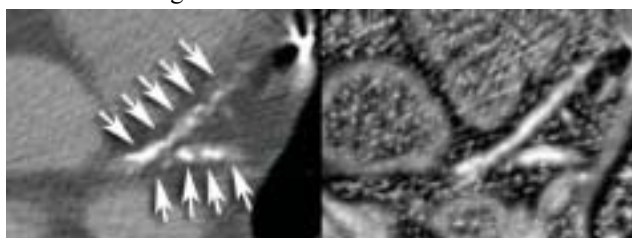


Figure 1: Left: image heart showing coronary arteries (arrows) with severe calcification. Right: filtered image shows enhanced arteries.

CONCLUSIONS

Our 2D matching method dramatically reduces the computation and increases accuracy. The algorithm is shown to be robust and highly effective in enhancing coronary arteries. It increases the reliability of isolating vessels from surrounding tissues, in turn, improves the efficiency and accuracy of vessel segmentation and automated center path generation for high quality CPR. It also reduces the amount the human interaction required CPR.

REFERENCES

1. Paik DS, Beaulieu CF, Jeffrey RB, Rubin GD, Napel S. Automated flight path planning for virtual endoscopy. *Medical Physics*, 1998; 25:629-37

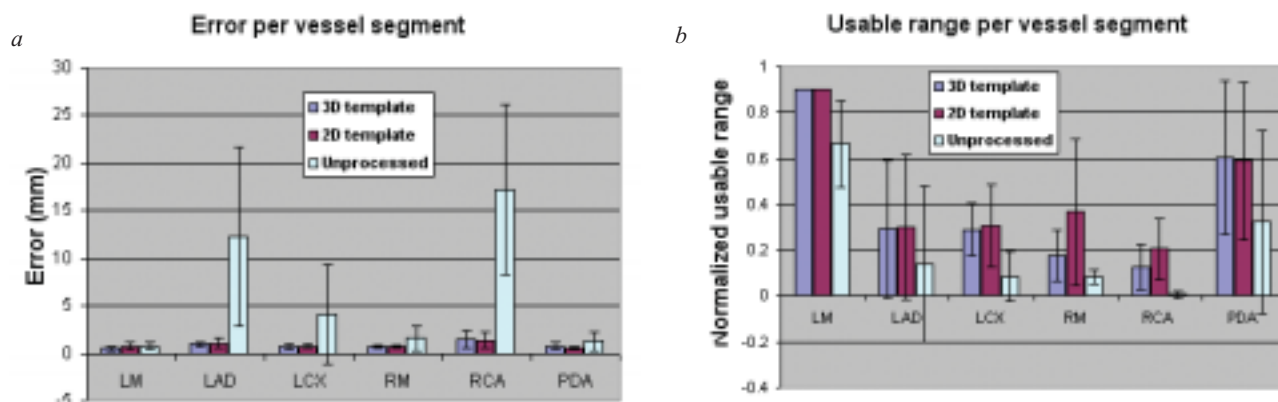


Figure 2: (a) Average path errors between estimated and gold standard for major arteries. (b) Usable threshold range that allows accurate segmentation and path generation.

3D IMAGING

3-D Visualization and Quantitation: Clinical Applications

Geoffrey D. Rubin, Sandy Napel, Laura J. Logan

Department of Radiology

MISSION AND GOALS

The mission of the 3-D medical imaging laboratory is to develop and apply innovative techniques for efficient analysis and display of medical imaging data through interdisciplinary collaboration. Our clinical goal is to deliver these advances as rapidly as possible following validation as services to the Stanford and worldwide communities. Our education goal is to train physicians and technologists locally and worldwide in the latest developments in 3-D imaging.

PROGRESS

INFRASTRUCTURE

The 3-D laboratory is on the first floor of the Lucas Center and includes space for four 3-D technologists, a software engineer, an administrative assistant, as well as cubicles and workstations for 6 students/post-docs/visiting scholars. A central area table accommodates ten advanced workstations for processing of clinical cases, and for research and development. A 50-inch wall mounted plasma display television monitor, with 1280 x 768 XGA resolution, aids in teaching and display of our work. Four General Electric Advantage Windows workstations are used to process 80% of the clinical cases. The remainder are processed on a Windows NT workstation running Vitrea software (Vital Images, Inc.), a W2K Aquarius 3-D workstation (TeraRecon, Inc.), and another W2K workstation running software for grading coronary calcification studies (AccuImage, Inc.). Real-time volume rendering is available to physicians over the network with our two AquariusNet servers (TeraRecon, Inc.). All workstations are linked to and supported by a 10/100 Mb/s switched network. This year we upgraded two of our GE Advantage Windows workstations with the new 4.1 software, designed for speed and efficiency on the HP x4000 Linux based platform.

We are also expanding our operation into the James H. Clark Center, a new building dedicated to interdisciplinary science. This opportunity will facilitate increased interactions between radiologists, clinicians, and researchers who seek to extend volumetric analyses into their practices and research programs.

CLINICAL

The clinical arm of the laboratory is staffed by four full-time 3-D technologists (Laura Logan, 3-D lab manager, Linda Novello, Sean Lee, and Marc Sofilos), an administrative assistant (Lakeesha Winston) and attended by a rotation of body fellows and radiology residents. New processing techniques have been introduced into clinical

practice this past year, including automatic bone removal and segmentation, and cardiac mass analysis and function. Our laboratory is a model for the future of 3-D interpretation and communication in radiology, with Laura, Linda, Sean, and Marc functioning as the world's leading and most accomplished 3-D technologists. We continue to regularly receive visits from radiologists and technologists from around the world, who wish to understand and duplicate our operations within their own departments. Many stay for several days of intensive hands-on training. In addition, we have excellent relationships with corporate developers of 3-D workstations (e.g., General Electric, TeraRecon, and Vital Images) who site their hardware here in anticipation of our valuable feedback.

The introduction of two new 16-row multidetector CT scanners at the medical center in 2002 has contributed to an increase in the number of exams processed by the lab (*Fig. 1*). Thus far, our annual 3-D volume is up 49% compared with last year. 88% of our referrals are from CT, and the remainder are from MRI.

We have provided reports to referring clinicians in Vascular, Cardiothoracic, Pediatric, Transplant, Neuro, Plastic and General Surgery, as well as Cardiology, Pulmonary Medicine, Orthopedics, Gastroenterology, Urology, and ENT. Outside referrals come not only from physicians at other Bay Area hospitals, but from hospitals in other states. Following 3-D analysis, we provide dedicated 3-D reports, including color images and the results of quantitative analyses (diameters, angles, tissue volume, and path lengths). These are universally preferred by the referring physicians, compared to viewing the hundreds or thousands of cross-sectional images generated by the scanners. In addition, all 3-D renderings are stored on Radiology's central PACS server and/or on the Web so that they can be accessed with the standard images and reports. Results of quantitation are stored in databases for future reference and statistical analyses.

We also work with medical device developers who use our expertise to evaluate their current and future products. These companies include Medtronic AneuRx, Biosense Webster, and CorazÛn Technologies, manufacturers of chest and abdominal aorta stent-grafts, balloon catheters, and drug therapies.

CONCLUSIONS

The 3-D Medical Imaging Lab continues to function as a major clinical and research facility. The confluence of clinical, medical, and engineering expertise has resulted in a steady stream of new developments of diagnostic and treatment planning approaches. It continues to advance the Department and the Lucas Center as leaders in this aspect of medical imaging science.

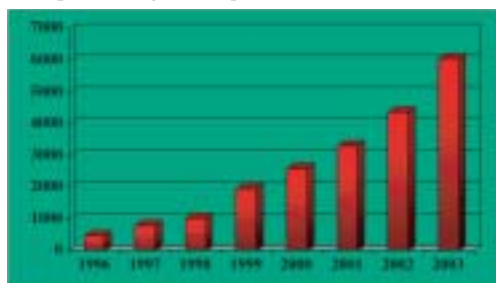


Figure 1: Case volume since inception. 2003 volume is estimated, and amounts to an average of 500 cases/month

An Automated System for the Creation and Management of Vascular Measurements in the 3-D Lab

Lalithakala Raman, Raghav Raman, Bhargav Raman, Sandy Napel, Geoffrey D. Rubin, Laura J. Logan

Department of Radiology

INTRODUCTION

As CT becomes a more commonly used diagnostic tool for the evaluation of vascular disease, the demand for the postprocessing of datasets is increasing. In addition to clinical use, the data is also used to conduct retrospective statistical analyses to investigate the natural history of vascular disease. However, because of the variety of data that can be collected, and the numerous measurement protocols used by Stanford Medical Center for the evaluation a patient, an organized, managed database was needed to keep track of the data. We have developed a database system to produce the required reports for clinical use and maintain the integrity of the data for future querying and analysis.

SYSTEM DESCRIPTION

SYSTEM

The database was developed using off-the-shelf hardware and development environments. On-the-fly web-page generation was accomplished using Active Server Pages (Microsoft, Redmond, WA). The back-end database was developed using Microsoft Access and is hosted on a server with Internet Information Services 6.0 running on Windows Server 2003.

STANDARDS

The system creates and maintains data on a wide variety of measurement protocols and standard measurement descriptions. These are used to guide the 3-d technologists in acquiring and entering the data into the database.

DEVELOPMENT PROCESS

The combined effort of all the 3-d technologists and administrative staff was very efficient in recognizing the workflow and format of the reports which in turn enabled the fast and positive development environment to produce a successful system.

USER INPUT

The forms used by the technicians are available solely to authenticated users on the hospital intranet for measurement entry and clinical report generation in any part of the hospital. The system presents a dynamic preformatted form displaying the desired protocol and specified measurement descriptions. The technicians fill in the measurement values only. Measurements entered are automatically validated based on predetermined clinically relevant limits.

REPORTING

Reports are automatically generated and presented comparing each study with previous studies for the same patient with automatically generated graphs showing trends in selected measurements. For reports concerning endovascular stent grafts, previous procedure dates is also shown on the graph. Clinicians can view the reports on the Stanford secured network using their ID and password.

RESEARCH

The measurements are stored separately on a research server for use in research. All patient health information are anonymized automatically using HIPAA-compliant methods. Researchers are able to access the data on the Stanford secured intranet. They can perform historical comparisons and generate graphs to highlight their findings.

RESULTS

3D Lab staff have reported a substantial decrease in repetitive manual workload and have reported an decreased turn around time for clinical report generation. Homogeneity and standardization of measurement descriptions has resulted in more accurate classification for research use. Modifications and additions to protocols and measurement descriptions have become streamlined and less cumbersome.

CONCLUSION

Our experience in developing and deploying this database solution shows that a thorough investigation of the clinical workflow can yield significant time-savings due to automation and standardization. We envision that this database can be expanded to provide scheduling, worklist management, and online report access for referring clinicians.



Figure 1: A sample chart automatically generated from information entered by 3-d technologists, showing the up-to-date trends in relevant quantitative measurements. The stent placement dates, if any, are also indicated. These trend graphs make it easier for radiologists and referring physicians to assess the need for, and response to treatment.

3D IMAGING

Database Management System for the Automated Reporting of Coronary Artery Calcium Screening using Multi-Detector CT

Lalithakala Raman, Raghav Raman, Bhargav Raman, Sandy Napel, Geoffrey D. Rubin, Laura J. Logan

Department of Radiology

INTRODUCTION

Coronary artery calcification has been identified as a predictive factor for coronary artery disease and future myocardial infarction. Coronary calcium screening using Computed Tomography has become popular as a modality for the assessment of coronary artery disease. At Stanford Medical Center, coronary calcium screening is conducted using a multi-detector CT scanner, after which the scans are sent to the 3D Lab at the Lucas Center to determine the amount of calcification on the coronary arteries. However, because of the interest in future clinical research using current data and the requirement that all reports be approved by a radiologist, an organized means of storing and maintaining the integrity of the data for current and future use was needed. We have developed a web-based database system that is integrated with the AccuImage calcium scoring software and automatically keeps track of patients as they are scored, reducing the turn-around time to final approval of the clinical reports by radiologists and speeding the delivery of the report to the referring physician.

DESCRIPTION OF SYSTEM

This system required an enormous effort from all the 3-d lab technologists in determining the workflow model which was used as the key factor in the development process. Our coronary calcium scoring data storage workflow starts at the calcium scoring workstation. Using the Accuimage software, technologists score patients and the scores and corresponding key images are automatically input into the database with minimal user input. A subsystem collects coronary artery risk

factor forms, filled out by patients at the time of the scan and sent electronically. Using this information, a portable document format (pdf) report is automatically created on the server-side on request by a logged-in user. Each report includes the Agatston calcium score, the mass, key images and a graph that shows the percentage risk for coronary artery disease for that patient (Figure 1). Different logins have different viewing and modifying permissions. For example, the referring radiologist has sole authority to approve the report and add additional comments, which is accomplished on the web site using an electronic signature specific to that radiologist. The report is then rebuilt, write-protected and marked as approved. Our database and web-reporting software is deployed on a dual processor server running Windows Server 2003 and IIS 6.0. This server allows access from Stanford secure network with integrated data encryption. Users from outside Stanford must create a virtual private network connection to increase security of transferred data.

RESULTS

There are currently 1724 studies stored in our database and 20 registered users. 98% of reports are approved and 100% have complete coronary artery disease risk factor data.

CONCLUSION

We have developed a system for the storage and reporting of coronary artery calcium screening data. Automatic reporting and web-based approval has greatly decreased the time and infrastructure resources required for a large-scale coronary artery screening program or risk-factor study.

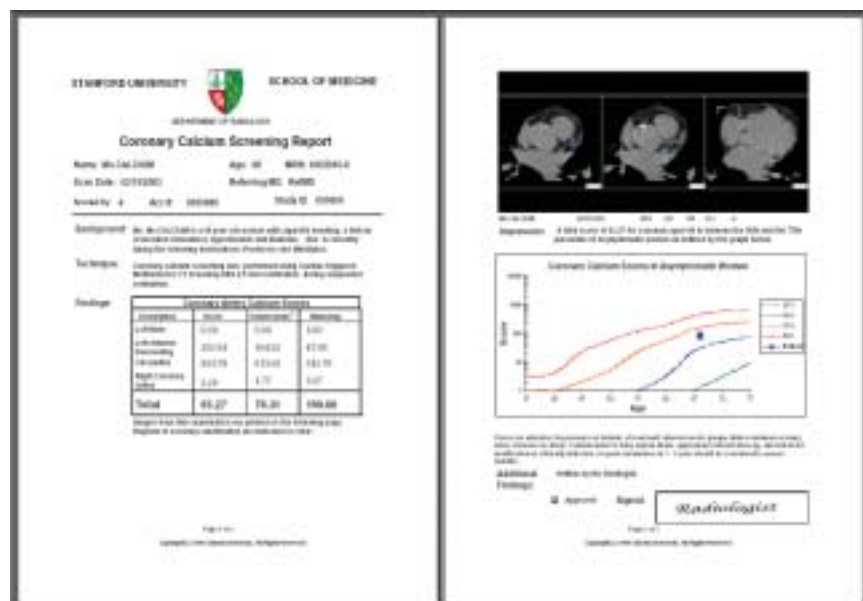


Figure 1: Sample of an automatically generated calcium screening report that includes the raw calcium scores and mass as well as demographic chart output to show the score in the context of the risk profile for the patient's age group. Based on the score, an automatically constructed impression is presented, outlining evidence-based recommendations for further investigations and treatment.

Improved System for the Creation and Management of Radiology Teaching Files

Lalithakala Raman, Raghav Raman, Bhargav Raman, Christopher F. Beaulieu

Department of Radiology

INTRODUCTION

The rapid transformation of radiology to the digital age has not only affected the way radiology is practiced, but also the way that radiology is taught. As CT and MRI come into more widespread use, the sheer amount of data that can be presented to students and colleagues will eventually move teaching away from the reading room lightbox. However current digital methods like saving screenshots or using a digital camera often yield low-quality images and require extensive manual effort for categorization and organization. Management of these individual images becomes cumbersome over time and the sharing is still a manual albeit digital, process. More sophisticated web-based teaching files however, require html coding that is time consuming and expensive to produce and maintain. Our aim was to develop an automated system of web-base teaching file creation and management that reduces the time needed to create, organize and share teaching files.

DESCRIPTION OF SYSTEM

Our teaching file creation and management workflow consists of three major components: PACS integration, automated categorization and Web-based deployment. As part of the GE Destination Digital Project, an add-on for the existing GE PACS workstations was created that enables the radiologist to send significant images to the teaching file server using the DICOM standard communication protocol. The categorization terms, as specified by the radiologist at the PACS workstation, and HIPAA-compliant DICOM information is used by the server to automatically categorize the image. All other DICOM information is anonymized. The service then adds the new images to a database. Movies are created automatically from large stacks of images, although

window/level and annotation functionality on movies is not implemented. The radiologist can then access the images using a Web interface, written using Active Server Pages. Here the radiologist can view and manipulate the images and modify the image information. For example, the radiologist can adjust window/level, add history and clinical findings and create quizzes and teaching file collections. In addition, radiologists can annotate the images. The images can be shared with the rest of the users of the teaching file system, if so desired. We have implemented a component to allow creation of a PowerPoint presentation automatically based on chosen images from the radiologist's teaching file collection. Each slide on the presentation has one image automatically added with all annotations and associated comments. Scan information such as scan modality are also shown.

RESULTS

Currently there are 15 clinicians with logins to the system. There are 1454 images organized into 241 teaching cases, of which 5% (12 cases) are currently shared with all the users of the system.

CONCLUSION

We have created a teaching file solution that reduces the amount of time that the radiologist needs to allocate to create and manage teaching files. Our system also enables the radiologist to share teaching files with other users with little effort and time and create teaching presentations automatically. We hope that this will lead to an increased rate of creation of teaching file modules for the benefit of the radiology community.



Figure 1: The teaching file view page that allows the user to access most of the functions of the software from one page, including window/level, questions, annotations, folders and collections and powerpoint integration. The user is able to reconfigure the page to accommodate screens of different sizes, and is able to zoom the images if required.

Advanced X-ray **Imaging**

Initial Clinical Experience using a Truly Hybrid X-ray/MR Imaging System

R. Fahrig¹, Z. Wen¹, B. L. Daniel¹, K. Butts¹, S. T. Kee¹, G. Heit¹, H. Yu¹, A. Shimikawa², A. Ganguly¹, N. J. Pelc¹¹Department of Radiology, Stanford University, ²GE ASL West, Menlo Park, CA

INTRODUCTION

Both X-ray fluoroscopy and MRI provide useful information during interventional procedures. X-ray imaging provides high-resolution, high-contrast, rapid real-time (30 frames/s) projections for guidance and placement of catheters, stents, platinum coils and other metallic devices. MRI provides tomographic information, soft-tissue contrast, and physiologic data. To fully exploit the strengths of each modality, a truly hybrid imaging system has been developed and characterized [1, 2]. Several patient studies have been carried out to shed insight into the potential utility of the hybrid system.

METHODS

We have integrated an x-ray fluoroscopy system into the bore of an interventional MRI unit (0.5 T GE Signa SP), thereby creating a truly hybrid imaging modality [1, 2]. Switching between modalities requires <1 minute. We have investigated the use of the system during three patient procedures: 1) placement of transjugular intrahepatic portosystemic shunt (TIPS), 2) dual-modality hysterosalpingogram (HSG) and 3) minimally invasive brain biopsy. All patients gave informed consent and the procedures were approved by our Institutional Review Board.

RESULTS AND CONCLUSIONS

To date, we have attempted to use the hybrid imaging system during sixteen patient procedures. The x-ray system operated reliably in all cases except one procedure where it failed to operate due to a broken cable. For all but one case, MR image quality was sufficient to guide the required intervention (TIPS visualization of trocar and portal vein, visualization of brain lesion – see Fig. 1), and also provided appropriate diagnostic image quality (HSG). The MR image quality was inadequate in two TIPS cases where flow in the portal vein was too slow to produce enhancement. More recently, we have used an SSFP sequence that yields more reliable blood-liver contrast since it is less dependent on inflow enhancement. The main limitation of the current implementation is the output limit of the x-ray high-voltage power supply. X-ray image quality was not adequate for two large TIPS patients (> 200 lbs.) and two HSG patients (lateral projections through the pelvis were not diagnostic) because the image noise dominated the signal from small guidewires and small, tortuous iodine-filled fallopian tubes. Note that this is not a fundamental limitation of the hybrid geometry, and an upgrade to a higher power generator and tube is underway. All procedures switched between x-ray and MR several times, typically starting with MR (to verify coil and patient position) and switching back and forth an average of six times. In addition, precise image registration was maintained dur-

ing switching (particularly important for HSG) and there was no risk to sensitive catheter placement (TIPS). The impact of the enhanced imaging capability on procedure accuracy, time and outcome is currently under study.

ACKNOWLEDGEMENTS REFERENCES

Support was provided by GE Medical Systems, NIH grants RR09784 and EB00198 and the Lucas Foundation. Cook Medical provided the modified TIPS catheter set.

1. Fahrig R., et al. *JMRI*, 2001; 13:294-300
2. Fahrig R., et al. *Acad Radiol* 2001; 8:1200-7

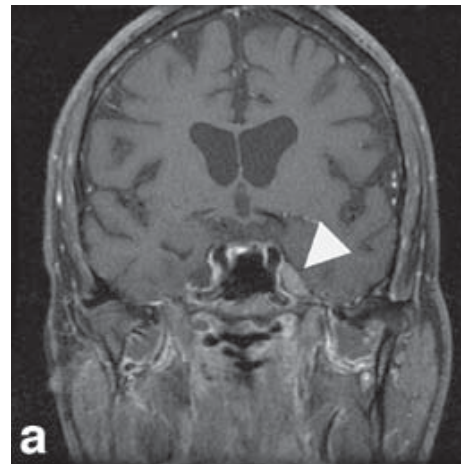
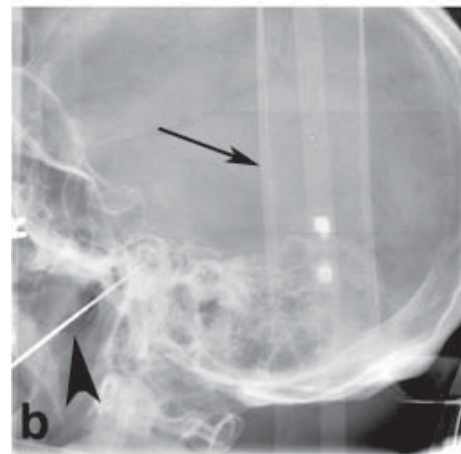
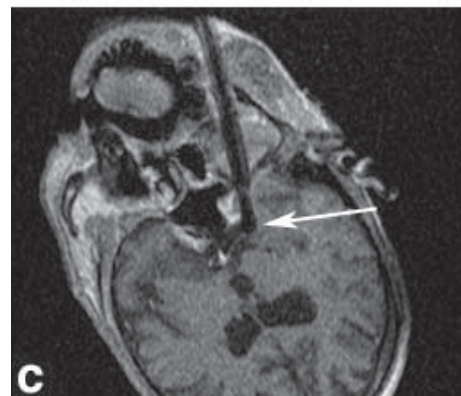


Figure 1:
a
Diagnostic MR pre-scan identifying location of lesion (arrow).



b
X-ray image allows planning of needle trajectory. Arrow points to flex coil visible in x-ray projection.



c
Biopsy under MR guidance avoids critical neural and vascular structures.

ADVANCED X-RAY IMAGING

Advanced X-ray/MR Hybrid Imaging System

Arundhuti Ganguly¹, Zhifei Wen^{1,2}, Rebecca Fahrig¹, Norbert J. Pelc¹

Departments of ¹Radiology and ²Physics

INTRODUCTION

We have developed a truly hybrid x-ray/MR imaging system that combines the advantages of x-ray fluoroscopy and interventional MR imaging into one unit. The first prototype system was successfully used to guide several patient procedures^{1,2}. Its limitations were identified and a recent upgrade to the x-ray system is expected to result in an advanced hybrid imaging system. Implementation and assessment of the improved system is currently underway.

MATERIALS AND METHOD

X-RAY SYSTEM DESCRIPTION

The new x-ray tube (GE OEC, Salt Lake City, UT) has an anode angle of 8° which was 12° in the previous system and has the same filament size of 0.6 mm as before. The x-ray tube now has new housing that allows a maximum thermal capacity of 700,000 J.

The high voltage generator power supply to the x-ray tube in the first prototype (GE Lunar, Madison, WI) permitted continuous fluoroscopy with a maximum of 90 kVp or 4.2 mA with a total output power of ~300 W. The present generator (GE OEC, Salt Lake City, UT), allows continuous as well as pulsed and single-shot fluoroscopic capabilities. For continuous fluoroscopy, a Low Level mode allows a maximum power output of 280 W or 4 mA, whichever is lower while a High Level allows 510 W or 8 mA. Pulsed fluoroscopy allows 1090 W or 13 mA while for the single film shot, 1700 W or 16 mA is permitted. A Peak voltage of 110 kVp is available. This increase in output power has been one of the major improvements in the new system since images in the previous version were photon limited, particularly for larger patients.

The new x-ray detector is an indirect detection Apollo[®] flat panel (FPD) that has similar features to the previous detector.

The new "Mainframe" system is a modified control system used in GE OEC model 9800, mobile C-arm units. The system allows almost unlimited real time data storage which is an improvement over the 20s limit in the previous system.

INITIAL SYSTEM TESTING

We have found new x-ray tubes to arc in the magnetic field, often resulting in system shut down. Arcing increases with field strength as well as with tube kVp. However, repeated usage of the tube stabilizes it and prevents arcing. Therefore a tube seasoning protocol was developed and was performed at 4 magnetic fields ~ 0, 0.009, 0.096, 0.296, 4.64 T. At each field and 2.5 mA current, the kVp was increased from 40 to 110 in steps of 10. Next, with kVp held at 110, the mA was increased to 1, 3, and 5. The tube was found to function stably for all values except at 3 and 5 mA at 110 kVp at about 0.5T. Cycling the power once at each of these values stabilized the tube. This was a major improvement from the previous tubes that were found to be very sensitive to magnetic fields and required a long seasoning process to stabilize.

We also measured the RF noise properties of the FPD. The wide band noise that was previously 3-5 times above baseline, was about 1.5-2 times in the new FPD. However, both detectors showed strong zipper artifacts in MR images and methods to provide better RF shielding are being considered.

CONCLUSIONS

The implementation of the advanced system is almost complete. Preliminary results show promise of better performance and hence increased clinical applicability.

REFERENCES

1. Fahrig R, et al. *JMRI* 2001; 13:294-300
2. Fahrig R, et al. *Acad Radiol* 2001; 8:1200-7

Permanent Magnet Shimming For A Detector Inside An iMRI

Zhifei Wen^{1,2}, Rebecca Fahrig², Norbert J. Pelc²

¹Departments of Physics and ²Radiology

INTRODUCTION

In our x-ray/MR hybrid system, a flat panel detector is placed under the patient cradle close to the MR volume of interest (VOI), where the magnetic field strength is $\sim 0.5\text{T}$. Ferromagnetic components inside the detector that cannot be replaced with non-magnetic substitutes create an additional magnetic field that is superimposed on the original field of the scanner. Even after linear shimming of the field with the detector in place (using scanner-implemented algorithms) the field homogeneity is diminished by the ferromagnetic components in the detector. Here we propose using a permanent magnet with optimized strength and position to compensate for the second and higher order components of the additional field.

METHODS AND MATERIALS

To obtain the field map, signals of a body phantom from both real and imaginary (I and Q) channels were collected at two echoes (1ms apart) using a fast GRE sequence. From their unwrapped phase difference map, the raw field map was then calculated. The zeroth order offset and the first order linear component of the additional field were removed using the shim correction algorithm of the scanner (assuming perfect performance). We assume that the ferromagnetic components inside the detector are distributed inside a volume only a few centimeters across, the size of which is much less than the distance from the detector to the MR VOI. The magnetic field from the ferromagnetic components may therefore be closely approximated by a magnetic dipole point-

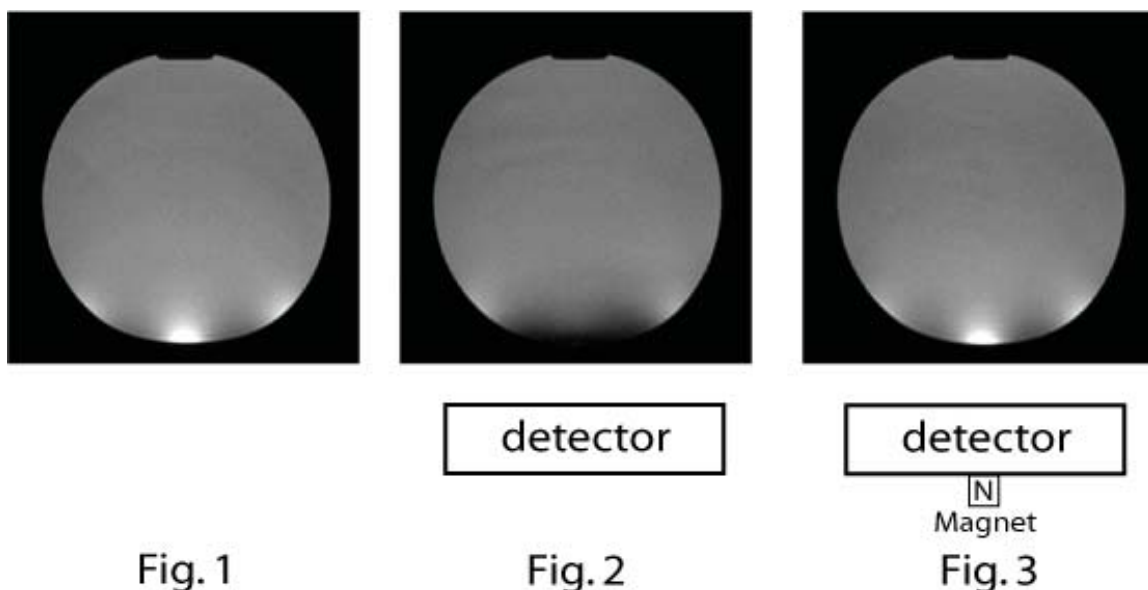
ing at the direction of the external field, located near these components. In practice a small permanent magnet can be used as this magnetic dipole. If the intrinsic coercivity of this magnet is sufficiently larger than the external magnetic field, reversing the poles of the magnet in space will change neither its magnetization nor its magnetic field. Therefore the undesired magnetic field from the detector can be canceled by a permanent magnet oriented in a direction opposite to that of the main magnetic field. A nonlinear least-squares iterative method was used to find the optimized strength and position of the shimming permanent magnet.

RESULTS

In the absence of the detector, the peak-to-peak deviation of the field map was 57mG (milligauss) and the standard deviation was 6.5mG, as compared to 144mG and 16.5mG with the detector inside the magnet. However, field homogeneity improved to 76mG and 7.3mG respectively when a shimming magnet was employed, its strength and location being as close to the optimized values as available. A GRE sequence (TE: 15ms; TR: 250ms; Flip Angle: 50), fairly sensitive to field inhomogeneity, was used to test the efficacy of the shimming magnet. Images without the detector (Fig. 1), with the detector (Fig. 2), and with both the detector and the shimming magnet (Fig. 3) are shown here.

CONCLUSIONS

Permanent shimming magnets are promising to improve the MR field homogeneity impaired by foreign magnetic material inside the scanner.



INTRODUCTION

An essential step to implement a real time interface of a truly hybrid x-ray/MR system is co-registration of x-ray and MR fields of view (FOVs). In our previous work, we have demonstrated the feasibility of a fiducial-based method to calibrate the system, thereby enabling the use of x-ray images as “scouts” to prescribe MR slices. In this work, we propose a method to improve the accuracy of this registration scheme by minimizing the errors caused by the system’s nonlinear gradients. In addition, image processing techniques are developed to assist automatic reading of the fiducial markers from x-ray and MR images.

METHODS AND MATERIALS

The key step of the co-registration is to find the accurate positions of the x-ray components in MR coordinates, the so-called geometric parameters. Sixteen fiducial markers that are visible in both MR and x-ray images are placed in the FOV. By fitting their MR and x-ray measurements to a nonlinear function describing the projection behavior, the values of these geometric parameters can be determined. This procedure can be viewed as the system calibration. The second or excitation phase is when the cross-calibration is used to excite the desired slice. Two points on the x-ray image of the target structure are identified and are used to calculate the target slice utilizing the previously fitted geometric parameters.

In this work, errors of the registration due to gradient nonlinearity were considered. In the calibration step, the effect of nonlinear gradients is corrected by the MR system’s software. In the excitation step, due to the nonlinear gradients, the actual excited slice is warped. We propose a least squares based method to minimize this error. Instead of the original calculated target slice, another plane is excited, whose corresponding warped plane is the least squares fit to the original target slice for locations within the system FOV.

A phantom was built in which the crossing points of two fishing line segments act as fiducial markers. The phantom contains 4 fiducial markers at each of two levels parallel to the x-ray detector. In practice, two sets of data are collected with different phantom positions, so that data for 16 fiducial markers are available. In order to find the MR locations of those crossing points, combinations of coronal and oblique slices are used (Figure 1). An algorithm to locate the crossing points was developed. The portion of the image that contains the crossing point is transformed into Radon space. A line in the image domain corresponds to a point in Radon space. Therefore, by identifying two peaks in Radon space, the two crossing lines can be found and the crossing point position can be calculated with sub-pixel accuracy and reproducibility. The phantom was also used to test the accuracy of the prescribed slice. A new x-ray image was collected. Two points on one line were chosen as the target structure and thus the target slice was calculated. Three contiguous 3 mm slices were acquired, the middle of which is the target slice.

RESULTS

Computer simulations show that the average error of the excited slice is about 0.5mm for target points uniformly distributed in the FOV when considering both fiducial marker’s measurement noise and gradient nonlinearity. With our least squares correction, this error is reduced to 0.4mm. Results of the accuracy test using the phantom are shown in Figure 2 for cases with and without least squares plane correction. The amount of the target line visualized is clearly improved with least squares correction.

CONCLUSIONS

We have shown a refined algorithm to co-register x-ray/MR FOVs with improved accuracy.

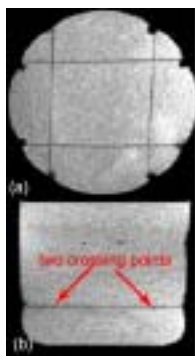


Figure 1: MR coronal slice (a) with 4 fiducial markers on one level, oblique slice (b) to determine AP positions of two fiducial markers.

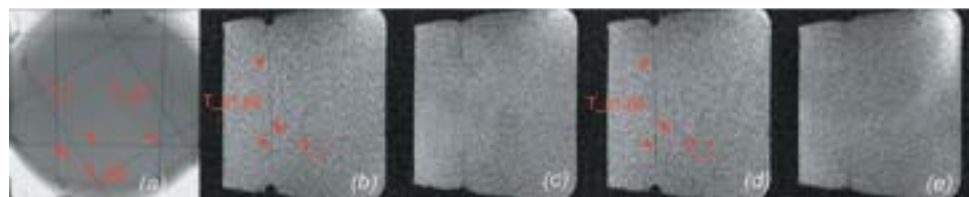


Figure 2: Registration accuracy test. (a): X-ray image with two target points (T_{p1} , T_{p2}) on a target line (T_l). (b) and (c): The target slice calculated without least squares correction and its neighboring slice. Slice warp can be seen here. (d) and (e): The excited target slice with least squares correction and its neighboring slice.

Fast SBDX Geometry Tomosynthesis for Lung Cancer Detection

Sung-Won Yoon, Angel R. Pineda, Edward G. Solomon, Ann N. Leung, Norbert J. Pelc, Rebecca Fahrig
Departments of Radiology and Electrical Engineering, NexRay Inc, Los Gatos

INTRODUCTION

Radiology-based lung cancer detection is a high-contrast imaging task, consisting of the detection of a small mass of tissue within much lower density lung parenchyma. This imaging task requires removal of confounding image details (resulting from over- and under-lying structures eg. ribs and vessels), fast image acquisition ($<0.1s$ for pericardial region), low dose (comparable to a chest x-ray), high resolution ($<0.25mm$ in-plane), and patient positioning flexibility. We present an investigation of tomosynthesis, implemented using the Scanning-Beam Digital X-ray (SBDX) system, to achieve these goals.

METHODS AND MATERIALS

We designed an image-based computer model of tomosynthesis by using a high-resolution ($0.15mm$ isotropic voxels which is slightly better than the in-plane resolution that can currently be achieved using the SBDX system) low-noise CT volume image of a lung phantom (stabilized heart and lung complex from a dog), numerically adding spherical lesions and simulated ribs (to increase the complexity of the detection task), and applying convolution-based tomographic blurring (by convolving each slice with a cylindrical blur function).

Lesion visibility was examined as a function of lesion diameter ($2.5mm$ and $4.0mm$), half-tomographic angle (ranging from 3 to 12), and location within the volume (approximately centered, or in the upper half close to the ribs).

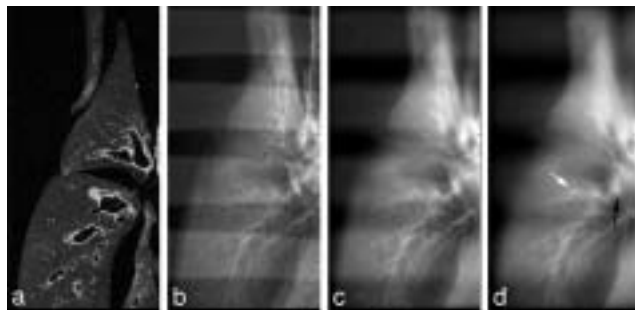


Figure 1 A 4mm nodule placed in a region of high complexity. a) CT slice through base data; b) simulated projection; tomosynthesis image with half-angle of c) 3, d) 6.

Images of a 4mm lesion placed in a region of heterogeneous tissue are shown in Figure 1. Although this detection task is probably more challenging than in vivo tissue, an increase in the tomographic half-angle to 6 improves visualization and the detection of the emerging nodule (pointed by the white arrow in Figure 1 d).

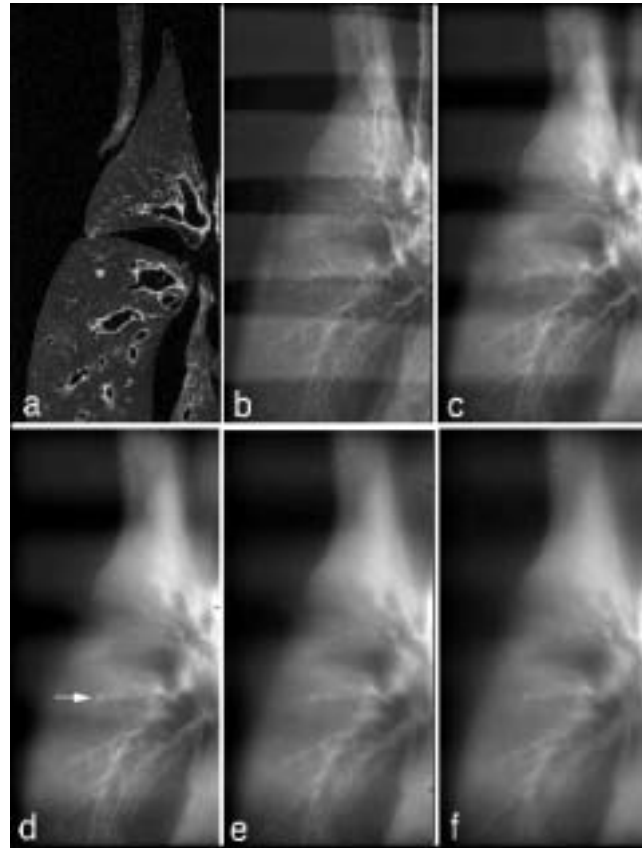


Figure 2 A 2.5mm, 40HU density nodule placed in relatively uniform lung parenchyma. a) slice through the CT base data at the location of the lesion; b) simulated projection; tomosynthesis image with c) half-angle 3, d) half-angle 6, e) half-angle 9, f) half-angle 12.

The results presented here are encouraging but do not provide sufficient information for design and optimization of a fast tomosynthesis scanner for lung cancer detection. More realistic plastinated lung phantom, added anthropomorphic chest phantom, and a more complex model of the nodules are some of the criteria external to the imaging system that need to be improved.

DISCUSSION

We will be looking into the system parameters, including the tomographic half-angle, image acquisition model, reconstruction algorithm, and pre- or post-processing of acquired data. As the preliminary results show, there exist correlations between the tomographic half-angle, nodule size, and the detectability of the resulting tomosynthesis; we are systematically investigating the relationship between these parameters. Specifically, the effect of the half-angle on the detectability of an ideal observer model for a fixed-size simple lung nodule model. We are also exploring iterative reconstruction algorithms that can include both the statistical nature of the measurements and non-linear constraints such as positivity. We will optimize the algorithms specifically for detection of lung nodules and then compare them to the standard filtered-backprojection.

Taly Gilat^{1,2}, Rebecca Fahrig¹, Norbert J. Pelc¹Departments of ¹Radiology and ²Electrical Engineering**INTRODUCTION**

This work investigates the performance of a reconstruction algorithm for an inverse geometry volumetric CT system (IGVCT). Within this investigation, a new method is developed for correcting artifacts introduced during data rebinning.

METHODS AND MATERIALS

The IGVCT system has been proposed to acquire volumetric images with negligible cone beam artifacts using a large array scanned-anode source and a smaller array of fast detectors. During an acquisition, an electron beam (and thus the x-ray source) is rapidly and electronically steered across a large transmission target as the gantry rotates about the patient. Ideally, a reconstruction algorithm would not introduce significant artifacts or blurring. The proposed reconstruction algorithm first rebins the acquired data into 2D parallel ray projections at numerous view angles and tilt angles to the axis of rotation. In order to have equally spaced 2D parallel ray projections, nearby rays must be binned together using some form of interpolation. This interpolation is carried out using gridding, which can introduce error if the nonuniform sampling density of the acquired data is not accounted for properly. A new method of locally correcting the gridding kernel has been developed to remove these artifacts. This correction uses a linear expansion in the neighborhood of the sample, which is acceptable over the small kernel width. Once the data are in the form of 2D parallel ray projections, the output volume can be reconstructed using a modified filtered backprojection. To verify the performance of the full reconstruction algorithm, data was simulated using the preliminary IGVCT system geometry. For comparison, ideal 2D parallel ray projections were also simulated.

RESULTS

Simulations using the IGVCT geometry show high frequency artifacts caused by data rebinning. These artifacts are reduced to below 1 HU when the proposed gridding correction is implemented, as shown in Figure 1. Overall, residual artifacts in the reconstructed volume are of the order of a few HU. Despite the slight blurring generated by the rebinning algorithm, spatial resolution better than 0.5mm in all directions is possible.

CONCLUSIONS

The local correction to the gridding kernel effectively reduces the data rebinning error. The investigated reconstruction algorithm provides high-resolution images with low artifact levels.

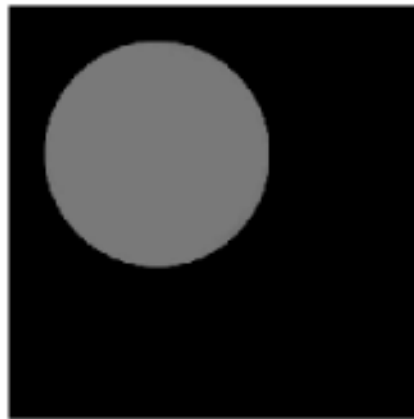
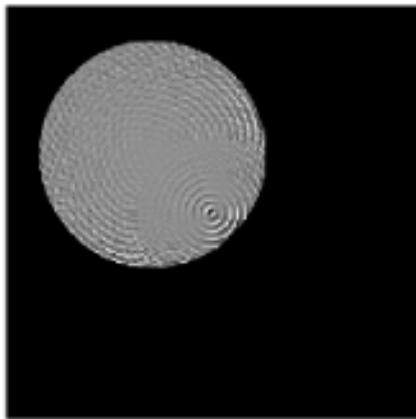


Figure 1: Central axial slice of simulated water sphere reconstructed without the gridding correction (left) and with the gridding correction (right). The images are windowed to a level of 0 HU with a window width of 4 HU (i.e., values -2 HU and $+2$ HU are mapped to black and white, respectively).

Outcomes & Cost **Effectiveness**

Estimating the Mean Tumor Volume Doubling Time of Breast Cancer from the HIP Screening Trial

Bronislava M. Sigal, Sylvia K. Plevritis

Department of Radiology

INTRODUCTION

Mathematical modeling of the natural history of breast cancer plays an important role in understanding disease progression. Properties of breast cancer such as tumor growth can not be observed for ethical reasons. In our earlier work, (Plevritis S.K., Math. Biosci., 2000) we proposed one such model assuming that tumor growth is exponential in the screen detectable stage of the disease. We assumed that the mean tumor volume doubling time was known from retrospective studies of serial mammograms, even though these studies are likely to be biased toward slower growing tumors. In our present work, we propose an approach for determining an unbiased estimate of the mean tumor volume doubling time using data from the HIP breast cancer screening trial and the SEER tumor registry.

METHODS AND MATERIALS

In the HIP trial, women ages 40 to 64 years were randomized to a study group that was invited to four annual screening sessions of mammography and clinical breast examination (CBE), and a control group that was not invited to any of the screening sessions. To estimate mean tumor volume doubling time (DT) from the HIP data, we use a simulation-based approach that uses the following inputs: (1) age distribution of women at entry to the trial (HIP data); (2) age-specific incidence of invasive BC symptomatically detected in the absence of screening (estimated from SEER for women detected between 1975 and 1981); (3) a natural history model of stage progression (estimated from SEER). We assume that the doubling time is gamma distribution and the probability of clinical detection is proportional to tumor volume. For each simulated woman, we assume that there is a tumor size threshold such that if at the time of screening the size of the tumor exceeds the threshold, then the woman is necessarily detected at that screening. Because HIP trial offered two examinations at each screening session, namely mammography and clinical breast examination, then the screen detection threshold is the minimum of two examinations. Parameter estimation based on a conditional likelihood function defined as the proportion of screen detected and symptomatically detected women given BC stage is assessed for each screening interval. The likelihood is conditioned on the number of women detected with breast cancer (BC) in each screening interval. We maximize the conditional likelihood function using a grid search over a two-dimensional parameter space, where the parameters are mean tumor volume doubling time and median tumor size detection threshold.

RESULTS

In a hypothetical population of 60 million simulated women, the mean tumor volume doubling was estimated at 5.5 months and median tumor size threshold at 1.1 cm. The contour plot of the conditional likelihood function is shown in Figure 1. This model produces a statistically significant goodness-of-fit to the data.

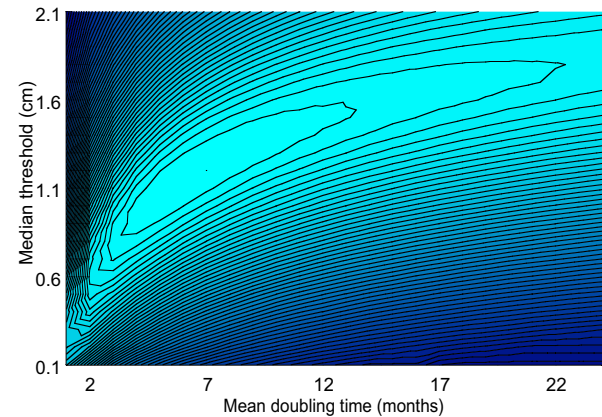


Figure 1: Counter plot of conditional likelihood function used to estimate the mean tumor volume doubling time and the mean screen detection threshold.

CONCLUSIONS

Our estimate for the mean doubling time of breast cancer is 5.5 months. Our estimate is within the range of 4 months to 12 months, which represents the reported values of doubling time in published sources. As expected, our estimate for the mean tumor volume doubling time is lower than that suggested from most empirical studies because the studies are most likely biased toward slower growing tumors.

OUTCOMES AND COST EFFECTIVENESS

Estimating the Progression Rates of Breast Cancer from Local, Regional to Distant Disease

Sylvia K. Plevritis¹, Peter Salzman^{1,2}, Bronislava M. Sigal¹, Peter Glynn²

Departments of ¹Radiology and ²Management Science and Engineering

INTRODUCTION

Invasive cancer is commonly staged as local, regional or distant disease. Larger tumors are more likely to be detected in advanced stages when compared to smaller tumors. Based on this observation, it is generally believed that cancer begins in the local stage and progresses from the local to the regional stage and then to the distant stage as the primary tumor increases in size. However, the rate of stage progression is not known. In addition, the primary tumor size at which the disease transitions from the local to the regional stage and from the regional to the distant stage is not known. These quantities would be biologically and clinically meaningful since they would provide new insight into progression of the disease and the expected stage shift due to cancer control programs in early detection. In this work, we use a natural history model of cancer to estimate (1) the relative rates of stage progression, (2) the primary tumor volume at stage transitions and (3) the impact of clinical detection on the observed stage distribution. By clinical detection, we are referring to tumor detection resulting from clinical symptoms in the absence of screening. We estimate model parameters from data that contains the tumor size and stage from clinically detected breast cancer patients.

METHODS AND MATERIALS

We developed a stochastic model of the natural history of cancer to quantify under the following assumptions: (1) the tumor volume grows exponentially; (2) the inverse growth rate R is gamma distributed; (3) the hazard for clinical detection is proportional to volume; (4) the tumor begins in the local stage and the hazard for the transition to the regional stage is proportional to volume; and (5) all patients who are initially diagnosed in the distant stage also have clinical detectable nodal involvement and the conditional hazard for the transition from regional to distant disease is proportional to volume. Maximum likelihood estimates are obtained based on data consisting of the tumor size and stage from breast cancer patients who were clinically detected with their disease. Because the observed data does not contain timing information, model rate parameters can not be estimated on an absolute scale but on a relative scale. The ratio of the parameters can be uniquely identified as well as the primary tumor volume at stage transitions.

RESULTS

Parameter estimates show an acceptable fit to the data. The estimates indicate that the rate of clinical detection in breast cancer is similar to the rate that the disease transitions from the local to the regional stage and an order of magnitude larger than the rate that the disease transitions from the regional to the distant stage. The estimated stage distribution conditioned on tumor size and computed in the absence of clinical detection is shown in Figure 1. The median breast tumor size at the transition from the local to the regional stage is 31.5mm, and the median breast tumor size at the transition from the regional to the distant stage is 68.0 mm. Our work also shows that the act of seeking medical attention when symptoms appear is preventing a significant fraction of breast tumors from progressing to advanced stages. We also find that a relatively small shift in the detected tumor size distribution by altering the clinical detection function can have a significant impact on the overall observed stage distribution.

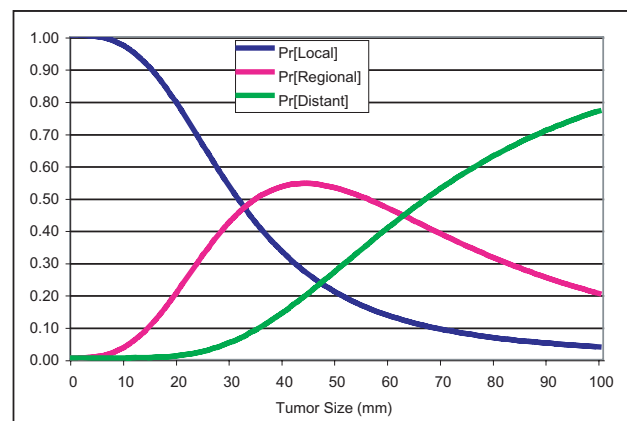


Figure 1: Estimated breast cancer stage distribution conditioned on tumor size assuming no tumor detection mechanism.

CONCLUSIONS

The natural history model presented here can explain observed data on tumor size and stage for breast cancer patients detected in the absence of screening. Using this model, we can infer unobservable properties about the stage progression of breast cancer. We find that the rate of clinical detection in breast cancer is similar to the rate that the disease transitions from the local to the regional stage and an order of magnitude larger than the rate that the disease transitions from the regional to the distant stage. The median breast tumor size at the transition from the local to the regional stage is 31.5mm, and 68.0 mm for the transition to regional disease.

Simulation of the HIP Breast Cancer Screening Trial

Bronislava M. Sigal, Sylvia K. Plevritis

Department of Radiology

INTRODUCTION

Screening trials can be costly and require long follow-up times to determine cancer-specific mortality reduction from early detection. We are developing a computer model to simulate screening trials in order to facilitate the design of future screening trials and bridge short-term endpoints to mortality endpoints. A fundamental component of our screening simulation model is a sub-model of the natural history of breast cancer that determines the mortality benefit from early detection. To validate our work, we compare simulated breast cancer incidence and mortality outcomes to the results obtained in a well-known breast cancer screening trial, namely the Health Insurance Program (HIP) of New York trial. HIP was a randomized-controlled study that demonstrated a breast cancer mortality reduction from screening mammography. In this work, we demonstrate how well our screening simulator reproduces the HIP trial.

METHODS AND MATERIALS

In the HIP trial, women ages 40 to 64 years were randomized to a study group that was invited to four annual screening sessions, and a control group that was not invited to any of the screening sessions. We simulated the HIP trial and generated estimates of breast cancer (BC) cumulative incidence and mortality in the study and control arms. For each simulated woman in the control arm we generate her age at symptomatic detection, death from causes other than BC. For each woman in the study arm, in addition, we generate her screening schedule and age at screen detection (if screen detected) based on a model of the natural history of BC. After the mode of detection is determined, her age at BC death is generated. Each woman is followed from the entry into the study till the BC death, death of other causes or the end of the study, whichever occurs first. Simulation program takes the following inputs: (1) Age distribution of women at entry to the HIP trial; (2) Age specific incidence of invasive BC (estimated from the SEER database for women detected between 1975 and 1981, for five-year age groups); (3) Parameters of the natural history model (estimated from the SEER database); (4) Mean volume doubling time (see previous abstract on the “Estimation of the Mean Tumor Volume Doubling Time of Breast Cancer from the HIP Screening Trial.”); (5) Distribution of the screen detection threshold; (6) Stage-size-age specific distribution of the time from symptomatic detection till death from BC (based on SEER 1975-1979 data), modified to account for the difference between SEER population and women in the HIP control arm; (7) Mortality from other than BC causes (Berkeley mortality tables); (8) Distribution of screening schedules estimated from HIP study arm (not all women were regularly screened). The simulation outputs cumulative number of BC incidence and BC deaths for each year from entry to the study.

RESULTS

Simulated cumulative breast cancer incidence rates for the control and study arms are in reasonable agreement with HIP data as demonstrated in Figure 1. Simulated cumulative breast cancer mortality rates match for the study group but are lower than observed for the control group, as shown in Figure 2. At 14 years from entry the simulated breast cancer mortality reduction was 8.2% and the reported was 13.9% for all age groups.

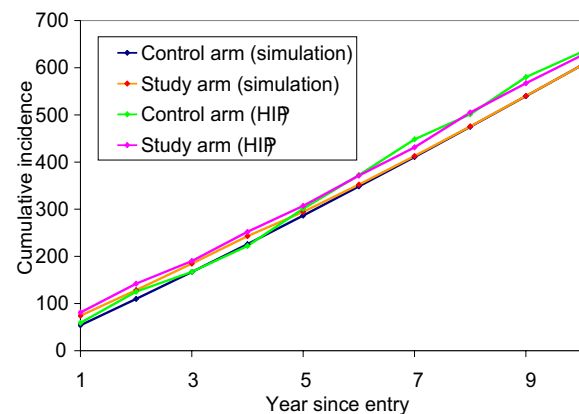


Figure 1: Simulated and actual cumulative breast cancer incidence in the control and study arms of HIP trial

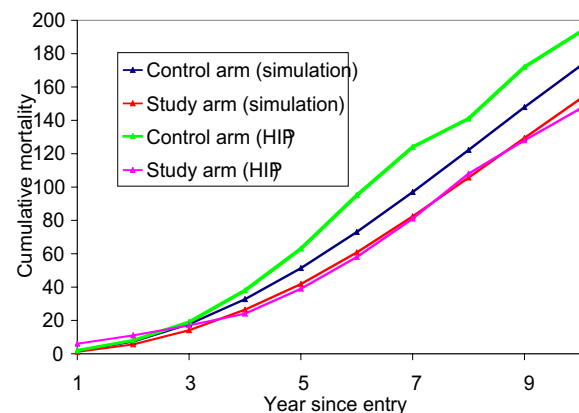


Figure 2: Simulated and actual cumulative breast cancer mortality in the control and study arms of HIP trial

CONCLUSIONS

Our simulation model closely reproduces the cumulative breast cancer incidence of the HIP trial but predicts a smaller mortality benefit than that observed. Because the HIP has been recently heavily criticized for biasing the control group to favor screening, we analyzed the HIP for evidence of a bias (see abstract “Was there a post-randomization bias in the HIP breast cancer screening trial?”). If the bias exists, the work presented suggests that the mortality benefit of screening mammography could be half of that reported in the trial.

OUTCOMES AND COST EFFECTIVENESS

Was There a Randomization Bias in the HIP Breast Cancer Screening Trial?

Sylvia K. Plevritis and Bronislava M. Sigal

Department of Radiology

INTRODUCTION

The Health Insurance Program (HIP) of New York screening trial is a well-known randomized-controlled study that demonstrated a breast cancer mortality reduction from screening mammography. Recently, the HIP trial has been criticized for allowing the possibility of a randomization bias. One of the exclusion criterion for entry into the trial was a prior history of breast cancer. After the initial trial randomization, enrollees were removed if they were later found to have had a prior history of breast cancer. More enrollees were removed from the study group compared to the control group. It has been suggested that the control group has more women with a prior history of breast cancer. If this is the case, then the control would have worse survival outcomes regardless of screening and the trial would be biased in favor of screening. Retrospective analysis of medical records of the breast cancer patients in the control group have not been sufficient to prove that randomization bias did not occur. In this work, we analyze the HIP survival data for potential evidence of this bias.

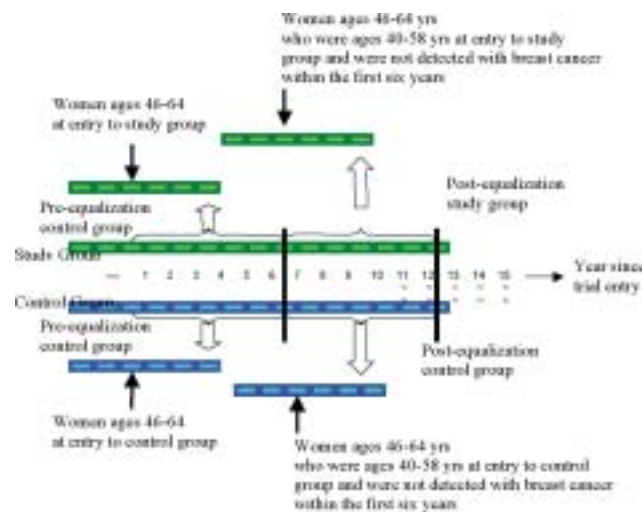


Figure 1: The pre- and post-equalization control groups and pre- and post-equalization study groups for women ages 46-64 years at entry assuming a six-year equalization period.

METHODS AND MATERIALS

In the HIP trial, women ages 40 to 64 years were randomized to a study group that was invited to four annual screening sessions, and a control group that was not invited to any of the screening sessions. Widely cited breast cancer mortality reduction estimates from the HIP trial were derived from a limited mortality analyses of the trial data assuming equalization periods of five, six and seven years. The equalization period is defined as the time from trial entry to the time when the cumulative number of cancer patients in the control group is equivalent to that in the study group. We analyze the post-equalization control group (POSTC) and the post-equalization study group (POSTS) which are comprised of breast cancer patients detected after equalization in the control and study arm respectively. Figure 1 shows one example of how these groups are formed and how they are distinct from the groups before equalization (PREC, PRES), which were analyzed in published HIP studies.

We test the null hypothesis that breast cancer survival in the PREC and POSTC are equivalent. The alternative hypothesis is that that breast cancer survival in the PREC is worse than breast cancer survival in the POSTC. The rationale for this is as follows: If the post-randomization bias did not occur, then breast cancer survival in the PREC and POSTC should be equivalent, assuming there was no period effect on survival. On the other hand, if the post-randomization bias did occur, then breast cancer survival in the PREC would be worse than breast cancer survival in the POSTC. Analysis is performed assuming six-year and seven-year equalization periods. Comparison of survival curves pre- and post-equalization was limited to groups with similar age distributions at entry and diagnosis. Reported p-values are based on one-sided tests comparing survival from diagnosis for PREC and POSTC.

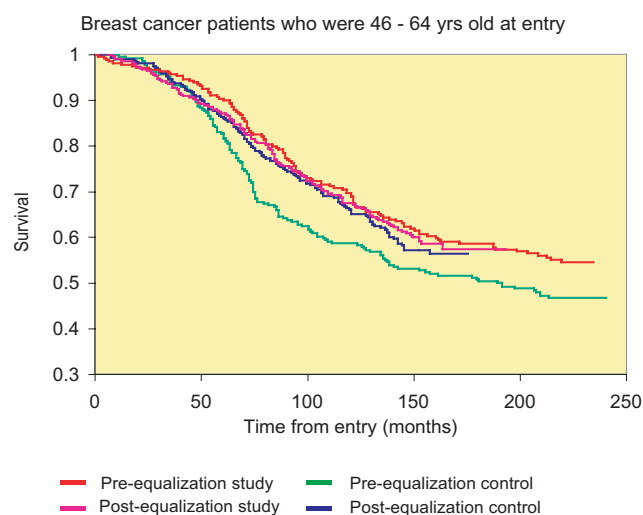


Figure 2: Survival curves based on a 6-year equalization period for women ages 51-59 years at entry.

RESULTS

For six-year equalization period and breast cancer patients ages 51-59 years at entry statistically significant difference between PREC and POSTC was observed ($p=0.063$ Peto-Peto-Wilcoxon test, $p=0.034$ Renyi test). Figure 2 display the corresponding survival curves for the six-year equalization period. Similar results were obtained for seven-year equalization period and breast cancer patients ages 52-59 years at entry ($p=0.012$ Peto-Peto-Wilcoxon test, $p=0.019$ Log-rank test).

CONCLUSIONS

Survival analysis of breast cancer patients in the post-equalization period suggests that there may have been a randomization bias in the HIP trial. This result implies that the survival benefit of the HIP trial may be lower than previously reported. Relevance to modern-day mammography is limited due to the advancements in X-ray imaging technology and image interpretation of the past 40 years.

Parameter Estimation in a Complex Model of Breast Tumor Growth using Stochastic Approximation Techniques

Yen Lin Chia¹, Peter Salzman^{1,2}, Peter Glynn¹, Sylvia Plevritis²

¹Management Science and Engineering, ²Department of Radiology

INTRODUCTION

Complex tumor growth models that were once considered analytically challenging can now be explored because of increased computational power. In this work, we consider a tumor growth model that allows stochastic variability in the tumor volume over time. A stochastic tumor growth law is in contrast to more common tumor growth laws, such as exponential or gompertz, that describe deterministic growth given parameters such as the growth rate. In the model presented here, tumor growth is modeled as geometric Brownian motion that exhibits exponential growth. The aim of this work is to estimate the parameters of this natural history model from data on tumor size at detection. Because a closed form expression for the likelihood function is complex, we employ stochastic approximation techniques that involve simulation.

METHODS AND MATERIALS

We assume that the tumor growth follows the stochastic differential equation: $V_t = \mu V_t dt + V_t dB_t$ where V_t is the volume at time t , B_t is standard Brownian motion at time t , and $\mu=0.5$ is the rate parameter for exponential growth. We assume that the probability of detecting the tumor increases linearly in the volume, i.e., $P(T_D \in (t, t + \Delta) | T_D > t, V(\cdot)) = \gamma V(t) \Delta + o(\Delta)$. Our goal is to find the parameters (γ, μ) that maximize the log-likelihood function. The log likelihood function is:

$l(\theta) = \sum N_i \log(p_i(\theta))$ where N_i is the number of women observed in tumor size category, and $p_i(\theta)$ is the proportion of tumors found in size category i . Because the expression for $p_i(\theta)$ is complex, the closed form solution of the log-likelihood is complex, and we adopt the method stochastic approximation for parameter estimation. In an iterative procedure, $\theta_{n+1} = \theta_n + \frac{a}{n} l'(\theta_n)$, where $\theta = (\gamma, \mu)$ are the parameters of

interest, $\frac{a}{n}$ with $a > 0$, is called the “gain”, and $l'(\theta)$ is the derivative of the log likelihood function. This is a stochastic version of Newton-Raphson method. Differentiating $l(\theta)$, we obtain the stochastic gradient, $\nabla l(\theta) = \sum n_i \frac{\nabla p_i(\theta)}{p_i(\theta)}$ where $\nabla p_i(\theta)$ is the gradient of $p_i(\theta)$ with respect to θ in i^{th} category. By a change of measure, we can express $\nabla p_i(\theta) = E_{\theta_0} [I(D \in i) \nabla L(\theta)]$. This method for gradient estimation is called Robbins-Monro (RM) method. An alternative method called Kiefer-Wolfowitz (KW) is adopted as well, where the derivative is approximated by finite differences: $l'(\theta) = \frac{l(\theta+h) - l(\theta-h)}{2h}$. We also compute the closed form solution of the likelihood through a system of ordinary differential equations (ODE), the likelihood is in terms of modified Bessel functions of the first and second kind.

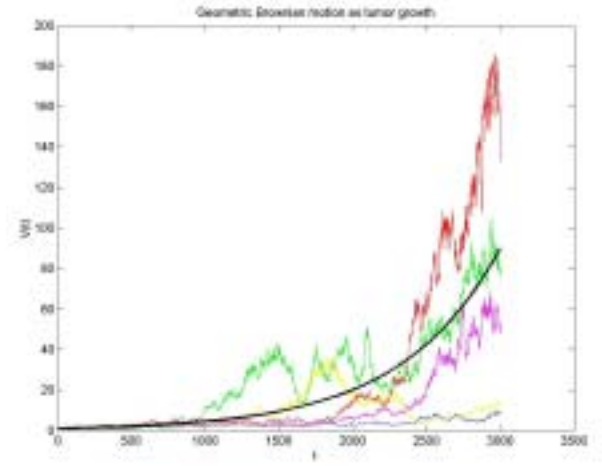


Figure 1: Different realizations of the growth pattern of tumor allowing stochastic nature.

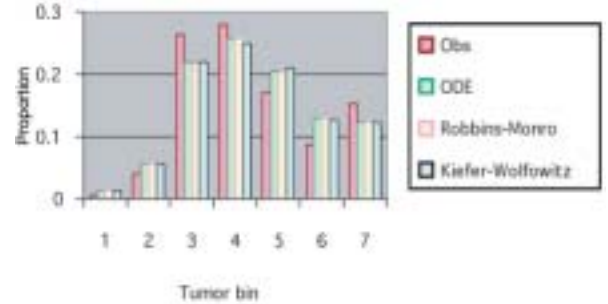


Figure 2: Distribution of sizes at detection observed (OBS) vs. predicted by the stochastic growth model, when solved by stochastic approximation techniques (Robbins-Monroe and Kiefer-Wolfowitz) and analytically using ordinary differential equations (ODE).

RESULTS

The maximum likelihood estimator using RM, KW, and ODE methods give consistent results. Based on these estimators the expected distribution of sizes at detection is shown in the Figure 2. Our work demonstrates that the stochastic exponential growth law can reproduce the data and could be a potential alternative to deterministic models. While the method of stochastic approximation requires less analytical sophistication, it has challenges of discretization, convergence and statistical error that were manageable in this work.

CONCLUSIONS

Stochastic approximation is a powerful tool for estimating parameters in complex biological models and demand less analytical sophistication on the part of the user. Our analysis shows the results obtained from both the Robbins-Monro and the Kiefer-Wolfowitz methods give reasonable fit to the observed data and are consistent with the closed form analytic solution of the log-likelihood function. This work also suggests that a stochastic exponential growth model is a potential alternative to the deterministic growth model. 145

OUTCOMES AND COST EFFECTIVENESS

Comprehensive Breast Cancer Screening with MRI and Ductal Lavage in Women at High Genetic Risk for Breast Cancer

Anne-Renee Hartman¹, Bruce Daniel², Allison Kurian¹, Meredith Mills¹, Kent Nowels³, Fred Dirbas⁴, Robert Herfkens², Kerry Kingham, Nicki Chun, James M. Ford¹ and Sylvia K. Plevritis²

¹Department of Radiology, ²Division of Oncology, ³Department of Pathology, ⁴Department of Surgery⁴

INTRODUCTION

Mutations in the breast cancer susceptibility genes BRCA1 and 2 account for greater than 60% of hereditary cases of breast cancer. By age 50, half of mutation carriers will develop breast cancer highlighting the need for very sensitive screening strategies that begin at an early age. Specific tumor characteristics and the young age of high-risk women being screened may contribute to the decreased sensitivity of mammography in this population. We developed a comprehensive screening protocol to determine the clinical utility of breast MRI and ductal lavage (DL) and to identify early cancer and premalignant lesions in women with a genetic predisposition to develop breast cancer.

METHODS AND MATERIALS

Patients for this study were recruited from the Stanford University Breast Cancer Genetics Clinic (CGC) (<http://www.stanford.edu/group/cgc/clinic.html>). This program serves the Northern California community through the identification, genetic counseling and testing, and high-risk oncology management of patients and families with an inherited predisposition to breast as well as other cancers. Women with inherited BRCA1 or 2 mutation or women with a greater than 10% risk of developing breast cancer at 10 years as estimated by The Claus model were enrolled in the study. Enrolled patients underwent biannual clinical breast exam, and annual mammography, breast MRI and ductal lavage. The MRIs were obtained on a 1.5T imager Signa LX using a dedicated 4-coil phased array breast coil (MRI Devices). Because the breast MRI protocol is currently optimized as a unilateral breast exam, women underwent two separate breast MRI exams, one for each breast, 1 to 3 days apart, and timed according to menstrual cycle. Fluid-yielding ducts were identified through nipple aspiration. A histopathological diagnosis of normal, insufficient fluid for diagnosis (ICMD), mild atypia, marked atypia, or malignant cells were given to each sample.

RESULTS

Forty-one women (median age 42.5 years) have undergone a first round of screening MRI. Eleven of the 41 had a prior oophorectomy and 3 of the 41 were on tamoxifen for at least 6 months prior to their first screen. Twenty-one of the 41 patients required either biopsy or a 6-month follow-up MRI. One case of high-grade DCIS was screen detected by MRI in a BRCA1 carrier at who did not have an oophorectomy and was not on tamoxifen. This lesion was missed on mammography and did not yield atypia on DL. Six patients were screen detected by MRI with premalignant lesions which

included radial scars, atypical lobular hyperplasia (ALH) and a papilloma. These lesions were not seen on mammography, except for one case of ALH. They did not yield atypia on DL. Ductal lavage detected 8 cases of atypia in 30 women with a normal MRI and mammography. Fifteen women have undergone a second round of MRI screening with no biopsies or follow-up required.

CONCLUSIONS

Breast MRI can identify high-grade DCIS and other premalignant lesions missed by mammography and DL. DL can detect atypia in a cohort of women at high risk for developing breast cancer with normal MRIs and mammography. A larger prospective, longitudinal screening trial is needed to determine if atypia, screened detected malignant and premalignant lesions can impact breast cancer mortality and which subgroups of high-risk women will benefit from intensive screening by breast MRI or DL or both.

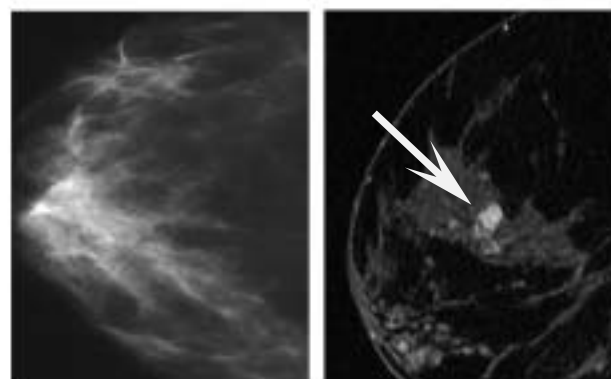


Figure 1: Breast MRI (shown on right) demonstrates a 7mm enhancing lesion that corresponds to a 5cm high-grade DCIS with comedo-necrosis in patient with BRCA1 mutation; lesion was missed on mammogram (shown on left).

Publications & **Presentations**

Published Papers, Book Chapter & Books

- Acar B, Beaulieu CF, Gokturk SB, Tomasi C, Paik DS, Jeffrey RB Jr, Yee J, Napel S. Edge displacement field-based classification for improved detection of polyps in CT colonography. *IEEE Trans Med Imaging* 2002; 21:1461-7.
- Adami A, Thijs V, Tong DC, Beaulieu C, Moseley ME, Yenari MA. Use of diffusion weighted MRI to predict the occurrence and severity of hemorrhagic transformation in a rabbit model of embolic stroke. *Brain Res* 2002; 944:32-9
- Atlas SW. Subspecialty health care in the United States: more is better. *The Weekly Standard* February 2003.
- Bammer R, Acar B, Moseley ME. In vivo MR tractography using diffusion imaging. *Eur J Radiol* 2003; 45:223-34.
- Bammer R, Herneth AM, Maier SE, Butts K, Prokesch RW, Do HM, Atlas SW, Moseley ME. Line scan diffusion imaging of the spine. *AJNR Am J Neuroradiol* 2003; 24:5-12.
- Bammer R, Markl M, Barnett A, Acar B, Alley MT, Pelc NJ, Glover GH, Moseley ME. Analysis and generalized correction of the effect of spatial gradient field distortions in diffusion-weighted imaging. *Magn Reson Med* 2003; 50:560-9.
- Bammer R. Basic principles of diffusion-weighted imaging. *Eur J Radiol* 2003; 45:169-84.
- Barnes PD. Editorial: Imaging in the pediatric patient with headache. *Int Pediatr* 2002; 17:67.
- Beaulieu CF, Paik DS, Napel S, Jeffrey RB. Advanced 3D display methods. IN: *Atlas of Virtual Colonoscopy*. Dachman AH (ed), Springer-Verlag, NY, 2003.
- Beaulieu CF, Rubin GD. Perspective rendering of spiral CT data: Flying through and around normal and pathologic anatomy. In: *Spiral CT*, 3rd Edition. Fishman EK, Jeffrey RB Jr (Eds), Lippincott-Raven, Boston, 2003.
- Bendeck SE, Nino-Murcia M, Berry GJ, Jeffrey RB Jr. Imaging for suspected appendicitis: negative appendectomy and perforation rates. *Radiology* 2002; 225:131-6.
- Birdwell RL, Morris E, Wang S-C, Parkinson B. *Pocket Radiologist: Breast; Top 100 Diagnoses*. WB Saunders; Amirsys Salt Lake City Utah, 2003.
- Birdwell RL. Commentary for "Ultrasound of ductal carcinoma in situ". *Radiographics* 2002; 22:280-281.
- Blankenberg F, Barnes P. Structural and functional imaging of hypoxic-ischemic injury in the fetal and neonatal brain. In *Fetal and Neonatal Brain Injury*, Stevenson DK, Benitz WE, Sunshine P (eds), 3rd Edition, Cambridge Press, UK, 2003.
- Busch E, Beaulieu C, de Crespigny A, Kreisler S, Diener HC, Moseley ME. Combined x-ray angiography and diffusion-perfusion MRI for studying stroke evolution after rt-PA treatment in rats. *Brain Res* 2002; 953:112-8.
- Butts K, Daniel BL, Chen L, Bouley D, Wansapura J, Maier SE, Dumoulin C, Watkins R. Diffusion-weighted MRI after cryosurgery of the canine prostate. *J Magn Reson Imaging* 2003; 17:131-5.
- Chang SD, Levy RP, Marks MP, Do HM, Marcellus ML, Steinberg GK. Multimodality treatment of giant intracranial arteriovenous malformations. *Neurosurgery* 2003; 53:1-11.
- Chen L, Wansapura JP, Heit G, Butts K. Study of laser ablation in the in vivo rabbit brain with MR thermometry. *J Magn Reson Imaging* 2002; 16:147-52.
- Chow LC, Bammer R, Moseley ME, Sommer FG. Single breath-hold diffusion-weighted imaging of the abdomen. *J Magn Reson Imaging* 2003; 18:377-82.
- Chow LC, Chan FP, Li KC. A comprehensive approach to MR imaging of mesenteric ischemia. *Abdom Imaging* 2002; 27:507-516.
- Contag CH, Ross BD. It's not just about anatomy: in vivo bioluminescence imaging as an eyepiece into biology. *J Magn Reson Imaging* 2002; 16:378-87.
- Daniel B, Herfkens R. Intraoperative MR imaging: can image guidance improve therapy? *Acad Radiol*. 2002; 9:875-7.
- Desmond JE, Chen SH. Ethical issues in the clinical application of fMRI: factors affecting the validity and interpretation of activations. *Brain Cogn* 2002; 50:482-97.
- Desmond JE, Chen SH, DeRosa E, Pryor MR, Pfefferbaum A, Sullivan EV. Increased frontocerebellar activation in alcoholics during verbal working memory: an fMRI study. *Neuroimage* 2003; 19:1510-1520.
- Desmond JE, Glover GH. Estimating sample size in functional MRI (fMRI) neuroimaging studies: statistical power analyses. *J Neurosci Methods* 2002; 118:115-28.
- Desser TS, Sze DY, Jeffrey RB. Imaging and intervention in the hepatic veins. *AJR Am J Roentgenol* 2003; 180:1583-91.
- Do HM, Gaeta RR, Marks MP. Percutaneous Therapy for the Spine. In: *Endovascular and Percutaneous Therapy of the Brain and Spine*. Marks MP, Do HM (editors). Lippincott Williams and Wilkins, Philadelphia, PA, 2002:449-473.
- Do HM, Kim BS. Percutaneous Vertebroplasty. In: *Endoscopic Spine Surgery and Instrumentation and Percutaneous Procedures*. Kim D, Fessler R, Regan J (eds). Thieme, New York, NY 2003. (In press).
- Do HM, Marks MP. Endovascular Therapy for Vasospasm. In: *Endovascular and Percutaneous Therapy of the Brain and Spine*. Marks MP, Do HM (editors). Lippincott Williams and Wilkins, Philadelphia, PA 2002:183-198.
- Do HM. Intraosseous venography during percutaneous vertebroplasty. Is it needed? *Am J Neurorad* 23:508-9, 2002.
- Do, HM. Percutaneous vertebroplasty: rationale, clinical outcomes, and future directions. *Neuroimaging Clin N Am* 2003; 13:343-363.
- Dodd RL, Barnes PD, Huhn SL. Spontaneous resolution of a prepontine arachnoid cyst: case report and review of the literature. *Pediatr Neurosurg* 2002; 37:152-157.

- Elkins CJ, Markl M, Pelc NJ, Eaton J. 4D magnetic resonance velocimetry for mean velocity measurements in complex turbulent flows. *Experiments in Fluids* 2003; 34:494-503
- Engelhorn T, Doerfler A, de Crespigny A, Beaulieu C, Forsting M, Moseley ME. Multilocal magnetic resonance perfusion mapping comparing the cerebral hemodynamic effects of decompressive craniectomy versus reperfusion in experimental acute hemispheric stroke in rats. *Neurosci Lett* 2003; 344:127-31.
- Fleetwood IG, Marcellus ML, Levy RP, Marks MP. Deep arteriovenous malformations of the basal ganglia and thalamus: natural history. *J Neurosurg* 2003; 98:747-50.
- Franc B, Goris M. Low uptake of Tc-99m tetrofosmin in lung cancer: a case report. *Clin Nucl Med* 2002; 27:698-700.
- Fredericson M, Salamanca L, Beaulieu CF. Sacral stress fractures: tracking down nonspecific pain in distance runners. *Phys Sportsmed* 2003; 31:31-42.
- Friedland S, Yu A, Rouse RV, Wong D, Nino-Murcia M, Soetikno RM. Gastric pancreatic rest leading to pyogenic liver abscess. *Gastrointes Endosc* 2002; 56:438-440
- Frisoli JK, Sze D. Mechanical thrombectomy for the treatment of lower extremity deep vein thrombosis. *Tech Vasc Interv Radiol* 2003; 6:49-52.
- Funabashi N, Kobayashi Y, Perlroth M, Rubin GD. Coronary artery: quantitative evaluation of normal diameter determined with electron-beam CT compared with cine coronary angiography initial experience. *Radiology* 2003; 226:263-71.
- Golby AJ, Poldrack RA, Illes J, Chen D, Desmond JE, Gabrieli JD. Memory lateralization in medial temporal lobe epilepsy assessed by functional MRI. *Epilepsia* 2002; 43:855-63.
- Gold GE, Hargreaves BA, Beaulieu CF. Protocols in sports magnetic resonance imaging. *Top Magn Reson Imaging* 2003; 14:3-23.
- Goldstein RA, Do HY, Jensen ME, Marks MP. Part 1. Neuroangiographic Complications: What to Do and When. *Contemporary Diagnostic Radiology* 2003; 26:1-6.
- Goldstein RA, Do HY, Jensen ME, Marks MP. Part 2. Neuroangiographic complications: What to do and when. *Contemporary Diagnostic Radiology* 2003; 27:1-6.
- Goris ML, Zhu HJ, Blankenberg F, Chan F, Robinson TE. An automated approach to quantitative air trapping measurements in mild cystic fibrosis. *Chest* 2003; 123:1655-63.
- Guccione S, Yang YS, Shi G, Lee DY, Li KC, Bednarski MD. Functional genomics guided with MR imaging: mouse tumor model study. *Radiology* 2003; 228:560-8.
- Hargreaves BA, Gold GE, Beaulieu CF, Vasanawala SS, Nishimura DG, Pauly JM. Comparison of new sequences for high-resolution cartilage imaging. *Magn Reson Med* 2003; 49:700-9
- Harper C, Garrick T, Matsumoto I, Pfefferbaum A, Sullivan EV, Adalsteinsson E, Dodd P, Lewohl J, Butterworth R. How important are brain banks for alcohol research? *Alcohol Clin Exp Res* 2003; 27:310-323.
- Hobbs SK, Shi G, Bednarski MD. The synthesis of polymerized thin films for immobilized ligand display in proteomic analysis. *Bioconjugate Chem* 2003; 14:526-531.
- Hossack JA, Sumanaweera TS, Napel S, Ha JS. Quantitative 3-D diagnostic ultrasound imaging using a modified transducer array and an automated image tracking technique. *IEEE Transactions on Ultrasonics, Ferroelectrics, and Frequency Control* 2002; 49:1029-1038.
- Hwang GL, Moffatt SD, Mitchell JD, Leung AN. Chronic expanding hematoma of the thorax. *AJR* 2003; 180:1182-3.
- Ikeda DM, Birdwell RL, O'Shaughnessy KF, Brenner RJ, Sickles EA. Analysis of 172 subtle findings on prior normal mammograms in women with breast cancer detected at follow-up screening. *Radiology* 2003; 226:494-503.
- Ikeda DM, Birdwell RL, Sickles EA, O'Shaughnessy K, Birdwell RL. Letter to the Editor: Reply. *Radiology* 2003.
- Illes J, Atlas SW. (Eds.) *Topics in Magnetic Resonance Imaging: Ethical Issues in MR Imaging*. Lippincott Williams & Wilkins, New York, 2002; vol 13(2).
- Illes J, Atlas SW. Introduction and commentary: Emerging ethical issues in MRI, IN *Topics in Magnetic Resonance Imaging: Ethical Issues in MR Imaging* Illes J, Atlas SW (Eds.), Lippincott Williams & Wilkins, New York, 2003; vol 13(2), pp. 71-72.
- Illes J, Desmond J, Huang LF, Raffin T, Atlas S. Ethical and practical considerations in managing incidental neurologic findings in fMRI. *Brain Cogn* 2002; 50:358-365.
- Illes J, Fan E, Koenig B, Raffin TA, Kann D, Atlas SW. Self-referred whole body imaging: Current implications for health care consumers. *Radiology* 2003; 228:346-351.
- Illes J, Kirschen M, Gabrieli JDE. From neuroimaging to neuroethics. *Nat Neurosci* 2003; 6:250.
- Illes J, Raffin T. Neuroethics: A new discipline is emerging in the study of brain and cognition. *Brain Cogn* 2002; 50:341-344.
- Illes J. (Ed.) *Ethical Challenges in Advanced Neuroimaging, Brain and Cognition*, Academic Press, New York, 2002; Vol 50(3).
- Illes J. Enduring qualities in mentoring. *Science NextWave* 2002; <http://nextwave.sciencemag.org/cgi/content/full/2002/03/26/10>.
- International Study of Unruptured Aneurysm Investigators. Unruptured intracranial aneurysms: natural history, clinical outcome, and risks of surgical and endovascular treatment. *The Lancet* 2003; 362:103-10.
- Jackman R, Birdwell RL, Ikeda DM. Atypical ductal hyperplasia: can some lesions be defined as probably benign after stereotactic 11-gauge vacuum-assisted biopsy, eliminating

- the recommendation for surgical excision? *Radiology* 2002; 224:548-54.
- Kim BS, Illes J, Kaplan RT, Reiss A, Atlas SW. Neurologic findings in healthy children on pediatric fMRI: Incidence and significance. *Am J Neurorad* 2002; 23:1-4.
- Kim DH, Adalsteinsson E, Glover GH, Spielman DM. Regularized higher-order in vivo shimming. *Magn Reson Med* 2002; 48:715-22.
- Kim DH, Adalsteinsson E, Spielman DM. Simple analytic variable density spiral design. *Magn Reson Med* 2003; 50:214-9.
- Kim P, Prapong W, Sze DY, So SK, Razavi MK. Treatment of hepatocellular carcinoma with sub-selective transcatheter arterial oily chemoinfusion. *Tech Vasc Interv Radiol* 2002; 5:127-31.
- Kinder EA, Birdwell RL, Kahn D. Iatrogenic intentional deflation of a saline breast implant after contralateral spontaneous implant deflation: a case report. *Journal of Women's Imaging* 2002; 4:179-181 2002
- Kuehne T, Fahrig R, Butts K. Pair of resonant fiducial markers for localization of endovascular catheters at all catheter orientations. *J Magn Reson Imaging* 2003; 17:620-4.
- Lee M, Birdwell RL, Dirbas F, Ikeda DM, Bergman GA, Rossiter S, Jeffrey SS. Breast specimen radiography. Is compression necessary? *Journal of Women's Imaging* 2002; 4:156-164
- Leibowitz R, Do HM, Marcellus ML, Chang SD, Steinberg GK, Marks MP. Parent vessel occlusion for vertebrobasilar fusiform and dissecting aneurysms. *Am J Neurorad* 2003; 24:902-7
- Leibowitz R, Marcellus ML, Chang SD, Steinberg GK, Do HM, Marks MP. Parent vessel occlusion in vertebrobasilar fusiform and dissecting aneurysms. *Am J Neurorad* 2003; 24:902-7
- Lewis-Carey MB, Kee ST, Feinstein JA. Temporary IVC filtration before patent foramen ovale closure in a patient with paradoxical embolism. *J Vasc Interv Radiol* 2002; 13:1275-8.
- Logan L, Neustel S, Higginbotham K. The changing CT environment. *Radiol Technol* 2003; 74:467-75.
- Lyons DM, Afarian H, Schatzberg AF, Sawyer-Glover A, Moseley ME. Experience-dependent asymmetric variation in primate prefrontal morphology. *Behav Brain Res* 2002; 136:51-9
- Marcus KJ, Dutton SC, Barnes P, Coleman CN, Pomeroy SL, Goumnerova L, Billet AL, Kieran M, Tarbell NJ. A phase I trial of etanidazole and hyperfractionated radiotherapy in children with diffuse brainstem glioma. *Int J Radiat Oncol Biol Phys* 2003; 55:1182-1185.
- Markl M, Alley MT, Pelc NJ. Balanced phase contrast steady state free precession (PC-SSFP): A novel technique for velocity encoding by gradient inversion. *Magn Reson Med* 2003; 49:945-52.
- Markl M, Chan FP, Alley MT, Wedding KL, Draney MT, Elkins CJ, Parker DW, Wicker R, Taylor CA, Herfkens RJ, Pelc NJ. Time-resolved three-dimensional phase-contrast MRI. *J Magn Reson Imaging* 2003; 17:499-506.
- Marks MP, Do HM (editors). *Endovascular and Percutaneous Therapy for the Brain and Spine*. Lippincott Williams and Wilkins, Philadelphia, PA, 2002.
- Marks MP. Endovascular Therapy for Arteriovenous Malformations. In: *Endovascular and Percutaneous Therapy for the Brain and Spine*. Marks MP, Do HM (eds). Lippincott, Williams and Wilkins, Philadelphia, PA, 2002:243-276.
- Marks MP. Endovascular Therapy for Intracranial Atherosclerotic Disease. In *Endovascular and Percutaneous Therapy for the Brain and Spine*. Marks MP, Do HM (eds). Lippincott, Williams and Wilkins, Philadelphia, PA, 2002:75-96.
- Mayer D, Dreher W, Leibfritz D. Fast U-FLARE based correlation peak imaging with complete effective homonuclear decoupling. *Magn Reson Med* 2003; 49:810-816.
- McAdams TR, Spisak S, Beaulieu CF, Ladd AL. The effect of pronation-supination on the minimally displaced scaphoid fracture. *Clin Orthop* 2003; 411:255-9.
- Min J. Book Review: *Fundamentals of Fluoroscopy*. *Abdom Imag* 2003; 28:150.
- Moseley M, Bammer R, Illes J. Diffusion-tensor imaging of cognitive performance. *Brain Cogn* 2002; 50:396-413.
- Moseley M. Diffusion tensor imaging and aging - a review. *NMR Biomed* 2002; 15:553-60.
- Muir-Robinson G, Hwang BJ, Feller MB. Retinogeniculate axons undergo eye-specific segregation in the absence of eye-specific layers. *J Neurosci* 2002; 22:5259-64.
- Napel S, Xu H, Paik DS, Ross BA, Sumanaweera TS, Hossack J, Jeffrey RB Jr. Carotid disease: Automated analysis with cardiac-gated three-dimensional us technique and preliminary results. *Radiology* 2002; 222:560-3.
- Nino-Murcia M, Jeffrey RB Jr. Multidetector-row CT and volumetric imaging of pancreatic neoplasms. *Gastroenterol Clin N Am* 2002; 31:881-896.
- Nino-Murcia M, Tamm EP, Charnsangavej C, Jeffrey RB Jr. Multidetector-row helical CT and advanced postprocessing techniques for the evaluation of pancreatic neoplasms. *Abdom Imag* 2003; 28:366-77.
- Nordahl TE, Salo R, Possin K, Gibson R, Flynn N, Leamon M, Galloway GP, Pfefferbaum A, Spielman DM, Adalsteinsson E, Sullivan EV. Low N-acetyl-aspartate and high choline in the anterior cingulum of recently abstinent methamphetamine dependent subjects: a proton MRS study. *Psychiatry Res* 2002; 116:43-52.
- Partik BL, Leung AN, Muller MR, Breitenseher M, Eckersberger F, Dekan G, Helbich TH, Metz V. Using a dedicated lung-marker system for localization of pulmonary nodules before thoracoscopic surgery. *AJR Am J Roentgenol* 2003; 180:805-9.

- Partik BL, Stadler A, Schamp S, Koller A, Voracek M, Heinz G, Helbich TH. 3D versus 2D ultrasound: accuracy of volume measurement in human cadaver kidneys. *Invest Radiol* 2002; 37:489-95.
- Post AM, Katsikis PD, Tait JF, Geaghan SM, Strauss HW, Blankenberg FG. Imaging cell death with radiolabeled annexin V in an experimental model of rheumatoid arthritis. *J Nucl Med* 2002; 43:1359-65.
- Prokesch RW, Chow LC, Beaulieu CF, Nino-Murcia M, Mindelzun RE, Bammer R, Huang J, Jeffrey RB Jr. Local staging of pancreatic carcinoma with multi-detector row CT: use of curved planar reformations initial experience. *Radiology* 2002; 225:759-65.
- Qayyum A, Birdwell RL, Daniel BL, Nowels K, Jeffrey SS, Agoston TA, Herfkens RJ. MRI of infiltrating lobular carcinoma of the breast: imaging-pathological correlation. *AJR* 2002; 178:1227-1232.
- Raman R, Napel S, Rubin GD. Curved-Slab Maximum Intensity Projection: Method and Evaluation. *Radiology* 2003; Aug 27 [Epub ahead of print]
- Razavi MK, Hwang G, Jahed A, Modanloo S, Chen B. Abdominal myomectomy versus uterine fibroid embolization in the treatment of symptomatic uterine leiomyomas. *AJR Am J Roentgenol* 2003; 180:1571-5.
- Razavi MK, Wolanske KA, Hwang GL, Sze DY, Kee ST, Dake MD. Angiographic classification of ovarian artery-to-uterine artery anastomoses: initial observations in uterine fibroid embolization. *Radiology* 2002; 224:707-12.
- Razavi MK, Wong H, Kee ST, Sze DY, Semba CP, Dake MD. Initial clinical results of tenecteplase (TNK) in catheter-directed thrombolytic therapy. *J Endovasc Ther* 2002; 9:593-8.
- Reeder SB, Pelc NJ, Alley MT, Gold GE. Rapid MR imaging of articular cartilage with steady-state free precession and multipoint fat-water separation. *AJR Am J Roentgenol* 2003; 180:357-62.
- Rosito O, Nino-Murcia M, Wolfe V, Kiratli J, Perkash I. The effects of colostomy on the quality of life in patients with spinal cord injury: A retrospective analysis. *J Spinal Cord Med* 2002; 25:174-183.
- Rubesova E, Berger F, Wendland MF, Hong K, Stevens KJ, Gooding CA, Lang P. Gd-labeled liposomes for monitoring liposome-encapsulated chemotherapy: quantification of regional uptake in tumor and effect on drug delivery. *Acad Radiol* 2002; 9 Suppl 2:S525-7.
- Rubin GD. 3-D imaging with MDCT. *Eur J Radiol* 2003; 45 Suppl 1:S37-41.
- Rubin GD. CT angiography of the thoracic aorta. *Semin Roentgenol* 2003; 38:115-34.
- Rubin GD. MDCT imaging of the aorta and peripheral vessels. *Eur J Radiol* 2003; 45 Suppl 1:S42-9.
- Santana P, Dessler TS, Teng N. Preoperative CT diagnosis of primary fallopian tube carcinoma in a patient with a history of total abdominal hysterectomy. *J Comput Assist Tomogr* 2003; 27:361-3.
- Schreiber JP, Jeffrey RB, Davila M, Beaulieu CF. Spiral and multidetector CT of the large intestine: virtual colonoscopy. In: Fishman EK, Jeffrey RB Jr (Eds), *Spiral CT*, 2nd Edition, Lippincott-Raven, Boston, 2003.
- Smith WS, Mindelzun RE, Miller B. Simultanagnosia through the eyes of an artist. *Neurology* 2003; 60:1832-4.
- Spencer D, Zitzelberger T, Spielman D, Kaye J. MRS in relation to hippocampal volume in the oldest old. *Neurology* 2003; 60:1194-1196.
- Stanley G, Jeffrey RB Jr, Feliz B. CT findings and mistopathology of intratumoral steatosis in focal nodular hyperplasia: case report and review of the literature. *J Comput Assist Tomogr* 2002; 26:815-7. Review. Erratum in: *J Comput Assist Tomogr* 2003; 27:103.
- Stevens GM, Birdwell RL, Beaulieu CF, Ikeda DM, Pelc NJ. Circular tomosynthesis: potential in imaging of breast and upper cervical spine—preliminary phantom and in vitro study. *Radiology* 2003; 228:569-75.
- Stevens K, Tao C, Lee SU, Salem N, Vandevenne J, Cheng C, Neumann G, Valentin-Opran A, Lang P. Subchondral fractures in osteonecrosis of the femoral head: comparison of radiography, CT, and MR imaging. *AJR Am J Roentgenol* 2003; 180:363-8.
- Sugimoto K, Hofmann LV, Razavi MK, Kee ST, Sze DY, Dake MD, Semba CP. The safety, efficacy, and pharmacoeconomics of low-dose alteplase compared with urokinase for catheter-directed thrombolysis of arterial and venous occlusions. *J Vasc Surg* 2003; 37:512-7.
- Sze DY, Freeman SM, Slonim SM, Samuels SL, Andrews JC, Hicks M, Ahrar K, Gupta S, Reid TR. Dr. Gary J. Becker Young Investigator Award: intraarterial adenovirus for metastatic gastrointestinal cancer: activity, radiographic response, and survival. *J Vasc Interv Radiol* 2003; 14:279-90.
- Szuba A, Razavi M, Rockson SG. Diagnosis and treatment of concomitant venous obstruction in patients with secondary lymphedema. *J Vasc Interv Radiol* 2002; 13:799-803.
- Tong D, Kim BS, Do HM. Developing Acute Stroke Imaging Capability. In: *Imaging of Acute Stroke*. N Kent TA (editor). Kluwer Press, Boston MA, 2003. (In press)
- Umana JP, Lai DT, Mitchell RS, Moore KA, Rodriguez F, Robbins RC, Oyer PE, Dake MD, Shumway NE, Reitz BA, Miller DC. Is medical therapy still the optimal treatment strategy for patients with acute type B aortic dissections? *J Thorac Cardiovasc Surg* 2002; 124:896-910.
- Weir RU, Marcellus ML, Do HM, Steinberg GK, Marks MP. Aneurysmal subarachnoid hemorrhage in patients with Hunt and Hess grade 4 or 5: treatment using the Guglielmi detachable coil system. *AJNR Am J Neuroradiol* 2003; 24:585-90.
- Wong W, Do HM. Spine Interventions. In: *Computed Tomography and Magnetic Resonance Imaging in the Whole*

Body, 3rd. Edition. Haaga J.R., Lanzieri CF, Zerhouni E. (editors). WB Saunders, Philadelphia, PA. 2002:814-837.

Xing L, Cotrutz C, Hunjan S, Boyer AL, Adalsteinsson E, Spielman DM. Inverse planning for functional image-guided intensity modulated radiation therapy. *Phys Med Biol* 2002; 47:3567-78.

Yoshioka H, Alley M, Steines D, Stevens K, Rubesova E, Genovese M, Dillingham MF, Lang P. Imaging of the articu-

lar cartilage in osteoarthritis of the knee joint: 3D spatial-spectral spoiled gradient-echo vs. fat-suppressed 3D spoiled gradient-echo MR imaging. *J Magn Reson Imaging* 2003; 18:66-71.

Zenzen W. Interventional magnetic resonance imaging: New techniques and devices. *Applied Radiology* 2002; Supplement to December 2002.

Papers, Book Chapter & Books in Press

Adalsteinsson E, Langer-Gould A, Homer RJ, Rao A, Sullivan EV, Pfefferbaum A, Atlas SW. Gray matter NAA deficits in secondary progressive but not relapsing-remitting multiple sclerosis. *Am J Neuroradiol*.

Arzoumanian Y, Mirmiran M, Barnes PD, Woolley K, Ariagno RL, Moseley ME, Fleisher BE, Atlas SW. Diffusion tensor brain imaging findings at term equivalent age may predict neurologic abnormalities in low birth weight preterm infants. *Am J Neuroradiol*,

Bammer R, Markl M, Acar B, Alley MT, Pelc NJ, Moseley ME, Glover G. Analysis and generalized correction of the effect of spatial gradient field distortions in diffusion-weighted imaging. *Magn Reson Med*.

Birdwell RL, Jackman R. Clip/marker migration 5-10 weeks after stereotactic 11-gauge vacuum-assisted breast biopsy: report of two cases. *Radiology*.

Daniel BL, Freeman LJ, Pyzoha J, McCoy T, Birdwell RL, Bouley D. An MRI-compatible semi-automated vacuum assisted breast biopsy system. *Magn Reson Imag*.

Daniel BL, Gardner R, Birdwell RL, Nowels K, Johnson D. MRI enhancement patterns of breast papillomas. *J Magn Resonan Imaging*.

Hahn JS, Lewis AJ, Barnes PD. Hydranencephaly owing to twin-twin transfusion: serial fetal US and MRI findings. *J Child Neurol*.

Hobbs S, Shi G, R Homer, G Harsh, S Atlas, M Bednarski. Magnetic resonance image guided proteomics of human glioblastoma multiforme. *J Magn Reson Imaging*.

Hunjan S, Adalsteinsson E, Kim DH, Harsh GR, Boyer AL, Spielman DM, Xing L. Quality assurance of magnetic resonance spectroscopic imaging-derived metabolic data. *Int J Radiat Oncol Biol Phys*.

Illes J, Kirschen MP. New prospects and ethical challenges for neuroimaging within and outside the health care system. Invited Editorial, Part II, *AJNR Am J Neuroradiol*.

Illes J. Neuroethics in a new era of neuroimaging. Invited Editorial, Part I. *AJNR Am J Neuroradiol*.

Kim BS, Razavi M, Do HM. N-butyl cyanoacrylate glue embolization in the treatment of splenic artery aneurysms. *JVIR*

Liu AY, Lopez JR, Steinberg GK, Do HM, Marks MP. Neurophysiologic monitoring in the endovascular therapy of aneurysms. *Am J Neuroradiol*.

Liu C. Generalized Diffusion Tensor Imaging (GDTI): A method for characterizing and imaging diffusion anisotropy caused by non-gaussian diffusion. *Isr J Chem*.

Markl M, Alley MT, Elkins CJ, Pelc NJ. Flow effects in balanced steady state free precession imaging. *Magn Reson Med*.

Markl M, Bammer R, Alley MT, Elkins CJ, Draney MT, Moseley ME, Pelc NJ. Generalized reconstruction of phase contrast MRI: analysis and correction of the effect of gradient field distortions. *Magn Reson Med*.

Markl M, Reeder SB, Chan FP, Alley MT, Herfkens RJ, Pelc NJ. Balanced steady state free precession and myocardial tagging (SSFP-Tagging): improved tag-persistence and SNR for the analysis of myocardial motion. *Radiology*.

Marks MP. Interventional neuroradiology In: *Anesthesiologist's Manual of Surgical Procedures*, 3rd Edition. Jaffee RA, Samuels SJ (eds). Lippincott, Williams and Wilkins, Philadelphia, PA.

Pfefferbaum A, Adalsteinsson E, Sullivan EV. Replicability of diffusion tensor imaging measurements of fa and trace in brain. *J Magn Resonan Imaging*.

Sundaram P, Beaulieu CF, Paik DS, Schraedley-Desmond P, Napel S, CT colonography: does improved z resolution help computer-aided polyp detection? *Med Phys*.

Swan GE, Cheng LS, Jack LM, Hemberger K, Carmelli D, Khroyan PTV, Ring HZ, Hops H, Andrews H, Tildesley E, McBride D, Benowitz B, Webster C, Wilhelmsen K, Feiler H, Koenig B, Caron L, Illes J. Environmental and genetic determinants of tobacco use: A multidisciplinary, longitudinal family-based design. *Cancer Epidemiol Biomarkers Prev*.
Vigen KK, Daniel BL, Pauly JM, Butts K. A triggered, navigated, multi-Baseline method for proton resonance frequency temperature mapping with respiratory motion. *Magn Reson Med*.

Wang S-C, Birdwell RL. MR Mammography. www.emedicine.com.

Wong H, Gotway MB, Sasson AD, Jeffrey RB. Periaortic hematoma at the level of the diaphragmatic crura as a sign of blunt traumatic aortic injury on helical CT. *Radiology*.

Yang Y-S, Guccione S, Bednarski, MD. Comparing genomic and histological correlation to radiographic changes: using a squamous cell carcinoma tumor model. *Acad Radiol*.

Peer-reviewed Presentations at Scientific Meetings

RSNA 2002

88TH SCIENTIFIC SESSION, CHICAGO, IL DECEMBER 2002

Acar B, Beaulieu C, Paik D, Yee J, Jeffrey RB, Napel S. 3D Differential Descriptors For Improved Computer-aided Detection (CAD) of Colonic Polyps in Computed Tomography Colonography (CTC)

Acar B. 3D differential descriptors for improved computer aided detection (CAD) of colonic polyps in CTC

Bammer R, Moseley ME, Sommer FG. Ultrafast diffusion-weighted imaging (DWI) of the abdomen.

Bandodkar P, Birdwell R, Ikeda D. Computer Aided Detection (CAD) with Screening Mammography in an Academic Institution: Preliminary Findings

Bilello M, Gokturk S, Beaulieu C, Jeffrey R, Napel S. Automatic Detection of Hypodense Hepatic Lesions on Contrast-enhanced Venous-phase CT: Method and Evaluation

Chan B, Desser T, Jeffrey RB, McDougall IR, Weigel R. Common and Uncommon High-Resolution Sonographic Features of Papillary Thyroid Carcinoma

Chan F, Koenig R, Blankenberg F. Soft Tissue Enhancement Characteristics of Nanoparticulate Iodinated Contrast Agent N1177

Chan F, Partik B, Chun S, Rubin G. Cardiac Vein Mapping with EKG-Gated Multidetector Row Computed Tomography

Chow L, Bammer R, Moseley M, Sommer G. Ultrafast Diffusion-Weighted Imaging (DWI) of the Abdomen

Chronik B, Scott G, Matter N, Venook R, Ungersma S, Xu H, Wong L, Morgan P, Macovski A, Gold G, Conolly S. Feasibility study of extremity imaging in humans using a prepolarized MRI system.

Do HM, Marcellus ML, Weir RU, Marks MP. Percutaneous vertebroplasty versus medical therapy for treatment of acute vertebral body compression fractures: a prospective randomized study.

Fahrig R, Wen Z, Nelson W, Pelc N. Development of a Hybrid X-ray/MR System for Interventional Guidance: Verification of X-ray Tube Behavior in Large Magnetic Fields Produces Surprising Results

Fontaine F, Ikeda D, Daniel B, Birdwell R, Nguyen M, Stables L. Contrast-enhanced Magnetic Resonance (MR) Imaging of Benign Fibrocystic Change of the Breast

Fuller S, Gold G, Stevens K, Hargreaves B, Beaulieu C. MR imaging of articular cartilage: comparison of driven equilibrium and fast spin echo with arthroscopy.

Gilat T, Fahrig R, Solomon E, Pelc N. Volumetric CT with a Large Array Scanned Source

Gokturk S, Bilello M, Napel S, Tomasi C, Jeffrey RB, Beaulieu C. Automatic Classification of Cysts and Metastases in Hepatic CT: Method and Evaluation

Gold G, Hargreaves B, Vasanawala S, Pauly J, Beaulieu C. Rapid imaging of articular cartilage using steady-state free precession.

Gold G, Shimakawa A, Hargreaves B, Brittain J, Pauly J, and Beaulieu C. High resolution three-dimensional knee cartilage imaging with FEMR.

Guccione S, Yang Y-S, Homer R, Harsh G, Atlas S, Bednarski M. Use of Clinical Contrast-enhanced MRI to Demarcate Functional Genomic Sample Acquisition in Human Glioblastoma Multiforme

Herneth A, Guccione S, Bammer R, Maier S, Bednarski M, Moseley M. The Role of Line-Scan-Diffusion-Imaging in the Characterization of Viable Tumor and Scar Tissue: Correlation of Quantitative Diffusion Measurements with Histopathologic and Genomics Data

Hobbs S, Shi G, Homer R, Harsh G, Atlas S, Bednarski M. Gadolinium-enhanced MRI Pattern Differences in Human Glioblastoma Multiforme Analyzed with Protein Microarray Profiles

Hundt W, Siebert K, Becker, Knez A, Rubin G, Reiser M. Assessment of Global Left Ventricular Function: Comparison of Multidetector Computed Tomography with Left Ventriculography

Hundt W, Yuh E, Seip R, Bednarski M. Magnetic Resonance Imaging and Gene Expression Changes in Focused Ultrasound Treated Muscle Tissue

Kao E, Ganaha F, Wang D, Wong H, Waugh J, Dake M. Stent-based Controlled Release of Intravascular Fas Ligand to Limit Plaque Progression and In-Stent Restenosis

Katz D, Ortiz A O, Wagner AJ, Cinnamon J, Beaulieu C, Math K. Newer and Emerging Applications of Multidetector Helical CT

Li P, Napel S, Paik D, Acar B, Jeffrey RB, Beaulieu C. A Statistical Approach for Registration of Polyps Detected in Prone and Supine CT Colonography (CTC)

Lyo J, Paik D, Chow L, Leung A, Napel S, Rubin G. Double Reading of Chest CT Scans: Comparison of Reader-reader Pairing versus Computer-aided Detection (CAD)-Reader Pairing for the Detection of Lung Nodules

Lyo J, Paik D, Zinck S, Naidich D, Napel S, Rubin G. Computer-aided Detection (CAD) of Lung Nodules on Thoracic CT Scans: Application to a Population Suspected of Having Nodules on Chest X-Ray (CXR) Interpretation

- Mani A, Napel S, Paik D, Olcott E, Yee J, Beaulieu C. CT Colonography: Improved Polyp Detection Sensitivity and Efficiency with Computer Aided Detection (CAD)
- Markl M, Reeder SB, Alley MT, Herfkens RJ, Pelc NJ. Balanced SSFP and myocardial tagging for improved tag-tissue contrast and SNR. Winner: Research Trainee Prize, Cardiovascular Imaging Section
- Paik D, Beaulieu C, Rubin G, Acar B, Jeffrey RB, Napel S. Optimization and Evaluation of a Computer Aided Detection (CAD) Algorithm for Both Colonic Polyps and Lung Nodules in CT
- Partik B, Zinck S, Leung A, Chan F, Voracek M, Rubin G. Primary Interpretation of Thoracic Multidetector-row CT (MDCT) Using Coronal Reformations
- Raman B, Raman R, Baek D, Rubin G, Napel S. Automated Measurement of Aortoortic and Aortoiliac Angulation for CT Angiography (CTA) of Abdominal Aortic Aneurysms (AAA) Prior to Endograft Repair
- Raman B, Raman R, Liu C, Frisoli J, Napel S, Rubin G. Automatic Identification of Major Arteries and Their Ostia for Postprocessing of CT Angiographic (CTA) Studies of the Chest, Abdomen and Pelvis
- Raman B, Raman R, Raman L, Beaulieu C. Radiology on Handheld Computers: Display Capabilities and PACS Integration Issues
- Raman R, Raman B, Hundt W, Stucker D, Napel S, Rubin G. Improved Speed of Bone Removal in CT Angiography (CTA) Using Automated Targeted Morphological Separation: Method and Evaluation in CTA of the Lower Extremity Occlusive Disease (LEOD)
- Raman R, Raman B, Logan L, Sofilos M, Novello L, Rubin G. Mobile Interactive Review of Automatically Post-processed CT Angiograms (CTA) for Planning Aortic Endograft Deployment in Abdominal Aortic Aneurysms
- Raman R, Raman B, Napel S, Rubin G. Automated Quantification of Arterial Calcification using CT Angiography (CTA): Method and Evaluation
- Raman R, Raman B, Raman L, Logan L, Rubin G. Technologies for Rapid Prototyping and Data Management in Medical Imaging Research
- Raman R, Raman B, Sofilos M, Zhuge F, Rubin G, Napel S. Automated Measurement of Diameters and Volumes of Abdominal Aortic Aneurysms (AAA) using Multiscale 3D Texture Analysis
- Reeder SB, Wen Z, Gold GE, Alley MT, Markl M, Pelc NJ. Multi-Point Dixon Fat-Water Separation and Steady-State Free Precession. Winner: Research Trainee Prize, Physics Section.
- Sasson A, Jeffrey RB, Nino-Murcia M. CT Patterns of Periapendiceal Inflammation in Acute Appendicitis
- Sherbondy A, Holmlund D, Schraedley P, Rubin G, Winograd T, Napel S. Alternative Input Devices for Efficient Navigation of Large CTA Studies
- Sundaram P, Beaulieu C, Paik D, Schraedley P, Jeffrey RB, Napel S. CT Colonography: Does Improved Through-plane (z) Resolution Aid Computer-aided Detection (CAD) of Polyps?
- Vigen K, Daniel B, Pauly J, Butts K. A Realtime Triggered, Navigated, Multi-baseline Method for PRF Temperature Mapping with Respiratory Motion
- Wong H, Sasson A, Gotway, Jeffrey R. Retrocrural Blood as a CT Sign of Aortic Injury
- Yuh E, Birdwell R, Daniel B, Ikeda D, Plevritis S, Herfkens R. Clinical Outcomes of Incidental Enhancing Lesions Detected on Contrast-Enhanced Breast MRI
- Zhughe F, Napel S, Raman R, Raman B, Rubin G. A Discrete Deformable Contour Model for Segmentation of Abdominal Aortic Thrombus

RSNA 2003

89TH SCIENTIFIC SESSION, CHICAGO, IL DECEMBER 2003

Alexander J, Bednarski M, Guccione S, Yao J, Menard C, Li KCP, Choyke P. Systemic prostate specific antigen (PSA) is a measure of vascular permeability: a study of dynamic contrast enhanced magnetic resonance imaging (DCE-MRI).

Chan FP, Lin W-T, Napel S. Correlative filtering to improve automated center path generation for MDCT coronary angiography

Ganguly A, Fahrig R, Wen Z, Pelc NJ. X-ray Image Quality Assessment in X-ray/MR Hybrid System

Gilat T, Fahrig R, Pelc NJ. A 3D Reconstruction Algorithm for an Inverse Geometry Volumetric CT System with a Large Array Scanned Source

Gold GE, Han E, Stainsby J, Wright GA, Brittain JH, Beaulieu CF. Relaxation Times and Contrast in Musculoskeletal MR Imaging at 3.0 Tesla

Gold GE, Pappas G, Blemker S, Whalen S, Campbell GT, Beaulieu CF. Abduction and External Rotation in Shoulder Impingement: An Open MRI Study

Hellinger JC, Draney MT, Markl M, Pelc NJ, Herfkens RJ. Application of Cine Phase Contrast Magnetic Resonance Imaging and SPAMM-Tagging for Assessment of Endoleaks and Aneurysm Sac Motion

Hellinger JC, Napoli A, Fleischmann D, Leung AN, Rubin GD. Multidetector Row CT (MDCT) Assessment of Thromboembolic Disease: Incremental Value of CT Venography (CTV) in 1240 Consecutive Exams

Li P, Napel S, Paik DS, Jeffrey RB Jr, Beaulieu CF. CT Supine and Prone Colon Data Registration: Algorithm Evaluations

Lo A, Song Y, Boyer AL, Pawlicki T, Xing L. Combining IMRT and MERT for Breast-Conserving Radiation Therapy

Nayak KS, Hargreaves A, Besier T, Delp S. High-Resolution Real-Time MRI of Knee Kinematics

Plevritis SK, Sigal BM, Salzman P. Estimating the stage shift and mortality reduction from CT lung cancer screening.

Raman B, Raman R, Carnethon C, Fortmann SP, Napel S, Rubin GD. Calcium Quantification In The Aortoiliac Arter-

ies: Interscan Variability of Agatston Scoring vs. Automated Mass Quantification In Noncontrast and Contrast Enhanced Scans.

Raman R, Raman B, Raman L, Beaulieu CF. Handheld Computers: Potential use as a Portable Volumetric Workstation.

Reeder SB, Markl M, Hellinger JC, Yu H, Herfkens RJ, Pelc NJ. Multi-Coil Cardiac CINE Imaging with "Dixon" Fat-Water Separation and Steady-State Free Precession

Reeder SB, Shimakawa A, Brittain JH, Yu H, Pelc NJ, Gold GE. Multi-Point "Dixon" Fat-Water Separation with Steady-State Free Precession at 3T: Application to Musculoskeletal Imaging

Rieke V, Vigen KK, Daniel BL, Pauly JM, Butts K. Referenceless PRF Shift Thermometry: Feasibility for Liver Applications

Rubin DL, Dessler TS. Building an Integrated Data Warehouse for Radiology Teaching, Process Improvement, and Research

Rubin GD, Lyo JP, Paik DS, Sherbondy AK, Naidich DP, Napel S. Impact of Computer-assisted Detection (CAD) Algorithm vs a Second Radiologist on Reader Sensitivity for Detecting Pulmonary Nodules in MDCT Scans

Rubin GD, Naidich DP, Sherbondy AJ, Lyo JP, Napel S. Inadequacy of Lung Nodule Reference Standard Based upon Standard Methods of Expert Consensus Review Using Cine-Paging of Transverse Thin-Section MDCT Lung Scans

Sherbondy A, Houston M, Napel S. Interactively Guided Volumetric Segmentation using Programmable Graphics Hardware.

Sommer G, Chow LC. Measurement of Renal Extraction Fraction Using Contrast-enhanced CT

Vasanawala SS, Hargreaves BA, Pauly JM, Nishimura DG, Beaulieu CF, Gold GE. Phase-Sensitive Steady-State Free Precession Musculoskeletal Imaging

Yun AJ, Lee P, Chao D, Schraedley-Desmond PK. The Lexicon Polemics in Radiology Reports: Disparity in Appreciated Probability Values Ascribed to Modifiers Used in Dictations among Radiologists and Clinicians

- Acar B, Bammer R, Moseley M. Comparative assessment of DT-MRI fiber tractography algorithms
- Adalsteinsson E, Pfefferbaum A, Sullivan E, Rao A, Langer-Gould A, Atlas S. Gray matter NAA deficits in secondary progressive but not relapse remitting multiple sclerosis: Quantification with volumetric MR spectroscopic imaging
- Alley M, Pineda A, Bammer R, Markl M, Pelc N. A method for MR eddy current characterization and compensation
- Angelos L, Shimakawa A, Daniel B, Maier C, Brittain J. Bilateral breast imaging using spiral acquisition with parallel imaging
- Aygula Z, Soher B, Young K, Maudsley A. GAVA—A graphical pulse sequence simulation, display and storage environment
- Bammer R, Chow L, F. Sommer, Moseley M. diffusion-weighted imaging of the abdomen within a single breath-hold
- Bangerter N, Hargreaves B, Nishimura D. General framework for the SNR analysis of multiple-acquisition SSFP
- Bangerter N, Nishimura D. Artifact reduction and SNR comparison of multiple-acquisition SSFP techniques
- Bock N, Beatty P, Chen X, Davidson L, Dazai J, Lifshitz N, Nieman B, Sled J, R Henkelman. In vivo high-field multiple-mouse MRI
- Brittain J, Shimakawa A, Wright G, Hargreaves B, Han E, Stainsby J, Hu B. Non-contrast-enhanced, flow-independent, 3D peripheral angiography using steady-state free precession at 3T
- Chan F, Levin J, Alley M, Herfkens R, Pelc N. Combined evaluation of ventricular wall motion and delayed myocardial enhancement using a 3D-cine technique
- Chen J, Daniel B, Pauly J, Butts K. Observations on the temperature dependence of apparent proton density in bovine adipose and muscle
- Cheng C, Taylor C, Herfkens R. In vivo quantification of abdominal aortic hemodynamic conditions at rest and during cycling exercise in healthy subjects aged 50-70
- Chhor C, Han E, Stainsby J, Wright G, Brittain J, Herfkens R. Quantitative measurements of T1 and T2 for the abdomen in a 3 Tesla whole-body imager
- Clayton D, Adalsteinsson E, Spielman D. Quantitation of 3D chemical shift data: nonlinear least-squares spectral estimation using a water reference and a priori knowledge
- Collins C, Chronik B. Modeling human tissues in pulsed gradient fields
- Cunningham C, Wright G, Vigneron D, Pauly J. Correction for RF inhomogeneity for improved spatial saturation
- Cunningham C, Wright G, Vigneron D, Pauly J. Method for “on-demand” generation of RF saturation pulses
- Daniel B, Dumoulin C, Watkins R, Rohling K, Giaquinto R, Presti J, Butts K, Bammer R, Moseley M. 3Tesla imaging of the prostate with a rigid endorectal coil
- Deutsch G, Dougherty R, Bammer R, Siok WT, Gabrieli J, Wandell B. Correlations between white matter structure and reading performance in children measured by diffusion tensor imaging
- DiCarlo J, Hu B, Nishimura D, Pauly J. Interleaved variable-density 1D Fourier velocity-encoding
- Fahrig R, Wen Z, Daniel B, Butts K, Kee S, Heit G, Yu H, Shimakawa A, Ganguly A, Pelc N. Initial clinical experience using a truly hybrid X-ray/MR imaging system
- Feng C-MJ, Tan LH, Spinks J, Siok WT, Perfetti C, Xiong J, Fox P, Gao J-H. Neural systems of second language reading are shaped by native language
- Gold G, Han E, Shimakawa A, Hargreaves B, Brittain J, Beaulieu C. High-resolution cartilage imaging at 3T using fat-suppressed SSFP
- Gold G, Shimakawa A, Hargreaves B, Vasanawala S, Brittain J, Beaulieu C. Spiral-out spiral-in CSI
- Gurr D, Shimakawa A, Wright G, Santos J, Levin J, Busse R, Herfkens B, Brittain J. Polar phase encode placement for 3D acquisition with time-resolved projections
- Han E, Gold G, Stainsby J, Wright G, Beaulieu C, Brittain J. In-Vivo T1 and T2 measurements of musculoskeletal tissue at 3T and 1.5T
- Hargreaves B, Nishimura D, Conolly S. Minimum-time multi-dimensional gradient waveform design using convex optimization
- Hargreaves B, Nishimura D. Relaxometry using transient steady-state free precession imaging
- Hargreaves B, Vasanawala S, Nayak K, Brittain J, Hu B, Nishimura D. Fat suppressed steady-state free precession imaging using phase detection
- Herzka D, Reeder S, McVeigh E. SNR behavior of SSFP: dependence on TR, bandwidth & gradient performance optimization
- Hobbs S, Shi G, Homer R, Harsh G, Atlas S, Bednarski M. Magnetic resonance image guided proteomics of human glioblastoma multiforme
- Hsu J-J, Glover G. Mitigation of susceptibility-induced signal loss in neuroimaging using localized shim coils
- Hundt W, Yuh E, Lee D, Bednarski M. MR imaging and gene expression changes in focused ultrasound-treated muscle tissue

- Hyon MS, Ikeno F, Kaneda H, Nayak K, Meyer C, Yeung A, McConnell M. Magnetic resonance imaging detects in-stent thrombosis
- Kim DH, Adalsteinsson E, Spielman D. Spiral-out spiral-in CSI
- Kim D, Sailasuta N, Hurd R, Adalsteinsson E, Spielman D. High resolution spiral PRESS at 3T
- Law C, Glover G. Novel spiral-in/out method for reduced susceptibility artifacts in BOLD fMRI
- Lee JH, Pauly J, Nishimura D. Broadband multi-coil reconstruction using spiral trajectories
- Lee JH, Pauly J, Nishimura D. Partial k-space reconstruction for under-sampled variable-density spiral trajectories
- Lew C, Chan F, Pelc N. Investigating UNFOLD with factors greater than 2
- Lew C, Pelc N. Artifacts caused by transient effects in multi-shot EPI
- Li T, Kim D-H. High-resolution diffusion-weighted MRI using variable density spiral acquisition
- Li T, Takahashi A, Wang Y, Mathews V, Glover G. Minimizing susceptibility artifacts in BOLD fMRI using 3D dual-echo spiral in (DSPIN) acquisition
- Liu C, Bammer R, Acar B, Moseley M. Generalized diffusion tensor imaging (GDTI) using higher order tensor (HOT) statistics
- Liu C, Bammer R, Moseley M. The effect of the concomitant magnetic field in diffusion weighted imaging
- Liu C, Chan F. Effects of breath holding on right and left ventricular stroke volumes in balanced-ssfp cine MRI
- Markl M, Alley M, Elkins C, Pelc N. Flow effects in balanced steady state free precession imaging
- Markl M, Bammer R, Alley M, Moseley M, Glover G, Pelc N. Generalized modeling of gradient field non-linearities and reconstruction of phase contrast MRI measurements
- Matsuo K, Toma K, Oishi K, Dinh T, Kato C, Glover G, Nakai T. Difference in motor planning for the use of a pen or a finger - functional magnetic resonance imaging during copying gestures
- Matter N, Chronik B, Conolly S, Scott G. Effects of electromagnet power supply performance on MRI
- Mayer D, Dreher W, Leibfritz D, Spielman D. Fast correlation peak imaging using spectroscopic RARE and circularly reduced chemical shift encoding
- Mayer D, Dreher W. Leibfritz D, Spielman D. Refocused echo amplitudes of J-coupled spin systems: effects on rare based spectroscopic imaging sequences
- Miller K, Hargreaves B, Gold G, Pauly J. Navigated 3D steady-state diffusion imaging of knee cartilage
- Miller K, Jongho Lee, Hargreaves B, deCharms C, Pauly J. Functional MRI using SSFP phase transitions
- Narayan G, Bulte J, Pauly J, Hu B, McConnell M, Yang P. Real-time imaging of transplantation of iron-oxide labeled mouse lymphocytes into ex-vivo porcine heart
- Nayak K, Amitai M, McConnell M, Hu B, Nishimura D. Imaging and quantitation of high-speed flow jets in a single breath-hold
- Nguyen P, Meyer C, Engvall J, Yang P, McConnell M. Assessment of coronary vasodilation by MRA in patients at high-risk for coronary artery disease
- Nguyen P, Nayak K, Narayan G, Liang D, Schnitger I, Brittain J, Pauly J, McConnell M, Hu B, Yang P. Dobutamine stress MR with real-time spiral SSFP – pilot clinical study
- Nguyen P, Santos J, Scott G, Engvall J, McConnell M, Wright G, Pauly J, Nishimura D, Hu B, Yang P. Adaptive real-time MR coronary angiography – prospective clinical trial
- Nguyen P, Shimakawa A, Brittain J, Hu B, McConnell M, Yang P. Spiral MR coronary angiography at 1.5T and 3T: A comparison of image quality, coverage, SNR, and susceptibility artifacts
- Orchard J, Greif C, Golub G, Bjornson B, M. Atkins. Combined registration and activation detection for fMRI: solving both problems simultaneously
- Park J, Liu C, Santos J, Sommer G, Nishimura D. Rapid measurement of superior mesenteric artery flow with ungated spiral phase-contrast
- Park J, Santos J, Nayak K, Nishimura D. Comparison of real-time and ungated phase-contrast imaging for rapid mean flow measurements
- Pauly J, Cunningham C, Daniel B. Independent dual-band spectral-spatial pulses
- Pavlin T, Scott G, Chronik B, Hughes E, Conolly S. Minimizing diffusion losses in low field hyperpolarized gas MRI using centrally ordered RARE
- Pfefferbaum A, Adalsteinsson E. Sullivan E. Reliability of brain diffusion tensor imaging
- Rakow R, Daniel B, Sawyer-Glover A, Glover G. T1 and T2 Measurements of breast tissue at 0.5 T, 1.5 T and 3.0 T
- Reeder S, Brittain J, Shimakawa A, Wen Z, Gold G, Pelc N. Imaging of articular cartilage at 3T with multi-point “Dixon” fat-water separation and SSFP
- Reeder S, Wen Z, Gold G, Pelc N. Multi-coil “Dixon” fat-water separation with ssfp imaging
- Reishofer G, Bammer R, Moseley M, Stollberger R. Automatic arterial input function detection from dynamic contrast enhanced MRI data
- Rieke V, Bammer R, Sommer G, Diederich C, Nau W, Ross A, Daniel B, Butts K. Phased array PRF shift thermometry in canine prostate
- Rieke V, Vigen K, Sommer G, Diederich C, Nau W, Ross A, Daniel B, Pauly J, Butts K. Referenceless PRF shift thermometry

Santos J, Hargreaves B, Nayak K, Pauly J. Real-time fat suppressed SSFP

Santos J, McConnell M, Scott G, Min Su Hyon, Pauly J. Multi-coil real-time interventional system

Schaffer R, Hargreaves B, Meyer C, Nayak K, Hu B, Nishimura D. Spiral steady state free precession imaging with the diminishing variance algorithm for high resolution coronary artery imaging

Scott G, Yu K, Chronik B, Conolly S. Prepolarized RF Current density imaging

Shankaranarayanan A, Carrillo A, Hu B, Wright G, Pauly J, Santos J, Brittain J. Real-time diagnostic cardiac imaging with a fast multi-coil multi-processor reconstruction system

Shankaranarayanan A, Hargreaves B, Brittain J. Steady state effects in continuously moving table axial imaging

Shankaranarayanan A, Herfkens R, Brittain J. Continuously moving table axial imaging with radial acquisitions at 3T

Slinkard M, Srinivasan V, Chronik B. Analysis of the quasistatic impedance approximation for gradient coil peripheral nerve stimulation

Thomason M, Preston A, Ochsner K, Glover G. Comparison of spiral-in/out and spiral-out BOLD fMRI at 1.5T and 3.0T

Ungersma S, Xu H, Scott G, Chronik B, Pauly J, Conolly S. Biradial shim coil design using a linear programming algorithm

Vasanawala S, Hargreaves B, Nayak K, Gold G, Pauly J, Nishimura D. Musculoskeletal imaging with phase sensitive SSFP

Venook R, Gold G, Hu B, Scott G. Automatic varactor tuning of interventional RF receiver coils

Vidarsson L, Lim K, Pauly J. Optimized T2 selective myelin imaging

Vigen K, Daniel B, Pauly J, Butts K. In vivo comparison of realtime triggered, navigated, multi-baseline thermometry with conventional respiratory triggered PRF thermometry for monitoring liver ablation

Vigen K, Jarrard J, Sullivan V, Culp J, Rieke V, Daniel B, Butts K. Simultaneous MR temperature mapping and radiofrequency ablation

Wen Z, Reeder S, Pineda A, Glover G, Pelc N. Noise performance study of symmetric three point dixon method

Yu H, Fahrig R, Pelc N. Co-registration of X-ray and MR fields of view in a truly hybrid system

Other Conferences

Baker L, Atlas SW. Managed Care and The Diffusion of MRI in the US. *International Society of Technology Assessment in Health Care (ISTAHC) 2003 International Scientific Assembly*, June 2003.

Barnes P et al. US, Conventional MRI, and DTI in very low birth weight preterm infants. *ASNR/ASPNR*. Washington, DC, April 2003 and *SPR* San Francisco, CA, May 2003.

Birdwell RL, Bandodkar P, Ikeda DM. Computer aided detection (CAD) with screening mammography in a university hospital setting. *European Congress of Radiology*. Vienna March 2003.

Cho SC, Marks MP, Do HM, Shieh P, Dejean C, Chang SD, Steinberg GK, Lopez JR. Utility of intraoperative monitoring in coiling of cerebral aneurysms. *Joint Meeting of the American Association of Electrodiagnostic Medicine and International Federation of Clinical Neurophysiology*, San Francisco, September 2003.

Chow LC, Olcott EW, Sommer FG. Clinical utility of double-bolus multidetector CT urography with sliding thin-slab MIP. *26th Annual Meeting of SCBT/MR*, March 23, 2003, Rancho Mirage, CA.

Cockroft KM, Marcellus ML, Marks MP, Chang SD, Huhn SL, Levy RP, Adler JRA, Sakamoto GT, Steinberg GK. The Stanford experience in multimodality treatment of high-flow AVMs in the pediatric population. *2003 Annual Meeting American Association of Neurologic Surgeons*, San Diego, CA, April 2003.

Do HM, Cockroft KM, Marcellus ML, Marks MP, Chang SD, Huhn S, Levy RP, Adler JR, Sakamoto GT, Steinberg GK. The Stanford experience in multimodality treatment of high-flow AVMs in the pediatric population. *Annual Meeting of the AANS*, San Diego, April 2003.

Gisondi MA, Reeder SB, Fuller SE. Need Analysis as a Curriculum Design Tool for Interdisciplinary Conferences. *Proceedings of CORD-EM: Best Practices in Residency Training—Reaching for Excellence*, Washington, DC. February 22-23, 2003,

Gobin YP, Starkman S, Duckwiler G, Pile-Spellman J, Higashida R, Marks MP, et al. MERCI 1: A safety study of embolectomy in acute ischemic stroke. *28th Annual Meeting of the Society of Interventional Radiology*, Salt Lake City, UT, March 2003.

Gold GE, Han E, J, Stainsby, GA Wright, RJ Herfkens, JH Brittain, C.F. Beaulieu. Optimization of Musculoskeletal MR Imaging at 3 Tesla. *Society of Computed Body Tomography and Magnetic Resonance 26th Annual Scientific Session*, March 23, 2003, Palm Springs, CA. Winner of Lauterbur Award for outstanding research on MRI.

Guccione S, Mari C, Yang Y-S, Lee D, Bednarski MD. Molecular Imaging of Platelet Derived Growth Factor Receptor Using MR-Guided Functional Genomic Analysis as a Method for Target Identification. *1st Annual Meeting of the Society of Molecular Imaging*, 2002.

- Guccione S, Yang Y-S, Mari, C, Li D, Bednarski MD. Molecular Imaging of Platelet Derived Growth Factor Receptor Using MR-Guided Functional Genomic Analysis as a Method for Target Identification. *AACR Special Scientific Conference Series*, 2002.
- Guccione S, Yang Y-S, Mari, C, Li D, Bednarski MD. Molecular Imaging of Platelet Derived Growth Factor Receptor Using MR-Guided Functional Genomic Analysis as a Method for Target Identification. *AACR Special Scientific Conference Series*, 2002.
- Guccione S, Yang Y-S, Homer RJ, Chang S, Harsh GR, Atlas SW, Bednarski MD. Search for Vascular Targets Using Contrast Enhanced MRI Guided Genomic and Proteomic Analysis in Human Glioblastoma Multiforme. *2nd Annual Meeting of the Society of Molecular Imaging*, 2003
- Guccione S, Yang Y-S, Homer RJ, Chang S, Harsh GR, Atlas SW, Bednarski MD. The Use of MRI in Patients with Glioblastoma Multiforme to Identify Regions of Vascular Permeability for Genomic Analysis. *94th Annual Meeting of AACR*, 2003.
- Guccione S, Yang Y-S, Homer RJ, Chang S, Harsh GR, Atlas SW, Bednarski MD. Genomic profile of Vascular Permeable Regions of Patients with Glioblastoma Multiforme for Identification of Blood Markers for Disease. *Annual Meeting of American Society of Clinical Oncology*, 2003.
- Guccione S, Yang Y-S, Shi G, Bednarski MD. Genomic and Proteomic Analysis of Temporal Changes in Tumor Progression as Delineated by Changes in Magnetic Resonance Imaging. *93rd Annual Meeting of AACR*, 2002 218-218
- Ikeda DM, Hujan S, Spielman D, Sawyer AM. Magnetic Resonance Spectroscopy of Breast Cancer. Department of Defense Era of Hope Scientific Assembly. Orlando, Florida. September 2002
- Illes J, Kirschen M, Gabrieli J.D. Emerging Trends in fMRI: Ethical Implications for Research and Clinical Medicine, Society for Neuroscience, Orlando, FL, November, 2002.
- Kirschen MP, Illes J, Gabrieli JD. New Crossroads: Neuroimaging and Neuroethics, *Stanford Brain Research Institute, Annual Retreat*, April 2003.
- Kondzioka D, Steinberg GK, Wechsler L, Meltzer C, Elder E, Gebel J, DeCesare S, Tong D, Marks MP. Neuronal transplantation for motor stroke from basal ganglia infarction: results from a phase II clinical trial. *2003 Annual Meeting American Association of Neurologic Surgeons*, San Diego, CA, April 2003.
- Lian J, Spielman D, Cotrutz C, Hunjan S, Adalsteinsson E, King C, Luxton G, Boyer A, Kim D, Daniel B, Xing L. Including Metabolic Uncertainty into Proton MR Spectroscopic Imaging (MRSI)-Guided Inverse Treatment Planning. *American Association of Physicists in Medicine (AAPM) Annual Meeting*, 2003.
- Lieskovsky Y, Spielman D, Pinto H, Goffinet D, Brown M, Le Q. Lactate-Edited MRS for Assessing Tumor Hypoxia in Head and Neck Cancer – A Comparison Study with the Eppendorf Microelectrode. *American Radium Society (ARS) Annual Meeting*, 2003.
- Marks MP, Marcellus ML, Steinberg GK, Do HM, Tong DC, Albers GW. Intracranial angioplasty for symptomatic atherosclerotic stenosis. *The Sixth Joint Meeting of the AANS/CNS Section on Cerebrovascular Surgery and the American Society of Interventional & Therapeutic Neuroradiology*, Phoenix AR, February 2003.
- Masutani T, Yoshikawa t, Aoki s, Ohtomo K, Sherbondy A, Napel S. EPI distortion correction for MR-DTI by using texture memory on graphics hardware. *17th International Congress on Computer Assisted Radiology and Surgery*. London, 2003.
- Mirmiran M, Arzoumanian Y, Barnes P, Atlas SW, Moseley M, Ariagno R. Quantitative Brain Magnetic Resonance Imaging In Preterm Infants May Predict Later Cerebral Palsy. *Annual Meeting of Society for Pediatric Research* 2002.
- Pfefferbaum A, Adalsteinsson E, Sullivan EV. Postmortem MR imaging in neuropsychiatric disorders. *American College of Neuropsychopharmacology*, San Juan, Puerto Rico, December 8-13, 2002.
- Pineda AR, Wen Z, Reeder SB, Pelc NJ. Cramer-Rao bounds in Dixon imaging using SSFP. *The Pacific Institute for the Mathematical Sciences Workshop on Inverse Problems & Medical Imaging*. University of British Columbia, August 4-8, 2003
- Reeder SB, Alley MT, Pelc NJ. Water and Fat SSFP Imaging with Four-Point Dixon Techniques. *102nd American Roentgen Ray Society Meeting*, Atlanta, GA 2002. Winner President's Award for 1st place in Radiology Resident Research Prize.
- Shi G, Hobbs SK, Homer R, Harsh G, Atlas SW, Bednarski M. Magnetic Resonance Image Guided Proteomics of Human Glioblastoma Multiforme. *AACR 2003 Annual Meeting* (Washington DC).
- Shi G, Wang Y, Hobbs SK, Guccione S, Homer RJ, Harsh GW, Atlas SW, Bednarski MD. Image Guided Proteome Analysis of Human Glioblastoma Multiforme by Two-Dimensional Differential Gel Electrophoresis. *Second Annual Meeting of the Society for Molecular Imaging* 2003, San Francisco, CA.
- Spencer D, Szumowski J, Kraemer D, Wang P, Spielman D. Temporal Lobe MRSI Following Successful and Unsuccessful Selective Amygdalohippocampectomy for Treatment of Resistant Epilepsy. *American Epilepsy Society (AES) Annual Meeting*, Dec. 2002.
- Spencer DC, Spielman DM, Zitzelberger T, Kaye JA. Magnetic Resonance Spectroscopy in the "Oldest Old" may predict progression to dementia. *American Academy of Neurology 54th Annual Meeting*, Denver, CO, April 13-20, 2002.
- Starkman S, Gobin YP, Higashida R, Marks MP, et al. The Concentric MERCI Retriever for the treatment of neurovas-

cular thrombotic occlusions MERCI: A phase I non-randomized trial. *28th American Heart Association Meeting*, Phoenix, AR, February 2003.

Wang SL, Dake MD, Razavi MK, Kee ST, Frisoli JK, Sze DY. Nitinol Stents in TIPS. Poster Session, *Society of Interventional Radiology Annual Meeting*. Salt Lake City, UT: March, 2003.

Xing L, Hunjun S, Cotrutz C, Boyer AL, Gibbs I, Le Q, Donaldson SS, Chang SD, Heilbrun P, Adalsteinsson E, Spielman DM. Inverse planning for functional image-guided IMRT. *American Society for Therapeutic Radiology and Oncology (ASTRO) Annual meeting*. Oct. 6—10, 2002, New Orleans, LA.

Yang Y-S, Guccione S, Bednarski MD. Comparing genomic and histological correlation to radiographic changes using a squamous cell carcinoma tumor model. *Proceeding of the 2nd Annual Meeting of the Society of Molecular Imaging*, San Francisco, 2003.

Yang Y-S, Guccione S, Shi G, Bednarski MD. Genomic analysis of squamous cell carcinoma tumors models based on spatial and temporal changes in contrast-enhanced MRI, *AACR Special Scientific Conference Series*, 2002.

Yang Y-S, Guccione S, Shi, G, Bednarski MD. Genomic analysis of squamous cell carcinoma tumors models based on spatial and temporal changes in contrast-enhanced MRI. *1st Annual Meeting of the Society of Molecular Imaging*, San Francisco, 2002